Institutsbereich Geophysik, Astrophysik und Meteorologie
Institut für Physik
Karl - Franzens - Universität Graz
Universitätsplatz 5, A-8010 Graz, Austria
http://www.uni-graz.at/igam

Wissenschaftlicher Bericht No. 22

Assimilation of GNSS Radio Occultation Data into GCM Fields for Global Climate Analysis

by
Armin Löscher

December 2004

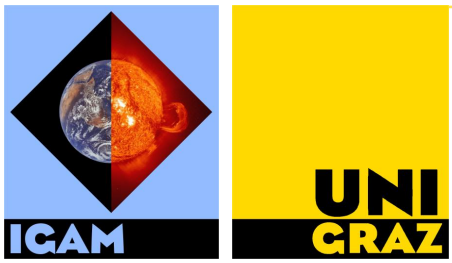

The presence of those seeking the truth.
is infinitely to be preferred to the presence.
of those who think they have found it.

Terry Pratchett; Monstrous Regiment

Contents

Acknowledgments

I would like to thank my supervisor Prof. Dr. Gottfried Kirchengast for his overall support, distinguished scientific discussions and the provided opportunity to work within the ARSCliSys team. This work was made possible due to the financial support by the START research award of G. Kirchengast, funded by the Bundesministerium für Bildung, Wissenschaft und Kultur (BMBWK, Vienna, Austria) and managed under the program No. Y130-N03 of the Fonds zur Förderung der wissenschaftlichen Forschung (FWF, Austria).

I am grateful to Prof. Reinhart Leitinger for co-reading this thesis and Prof. Helfried K. Biernat for the support to conclude my thesis as part of the examination committee.

I want to thank the team at DMI , and I am especially grateful to Dr. Hans Huang for many fruitful discussions and Prof. Per Høeg for the unbureaucratic way my three-month working visit was handled at DMI Copenhagen.

Furthermore, I would like to thank all the members of the Institute for Geophysics, Astrophysics, and Meteorology (IGAM), Institute of Physics, University of Graz, Austria, for fruitful discussions and support concerning many scientific and programming related topics and issues. Not to mention the good teamwork and excellent personal working environment. Special thanks goes to my colleagues of the ARSCliSys research group, especially to Andrea Steiner for providing the error characteristics of the CHAMP data, Ulrich Foelsche for discussions concerning geophysics and providing plots, Marc Schwärz, Christian Retscher, and Johannes Fritzer for helping to solve programming and computational issues and other fruitful discussions and Andreas Gobiet and Michael Borsche for support concerning the CHAMP data and providing the CHAMP based climatologies.

Thanks go to ECMWF for providing data and especially to Mike Fisher and Eric Anderson for providing the error characteristics, to Jens Wickert and Thorsten Schmidt at GFZ Potsdam for the excellent cooperation concerning CHAMP and to INRIA and their very useful adjoint compiler.

Most of all I want to thank my family for the moral and financial support in hard times and precarious financial situations and the faith in me over all those years. Even though some of the problems only a physicist really understands they where always there when I needed them.

In the end, I want to thank all my local and international friends, who strolled out with me for a beer or two, and all the pubs and bars which served the drinks, and helped me to endure rainy days and times of stress. Finally I'm grateful to all the locations around my office which prevented me from starvation, by providing some kind of food and drinks.

Introduction

The issue of global climate change mostly known under the concept of *global warming* encounters growing public interest during the recent years. This issue is tackled on an international base by the IPCC (Intergovernmental Panel on Climate Change), and the ongoing debate whether there is a climate change triggered by human influence, and if what are the consequences, is quite lively.

NWP (Numerical Weather Prediction) systems have reached a certain level of maturity due to ongoing research and development on the one hand an exponential increase in computing power on the other hand. With these developments also GCM's (Global Circulation Models) to simulate the global climate within an expanded timeframe inherited many advanced techniques. Not to mention the increase of available information, namely observations, which are available in numbers which tremendously increased during the recent decades.

A key role for these new observations plays the increasing number of satellite platforms carrying a wide variety of new instruments delivering an increasing amount of data with global coverage. New observation concepts have to prove to be superior to older ones and/or provide added *value* till they are used on an operational base. In contrast *purely* scientific missions such as ENVISAT (Environmental Satellite) or CHAMP (Challenging Mini Satellite Payload) often play the role of *proof of concept missions* and quasi operational testbed for future fully operational platforms (the term *operational* often concerns standard quality assurance procedures and stringent time constraints, as for example NWP systems can only use observations within limited time windows).

Relatively new concepts like RO (Radio Occultation) offer the opportunity to develop new processing techniques and strategies to exploit the data in the best possible and most efficient way. The RO experiment on-board CHAMP is the first system which delivers continuous observations on a quasi-operational basis, preparing the ground for the first RO-only based global climatologies. With the GRAS (GNSS Receiver for Atmospheric Sounding) sensor on-board the METOP (Meteorological Operational Satellite) satellite a fully operational system delivering RO observations will be available soon. On the other hand the development of NWP systems during the last years improved the forecast skill and the quality of the analyses continuously. So it would be interesting to use the NWP methodology to introduce data into the model (in our case 3D-Var), first with single sets of observations, later with whole climatologies, to study the increments of monthly and seasonal mean fields.

This would allow to deliver a second set of global climatologies, which are somewhat adjusted by ECMWF analyses, to the community, besides the RO-only based ones. Secondly this would allow interesting insights into potential biases in the ECMWF analyses,

which are assumed to be the dominating error structure of monthly and seasonal mean fields. Furthermore, the future prospect of an unbroken chain of RO instruments on orbital platforms is realistic and would deliver an unmatched record of global climate data if continued for several decades, possibly being a key factor in distinguishing between natural variability and anthropogenic climate change in future. This work is dedicated to contribute achievement of these goals, and to exploit RO data in the best possible way via climate data assimilation systems. The work is organized as follows.

Chapter 1 A brief overview on the atmosphere and climate in general and on detecting trends and climate change in some more detail is given. Building of climatologies based on remote sensing data is briefly explained and illustrated by a state-of-the-art example, utilizing RO data.

Chapter 2 The principles of data assimilation are explained, with a focus on 3D-Var, the methodology used in this work. Some of the numerical pitfalls are shown, and the mathematical background is explained briefly.

Chapter 3 The kind of data which is used for the assimilation experiments is introduced. On one hand the ECMWF model data, which we used as background and on the other hand the CHAMP RO data. Both sources of information are specified here in some detail, with a brief outlook on future model updates and RO missions.

Chapter 4 Here the specific implementation of the refractivity-only and the temperature, specific humidity and surface pressure (TQPsurf) 3D-Var systems is described in detail. The realization of control space transformations and the preconditioning is explained, as well as the use of recursive filters within this framework. The observation and background covariance matrices are defined, and the derivations of background refractivity standard deviation and correlations are illustrated. The observation operators are described in detail and the minimization routine is introduced.

Chapter 5 Within this Chapter, the test procedures of both modes of the assimilation framework (refractivity and TQPsurf analysis), are described. The error patterns methodology was applied for first experiments, to simulate real conditions, and assimilation runs with raytraced data were conducted. The data thinning as part of the preprocessing of observations is described here. The convergence behavior of both assimilation modes is shown.

Chapter 6 Here the results of assimilating real CHAMP data for both assimilation modes are shown. Deficiencies of the input data (at the moment retrieved CHAMP refractivity profiles are showing a small systematic deviation), of the background data (southern winter hemisphere polar vortex model representation), analysis increments, and the convergence behavior are shown. The result of processing one month of CHAMP data is presented, which served as the monthly mean analysis test case completing this work.

Conclusions The conclusions of three and a half year of work, concerning the assimilation of radio occultation data to build global climatologies are drawn here, an outlook is given and future perspectives are discussed.

Appendices Additional information

1

Atmosphere and Climate

1.1 The Atmosphere

The Earth's atmosphere is characterized by an exponential decrease of density and pressure. Here the atmosphere is denoted as the volume below the exosphere (height 500 - 600 km), nevertheless 80% of the total mass is concentrated in the troposphere. The vertical structure and its classification is shown in Fig. 1.1. Also almost all weather phenomenons are bound to the troposphere, the main constituents of the atmosphere are shown in Tab. 1.1, [*Malberg* (2002)].

Name	**Chemical Symbol**	**Dry Air [Vol%]**	**Moist Air[Vol%]**
Nitrogen	N_2	78.08	77.0
Oxygen	O_2	20.95	20.7
Argon	Ar	0.93	0.9
Carbon Dioxide	CO_2	0.033	0.03
Trace Gases	Ne, He, Kr, CH_4, H_2, O_3, SO_2	< 0.01	< 0.01
Water Vapor	H_2O	-	1.3

Table 1.1: Main atmospheric constituents.

From the climatological point of view H_2O as water vapor, CO_2, O_3 and CH_4 are playing key roles in the atmospheric radiation budget. They are denoted as *Greenhouse* gases beside other trace gases of minor importance.

1.1.1 The Physical Composition of the Atmosphere

The atmosphere can be described by the laws of thermodynamics and the Newtonian equations of motion, and is dominated by the incident solar flux (at the top of the atmosphere ~ 1372 Wm^{-2}) [*Salby* (1996)]. Secondly; the global biosphere is dominated by the radiative equilibrium, which is determined by the in- and outgoing electromagnetic fluxes (cf. Section 1.2.1). In Fig. 1.1 a vertical profile of temperature against altitude and

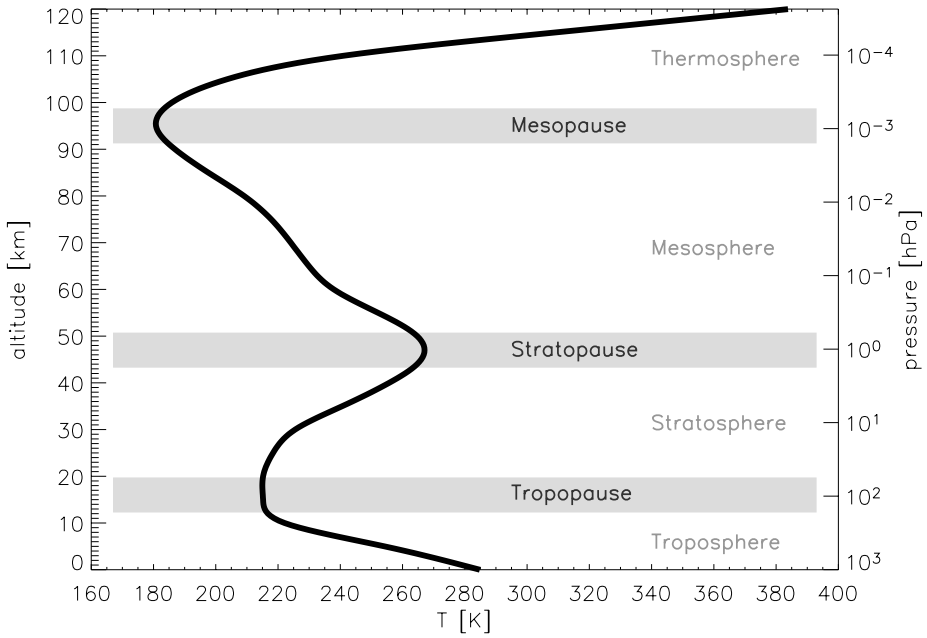

Figure 1.1: Atmospheric temperature profile based on the CIRA-86 climatology (courtesy C. Retscher, IGAM/UniGraz).

pressure is depicted (based on the CIRA-86 climatology), showing the principal vertical classification of the atmosphere in a thermal sense. An alternative approach is to use the physical-chemical mixing behavior of the atmospheric constituents. This classification is based on homogenous mixing of the atmospheric constituents; up to 100 km (homosphere) caused by turbulent air motions (mostly large scale convections in the troposphere and small scale eddies beyond that region) whereas above, diffusion stratifies the constituents according to their molecular and atomic mass, respectively [*Raith* (1997)]. In our application we are confined to the troposphere and stratosphere, considering especially the vertical interval between the surface and 35 km.

1.1.2 Parameters Describing the Atmospheric State

In principle there is a wide variety of parameters necessary to describe the atmospheric state. In practice, i.e., in the case of GCM's, used for numerical weather prediction or climate change simulations, the number of simulated parameters has to be cut down to computational feasible numbers. In fact most parameters depend on each other, making the overall situation even more complicated. Nevertheless, dependent on the specific application, the atmospheric state can be broken down into a limited number of largely independent parameters with, to a certain extend, small cross correlations. These decompositions (for example PCA) have to be done very carefully, by reducing the number of variables one has to be deliberate not to discard essential information. Besides these facts, the atmosphere is closely coupled with the oceans and the land, which makes it even more

complicated to describe the global atmosphere within a numerical model, where all these correlations should be taken into account (coupled atmosphere, ocean, ice sheets and land models).

In our application the atmospheric key parameters such as temperature, specific humidity and surface pressure are taken into consideration. The derivation of further parameters like, geopotential height, pressure and refractivity are occupying a central position in our considerations.

1.2 Climate

1.2.1 Climate Change

Climate change on a global scale is classifiable into two categories, natural variability and anthropogenic climate change. The Earth's climate is not a static system and is subject to constant changes over the centuries. Careful analysis shows some periodicity within the parameters used for climate analysis over long time frames [*Burroughs* (2001)].

Periodic Climate Cycles

The main source of energy to drive the global atmospheric system is the sun, which behaves approximately like a black body of 6000 K surface temperature. The emission of radiation by the Earth is more complicated to describe, but a simple model would be a black body of 287-288 K surface temperature. Changes in the Earth's climate must be discussed in the context of factors which control the radiation balance of the Earth. One important factor is how the Earth's orbit around the sun and its own rotation around its tilted axis controls the amount of solar radiation falling on the globe. This regular changes are almost constant in time[1] and control the daily (*diurnal*), seasonal and annual cycles which dominate the climate on Earth. Beside this rather short term variations, the long term variations in orbital parameters like eccentricity (e) of the Earth's orbit, the tilt of the Earth's axis to the orbital plane and obliquity of the ecliptic (ε), which change periodically, do matter. Each of this orbital elements is a quasi-periodic function of time. The variation of these parameters combine to effects affecting the amount of received solar radiation over time scales from thousands of years to million of years. The sun's activity follows a mean 11.2 years cycle with distinctive maxima and minima where the total amount of emitted energy varies about 0.1%, which is rather little, but much of the change in the solar output is concentrated in the UV part of the spectrum. The theory of the climatic effects of the orbital variations are often denoted as the Milankovitch cycles.

Causes for Climate Change

Beside the already mentioned cyclic variations, the climate can be changed, at least temporary by *single events*. This might be volcanic eruptions or even bolide impacts, which happened regularly in the past. These and other causes for climate change can be denoted

[1] Earth's rotation is slowing down $\sim$ 2 milliseconds per century due to tidal friction.

as natural, whereas especially during the last century the human race developed the potential to alter the climatic circumstances on a global scale, which will be discussed briefly within the next Section.

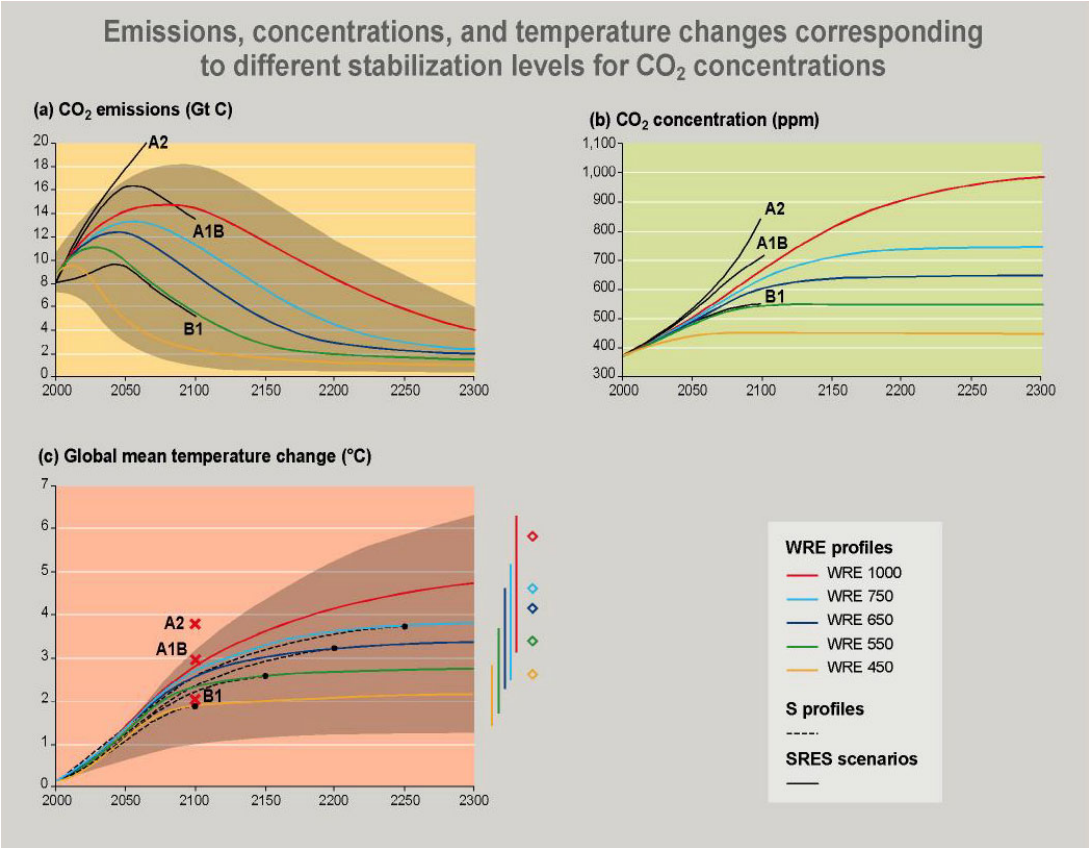

Figure 1.2: Comparison of different CO_2 emission scenarios, their impact on atmospheric CO_2 concentrations and the consecutive forecasted increase of global mean temperature, IPCC Report 2001.

Anthropogenic Climate Change

Common opinion suggests that at least a fraction of recent climate change can be attributed to human activities. Not only the production of greenhouse gases have to be taken into account, but also the change of land use like deforestation and urbanization have to be considered. Nevertheless the most prominent issue is the increase of the global atmospheric concentration of radiative active gases like CO_2, which contributes significantly to the *global warming* in every scenario. Estimations suggest a radiative forcing of about ~ 2.5 Wm^{-2} caused by the, since the industrialization, constantly increasing atmospheric levels of CO_2. Fig. 1.2 depicts several emission scenarios and their expected impact onto global mean temperatures [*Houghton et al.* (2001)]. One has to be aware that besides the green house gases other factors may damp down or enhance global warming in a highly non linear way, like change in albedo or dust content of the atmosphere. Pre-

dicting climate change is a delicate task, taking into consideration that numerical weather prediction models are able to deliver relatively reliable forecast for up to 10 days. These models, which are constantly at the limit of which is numerically manageable concerning resolution and number of variables, still have problems to cope with sudden switches in circulation patterns of stable regimes. To overcome this problem a statistical approach is used to identify these regimes by starting with slightly different initial conditions (ensemble forecasts). For climate models, which have to calculate global data fields for decades or even hundreds of years into the future, the general approach concerning the resolution and number of variables has to be different. One of the probably most important things that climate models can inherit from NWP models is the physics behind several processes (e.g. cloud formation, surface fluxes, etc.), which are extremely important on the long run.

Retrospective Climate Analysis

Retrospective climate analysis brought a lot of insight into natural variability and the occurrence of natural cycles. As mentioned later the historical data record is quite limited. In the Section about proxy data some of the sources of information are mentioned to reconstruct paleoclimatic circumstances. These retrospective analyses over great time frames also helped to discover cyclic changes mentioned earlier, which are very important to distinguish between the several causes, which trigger alteration within the global climate system. These kind of analysis leads to important insights into the climate system. Another kind of retrospective analysis in known as *reanalysis* which basically means to run a NWP system with a fixed development state of the model for several past years, using all the available observations (e.g. ECMWF, ERA40). This exercise helps on one hand to find model deficiencies and on the other hand to get an unbroken record over a longer time-frame. In practice a model is updated and enhance in a regular manner, making it complicated to compare results of different model versions. Furthermore the newer model versions can exploit historical data in a more sophisticated way, delivering added value.

Climate Monitoring

During the last century a dense global observation network evolved, mainly for the purpose of weather prediction. It consists of a global network of ground stations which conduct measurements to agreed times and various stations are starting balloon sondes for vertical atmospheric sounding. Furthermore observations are carried out from planes, ships and buoys. The global observation network is complemented by satellite observations, which are steadily growing in importance. This information is collected and incorporated into the numerical weather prediction models by the NWP centers globally. The variety of information, often in conjunction with sophisticated computer models is also the main source of present global climate change monitoring.

Direct Observations The time frame of which direct observations are available is naturally very limited compared to the age of the Earth. Some time series of temperature measurements, spanning several hundred years, are available from the same location. Even to interpret this data is tricky, taking the change of instrumentation and land use of the

surrounding area (e.g. deforestation, urbanization) during the centuries into consideration. Another example is sea surface temperature along the trade routes. During the last century the number of global observations increased continually, covering even the most remote places on Earth during the last decade, by the use of remote sensing techniques.

Proxy Data Most of the data used nowadays to reconstruct past global climate is so called *proxy data* which allows to derive parameters like mean temperature or precipitation. But one has to be very careful to interpret the various sources of information correctly. Typical examples of proxy data are tree rings, lake and ocean sediments, ice cores and chemical composition of sea shells. Many of these methods depend on chemical analysis and the proportion of isotopes, derived by mass spectroscopy. Some information can also be derived from human records other than direct observations, like time of wine harvest or amount of harvest and crop prizes.

Atmosphere Model	ECHAM5-MA(MPIM Hamburg)	Change Monitoring:	in JJA seasonal average fields as they evolve from 2001 to 2025
Model Resolution	T42L39	Domain:	17 latitude bins of 10° width 24 height levels from 2 km to 50 km
Model Mode	Atmosphere only (monthly mean SST)	Vertical Resolution:	1-2 km
Model Runs	1 run with transient GHGs+Aerosols+O_3, 1 control run (natural forcing only)		

Table 1.2: ECHAM5 model run parameters.

1.2.2 Detecting Climate Change

One issue in detecting climate change, is the dispensability of accurate and consistent observations over long time frames, where you can identify and remove periodic cycles, prior to the analysis, which yields the natural variability and possibly underlying trends. That kind of data is not available, neither locally, nor least of all globally. The global coverage was significantly improved over the last decades, using Earth observation satellites. The nature of that kind of observations is mostly indirect, i.e. parameters like temperature can not be deduced directly. As an example, radiometers to determine vertical temperature profiles are in fact measuring radiances. Another problem in getting consistent data series is the change in instrumental properties during the lifetime of these instruments. The same applies to successive generations of instruments in orbit, which makes it difficult to merge the data series in a consistent way (e.g. appearance of discontinuities). To be able to merge the data sets in a consistent way, a substantial overlap in time of different instruments and different generations of instruments is necessary.

One of the advantages of the radio occultation technique is the theoretical *self calibrating* nature of the observation (cf. Section 3.2), which makes it comparably easier to confer and match the observations of different instruments and platforms.

Another challenge is the choice of atmospheric parameters to detect climate change. For example if one uses refractivity, which is a derived parameter, one has to be aware what exactly happens, if different atmospheric parameters are changing. A very interesting example is the change in zonal refractivity as it evolves during a 25 years model run, which was performed in the CLIMATCH project of IGAM/UniGraz with MPI Hamburg [*Foelsche et al.* (2003)]. The used parameters for this model run can be seen in Tab. 1.2.

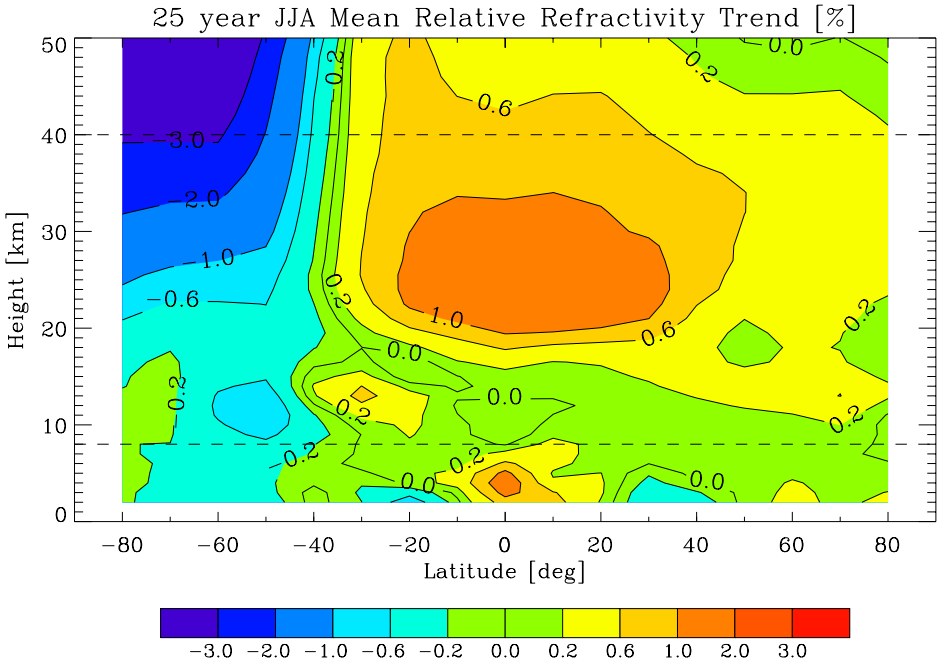

Figure 1.3: JJA mean relative refractivity trend of a 25 year ECHAM5 model run (courtesy U. Foelsche, IGAM/UniGraz).

A positive temperature trend of about 1 K, roughly between 10 km and 20 km, can be seen evolving after 25 years (cf. Fig. 1.4, upper panel), which is not mirrored in the refractivity trend (cf. Fig. 1.3). The relative change of refractivity in the same region is effectively zero. This surprising fact can be easily explained, looking at the change in pressure at Fig. 1.4 lower panel, which compensates the change in refractivity, caused by the increase in temperature (for the exact correlations see equation 4.3). This example shows, that conclusions can only be drawn after careful considerations, and taking the *big picture* into account.

1.2.3 Climatologies

Applications for climatologies are not only found within a framework for studying climate change, but also as first guess for retrieval procedures, guidelines in engineering and

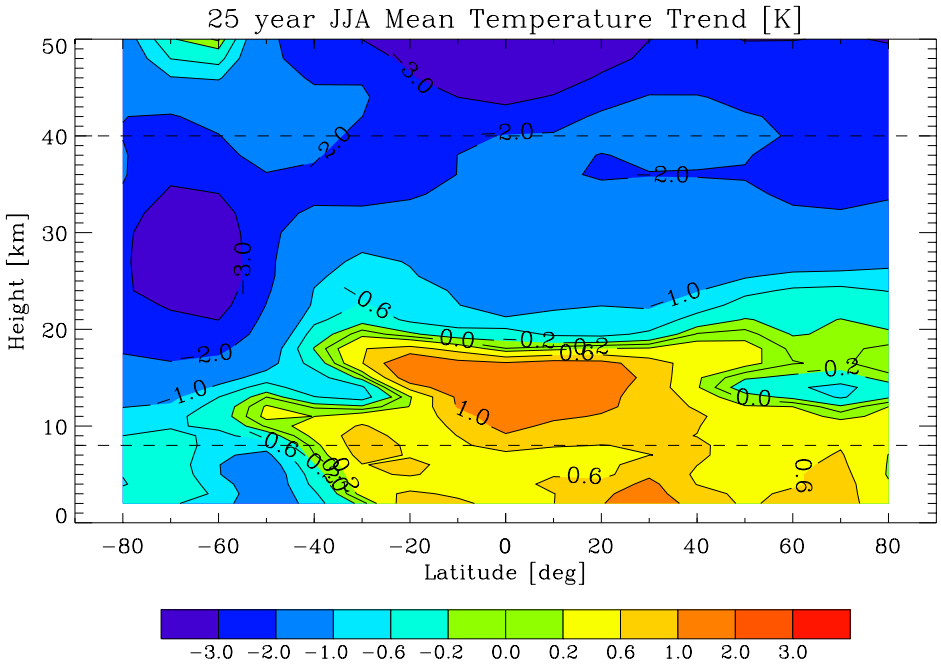

JJA mean relative temperature trend of a 25 year ECHAM5 model run.

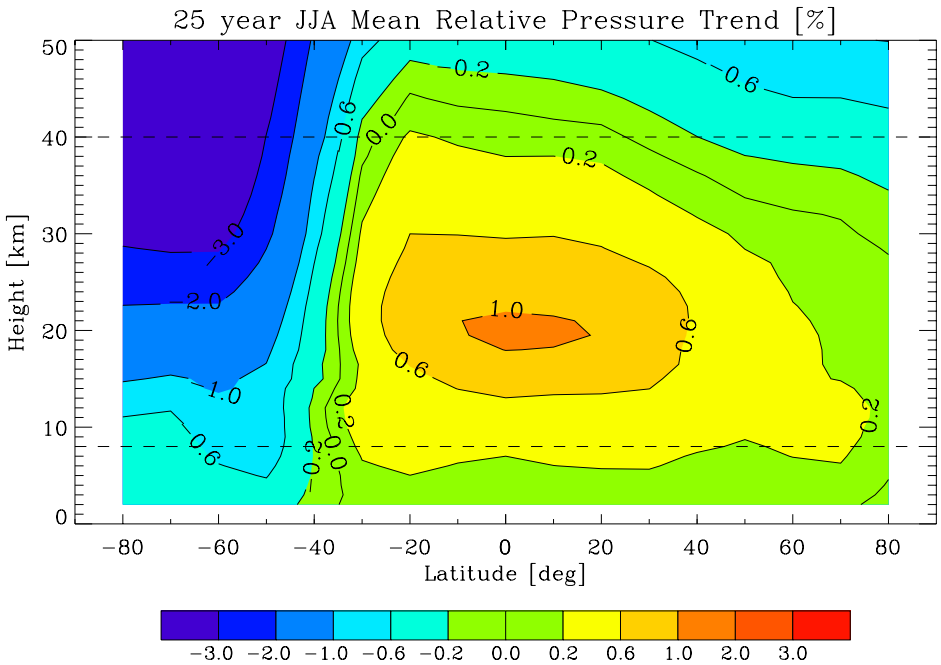

JJA mean relative pressure trend of a 25 year ECHAM5 model run.

Figure 1.4: Validation of error patterns implementation by reconstructing the refractivity standard deviation and the bias (courtesy U. Foelsche, IGAM/UniGraz).

construction, or as a first step for cost assessments of insurance companies, just to mention a few applications. There are *standard* climatologies existing like CIRA [*Rees* (1988)] and MSISE [*Hedin* (1991)] which have their deficiencies [*Randel et al.* (2002)].

As for the weather as a *chaotic* system it is vital to know the initial state of the atmosphere as accurate as possible before a new forecast run of a NWP system is conducted. Due to recent developments (4D-Var) this *initial state* is somewhat *blurry* because of taking the time dimension into consideration, which means comparing the observations at the appropriate time with the model values, instead of condensing this comparison at fixed time intervals (cf. Section 2.8). Another interesting application would be the comparison of independent climatologies of monthly or seasonal means with the corresponding mean analysis fields of e.g. ECMWF to detect model biases.

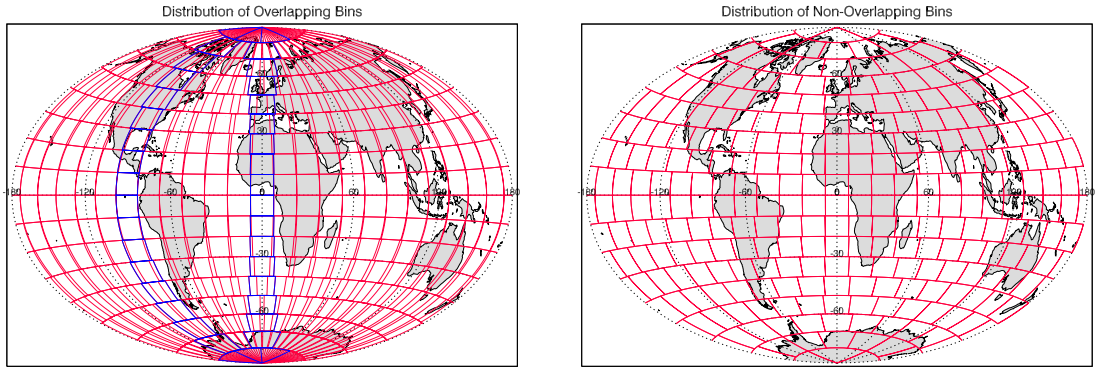

Figure 1.5: The two modes of the direct binning. Overlapping equal area bins at regular 18 latitude x 24 longitude grid, with three exemplary latitude bins highlited to the left and non overlapping equal area bins at 18 latitude x longitude dependent longitude grid to the right (courtesy M. Borsche, IGAM/UniGraz).

Radio Occultation Based Climatologies

As an example the radio occultation based climatologies, which are the main product of the CHAMPCLIM project, a joint undertaking of the IGAM/UniGraz and the GFZ Potsdam are explained here briefly. The main objective of this project is to exploit the CHAMP radio occultation data in the best possible manner for climate monitoring. The climatologies are based on the complete CHAMP RO data set provided by GFZ at excess phase level (GFZ level 2), which is processed to obtain atmospheric profiles of refractivity, geopotential height and temperature (humidity profiles are foreseen for the near future). The processed data is validated against ECMWF analysis fields at T42L60 resolution, which serve as a reference. The goal is to provide monthly and seasonal mean climatologies by direct binning and comprising rigorous error statistics in order to monitor the error characteristics of both RO profiles and ECMWF data. Additional quality checks will be performed using selected RAOB sites and complementary satellite data (e.g. Envisat/ MIPAS). The direct binning grids for the climatologies are set up in two modes, which differ in the arrangement of the equal area bins into which the profiles are averaged (cf. Fig. 1.5). Along latitude, both modes have the meridian divided into 18 bins of 10°

width (or a multiple/fraction thereof). Along longitude, the first mode (cf. Fig. 1.5 left panel) uses a fixed 24 bins (baseline) at all latitudes, leading to bin overlapping, whilst the second mode (cf. Fig. 1.5 right panel) uses a latitude-dependent number of bins such as to obtain non overlapping equal area bins. While climatologies on the regular latitude $\times$ longitude are most convenient to handle, comparison to the second mode allows study of the potential relevance of error correlations between overlapping bins. In Figs 1.6 to 1.9 the first preliminary results for seasonal zonal mean climatologies of dry temperature of the year 2002 and 2003 are presented[2]. One of the striking features is the southern winter polar vortex which can be seen for 2002 as lower panel in Fig. 1.8 and for 2003 as lower plot in Fig. 1.8, showing the potential of RO based climatologies (more details on RO data cf. Section 3.2). Within the next chapters a second approach to exploit the radio occultation data will be presented, adding another set of climatologies, which are the result of an optimal fusion process, of the RO observations and ECMWF analysis fields, performing a statistical approach (in our case 3D-Var). These climatologies will offer interesting insights into the error characteristics of the data fields as mentioned in Section 1.2.3. It is vital for this statistical optimization procedure, to have a good idea about the error characteristics of all fields which enter the assimilation procedure, so great emphasis is given to a rigorous error estimation of the RO-only based climatologies.

[2]Data and plots provided by M. Borsche, worked out by the CHAMPCLIM project team of IGAM/UniGraz [*Gobiet et al.* (2004)].

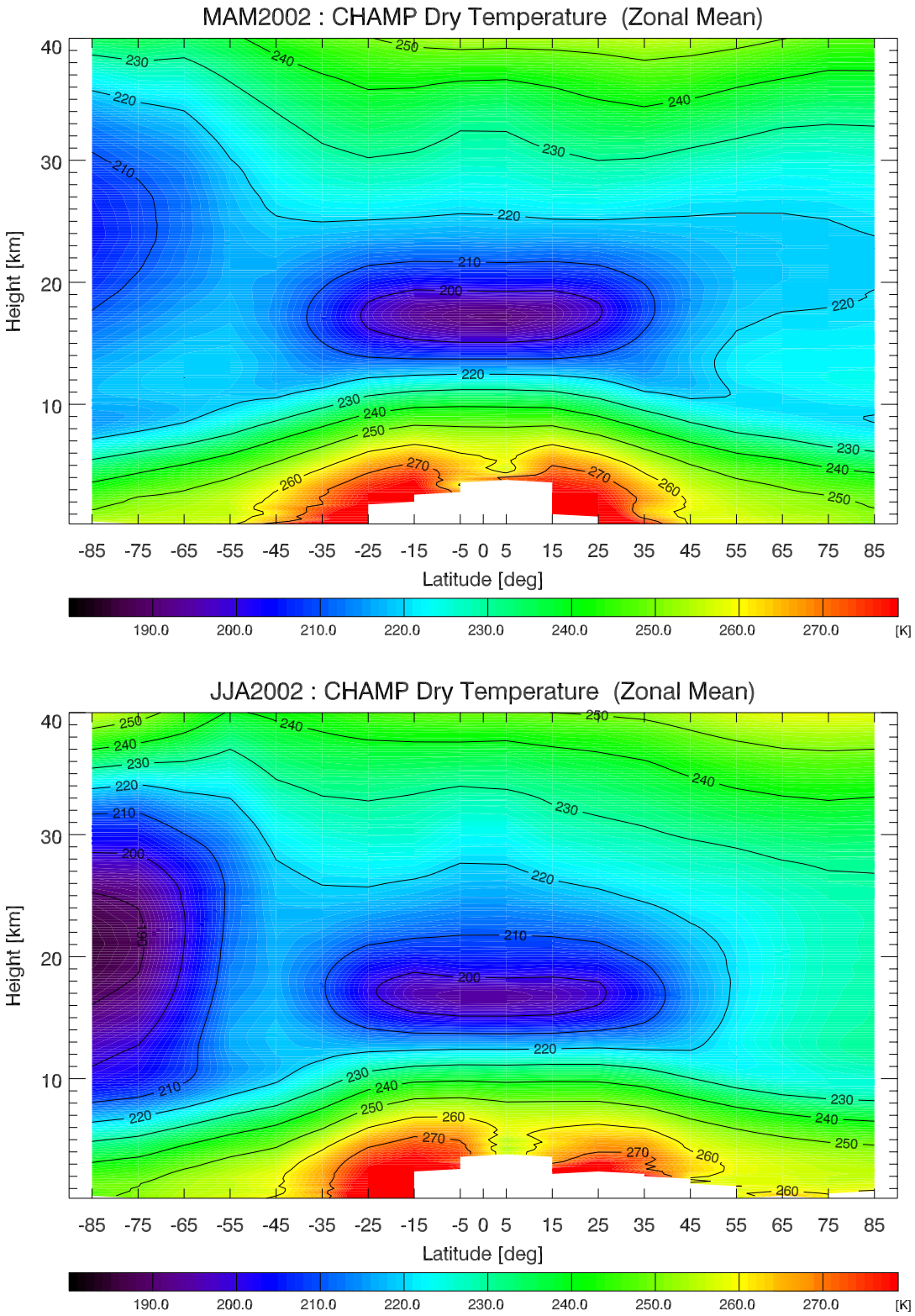

Figure 1.6: CHAMP based seasonal climatologies for March, April, May and June, July, August 2002 (courtesy M. Borsche, IGAM/UniGraz).

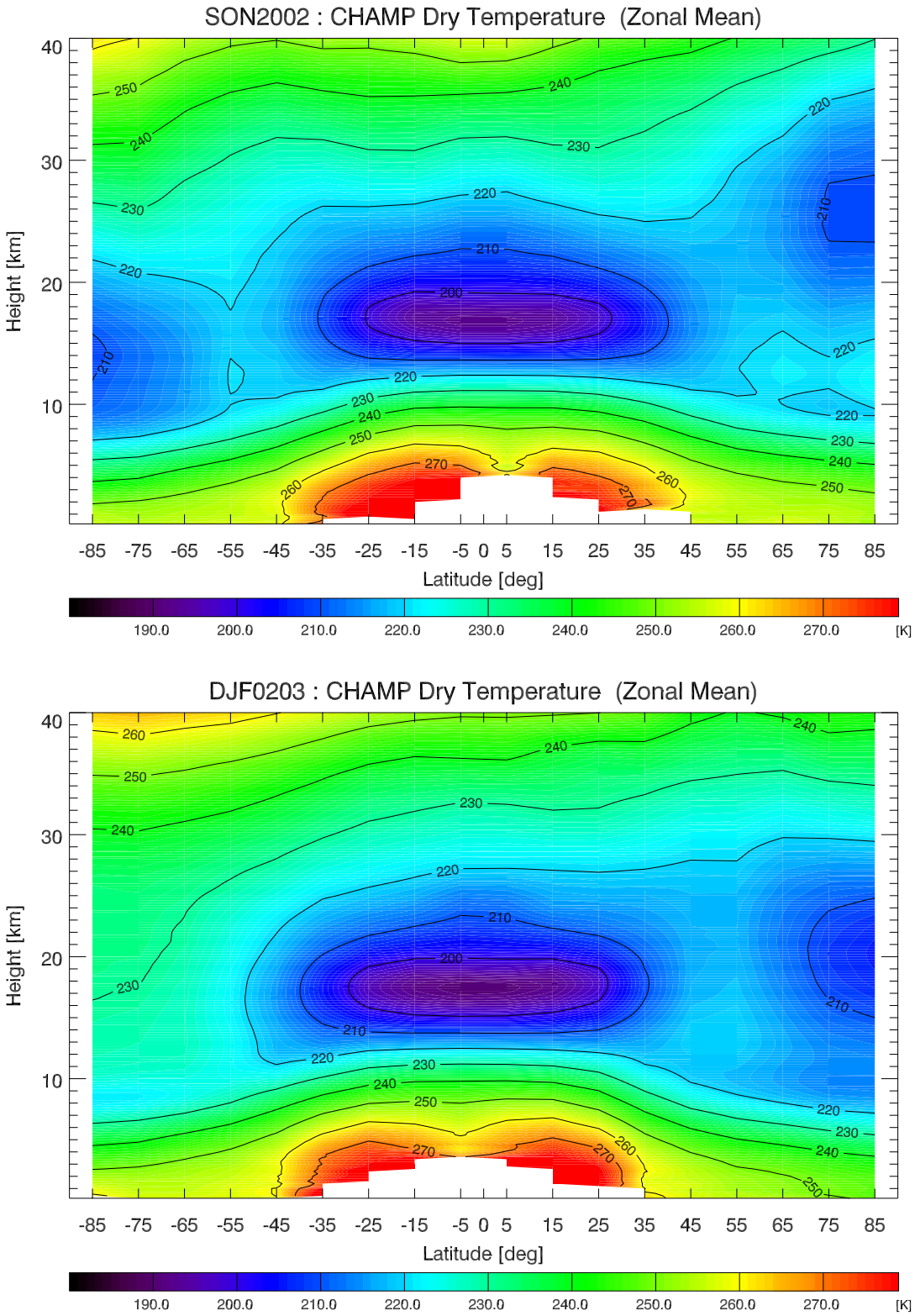

Figure 1.7: CHAMP based seasonal climatologies for Sep., Oct., Nov. and Dec., Jan., Feb. 2002/2003, (courtesy M. Borsche, IGAM/UniGraz).

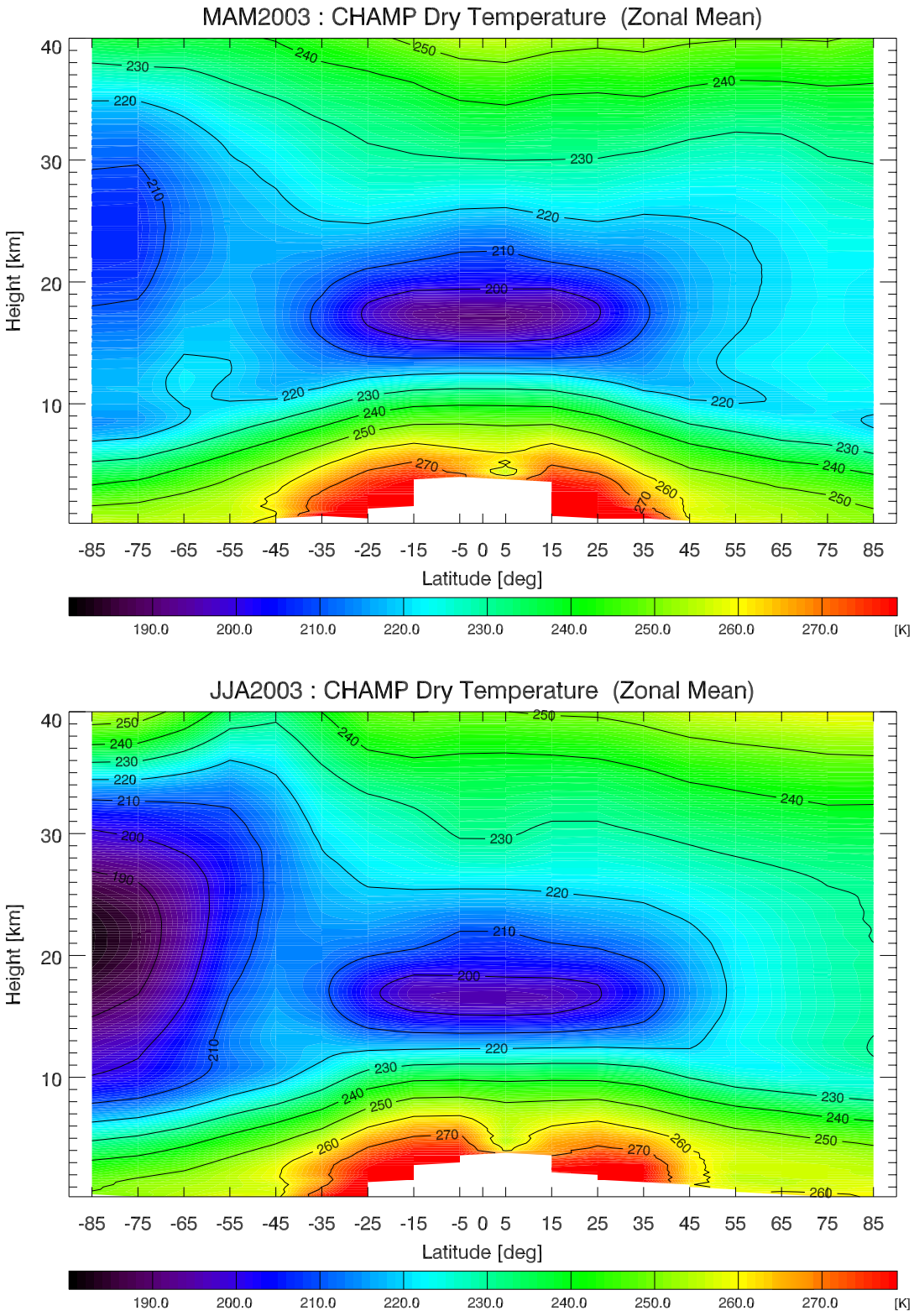

Figure 1.8: CHAMP based seasonal climatologies for March, April, May and June, July, August 2003 (courtesy M. Borsche, IGAM/UniGraz).

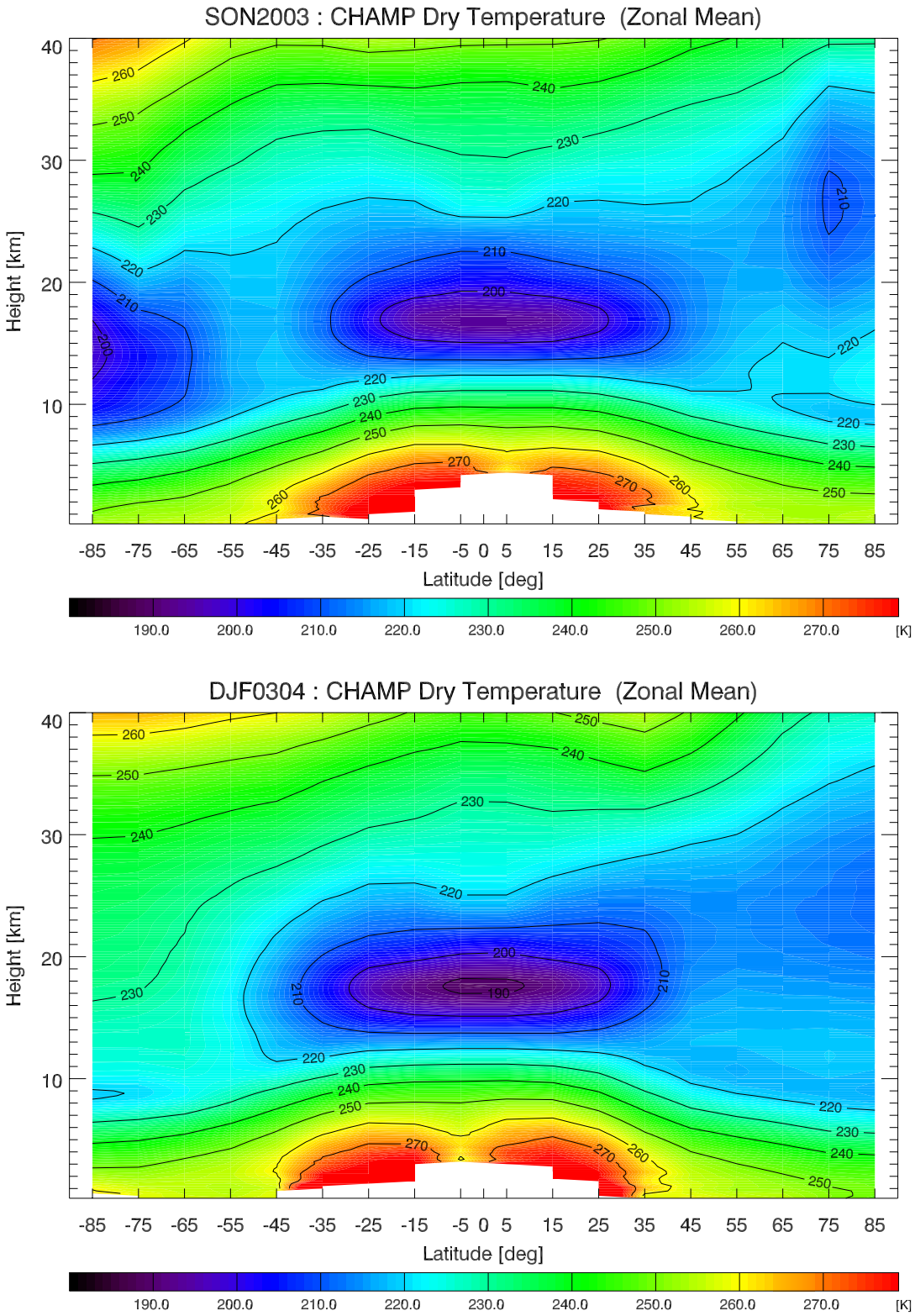

Figure 1.9: CHAMP based seasonal climatologies for Sep., Oct., Nov. and Dec., Jan., Feb. 2003/2004, (courtesy M. Borsche, IGAM/UniGraz).

2

Assimilation Concepts

The atmospheric system can be simulated effectively by discrete numerical models, and, provided that the initial state of the system is known, accurate forecasts of future dynamic behavior can be determined. Complete information defining all of the states of the system at a specific time are, however, rarely available. Moreover, both the models and the measured data contain inaccuracies and random noise. In this case, observations of the system measured over an interval of time can be used in combination with the model equations to derive estimates of the expected values of the states. The problem of constructing a *state estimator*, or *observer*, for the system can be treated by using feedback design techniques from control theory. For the very large nonlinear systems arising in climate, weather and ocean prediction, however, traditional control techniques are not practicable and *data assimilation* schemes are used instead, to generate accurate state-estimates. The aim of data assimilation is to incorporate measured observations into a dynamic system model in order to produce accurate estimates of all the current (and within a model framework future) state variables of the system in a statistically *optimal* way. The problem can be stated as follows.

Problem 1 *Given a (noisy) discrete model of the dynamics of a system, find estimates of the system states from (noisy) observations.*

So the basic goal of an assimilatation procedure is the generation of an analysis, which is an accurate image of the true state of the atmosphere at a given time, represented in a model as a collection of numbers. An analysis is useful in itself as a comprehensive and self-consistent diagnostic of the atmosphere, but is also used as input data to other operations like the initial state for a numeric weather forecast system, or it can provide a reference against which to check the quality of observations. The basic objective information which is available to produce the analysis is a collection of various observed values provided by observations of the true state. If the model state is overdetermined by the observations then the analysis is reduced to an interpolation problem. Usually the analysis problem is under determined because of data sparse areas and data which is only indirectly related to the model variables. Nevertheless the problem is sometimes locally overdetermined in areas of high data density. In order to make the problem well

posed, it is necessary to rely on some *background* information in the form of an a priori estimate of the model state, which can be a climatology, a trivial state, generated from the output of a previous analysis, using some assumptions of consistency in time of the model state, or the evolution predicted by a forecast model. Some physical constraints on the analysis problem can also help to get a better posed problem. So the basic concept of data assimilation is, that a well behaved system allows to accumulate information in time into the model state and to propagate it to all variables of the model.

Definition 2 *Data assimilation is an analysis technique in which the observed information is accumulated into the model state by taking advantage of consistency constraints with laws of time evolution and physical properties.*

There are two approaches to this problem, which is *sequential* assimilation, a technique which only considers observation made in the past until the time of analysis (real time assimilation systems) and *non-sequential* or *retrospective* assimilation, where observations from the future can be used (for example in a reanalysis). Another way to break down the methods is the distinction if they are *intermittent* or *continuous* in time. The physically more realistic approach of continuous assimilation considers observations over longer periods, so the correction to the analyzed state is smooth in time. The technically more convenient intermittent method considers observations only in small patches [*Nichols* (2003)], [*Swinbank et al.* (2003)], [*Kozo* (1997)].

2.1 A Simple Approach-the Cressman Scheme

Most material presented in this Chapter is based on presentations during a NATO ASI workshop in Italy 2003 and ECMWF training courses [*Swinbank et al.* (2003)], [*F. Bouttier* (1999)], [*ECMWF* (2004b)]. The Cressman analysis scheme is a simple algorithm in which the model state is set equal to the observations in the vicinity of available observations, and to an arbitrary state (like a climatology) otherwise. If we assume the model state as univariate and in a grid-point representation, and denote by $\mathbf{x}_b$ a previous estimate of the model state (*background*) provided by climatology, persistence or a previous forecast, and by $\mathbf{y}(i)$, a set of $i = 1...n$ observations of the same variable. The following *update* equation defines a simple Cressman scheme, provided by the model state $\mathbf{x}_a$ defined at each grid point j

$$\mathbf{x}_a(j) = \mathbf{x}_b(j) + \frac{\sum_{i=1}^{n} w(i,j)\,[\mathbf{y}(i) - \mathbf{x}_b(i)]}{\sum_{i=1}^{n} w(i,j)} \;, \tag{2.1}$$

$$w(i,j) = \max\left(0, \frac{R^2 - d_{i,j}^2}{R^2 + d_{i,j}^2}\right) \;, \tag{2.2}$$

Where $d_{i,j}$ defines a measure of distance between the points i and j. The $\mathbf{x}_b(i)$ is the background state interpolated to point i. The weight function $w(i,j)$ equals one if the grid point j is collocated with the observation i (zero distance response). It is a decreasing

function of distance defined by the user provided *radius of influence* R beyond which observations have no influence (weight is zero if $d_{i,j} > R$). There are many variants of the Cressman correction, a more general algorithm is the *successive correction* or *observation nudging*. The key problem with these kinds of algorithms is the lack of a direct method to determine the optimal weights. As there are errors in the model and in the observations, we can never be sure which one to trust. So it is necessary to represent the uncertainty of the data mathematically, which means deriving or assuming the error statistics, and model it, using probabilistic concepts. This allows to design the analysis algorithm in a way that in the average the analysis error must be minimal, which means that the analysis problem can be written as an optimization problem.

2.2 State Vector, Observations and Control Space

2.2.1 State Vector

The values representing the state of the atmosphere are stored in the so called *state vector* $\mathbf{x}$. The $\mathbf{x}_t$ is the *best possible* representation of reality (but of course is not equivalent to reality, which is too complex), also called the true state at the time of the analysis. Other values of the state vector $\mathbf{x}$ are $\mathbf{x}_b$, the *a priori* or *background* estimate of the true state also called *first guess*, before the analysis, valid at the same time. The analysis itself is denoted $\mathbf{x}_a$.

2.2.2 Observations

To derive an analysis we need observed values, which are gathered into an *observation vector* $\mathbf{y}$. The observations stored in the vector $\mathbf{y}$ have to be compared with the state vector during the analysis procedure. Usually the location of the observations do not correspond with the discrete representation of the state vector. Furthermore the measured physical quantities are often not represented in the state vector, but linked to the state vector values by physical laws. This observations are denoted as *indirect measurements.* To compare them with the state vector the so called *observation operator* $\mathbf{H}$, which is in fact a function from model state space to observation space, is needed. This operator generates the values[1] $\mathbf{H}(\mathbf{x})$ that the observation would take if both the observations and the state vector would be perfect and error free. In the simple case of corresponding physical quantities in state and observation vector $\mathbf{H}$ is reduced to an interpolation operator. In practice, conversion functions from model variables to observed parameters are also part of $\mathbf{H}$, especially if data from remote sensing platforms is used, which is usually indirect.

2.2.3 Control Space

In practice there are often technical reasons not to solve the analysis problem in the model space. It is often convenient to solve the problem in a so-called *control variable space.* The analysis problem is to find the optimal correction $\delta\mathbf{x}$ (*analysis increment*) so that

$$\mathbf{x}_a = \mathbf{x}_b + \delta\mathbf{x} \tag{2.3}$$

[1] The values $\mathbf{H}(\mathbf{x})$ are also called *model equivalents of the observations.*

is as close as possible to the true state $\mathbf{x}_t$.

2.2.4 Departures

The analysis procedure is driven by the discrepancies between the state and the observation vector which is given by[2]

$$\delta\mathbf{x}_{\text{inov}} = \mathbf{y} - H(\mathbf{x}) \ , \tag{2.4}$$

with $\delta\mathbf{x}_{\text{inov}}$, the *innovation vector*. Evaluating equation (2.4) with the background $\mathbf{x}_b$ gives the *innovations* with the analysis $\mathbf{x}_a$ the so called *analysis residuals.*

2.3 Modelling of Errors

One of the most important aspects of data assimilation is to take the uncertainties of background and observations into account in a correct way. The standard approach to this problem is the usage of pdf's (*probability density functions*) to represent each kind of error. Assuming a background field $\mathbf{x}_b$ before the analysis there is only one vector, containing the errors, which separates the background $\mathbf{x}_b$ from the true state $\mathbf{x}_t$.

$$\boldsymbol{\varepsilon}_b = \mathbf{x}_b - \mathbf{x}_t$$

If it would be possible to repeat the analysis under exactly the same conditions a large number of times, with different realizations of errors $\boldsymbol{\varepsilon}_b$ generated by unknown causes, it would be possible to calculate statistics of $\boldsymbol{\varepsilon}_b$. In the limit of a very large number of realizations the error statistics should converge to values which only depend on the physical processes responsible for the errors. For an other equivalent analysis we would not know the error $\boldsymbol{\varepsilon}_b$, but we would know its statistics. The *probability density function* of $\boldsymbol{\varepsilon}_b$ gives the best information about the distribution of $\boldsymbol{\varepsilon}_b$ and is given by the limit of the histogram when the classes are infinitely small, which is a scalar function of integral one. It is possible to derive all statistics from this function, a standard model of a scalar pdf is the Gaussian function, which can be generalized to a multivariate pdf.

2.3.1 Error Variables

Background Errors

The background errors are defined as

$$\boldsymbol{\varepsilon}_b = \mathbf{x}_b - \mathbf{x}_t \ , \tag{2.5}$$

with the average

$$\overline{\boldsymbol{\varepsilon}_b} \ , \tag{2.6}$$

and with the covariance

$$\mathbf{B} = \overline{(\boldsymbol{\varepsilon}_b - \overline{\boldsymbol{\varepsilon}_b})(\boldsymbol{\varepsilon}_b - \overline{\boldsymbol{\varepsilon}_b})^T} \ . \tag{2.7}$$

These errors do not include the discretization errors caused by the discrete representation of reality, they describe only the difference between the background state and the true state.

[2] Linearized observation operator $\mathbf{H}$, cf. Section 2.17.

Observation Errors

The observation errors are defined as

$$\boldsymbol{\varepsilon}_o = \mathbf{y} - H(\mathbf{x}_t) \ , \tag{2.8}$$

with the average

$$\overline{\boldsymbol{\varepsilon}_o} \ , \tag{2.9}$$

and with the covariance

$$\mathbf{R} = \overline{(\boldsymbol{\varepsilon}_o - \overline{\boldsymbol{\varepsilon}_o})(\boldsymbol{\varepsilon}_o - \overline{\boldsymbol{\varepsilon}_o})^T} \ . \tag{2.10}$$

These errors contain the observation errors themselves, processing errors, representativeness errors and errors in the design of $\mathbf{H}$ itself.

Analysis Errors

The analysis errors are defined as

$$\boldsymbol{\varepsilon}_a = \mathbf{x}_a - \mathbf{x}_t \ , \tag{2.11}$$

with the average:

$$\overline{\boldsymbol{\varepsilon}_a} \ . \tag{2.12}$$

The trace of the analysis error covariance matrix $\mathbf{A}$ gives a measure $\overline{\|\boldsymbol{\varepsilon}_a - \overline{\boldsymbol{\varepsilon}_a}\|}$ of these errors

$$Tr(\mathbf{A}) = \overline{\|\boldsymbol{\varepsilon}_a - \overline{\boldsymbol{\varepsilon}_a}\|^2} \ . \tag{2.13}$$

These are the estimation errors of the analysis state, which we want to minimize. The averages of errors are called *biases* which are a sign of systematic problems, either with the model or the observations. Before using any kind of observation in an assimilation scheme it must be assured that the observations are bias free, otherwise a bias correction must be applied.

2.3.2 Error Covariances

If you assume a scalar system the background error covariance is the variance, i.e. the root-mean-square (r.m.s.) average of departures from the mean

$$\mathbf{B} = \sigma^2(\boldsymbol{\varepsilon}_b) = \overline{(\boldsymbol{\varepsilon}_b - \overline{\boldsymbol{\varepsilon}_b})^2} \ . \tag{2.14}$$

If the system is multidimensional the covariances are square symmetric matrices of the dimension n corresponding to a model state vector of the dimension n. The diagonal contains the variances, the off-diagonal elements are the cross-covariances between each pair of variables. A covariance matrix can be decomposed into a vector of the dimension n containing the variances and a correlation matrix of the dimension $n \times n$. Error covariance matrices are positive definite. An example for a three dimensional model state is

$$\mathbf{B} = \begin{bmatrix} \sigma^2(\varepsilon_1, \varepsilon_1) & cov(\varepsilon_1, \varepsilon_2) & cov(\varepsilon_1, \varepsilon_3) \\ cov(\varepsilon_1, \varepsilon_2) & \sigma^2(\varepsilon_2, \varepsilon_2) & cov(\varepsilon_2, \varepsilon_3) \\ cov(\varepsilon_1, \varepsilon_3) & cov(\varepsilon_2, \varepsilon_3) & \sigma^2(\varepsilon_3, \varepsilon_3) \end{bmatrix} \ . \tag{2.15}$$

Assuming non zero variances, the off-diagonal terms can be transformed into error correlations:

$$\mathrm{corr}(\varepsilon_i, \varepsilon_j) = \frac{\mathrm{cov}(\varepsilon_i, \varepsilon_j)}{\sqrt{\sigma^2(\varepsilon_i)\sigma^2(\varepsilon_j)}} \ . \tag{2.16}$$

Linear transforms can only be applied to covariances as full matrix transforms. If a linear transformation by a matrix $\boldsymbol{P}$ is defined (i.e. a matrix whose rows are the coordinates of the new basis vectors in terms of the old ones, so that the new coordinates of the transform of $\mathbf{x}$ are $\boldsymbol{P}\mathbf{x}$), then the covariance matrix in terms of the new variables is $\boldsymbol{P}\mathbf{B}\boldsymbol{P}^T$. The notation used to describe the error covariances is related to the background error, but is equally valid for the observation error.

2.3.3 Practical Estimation of Error Statistics

The error statistics describing biases and covariances are functions of physical processes and the observations, and also depend on our a priori knowledge of the errors. The error variances reflect the uncertainty in features of the background and the observations. To be able to estimate statistics, the assumption of *ergodicity* has to be made, which means that they are stationary over a period of time and uniform over a domain. So taking a number of error realizations to make empirical statistics is possible. Error statistics can also be specified by taking them to be a fraction of the climatological statistics of the fields themselves. Approximations are unavoidable because in practice there is no data available to calibrate the statistics, the estimation errors cannot be observed directly. As a practical example the NMC method uses forecast differences to derive short-range forecast errors [*Parrish and Derber* (1992)]. There are also the *Hollingsworth and Lönnberg method* [*Hollingsworth and Lönnberg* (1986)], which looks at the spacial covariance of differences between observations and background, and the *analysis ensemble method*, which estimates background error statistics by running an ensemble of independent analysis experiments.

2.4 Least-Squares Estimation

Several hypotheses have to be stated:

- Linearized observation operator

$$H(\mathbf{x}) - H(\mathbf{x}_b) \approx \mathbf{H}(\mathbf{x} - \mathbf{x}_b) \ . \tag{2.17}$$

  Equation 2.17 assumes that the variation of the observation operator in the vicinity of the background state is linear for any $\mathbf{x}$ close enough to $\mathbf{x}_b$, where $\mathbf{H}$ is a linear operator. $\mathbf{H}$ is called the first derivative, differential or tangent linear function of H.

- Non trivial errors, which means that $\mathbf{B}$ and $\mathbf{R}$ are positive definite matrices.

- The errors must be unbiased, what means that the expectation of the background and observation errors are zero

$$\begin{aligned} \overline{\mathbf{x}_b - \mathbf{x}_t} &= 0 \\ \overline{\mathbf{y} - H(\mathbf{x})} &= 0 \ . \end{aligned} \tag{2.18}$$

- Observations and background are mutually uncorrelated

$$\overline{(\mathbf{x}_b - \mathbf{x}_t)\left(\mathbf{y} - H(\mathbf{y}_t)\right)^T} = 0 \ . \tag{2.19}$$

- The analysis we are looking for is defined to corrections of the background which depend linearly on background observation departures.
- The analysis should be as close as possible to the true state in the sense of a minimum variance estimate.

2.4.1 The Least-Squares Analysis Equations

The *optimal least-squares estimator,* which is also called *BLUE analysis* (Best Linear Unbiased Estimator), is defined by the following interpolation equation

$$\mathbf{x}_a - \mathbf{x}_b + \mathbf{K}\left(\mathbf{y} - H(\mathbf{x}_b)\right) \ . \tag{2.20}$$

The linear operator $\mathbf{K}$ is called *gain,* or *weight matrix*, of the analysis

$$\mathbf{K} = \mathbf{B}\mathbf{H}^T(\mathbf{H}\mathbf{B}\mathbf{H}^T + \mathbf{R})^{-1} \ . \tag{2.21}$$

The *analysis error covariance matrix* is given for any $\mathbf{K}$ by

$$\mathbf{A} = (\mathbf{I} - \mathbf{K}\mathbf{H})\mathbf{B}(\mathbf{I} - \mathbf{K}\mathbf{H})^T + \mathbf{K}\mathbf{R}\mathbf{K}^T \ . \tag{2.22}$$

If $\mathbf{K}$ is the optimal least-squares gain, the expression becomes

$$\mathbf{A} = (\mathbf{I} - \mathbf{K}\mathbf{H})\mathbf{B} \ . \tag{2.23}$$

The BLUE analysis is obtained as solution of the equivalent *variational optimization problem*:

$$\mathbf{x}_a = \text{Arg} \ \min \ J \ . \tag{2.24}$$

Where J is defined as:

$$J(\mathbf{x}) = J_b(\mathbf{x}) + J_o(\mathbf{x}) \ , \tag{2.25}$$

or in detail:

$$J(\mathbf{x}) = \left(\mathbf{x} - \mathbf{x}_b\right)^T \mathbf{B}^{-1} \left(\mathbf{x} - \mathbf{x}_b\right) + \left(\mathbf{y} - H(\mathbf{x})\right)^T \ \mathbf{R}^{-1} \left(\mathbf{y} - H(\mathbf{x})\right) \ , \tag{2.26}$$

with its gradient:

$$\nabla_x J(\mathbf{x}) = 2\mathbf{B}^{-1}(\mathbf{x} - \mathbf{x}_b) - 2H^T\mathbf{R}^{-1}(\mathbf{y} - H(\mathbf{x})) \ . \tag{2.27}$$

J is called the *cost* or *penalty function* of the analysis, which consists of the background term J_b and the observation term J_o. The calculated analysis $\mathbf{x}_a$ is optimal, which means it is closest in a r.m.s. sense to the true state $\mathbf{x}_t$. In case of Gaussian background error pdf's $\mathbf{x}_a$ is the *maximum likelihood estimator* of $\mathbf{x}_t$.

Necessary Assumptions

The assumption that there is no correlation between background and observation errors is usually justified, because the causes of the errors are supposed to be completely independent. However, one must be careful about observation preprocessing, like retrieval procedures, which use background information. These procedures can cause a bias of the observations towards the background. If observations, containing background information are used in an assimilation procedure, we are confronted with the so-called *incest problem*. The analysis is drawn closer to the background, which is caused by observations already containing background information, reducing the apparent background departures. If additional information is necessary in the observation preprocessing procedure, one should carefully decide, which background will not influence the analysis result. The analysis is only optimal if the assumption of bias-free errors holds. In practice background and observations are often significantly biased. If the biases are known, they can be subtracted from the background and observations, which is in practice a delicate problem. Bias monitoring and removal are subjects of ongoing improvement and research. Finally the hypothesis of linearized observation operators is needed to derive the analysis equations for an optimal $\mathbf{K}$ in an algebraic rigorous way.

2.4.2 A Simple Example of Least Squares Estimation

To determine the temperature T_t, two observations T_1 and T_2 with known accuracy σ_1 and σ_2 are available. These observations are assumed to be unbiased. T_1 and T_2 can be combined to provide an analysis T_a which provides a better estimate of T_t than any of the observations alone. A linear weighted average of T_1 and T_2:

$$T_a = kT_1 + (1-k)T_2 \ , \tag{2.28}$$

which can be rewritten as

$$T_a = T_2 + k(T_1 - T_2) \ . \tag{2.29}$$

Under the assumption that T_1 denotes the observation and T_2 denotes the background within an assimilation framework, Eq. 2.29 is a correction of the background which is a linear function of the difference between the observation and the background. The error variance of the estimate is given as

$$\sigma_a^2 = (1-k)^2\sigma_2^2 + k^2\sigma_1^2 \ , \tag{2.30}$$

with the assumption that T_1 and T_2 respectively observation and background are uncorrelated. The optimal value of k minimizes the analysis error variance

$$k = \frac{\sigma_2^2}{\sigma_1^2 + \sigma_2^2} \ , \tag{2.31}$$

which is equivalent to minimize

$$\begin{aligned} J(T) &= J_2(T) + J_1(T) \\ &= \frac{(T-T_2)^2}{\sigma_2^2} + \frac{(T-T_1)^2}{\sigma_1^2} \ . \end{aligned} \tag{2.32}$$

The consequences are:

- In the first limiting case of very low quality measurements ($\sigma_1 \gg \sigma_2$) $\Longrightarrow k = 0$ and the analysis remains equal to the background.
- In the second limiting case of very high quality measurements ($\sigma_1 \ll \sigma_2$) $\Longrightarrow k = 1$ and the analysis is equal to the observation.
- If both T_1 and T_2 have the same accuracy ($\sigma_1 = \sigma_2$) $\Longrightarrow k = \frac{1}{2}$ the analysis is the average of T_1 and T_2.
- In the other cases $0 \leq k \leq 1$ the analysis is a weighted background of T_1 and T_2.

The analysis error for the optimal k is given as

$$\frac{1}{\sigma_a^2} = \frac{1}{\sigma_1^2} + \frac{1}{\sigma_2^2} \ , \tag{2.33}$$

$$\sigma_a^2 = \frac{\sigma_1^2}{1 + (\frac{\sigma_1}{\sigma_2})^2} \tag{2.34}$$

$$= \frac{\sigma_2^2}{1 + (\frac{\sigma_2}{\sigma_1})^2} \tag{2.35}$$

$$= (1 - k)\sigma_2^2 \ . \tag{2.36}$$

It follows that the analysis error variance σ_a^2 is always smaller than both the background and observation error variances respectively σ_2^2 and σ_1^2 as shown in equation 2.36.

2.5 Optimal Interpolation

The optimal interpolation (OI) analysis scheme is an algebraic simplification of the calculation of the weight matrix $\mathbf{K}$ in the analysis Eq. 2.20 and 2.21. In fact one assumes that only a few observations are important to determine the analysis increment for each background variable. Suitable selection criteria for the influencing observations surrounding each background variable have to be found. In this approach, only sub-matrices of the background and observation covariance matrices have to be inverted, which saves considerable computing time. It is only necessary to define $\mathbf{B}$ locally, which can also be a drawback if it is difficult to describe $\mathbf{B}$ as a model, which can easily be applied to pairs of background and observed variables.

2.6 3D-VAR

3D-Var avoids the computation of the gain matrix $\mathbf{K}$ in Eq. 2.21 completely by finding the analysis as an approximate solution to the equivalent minimization problem given by the cost function J given in Eq. 2.26. The solution can be computed iteratively by performing several evaluations of the cost function cf. Eq. 2.26 and its gradient cf. Eq. 2.27 in order to approach the minimum using a suitable minimization algorithm. The final solution is only an approximation, because of the fact, that only a limited number of iterations

is performed. A standard procedure is to chose as initial point of the minimization, the so-called *first guess,* or the background $\mathbf{x}_b$. The first guess just initiates the minimization procedure and is not necessary equal to the background (Principal program flow chart of a 3D-Var system see Appendix E).

The solution of the minimization problem can be performed either in terms of full-fields $J(x_a)$ or the analysis of increments $J(x'_a) = J(x'_a = x_a - x_b)$ [*F. Bouttier* (1999)]. The latter solution method provides *optimal* analysis increments, which are added to the unmodified background field. This procedure has a number of advantages like the use of linearized control variable transforms which allow the straightforward use of adjoints to calculate the gradient of the cost function. Another advantage is that any imbalance introduced through the analysis procedure is limited to the small increments which are added to the balanced first guess.

2.7 FGAT

FGAT means *First Guess at Appropriate Time* for use of observations, which is an intermediate approach. It means that, even if the correction does not depend on time, the observations are taken into account at their time and are compared with the first guess at the appropriate time.

2.8 4D-VAR

4D-Var is a generalization of the 3D-Var scheme, which takes into account the distribution of measurements in time. The analysis equations are the same as in 3D-Var, but the observation operators includes a forecast model, that allows to compare the observations with the model state at the appropriate time. That allows that NWP systems, using 4D-Var techniques, can utilize more observations, due to the fact that the assimilation window is broad in the time dimension. The 4D-Var problem is solved by minimization of the following cost function (i denotes the time intervals of the observations):

$$J(\mathbf{x}) = (\mathbf{x} - \mathbf{x}_b)^T \mathbf{B}^{-1} (\mathbf{x} - \mathbf{x}_b) + \sum_{i=0}^{n} (\mathbf{y}_i - H_i(\mathbf{x}_i))^T \ \mathbf{R}_i^{-1} (\mathbf{y}_i - H_i(\mathbf{x}_i)) \ . \tag{2.37}$$

2.9 Other Methods

Other developments of the least square analysis scheme are the Kalman Filter and the Extended Kalman Filter. It can be shown that a 4D-Var analysis at the end of the analysis time interval is equivalent to a Kalman Filter analysis at the same time. The formulation of the Linear Extended Kalman Filter is equivalent to the least squares formulation, where each background is provided by a forecast that starts from the previous analysis.

2.10 Numerical Cost

One of the main design drivers for a data assimilation system is the numerical cost. The covariance matrices $\mathbf{B}$ and $\mathbf{R}$ have to be specified, which contain $\frac{n^2}{2}$ respectively $\frac{p^2}{2}$ coefficients. Alternatively, covariance matrices can be approximated by the use of filters, which reduce the numerical costs significantly. To determine $\mathbf{K}$, matrices of the size $p \times p$ have to be inverted, which has an asymptotic complexity of the order of $p^2 \log(n)$. In the variational form of the least squares framework the inverse of the matrices $\mathbf{B}$ and $\mathbf{R}$ is needed. By the use of transformations and reformulations, especially of $\mathbf{B}$, the numerical cost can be dramatically reduced. Finally the exact minimization of J would require $n + 1$ evaluations of the cost function and its gradient, assuming that J is quadratic and there are no numerical errors. That means that beside a suitable minimization algorithm, practically feasible abort criteria for the iteration have to be defined [*F. Bouttier* (1999)], [*Kozo* (1997)], [*ECMWF* (2004b)], [*Kalnay* (2003)].

3

Data Base for Radio Occultation Data Assimilation

3.1 Background Data

In general, background data provided by ECMWF, is used, due to its high standards, accuracy and availability. The ECMWF, spectral model (IFS) runs currently with a T511L60 resolution, which is foreseen to be upgraded to T511L90 during 2004. After increasing the vertical resolution from 60 to 90 model levels, the next scheduled step is an upgrade of the horizontal resolution to T711 [*ECMWF* (2004a)].

3.1.1 ECMWF Analysis Fields

As background for the assimilation procedure are used, ECMWF T42L60 analysis fields, corresponding to a Gaussian grid composed of 128×64 geographic areas, and 60 standard model levels up to a height of ~ 64 km. The resolution of the vertical grid is highest in the planetary boundary layer and lowest in the stratosphere and lower mesosphere. These vertical levels are realized as hybrid levels, which means they are composed as
σ - levels which follow the Earth's surface in the lower and mid tropospere, but are surfaces of constant pressure (pressure levels) in the upper stratosphere and mesosphere with a smooth transition between these types of levels. ECMWF uses two different numerical representations for the horizontal grid. A *spectral* method, based on a spherical harmonic expansion, truncated at total wavenumber 511, for the representation of upper air fields and the computation of the horizontal derivatives. Apart from the T511L60 operational model a T255L40 model is run for ensemble prediction, a T159L40 model for the 4D-Var assimilation and a T63L31 model for seasonal forecast. In addition there is a grid point representation used for computing dynamic tendencies and the diabatic physical parametrization. This so called Gaussian grid, is regular in longitude and almost regular in latitude. Due to the convergence of the longitudes towards the poles, the east-west distance between the grid points decreases polewards. To avoid some numerical problems around the poles and most importantly, to save computing time, a reduced Gaussian grid

was introduced by reducing the number of grid points along the shorter latitude lines near the poles, so as to keep the east-west separation between points on different latitudes almost constant. With the current resolution the grid is identical to a regular Gaussian grid between 24°N and 24°S. The model surface is logically divided into sea and land points, by using a *land-sea-mask*. The representation of the *orography* uses the mean orography and is significantly smoother than reality (Fig. 3.1).

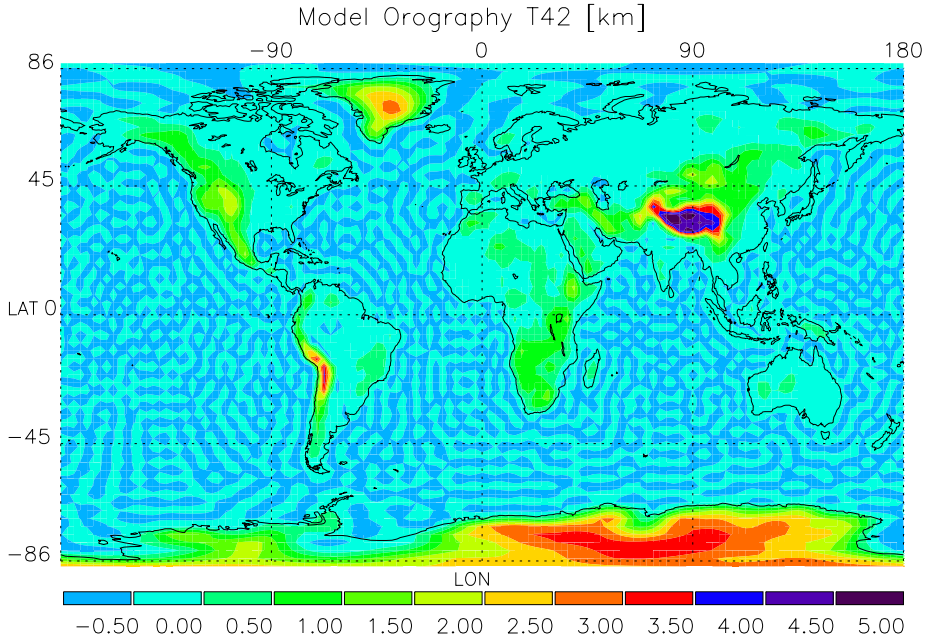

Figure 3.1: Model orography for the T42 resolution.

At ECMWF four global analyses per day are produced at 00, 06, 12 and 18 UTC. These are obtained by two 4D-Var minimization cycles running from 03 to 15 UTC and from 15 to 03 UTC. The analysis is performed by comparing the observations directly with a very short forecast, using exactly the same model as the operational medium-range forecast. The differences between the observed values and the equivalent values predicted by the short-range forecast are used to make a correction to the first guess field in order to produce the atmospheric analysis.

For our climatological application the T42L60 resolution of the analyses was chosen due to computational constraints and some unique advantages. As discussed below the spatial characteristics of Radio Occultation data (moderate horizontal, high vertical resolution) fits quite well to this background grid spacing. ECMWF offers a broad spectrum of analysis products, for our application global temperature, specific humidity, and surface pressure fields are used [*Person* (2003)], [*Gobiet and Kirchengast* (2004a)].

3.1.2 Accuracy of ECMWF Analysis Fields

For climatological applications the knowledge of error bounds is crucial. For the operational daily analyses, information about the standard deviations and correlations of the

atmospheric parameters are available. It is possible to derive them with statistical methods like the NMC method, where the error characteristics are derived by averaged forecast differences. The error characteristics of monthly and seasonal means are still unknown and believed to be bias driven (Mike Fisher ECMWF Reading, U.K., pers. communication 2003). The error characteristics of the used background fields are discussed in detail in Section 4.7.

3.2 Radio Occultation Data

With the successful launch of the CHAMP satellite in summer 2000 and the start of its GPS Radio Occultation experiment in February 2001, the number of available RO-based atmospheric profiles increased in a way that long term climatological studies become feasible. In addition to CHAMP, also the RO experiments on the Argentinean SAC-C satellite contributes data (SAC-C data is fragmentary and limited to certain periods, at the moment further data from SAC-C is questionable), and the GRACE mission is expected to constitute data in 2004. The first successful processed GRACE RO profiles were published by JPL on 29 of July 2004. Furthermore, a RO receiver (GRAS) [*EUMETSAT* (2003)] is part of the payload of the METOP series of polar-orbiting, operational meteorological satellites currently prepared by EUMETSAT and ESA. Other RO missions are scheduled like COSMIC (US-Taiwan) and ACE+ (ESA) whose further implementation was unfortunately stopped recently. The global coverage, all-weather capability, high vertical resolution, accuracy and long term stability of RO data makes them an ideal candidate to build global climatologies of fundamental variables such as temperature, geopotential height and water vapor [*Kirchengast et al.* (2004)], [*Gobiet and Kirchengast* (2004a)].

3.2.1 The RO Technique

Radio Occultation (RO) is a novel active limb sounding technique to derive atmospheric key parameters. The measurement setup comprises a receiver mounted on a low Earth orbit (LEO) satellite, which tracks the signal of a global navigation system (GPS) satellite positioned in a medium Earth orbit (MEO), in an occultation geometry. The challenges from a technical point of view imply the necessity of an extremely high frequency stability in the signal and the positions and velocities of transmitter and receiver must be known to very high accuracy. The concept was successfully proven on-board the Micro Lab 1 satellite (GPS/MET experiment) [*Kursinski et al.* (1996)] and is now quasi operationally implemented as part of the CHAMP mission. Fig. 3.2 illustrates the concept of the RO technique, which is the interaction of electromagnetic waves (GPS signals) and the (in our application) terrestial atmosphere. An electromagnetic ray passing through the atmosphere is bent and retarded due to the ionosphere and the Earth's refractivity field. In our application the signal must be corrected for the influence of the ionosphere which is accomplished by a differential approach. For other applications this part of the signal is used to derive maps of the ionosphere and the total electron content (TEC). The effect of the atmosphere onto the electromagnetic waves can be characterized by a total bending angle (α) as a function of the impact parameter (a). The impact parameter is defined, assuming spherical symmetry, as the perpendicular distance between the center of local

curvature at the perigee of the occultation ray and the ray asymtote at the GPS or LEO satellite.

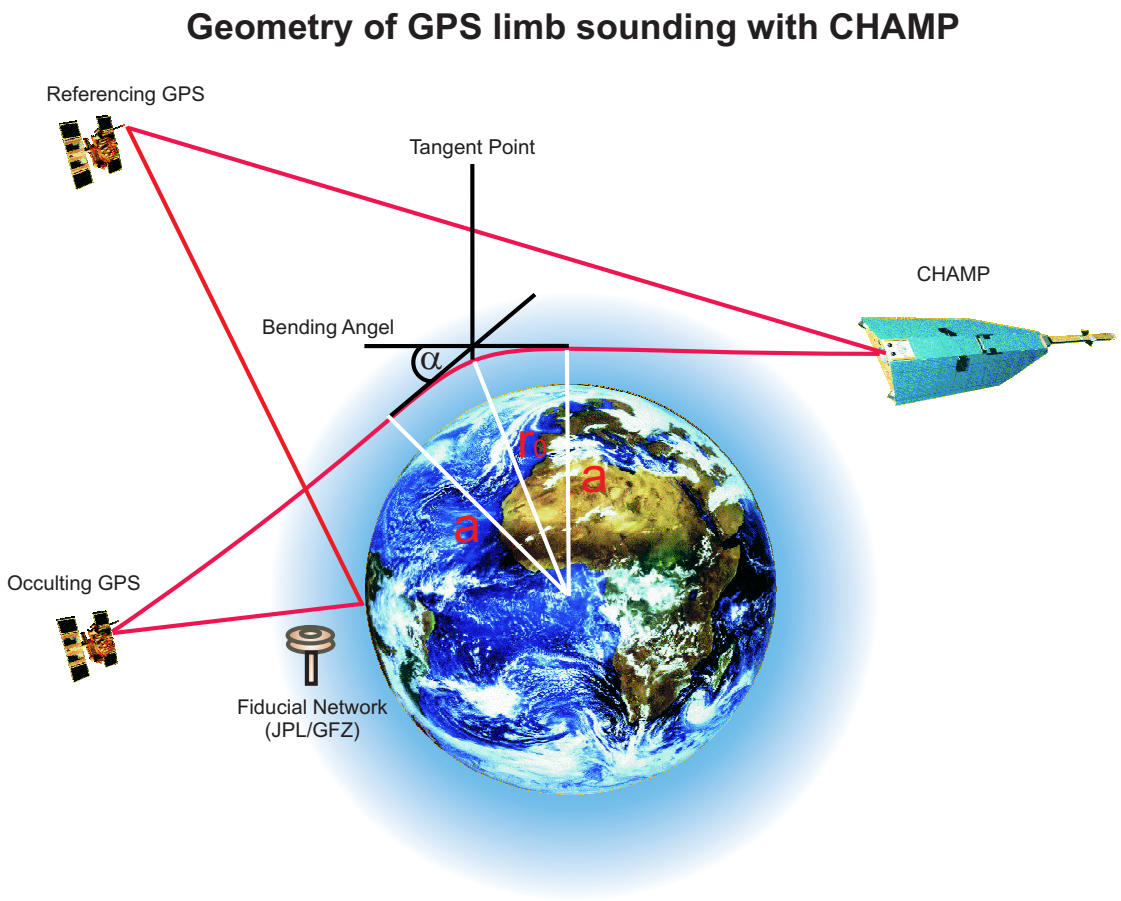

Figure 3.2: Principal geometry of an radio occultation measurement including LEO satellite (CHAMP), GPS satellites and fiducial network.

Unique Advantages for Monitoring of Atmospheric Key Parameters

Due to the measurement principle, Radio Occultation features some preferable characteristics which makes it an ideal technique for a long term monitoring of atmospheric key parameters. Its long term stability and selfcalibrating concept makes it an ideal candidate for climate studies.

- The atmospheric profiles are not derived from absolute intensities or phase delays.
- The profiles are derived from transmissions (normalized intensities) and the Doppler shift (phase change) profiles (intrinsic self-calibration).
- Only short-term stability is nescessary during the occultation event.

Characteristic Horizontal and Vertical Resolution of RO Measurements

One of the characteristics of RO measurement is its high vertical (Δz) and moderate to low horizontal (ΔL) spatial resolution. The following relation is valid

$$\Delta L = 2 \cdot \sqrt{2 \cdot R \cdot \Delta z} \ , \tag{3.1}$$

where ΔL denotes the chord, which is defined by the tangent of the inner of two concentric circles with radii which differ about Δz. R is the radius of the inner circle, which is in fact the atmospheric radius at the tangent point of the ray path. If geometric optics is applied, the vertical resolution is limited by the diameter of the first Fresnel Zone d_F. For occultation geometry, this can be calculated by negligible atmosphere (stratosphere) as follows

$$d_F = 2 \cdot \sqrt{\lambda \cdot D} \ ,$$

where λ denotes the wavelength of the GPS signal and D the distance between the GPS receiver on-board CHAMP and the tangent point. With $\lambda = 19$ cm and $D = 2.600$ km (orbit height of 500 km) for the diameter of the first Fresnel Zone follows 1.4 km. Using Eq. 3.1 a horizontal resolution ΔL of ~ 270 km can be calculated. Caused by the exponential increase of the refractivity towards the Earth's surface (troposphere) d_F becomes smaller and reaches close to the Earth's surface a value of 0.5 km [*Kursinski et al.* (1997)] which translates into a horizontal resolution of about ~ 80 km. It is possible to enhance the vertical resolution by using methods which take diffraction effects into account [*Gorbunov and Gurvich* (1998)], [*Wickert* (2002)].

3.2.2 Retrieval

General RO Retrieval

As a basic idea the radio signals emitted by the GNSS satellites can be treated as rays, which means a geometric optics assumption. This is a valid simplification from the mid-troposphere upwards. However below some 5 km wave optics methods, which can cope with complex signal structures in the presence of strong refractivity gradients enhance the retrieval performance significantly [*Gorbunov* (2002)], [*Hocke et al.* (1999)], [*Sokolovskiy* (2003)]. At the moment the IGAM retrieval for CHAMP data uses only the geometric optics approach. The use of a retrieval procedure which blends geometric optics assumption from the mid-troposphere upwards with wave optics methods derived data in the lower regions is foreseen to be used in the near future.

$$\begin{aligned} \text{GPS Frequencies} \quad & L_1 = 1575.42 \text{ MHz} \\ & L_2 = 1227.60 \text{ MHz} \end{aligned}$$

The primary observables are the phase delays of GNSS signals, resulting from the deceleration of the electromagnetic wave's phase velocity by the atmosphere. The Doppler shifts and total bending angles α as function of the ray's impact parameter a can be deduced from the phase delays [*Kursinski et al.* (1997)]. The basis to derive α is the Doppler-Shift equation [*Gorbunov et al.* (1996)]:

$$f_d = f_c \left(\frac{c - \overrightarrow{\nu_2} \overrightarrow{m_2} n_2}{c - \overrightarrow{\nu_1} \overrightarrow{m_1} n_1} - 1 \right) \ , \tag{3.2}$$

where $\overrightarrow{\nu_1}$ and $\overrightarrow{\nu_2}$ denote the velocity vectors of the occulting GPS and CHAMP satellites, $\overrightarrow{m_1}$ and $\overrightarrow{m_2}$ are the unit vectors of the wave vector of the transmitted and received signals, n_1 and n_2 are the refractivities at the corresponding satellite positions. The Doppler shift f_d corresponds to the measured phase as

$$f_d = -\frac{f_c}{c}\frac{dL}{dt} \ , \tag{3.3}$$

with the carrier frequency f_c and the vacuum speed of light c. It is possible to decompose L as

$$L = L_0 + dA_{L0} \ , \tag{3.4}$$

so it is possible to decompose the Doppler shift

$$f_d = f_{d0} + f_{dA} \ . \tag{3.5}$$

The first term describes the frequency shift without atmospheric influence, caused by the relative motion of the satellites and can be calculated from precise orbit data. The second term is the time derivative of calibrated atmospheric induced signal delay of the occultation link which is composed of an ionospheric part and a part of the neutral atmosphere. The angle of refraction α can be derived as follows

$$\alpha = \Phi_1 + \Phi_2 + \Theta - \pi \ . \tag{3.6}$$

The angles Φ_1 and Φ_2 are the only unknowns in Eq. 3.6, after solving the scalar product and the introduction of the measured Doppler shift in Eq. 3.2 [*Kursinski et al.* (1997)], and can be derived under the assumption of local spherical symmetry of the refractivity $n = n(r)$ using Snells law

$$r_1 n(r_1) \sin \Phi_1 = r_2 n(r_2) \sin \Phi_2 = a \ . \tag{3.7}$$

Eqs. 3.2 and Eq. 3.7 are a non linear system which can not be solved analytically, but with a simple iterative procedure [*Gorbunov et al.* (1996)]. Eq. 3.7 also provides the impact parameter a. Furthermore an ellipsoid and an ionosperic correction have to be applied. As a next step the refractivity index n can be derived via an inverse Abel transform [*Fjeldbo et al.* (1971)]

$$n(a) = \exp\left[\frac{1}{\pi} \cdot \int_a^\infty \frac{\alpha(a')}{\sqrt{a'^2 - a^2}} da'\right] \ . \tag{3.8}$$

The refractivity as a function of height $N(a)$ is obtained via Eq. 3.8

$$N(a) = 10^6 \cdot (n(a) - 1)$$
$$z(a) = \frac{a}{n(a)} - R_c$$

where R_c denotes the local radius of curvature of the Earth's ellipsoid at the occultation location. Bending angles above $\sim$ 45 km are dominated by ionospheric effects [*Hocke* (1997)]. Since the ionosphere is a dispersive medium and thus causes different L_1 and L_2 phase delays, it is possible to remove this effects to first order by linear combination of this

two signals. The method of linear correction of bending angles Eq. 3.9 has been applied most successfully [*Vorobev and Krasnilnikova* (1994)] by

$$\alpha_{LC}(a) = \frac{f_1^2\alpha_1(a) - f_2^2\alpha_2(a)}{f_1^2 - f_2^2} \ , \tag{3.9}$$

where α_{LC} denotes the ionosphere corrected bending angle, α_1 and α_2 the uncorrected bending angles of the L_1 and L_2 signals. Still, retrieval results above $20-30$ km are sensitive to residual ionospheric noise (resulting from higher order terms, which are not corrected by Eq. 3.9) and other errors like receiver noise, residual clock errors, local multipath and orbit uncertainties. Since the upper integration limit of the inverse Able transform Eq. 3.8 ranges to infinity it needs in practice some kind of high altitude initialization to avoid downward propagation of errors via the Abel transform itself and subsequently via the hydrostatic integration Eq. 3.23. To minimize these errors the concept of statistical optimization is applied [*Sokolovskiy and Hunt* (1996)]. The best linear unbiased estimator (BLUE Eq. 2.20) α_{opt} is derived from an observed α_O and a background α_B bending angle profile under the assumption of unbiased Gaussian errors. The $\mathbf{O}$ and $\mathbf{B}$ are the observation and background error covariance matrices, respectively. The α_{opt} is derived by

$$\alpha_{\text{opt}} = \alpha_B + \mathbf{B} \cdot (\mathbf{B} + \mathbf{O})^{-1} \cdot (\alpha_O - \alpha_B) \ . \tag{3.10}$$

Where α_{opt} is a fused bending angle profile dominated by the background in the upper part and by the observation in the lower part. The IGAM retrieval schemes integrate background information only at one point of the retrieval (at bending angle level), so that the results have well defined error characteristics. One has to be careful if background information is used in a retrieval procedure, if the retrieved data is used in a consecutive assimilation framework. If the assimilation framework uses the same background data as the retrieval we end up with a so-called *incest problem*[1]. The analysis in the assimilation procedure is artificially drawn to the background. At IGAM, statistical optimization is implemented in two ways, both relying on Eq. 3.10, but using different sources of background information and different ways of preprocessing of this information. IGAM/MSIS uses bending angle profiles extracted from the MSIS-90 climatology [*Hedin* (1991)] and applies best fit profile library search and bias correction procedures [*Gobiet et al.* (2004)] in order to diminish known biases in the climatology [*Randel et al.* (2002)]. IGAM/ECMWF uses bending angle profiles derived from ECMWF operational analyses. For assimilation purposes only data derived with the IGAM/MSIS framework was used to avoid the incest problem.

[1] cf. Section 2.4.1.

	IGAM/MSIS	**IGAM/ECMWF**
Outlier Rejection and Smoothing	3σ outlier rejection on phase delays and smoothing using regularisation	Like IGAM/MSIS
Ionospheric Correction	Linear combination of bending angles. Correction is applied to low-pass filtered bending angles (1 km sliding average), L_1 heigh-pass contribution is added after correction. L_2 bending angles $<$ 15 km derived via $L_1 - L_2$ extrapolation.	Like IGAM/MSIS
Bending Angle Initialisation	Statistical optimisation of bending angles 30-120 km. Vertical correlated background (corr. lenght L=6 km) and observation (L=1 km) errors. Obs. error estimated from obs. profile $>$ 60 km. Background error:15%. Background information: MSIS-90 best fit-profile, bias corrected.	Like IGAM/MSIS, but co-located bending angel profile derived from ECMWF operational analysis (above $\sim$60 km: MSISE-90) as background information. No further processing.
Hydrostat. Integral Init.	At 120 km: pressure=p(MSISE-90).	Like IGAM/MSIS
Qality Control	Refractivity 5-35 km $\frac{\Delta N}{N} < 10\%$; Temperature 8-25 km: $\frac{\Delta T}{T} < 25K$; Reference: ECMWF analysis.	Like IGAM/MSIS

Table 3.1: Overview of IGAM CHAMP-RO retrival schemes (EGOPS/CCR Version 2, March 2004.)

3.2.3 Data Products

From the phase delay measurements a variety of atmospheric parameters can be derived. In theory, some parameters (e.g. dry temperature) could be derived without any background information, but in practice, as mentioned above, the retrieval procedure has to be initialized. For a detailed description of the refractivity formulas (Smith-Weintraub and Thayer formula) cf. Section 4.5.2.

Refractivity Profiles

Refractivity profiles are derived as described above from the statistical optimized bending angle α. This is the retrieval product which is used within the assimilation framework. To

avoid the so called *incest problem*, which is mentioned in more detail in Chapter 2**,** only data processed with the IGAM/MSIS retrieval scheme is used.

Temperature Profiles

The dry temperature T_{Dry} can then be derived from Eq. 4.3 or Eq. 4.4 by neglecting the effect of water vapor (ignoring the wet terms, k_1 empirical constant cf. Section 4.5.2)

$$N = k_1 \cdot \frac{p_A}{T_{\mathrm{Dry}}} \ , \tag{3.11}$$

which is valid in the mid- to upper troposphere and stratosphere. If the temperature is below 250 K, the temperature error caused by a 50% error of the water vapor climatology is less than 1 K [*Kursinski et al.* (1996)]. So the assumption of a *dry atmosphere* can be expanded down to the ground at high latitudes beginning from the subpolar regions on. If this assumption does not hold *a priori* information about the humidity below ~ 6 km is necessary to solve the ambiguity. Assuming a *dry atmosphere*, using Eq. 3.11 and introducing the ideal gas law

$$p_A = \frac{\rho_A T_{\mathrm{Dry}} R_{\mathrm{Dry}}}{m_A} \ , \tag{3.12}$$

where ρ_A denotes the dry air density, T_{Dry} the *dry air temperature*, R_{Dry} the universal gas constant for dry air, p_A the *dry air pressure* and m_A the mean molar mass of dry air, it follows with the use of Eq. 3.11

$$\rho_A = \frac{m_A}{k_1 R_{\mathrm{Dry}}} \cdot N \ , \tag{3.13}$$

what means that the density of air is directly proportional to the refractivity and thus can be derived directly. If the vertical air density $\rho(z)$ is known the vertical pressure can be derived using the equation of hydrostatic equilibrium

$$dp_A(z) = -g(z)\rho_A(z)dz \ , \tag{3.14}$$

and integration over z

$$p_A(z) = \int_z^\infty g(z')\rho_A(z')dz' \ .$$

A second application of Eq. 3.12 allows to derive the vertical profile of the dry temperature T_{Dry}

$$T_{\mathrm{Dry}} = k_1 \frac{p_A(z)}{N(z)} \tag{3.15}$$

Humidity Profiles

To derive humidity profiles *a priori* information about the humidity is necessary to resolve the ambiguity. An iterative procedure to calculate specific humidity profiles works as follows:

1. Assumption of dry atmosphere

$$q(z) = 0. \tag{3.16}$$

2. Calculation of the virtual temperature profile

$$T_v(z) = T(z) \cdot (1 + 0.608 \cdot q(z)) \ . \tag{3.17}$$

3. Calculation of the pressure profile as in Eq. 3.23

$$p(z) = \frac{T(z)^2}{c_2} \cdot \left(n(z) - 1 - c_1 \cdot \frac{p(z)}{T(z)} \right), \tag{3.18}$$

4. Calculation of the specific humidity profile

$$q(z) = \frac{0.622 \cdot p_w(z)}{(p(z) - 0.378 \cdot p(z))} \ . \tag{3.19}$$

With the calculated $q(z)$ the iteration starts again at step 2, the procedure converges fast. An other approach would be a 1D-Var procedure to determine the most likely state of the atmosphere taking background information into account [*Gorbunov and Sokolovskiy* (1993)].

Geopotential

The geopotential height profile can be computed corresponding to a given geometric height profile. The (geodetic) latitude dependence of gravitation weighted by $\frac{g_{\mathrm{Equ}}}{g_0}$ is needed and calculated as factor

$$g_{\mathrm{fact}} = \frac{g_{\mathrm{Equ}}}{g_{\mathrm{Mean}}} + \frac{0.00531}{g_{\mathrm{Mean}}} \cdot \sin\left(\varphi_j\right)^2 \ . \tag{3.20}$$

To calculate the geopotential height the relation

$$dZ = \frac{g}{g_0} dz \tag{3.21}$$

is used. The geopotential height is calculated from the geometric height by integration

$$Z(z) = \int_{z_1}^{z_n} \left(\frac{r_{\mathrm{Mean}}}{r_{\mathrm{Mean}} + \frac{1}{2} \cdot h(z')} \right)^2 \cdot g_{\mathrm{fact}} \cdot h(z') dz' \ . \tag{3.22}$$

Pressure

Eq. 3.23 describes the calculation of dry pressure $p_A(z)$ which is equal to the atmospheric pressure if humidity $p_W(z)$ can be neglected, i.e., everywhere above the lower to middle troposphere

$$p_A(z) = \frac{M_d}{k_1 R} \cdot \int_z^{\infty} g(z') \cdot N(z') dz' \ . \tag{3.23}$$

Total Electron Content

For the ionosphere, phase changes measured with a dual band GPS receiver can be used to calculate electron density profiles. This specific data product is especially valuable for Space Weather applications [*Jakowski et al.* (2004)].

3.2.4 The CHAMP Satellite

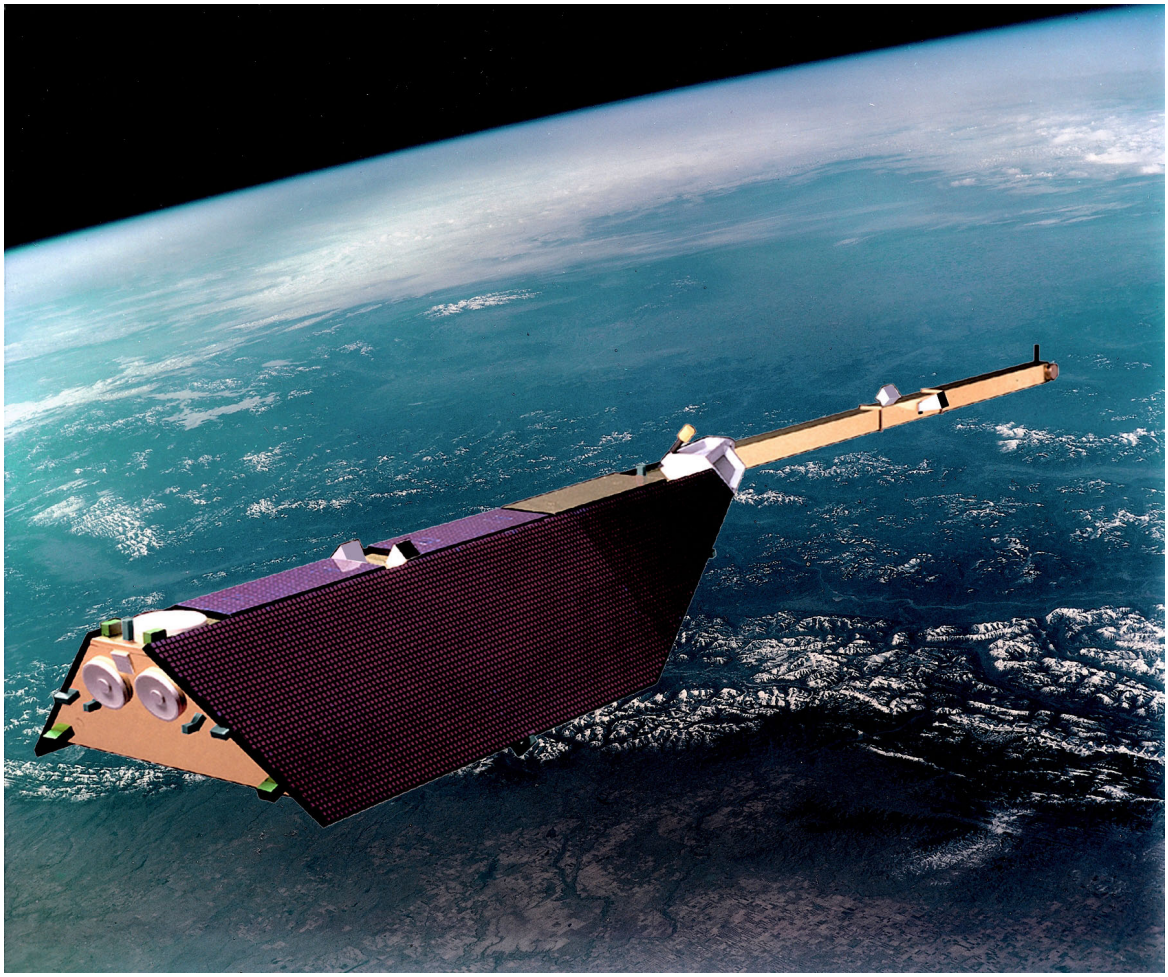

Figure 3.3: Artist view of the CHAMP satellite in orbit (courtesy GFZ Potsdam, NASA picture archive, 2004)

The CHAMP satellite was launched from the COSMODROM at Plesetzk, $\sim$ 800 km North of Moscow, at the 15 July 2000, 12:00 UTC on-board a COSMOS-3B launcher. The initial orbit was nearly circular ($\varepsilon = 0.004$) at a height of 454 km and an inclination of 87.3°. Due to the atmospheric drag the orbit height is decreasing approximately 50 to 200 m/day, depending on the solar activity. The TRSR-2 (*Black Jack*) receiver used for the RO experiment is a key component of the science payload and serves several purposes onboard CHAMP [*Reigber et al.* (1995)], [*Wickert et al.* (2002)], [*Wickert et al.* (2001)], [*Reigber et al.* (2003)].

Global Coverage in Space and Time

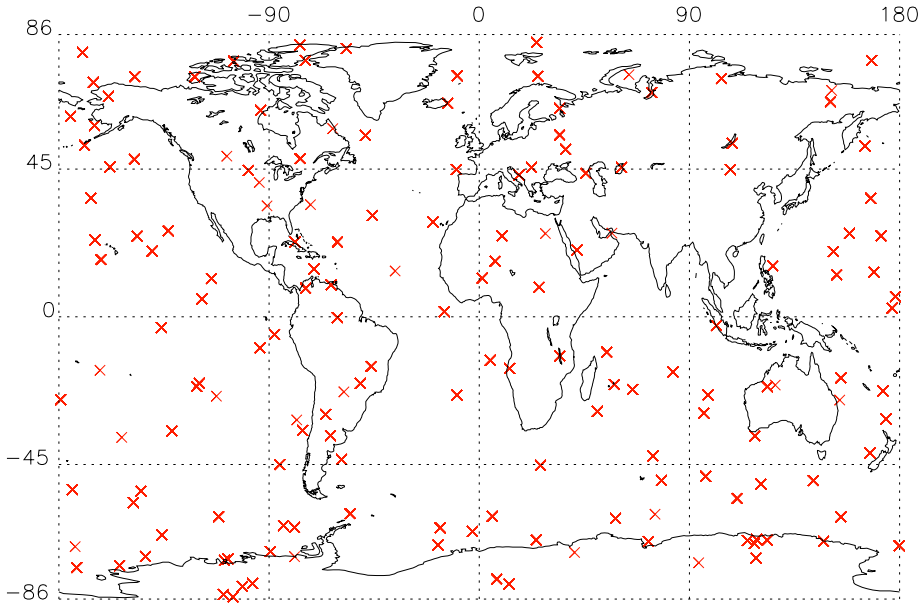

Global distribution of 24 hours of processed and quality controlled CHAMP occultations for day 225 of 2003 (142 profiles).

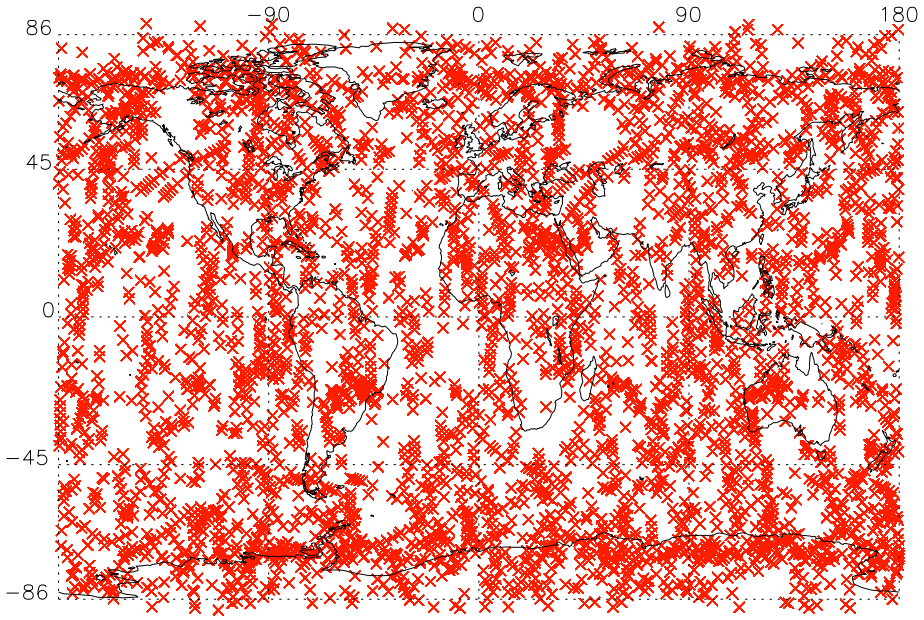

Global distribution of one month of CHAMP occultations for August 2003 (5624 profiles).

Figure 3.4: An example for the daily and monthly measurement distribution of CHAMP.

3.2.5 Future Perspectives

One of the advantages of the RO technique is the excellent global coverage which is achieved due to the nearly polar orbit of the satellite. Atmospheric data derived from RO measurements are available from remote and data sparse areas like the Pacific Ocean and the polar regions. The average number of occultation events recorded by CHAMP lies within 217 to 247 within 24 hours. Given a specific number of GPS satellites, the amount of recordable occultation events is mainly dependent on the field of view of the occultation antenna. In practice, the number of useful measurements is reduced, during the data processing chain for several reasons. At the moment, the *in-house* processing generates an average number of 150 profiles within 24 hours (GFZ Potsdam achieves a slightly higher rate per day). Fig. 3.4 upper panel shows the distribution of 142 processed CHAMP profiles from a 24 hour period during day 225 in 2003, the lower panel shows a typical measurement distribution during one month (5624 profiles).

GRAS and COSMIC

The GRAS receiver is part of the METOP [*Edwards and Pawlak* (2000)] payload, which is scheduled for launch early 2006. The new designed GRAS receiver is expected to have a significant better performance than the Black Jack receiver used onboard CHAMP. METOP-1 will be the first of a series of operational satellites providing services well into the second decade of the 21st century. METOP is the European component of a joint European/US polar satellite system. EUMETSAT plans to assume responsibility for the *morning* (local time) orbit and the US will continue with the *afternoon* coverage.

Figure 3.5: Artists view of METOP-1 (courtsey EUMETSAT, 2004).

COSMIC is the Constellation Observing System for Meteorology, Ionosphere and Climate, also known as ROCSAT-3, which is a joint U.S.-Taiwan project. The COSMIC constellation is currently planned to be launched in the spring of 2005, and is expected to

last for five years. It consists of a six satellite constellation carrying an improved version of the Black Jack receiver. Over the first year, the satellites will be gradually boosted from their initial orbit of 400 km to the final orbit of roughly 800 km. Furthermore the system comprises a satellite operations control center (SOCC) in Taiwan, the COSMIC Data Analysis and Archive Center (CDAAC) in Boulder, Colorado, and a global ground fiducial network (built upon existing NASA and international fiducial networks). This future

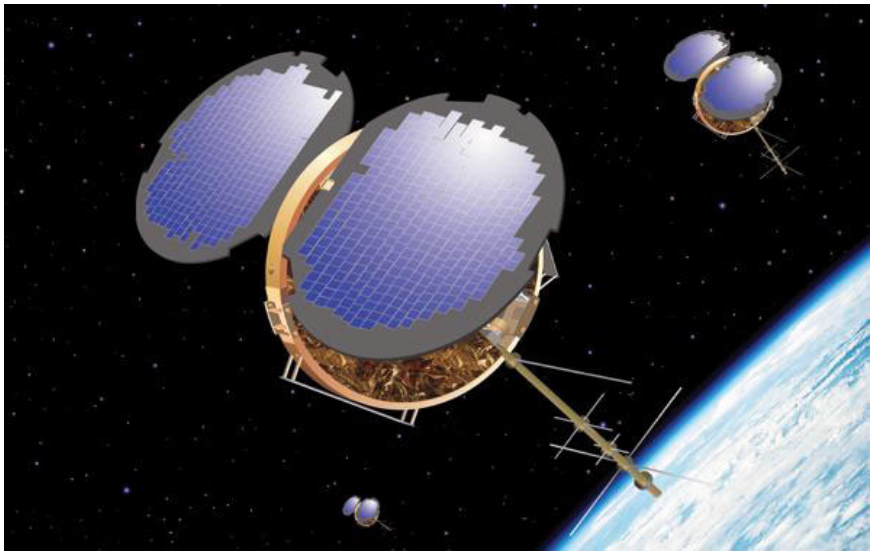

Figure 3.6: Artists view of a COSMIC satellite (courtsey UCAR, 2004)

missions will provide a continuos flow of data with excellent global coverage. Especially the long term METOP program will offer the opportunity to generate a consistent data set over many years.

Beside METOP, NPOESS/GPSOS is scheduled around 2010 for operational meteorology, carrying a GPS occultation sensor. With the European navigational satellite system GALILEO, which will be operational around 2008, the number of possible occultations using dual receivers will be roughly doubled, providing a dense global distribution of observations.

4

Specific Implementation

The system is implemented as a 3D-Var scheme using control space transformations and recursive filters. The dimensions of the background are flexible, but due to the specific application a GCM compliant Gaussian grid corresponding to T42L60, i.e., 64 latitudes $\times$ 128 longitudes comprising 60 model levels is used (the system was tested with a T21L60, i.e., 32 latitudes $\times$ 64 longitudes setup too). To increase performance the number of used model levels can be specified for the refractivity assimilation framework independent of the grid.

4.1 Coordinate System

As mentioned above a GCM compliant Gaussian grid corresponding to T42L60, i.e. 64 latitude $\times$ 128 longitude, comprising 60 model levels is used. The vertical coordinate system is derived from the surface pressure and the A and B vectors provided by ECMWF. This vertical grid comprises 60 hybrid levels. From this basic vertical coordinate system grids of geopotential height and geometric height (over reference ellipsoid) can be derived. The assimilation scheme can be used either with geometric height or geopotential height. The necessary operators are discussed later within this Chapter.

4.2 N and TQPsurf Analysis

The whole system can be run in two different modes. The first one performs a refractivity analysis, what means refractivity observations are assimilated into a refractivity background. This background field is derived from ECMWF temperatures, specific humidity, and surface pressure fields using basically the same operators which are used in the TQP-surface version of the assimilation scheme. This operation is performed at the beginning of the procedure, during the assimilation itself only the interpolation operators are used. The TQPsurface version of the assimilation scheme directly updates the temperature, specific humidity, and surface pressure input fields, what means that all fields are interpolated separately. At each iteration the new pressure field has to be derived from the updated

surface pressure field and the refractivity has to be calculated at the location of the observation. After comparison of background refractivity (also denoted as *model observation*) and observation the gradients of the input fields and observations are calculated and a suitable correction is applied. The next Sections of this Chapter applies for both versions of the scheme it is just necessary to keep the different use of the observation operators in mind.

4.3 Incremental 3D-VAR

The solution of the minimization problem can be performed either in terms of full-fields $J(x_a)$ or the analysis of increments $J(x_a) = J(x'_a = x_a - x_b)$ [*F. Bouttier* (1999)]. The latter solution method provides *optimal* analysis increments, which are added to the unmodified background field. This procedure has a number of advantages like the use of linearized control variable transforms which allow the straightforward use of adjoints to calculate the gradient of the cost function. Another advantage is that any imbalance introduced through the analysis procedure is limited to the small increments which are added to the balanced first guess.

4.4 Implementation Technique

4.4.1 Control Variables

The control variables used in the analysis are temperature, specific humidity and surface pressure, or refractivity transformed to *LOG* space, to get a better posed problem, within the refractivity only assimilation framework. To avoid negative specific humidities in the analysis and to get a better posed problem, the specific humidity is transformed to *LOG* space before any other transformation is applied. The cross correlations between the control variables are assumed to be small enough to be neglected. This assumption serves to effectively block-diagonalize the background error covariance matrix. For each control variable there still remains both, horizontal and vertical correlations. Those are assumed to be separable, which is a widely used assumption.

4.4.2 Minimization

The cost function is minimized by using an iterative descent algorithm, which is in our case the L-BFGS-B routine. The cost of the analysis is proportional to the number of cost function and its gradient evaluations, denoted as *simulations*. If a new state $\mathbf{x}$ is found, an *iteration* is performed, which means that to find a new $\mathbf{x}$, several simulations may be required (cf. Section 4.10).

4.4.3 Preconditioning

A preconditioning of the problem is performed as part of the control space transformations (cf. Section 4.8).

4.4.4 The Adjoint Technique

The adjoint technique allows to calculate the gradients, needed for the minimization procedure, at reasonable numerical cost (cf. Acknowledgments) [*INRIA* (2002)].

4.5 Observation Operators

4.5.1 Interpolation Operator

To calculate the background values at the spatial location of the measurements two bilinear horizontal and one logarithmic vertical interpolation are performed for each observation. A cubic spline version for the vertical interpolation is also available for performance tests.

Horizontal Interpolation

The bilinear interpolation consists of a weighted average of the four surrounding grid points to determine their interpolated value. Two linear interpolations on opposite sites are performed followed by a consecutive interpolation of these intermediate results. This horizontal interpolation is performed for the atmospheric layer above and below the observation

$$f(x,y) = (1-u)(1-v)f_{i,j} + u(1-v)f_{i+1,j} + (1-u)vf_{i,j} + uvf_{i+1,j+1} \ , \tag{4.1a}$$

$$u = \frac{(x-x_i)}{(x_{i+1}-x_i)} \ , \tag{4.1b}$$

$$v = \frac{(y-y_j)}{(y_{j+1}-y_j)} \ , \tag{4.1c}$$

where $x_i < x < x_{i+1}$ and $y_j < y < y_{j+1}$.

Vertical Interpolation

Due to the fact of a globally non uniform vertical grid, the heights of the horizontal interpolated values are also calculated by bilinear interpolation from the vertical background grid.

Linear Interpolation in *LOG* Space Given the background value above and below the spatial location of the observation a logarithmic interpolation is performed to get the final value of the background at the location of the observation.

$$\text{Interpolated Value} = e^{(\log(Z_1)*\text{Weight}_1)} \cdot e^{(\log(Z_2)*\text{Weight}_2)} \tag{4.2}$$

where Z_1 and Z_2 denote the horizontal interpolated values of the layers above and below the observation which are weighted with Weight_1 and Weight_2, calculated from the vertical distance between observation and Z_1, Z_2.

Cubic Spline Interpolation in *LOG* Space As second option a cubic spline interpolation was implemented, using three vertical points above and below the vertical measurement location to interpolate the background. Experiments proved that the chosen number of background points is sufficient to obtain accurate results [*Press et al.* (1987)].

4.5.2 Refractivity Operator

To calculate the refractivity at a given point, it is necessary to know the atmospheric variables absolute temperature, specific humidity and pressure. There are two standard formulas used, which are the Thayer and the Smith-Weintraub formula. The Thayer Formula is the more accurate one, the Smith-Weintraub formula is basically the same, but assumes an ideal gas.

Thayer Formula

$$N = k_1 \cdot \frac{p_A}{T} \cdot \frac{1}{z_A} + k_2 \cdot \frac{e}{T} \cdot \frac{1}{z_W} + k_3 \cdot \frac{e}{T^2} \cdot \frac{1}{z_W} \tag{4.3}$$

Smith-Weintraub Formula

$$N = k_1 \cdot \frac{p_A}{T} + k_2 \cdot \frac{e}{T} + k_3 \cdot \frac{e}{T^2} \tag{4.4}$$

N	=	Refractivity	[ ]
T	=	Absolute Temperature	[K]
e	=	Partial pressure of water vapor	[hPa]
p_A	=	Partial pressure of "dry Air"	[hPa]
z_A	=	Compressibility factor of "dry Air"	[ ]
z_W	=	Compressibility factor of water vapor	[ ]
k_1	=	Empirical constant Thayer Formula	[K/hPa]
k_2	=	Empirical constant Thayer Formula	[K/hPa]
k_3	=	Empirical constant Thayer Formula	[K^2/hPa]

Table 4.1: Parameter and Variables used in Thayer & Smith-Weintraub formula.

Further explanations of parameters cf. Appendix A.1

Calculation of Refractivity Fields from ECMWF Analyses

Given the fields of temperature, surface pressure and specific humidity (in our case analysis fields of ECMWF), we can calculate the field of refractivity using either the Thayer or Smith Weintraub- formula. A comparison of the two formulas shows no significant differences, but because of negligible additional computing cost, the more accurate Thayer formula was chosen to calculate the background in the case of pure refractivity assimilation, and as forward operator, to calculate refractivity from temperature, humidity, and surface pressure analysis fields. To derive the error characteristics in case of the pure refractivity assimilation scheme the Smith-Weintraub formula was used.

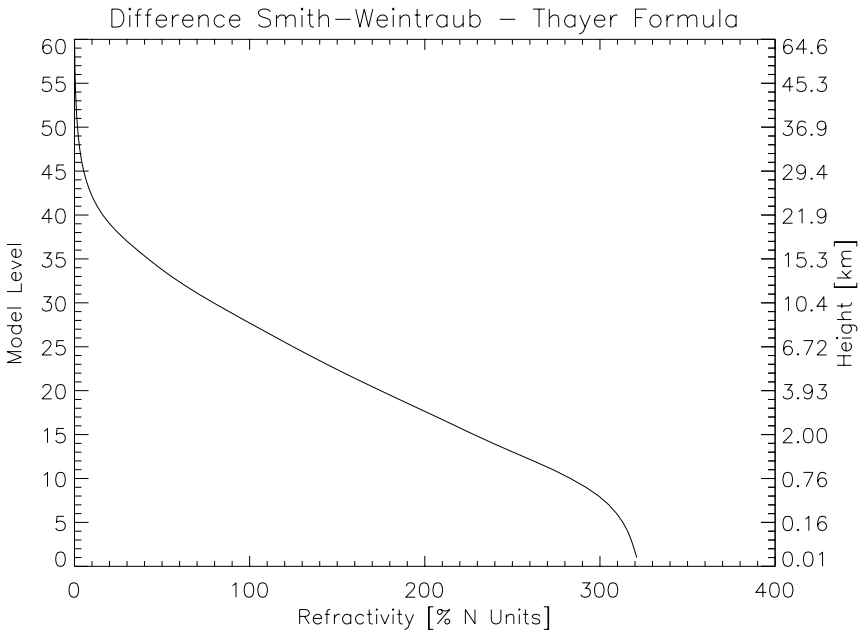

Figure 4.1: Mean global refractivity profile calculated from T42L60 ECMWF analysis fields.

Fig. 4.2 shows the negligible difference of the mean global refractivity profile calculated with the Thayer and the Smith Weintraub formula using an ECMWF T42L60 analysis field (Date: 2003.01.03; 12 UTC). First we have to do some general calculations. We need the amount of water vapor Mm_W and and dry air Mm_A in [mol]. Given the specific humidity q the molar mass of water vapor m_W and the molar mass of dry air m_A we can calculate

$$Mm_W = \frac{q}{m_A} \text{ and } Mm_A = \frac{1.0 - q}{m_A} \ . \tag{4.5}$$

Further we need the partial pressure of water vapor e which is given by

$$e = R_W \cdot \rho_W \cdot T \ , \tag{4.6}$$

using the formulas $q = \frac{\rho_W}{\rho}$ and $\rho_W = q \cdot \rho$ we can derive

$$e = R_W \cdot \rho_W \cdot T \ , \tag{4.7a}$$

$$e = R_W \cdot q \cdot \rho \cdot T \ , \tag{4.7b}$$

$$e = R_W \cdot q \cdot \frac{1}{R_A \cdot T} \cdot \frac{p}{\left(1 + \frac{R_W - R_A}{R_A} \cdot q\right)} \cdot T \ , \tag{4.7c}$$

where ρ_W is given by

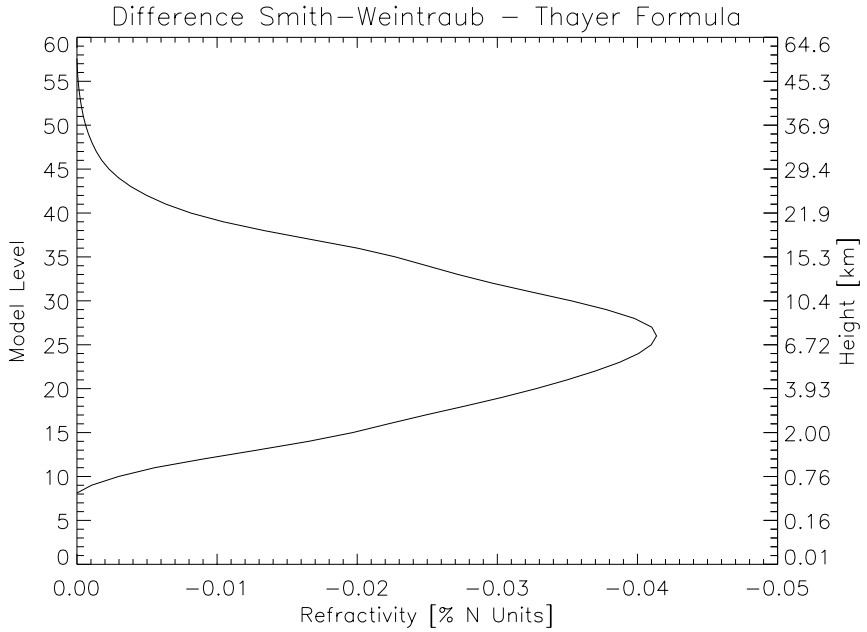

Figure 4.2: Difference in global mean refractivity calculated with Smith-Weintraub and Thayer Formula.

$$\frac{p_i}{p} = \frac{M_i^*}{M^*} \ , \tag{4.8}$$

$$\frac{p_W}{p} = \frac{M_W^*}{M^*} \ , \tag{4.9}$$

$$M_W^* = \frac{M_W}{m^*} \ , \tag{4.10}$$

$$q = \frac{M_W}{M} \ , \tag{4.11}$$

$$p_W = p \cdot \frac{1}{M^*} \cdot \frac{M_W}{m_W^*} \ . \tag{4.12}$$

Deviations from the ideal gas law (*Van-Der-Waals-Formula*) are negligible within meteorological applications so q can be expressed as

$$q = 0.622 \cdot \frac{e}{p - 0.378 \cdot e} \ . \tag{4.13}$$

It is reasonable to neglect $0.378 \cdot e$ in Eq. 4.13 which leads as expression for e as

$$e = \frac{q \cdot p}{0.622} \ . \tag{4.14}$$

Finally we need

$$p_A = p - e \tag{4.15}$$

to be able to solve the Thayer equation.

4.5.3 Vertical Coordinate Operator

As can be seen in Eq. 4.3 and Eq. 4.4 the pressure at the location of the observation is needed to calculate the refractivity. ECMWF provides temperature, specific humidity, and surface pressure fields. The background pressure field is derived by a series of operators. This operators are also used to set up the vertical coordinate system of the assimilation scheme either as a vertical grid of geopotential heights or a vertical grid of geometric heights. Since the pressure field is also derived, pressure coordinates are possible but not implemented at the moment. The values of $T_{i,j,z}$ and specific humidity $q_{i,j,z}$, are given for the Gaussian grid of the latitudes φ_j and the homogenous grid of the longitudes λ_i, and an irregular spaced height grid $z_{i,j,z}$. For the T42L60 grid the index ranges are i =1...64, j = 1...128, and z = 1...60 for full level quantities and z =0...60 for half level quantities. Here and in other parts of this thesis z simply denotes the height coordinate wether if it is geometrical height or geopotential height, but further on in this Section z denotes geometrical height and ϕ geopotential height. The vertical index of all quantities is always denoted as z. Coordinates are geocentric except denoted otherwise.

The pressure corresponding to the zth half and full levels are calculated by the means of formulas,e.g., [*Roeckner et al.* (2003)]

$$P_{i,j,z+\frac{1}{2}} = A_{z+\frac{1}{2}} + B_{z+\frac{1}{2}} \cdot P_{\mathrm{Surf}_{i,j}} \ , \tag{4.16}$$

$$P_{i,j,z} = \frac{1}{2}\left(P_{i,j,z+\frac{1}{2}} + P_{i,j,z-\frac{1}{2}}\right) \ , \tag{4.17}$$

where $P_{\mathrm{surf}_{i,j}}$ denotes the surface pressure at the ith longitude and the jth latitude. The $A_{z+\frac{1}{2}}$ and $B_{z+\frac{1}{2}}$ are the vertical coordinate parameters provided by ECMWF. The calculation of the geopotential heights is based on the hydrostatic equation and on an interpolation between the half and the full levels [*Gorbunov and Kornblueh* (2003)]

$$\phi_{i,j,z+\frac{1}{2}} - \phi_{i,j,z-\frac{1}{2}} = R_{\mathrm{Dry}} T_{v,i,j,z} \cdot Ln\left(\frac{P_{i,j,z+\frac{1}{2}}}{P_{i,j,z-\frac{1}{2}}}\right) \ , \tag{4.18}$$

$$\phi_{i,j,z_{\mathrm{max}}+\frac{1}{2}} = \phi_{i,j,z_{\mathrm{Surf}}} \ , \tag{4.19}$$

$$\phi_{i,j,z} = \phi_{i,j,z+\frac{1}{2}} + \alpha_{i,j,z} \cdot R_{Dry} T_{v,i,j,z} \ , \tag{4.20}$$

$$\alpha_{i,j,z} = Ln(2) \text{ for } z = 1 \ , \tag{4.21}$$

$$\alpha_{i,j,z} = 1 - \frac{P_{i,j,z-\frac{1}{2}}}{P_{i,j,z+\frac{1}{2}} - P_{i,j,z-\frac{1}{2}}} \cdot Ln\left(\frac{P_{i,j,z+\frac{1}{2}}}{P_{i,j,z-\frac{1}{2}}}\right) \text{ for } z > 1 \ , \tag{4.22}$$

where T_v denotes the virtual temperature as defined in Eq. 4.34 and ϕ_{Surf} is the surface geopotential which is equal the orography. The geometrical heights over reference ellipsoid were calculated from the geopotential heights by the approximate formula from the *US Standard Atmosphere*:

$$R_0 = \frac{2 \cdot 10^{-3} \cdot g_{\mathrm{Surf}i,j}}{3.085462 \cdot 10^{-6} + 2.27 \cdot 10^{-9} \cdot \cos(2\varphi_j) - 2 \cdot 10^{-12} \cdot \cos(4\varphi_j)} \ , \tag{4.23}$$

$$z_{i,j,z} = R_0 \cdot \frac{\phi_{i,j,z} \cdot (g_{\mathrm{Mean}} - \phi_{i,j,z})}{g_{\mathrm{Surf}i,j} \cdot R_0} \ , \tag{4.24}$$

where R_0 denotes the effective Earth's radius, g_{Mean} the mean gravity acceleration and $g_{\text{Surf}i,j}$ the local gravity acceleration on the surface. $g_{\text{Surf}i,j}$ itself is calculated by the *International gravity formula plus standard z dependence*:

$$g_{\text{Equator}} = 9.7803 \text{ m/s}^2 \tag{4.25}$$

$$g_{\text{Surf}_{i,j}} = g_{\text{Equator}} \cdot \left(1 + 0.00531 \cdot \sin\left(\varphi_{\text{Geodetic}_j}\right)^2\right) \ . \tag{4.26}$$

finally the standard height dependency of $g_{\text{Surf}_{i,j}}$ is calculated

$$R_{Mean} = 6371.0 \text{ km} \ , \tag{4.27}$$

$$f_{gz} = \left(\frac{R_{\text{Mean}}}{R_{\text{Mean}} + z}\right)^2 \ , \tag{4.28}$$

$$g_{\text{Surf}_{i,j},z} = g_{\text{Surf}_{i,j}} \cdot f_{gz} \ , \tag{4.29}$$

g_{Equator} is the gravity acceleration at the equator and R_{Mean} the mean Earth's radius.

4.6 Observation Error Covariance

The observation covariance takes only vertical correlations into account. Due to the separation in space and time between the different RO events this simplification is justified.

4.6.1 Formulation of the Observation Error Covariance Matrix

A simple error covariance matrix formulation was deduced from the empirical estimated matrices [*Steiner* (2004)]. A least square method was used to fit analytical functions to the relative standard deviation which shows a different behavior below and above the tropopause height. The empirical relative standard deviation can be approximated with an exponential increase above the tropopause height (4.30) and with a decrease proportional $\frac{1}{\text{Height}}$ below the tropopause height (cf. Eq. 4.31). The tropopause height is defined globally at 15 km. To be able to scale the error magnitude, which is receiver dependent, the standard deviation at tropopause height (s_{Tropo}) can be tuned. Eq. 4.30 gives the exponential function for the relative standard deviation y above the tropopause height z_{Tropo} with the parameter H_{Strato} which is the scale height of the error increase over the stratosphere. The best fit value for H_{Strato} is 11.9 km for the error scale height z, denotes the height [*Steiner and Kirchengast* (2004)]

$$s_{z>\text{Tropo}} = s_{\text{Tropo}} \cdot \exp\left[\frac{z - z_{\text{Tropo}}}{H_{\text{Strato}}}\right] \ . \tag{4.30}$$

Eq. 4.31 gives the analytical function for the relative standard deviation below the tropopause height with the parameter $b = 4.461$

$$s_{z<\text{Tropo}} = s_{\text{Tropo}} + b \cdot (z^{-1} - z_{\text{Tropo}}^{-1}) \ . \tag{4.31}$$

This formulation of the observation error covariance also accounts for the error of representativeness, so there is no additional specification within the assimilation framework necessary.

4.7 Background Error Covariance

The used background fields of temperature, specific humidity, and surface pressure, are provided by ECMWF. So the basis of our considerations concerning the errors and correlations are based on ECMWF recommendations[1].

4.7.1 Temperature, Specific Humidity, and Surface Pressure

Standard deviations for temperature, specific humidity and surface pressure are provided by ECMWF as global means. The same applies to the vertical and horizontal correlations.

[1] Data provided by Mike Fisher, ECMWF, Reading U.K., 2003.

Standard Deviation Temperature

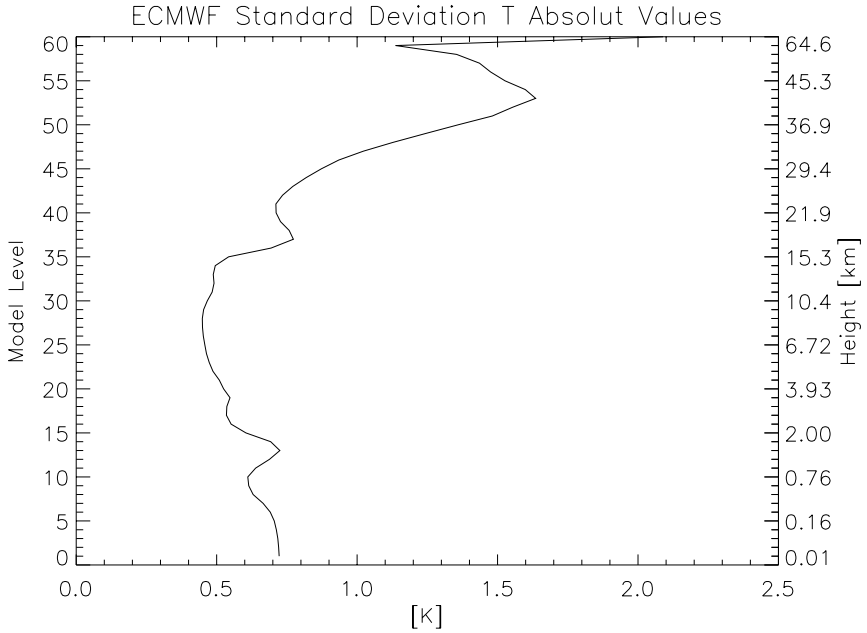

ECMWF global mean temperature standard deviation absolut values.

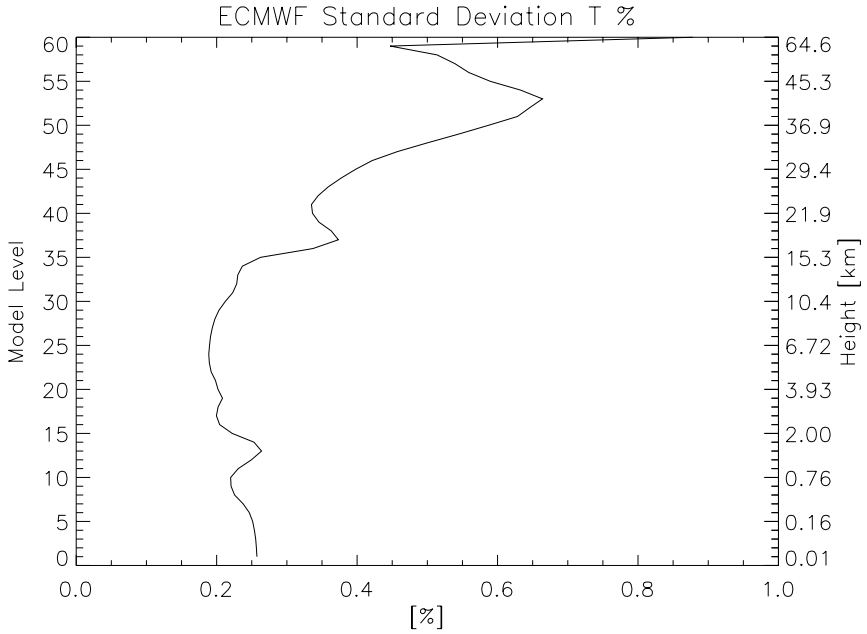

ECMWF global mean temperature standard deviation relative values.

Figure 4.3: Global mean standard deviation of ECMWF temperature fields.

Vertical and Horizontal ECMWF Temperature Error Correlations

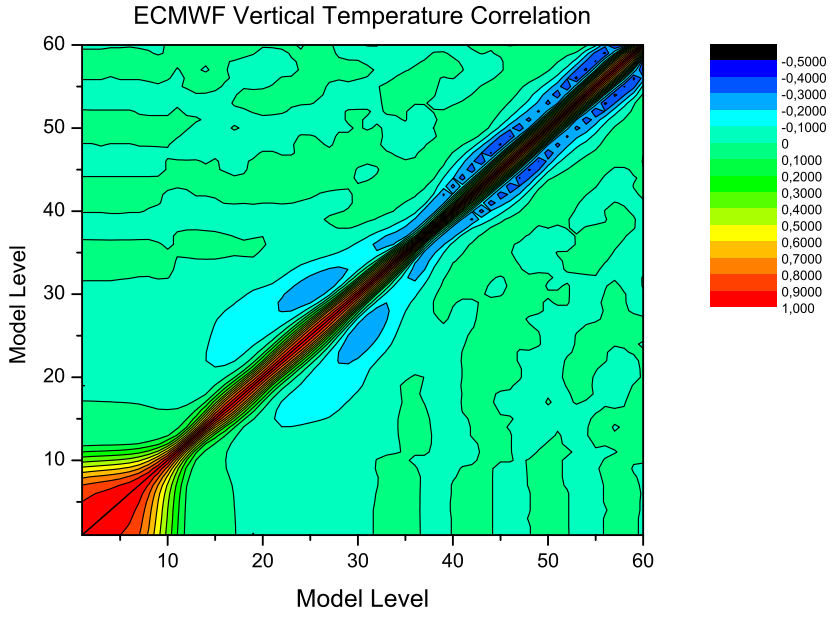

ECMWF vertical temperature error correlation, L60.

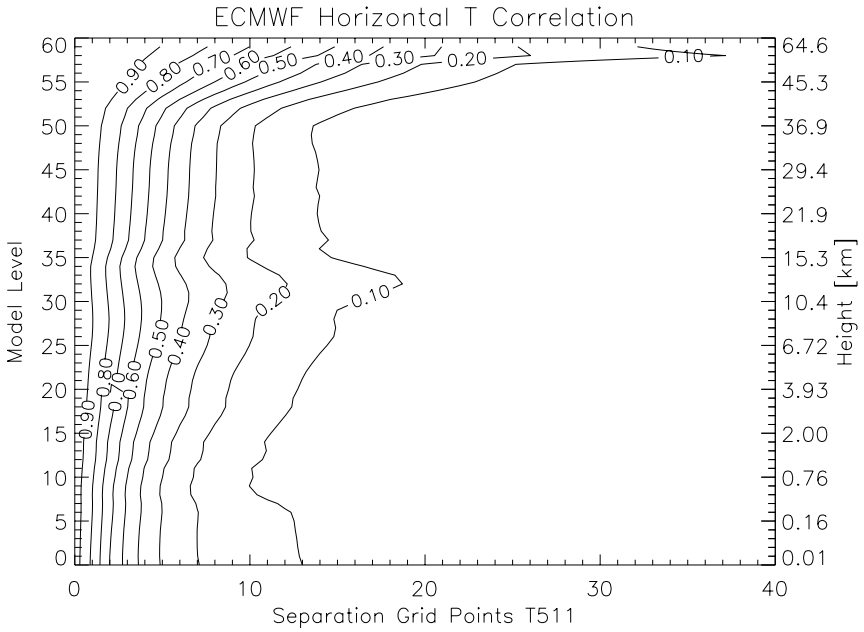

ECMWF horizontal temperature error correlation.

Figure 4.4: Global mean vertical and horizontal error correlations of ECMWF temperature fields.

Standard Deviation Specific Humidity

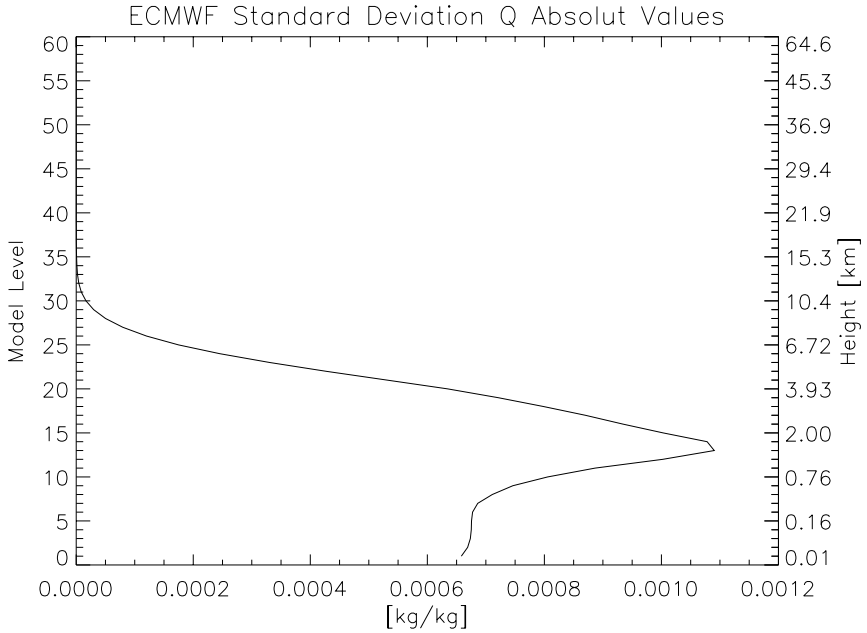

ECMWF global mean specific humidity standard deviation absolut values.

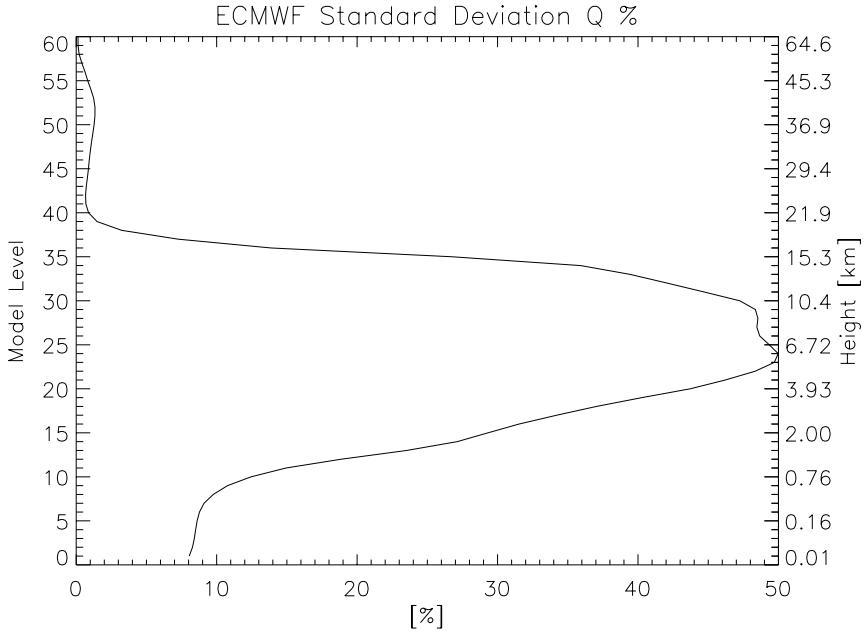

ECMWF global mean specific humidity standard deviation relatve values.

Figure 4.5: Global mean standard deviation of ECMWF specific humidity fields.

Vertical and Horizontal ECMWF Error Correlation Specific Humidity

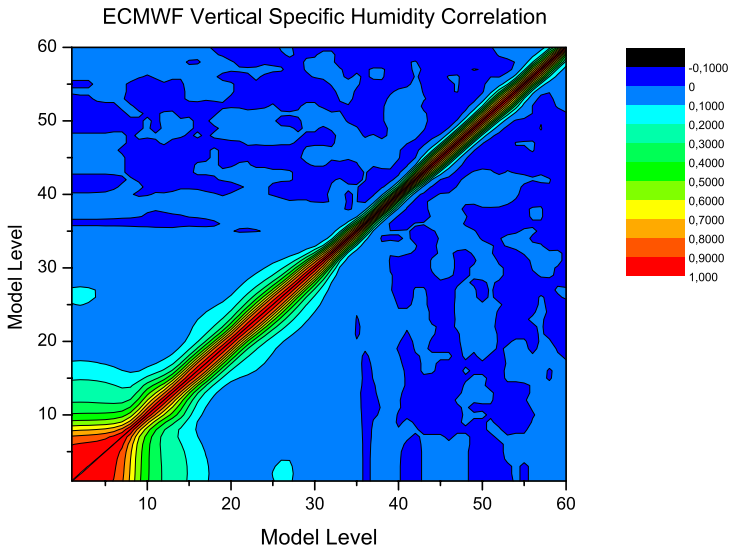

ECMWF vertical error correlation of specific humidity, L60.

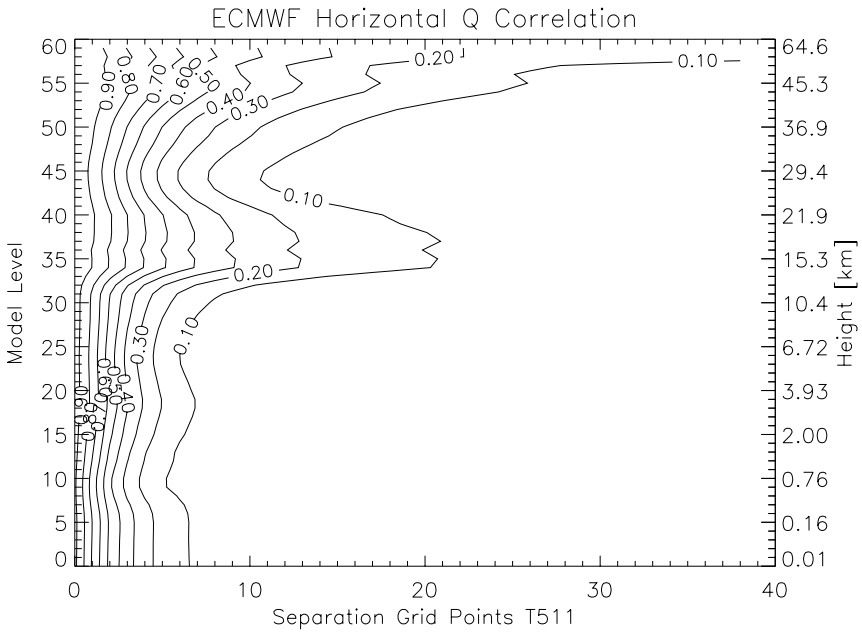

ECMWF horizontal error correlation of specific humidity.

Figure 4.6: Global mean vertical and horizontal error correlations of ECMWFspecific humidity fields.

Standard Deviation Surface Pressure

The global mean standard deviation of surface pressure provided by ECMWF is 250 Pa.

Horizontal ECMWF Error Correlation Surface Pressure

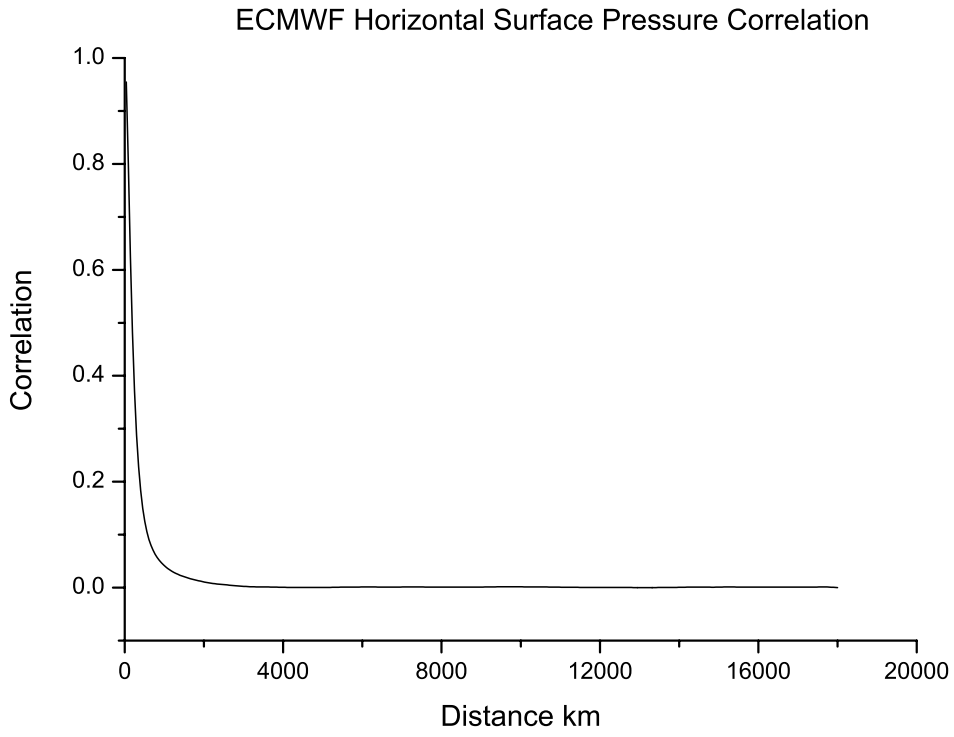

Figure 4.7: Global mean ECMWF horizontal error correlation of surface pressure.

4.7.2 Derivation of the Refractivity Error Covariance

To calculate the refractivity standard deviation error propagation techniques were used, assuming that the Smith-Weintraub formula is accurate enough for this purpose. The ECMWF provided temperature standard deviation was taken times two to achieve realistic error characteristics. The vertical correlation was derived by a weighted combination of temperature and specific humidity correlations.

Standard Deviation

The Smith-Weintraub formula was used to derive the global mean standard deviation σ_N of refractivity background fields

$$N = k_1 \cdot \frac{p_A}{T} + k_2 \cdot \frac{e}{T} + k_3 \cdot \frac{e}{T^2} \ .$$

e can be related to given values as shown in Eq. 4.14, and p_A can be related to given values as shown in Eq. 4.15

$$N = k_1 \cdot \frac{p - \frac{q \cdot p}{0.622}}{T} + k_2 \cdot \frac{\frac{q \cdot p}{0.622}}{T} + k_3 \cdot \frac{\frac{q \cdot p}{0.622}}{T^2} \ . \tag{4.32}$$

Applying standard error propagation techniques (Gaussian error propagation) a formula for σ_N can be derived by calculating the partial derivatives of all variables (T, q, p) afflicted with errors ($k1, k2$ and $k3$ are assumed to be error free). Since only the error of the surface pressure is known, the error of p has to be derived first. To derive a formula for σ_p the following equation is used

$$p_2 - p_1 = e^{-\frac{\phi_2 - \phi_1}{R_L T_v}} \ , \tag{4.33}$$

where T_v denotes the virtual temperature which is defined by

$$T_v = \left(1 + \underbrace{\frac{R_w - R_{Dry}}{R_{Dry}}}_{0.608} \cdot q \right) \cdot T \ . \tag{4.34}$$

This expression can be simplified with

$$e = 0.608 \ ,$$

thus leading to

$$T_v = T \cdot (1 + e \cdot q) \ . \tag{4.35}$$

The virtual temperature takes implicitly the humidity into account. The σ_{T_v} can be calculated the following way (Gaussian error propagation) assuming T and q are afflicted with errors

$$1 + e \cdot q = \frac{\partial}{\partial T} T \cdot (1 + e \cdot q) \ , \tag{4.36a}$$

$$T \cdot e = \frac{\partial}{\partial q} T \cdot (1 + e \cdot q) \ , \tag{4.36b}$$

$$\sigma_p = \sqrt{(1 + e \cdot q)^2 \cdot \Delta T^2 + (T \cdot e)^2 \cdot \Delta q^2} \ . \tag{4.36c}$$

Now σ_p can be calculated the same way assuming T_v and p_{Surf} are afflicted with errors

$$e^{-\frac{\phi_2-\phi_1}{R_L T_v}} = \frac{\partial}{\partial p_0} p_0 \cdot e^{-\frac{\phi_2-\phi_1}{R_L T_v}} \ , \tag{4.37a}$$

$$\frac{p_0 \cdot (\phi_2-\phi_1)\, e^{-\frac{\phi_2-\phi_1}{R_L T_v}}}{R_L T_v^2} = \frac{\partial}{\partial T_v} p_0 \cdot e^{-\frac{\phi_2-\phi_1}{R_L T_v}} \ , \tag{4.37b}$$

$$\sigma_p = \sqrt{\left(e^{-\frac{\phi_2-\phi_1}{R_L T_v}}\right)^2 \cdot \Delta p_0^2 + \left(\frac{p_0 \cdot (\phi_2-\phi_1)\, e^{-\frac{\phi_2-\phi_1}{R_L T_v}}}{R_L T_v^2}\right)^2 \cdot \Delta T_v^2} \ . \tag{4.37c}$$

Finally σ_N can be derived

$$\frac{\partial}{\partial T}\left(k_1 \cdot \frac{p - \frac{q\cdot p}{0.622}}{T} + k_2 \cdot \frac{\frac{q\cdot p}{0.622}}{T} + k_3 \cdot \frac{\frac{q\cdot p}{0.622}}{T^2}\right) \tag{4.38a}$$

$$= \frac{k_1 \cdot p - \frac{q\cdot p}{0.622}}{T^2} - \frac{k_2 \cdot q \cdot p}{0.622 \cdot T^2} + \frac{2 \cdot k_3 \cdot q \cdot p}{0.622 \cdot T^3} \tag{4.38b}$$

$$= \frac{p \cdot (-k_1 \cdot p \cdot 0.622 + k_1 \cdot T \cdot q - k_2 \cdot T \cdot q - 2 \cdot k_3 \cdot q)}{0.622 \cdot T^3} \ , \tag{4.38c}$$

$$\frac{\partial}{\partial q}\left(k_1 \cdot \frac{p - \frac{q\cdot p}{0.622}}{T} + k_2 \cdot \frac{\frac{q\cdot p}{0.622}}{T} + k_3 \cdot \frac{\frac{q\cdot p}{0.622}}{T^2}\right) \tag{4.39a}$$

$$= \frac{k_1 \cdot p}{0.622 \cdot T} - \frac{k_2 \cdot p}{0.622 \cdot T} + \frac{k_3 \cdot p}{0.622 \cdot T^2} \tag{4.39b}$$

$$= \frac{p \cdot (k_1 T - k2 \cdot T - \cdot k_3)}{0.622 \cdot T^2} \ , \tag{4.39c}$$

$$\frac{\partial}{\partial p}\left(k_1 \cdot \frac{p - \frac{q\cdot p}{0.622}}{T} + k_2 \cdot \frac{\frac{q\cdot p}{0.622}}{T} + k_3 \cdot \frac{\frac{q\cdot p}{0.622}}{T^2}\right) \tag{4.40a}$$

$$= \frac{k_1 \cdot \left(1 - \frac{q}{0.622}\right)}{T} + \frac{k_2 \cdot q}{0.622 \cdot T} + \frac{k_3 \cdot q}{0.622 \cdot T^2} \tag{4.40b}$$

$$= \frac{-k_1 T \cdot 0.622 + k_1 \cdot T \cdot q - k_2 \cdot T \cdot q - k_3 \cdot q}{0.622 \cdot T^2} \ . \tag{4.40c}$$

As already done before to calculate σ_{T_v} and σ_p, $\partial T, \partial q$ and ∂p can be assumed to be equal the errors $\Delta T, \Delta q$ and Δp

$$\begin{aligned}\sigma_N^2 = &\left(\frac{p \cdot (-k_1 \cdot p \cdot 0.622 + k_1 \cdot T \cdot q - k_2 \cdot T \cdot q - 2 \cdot k_3 \cdot q)}{0.622 \cdot T^3}\right)^2 \cdot \Delta T^2 + \\ &\left(\frac{p \cdot (k_1 T - k2 \cdot T - \cdot k_3)}{0.622 \cdot T^2}\right)^2 \cdot \Delta q^2 + \\ &\left(\frac{-k_1 T \cdot 0.622 + k_1 \cdot T \cdot q - k_2 \cdot T \cdot q - k_3 \cdot q}{0.622 \cdot T^2}\right)^2 \cdot \Delta p^2 \ .\end{aligned} \tag{4.41}$$

Derived Pressure Standard Deviation

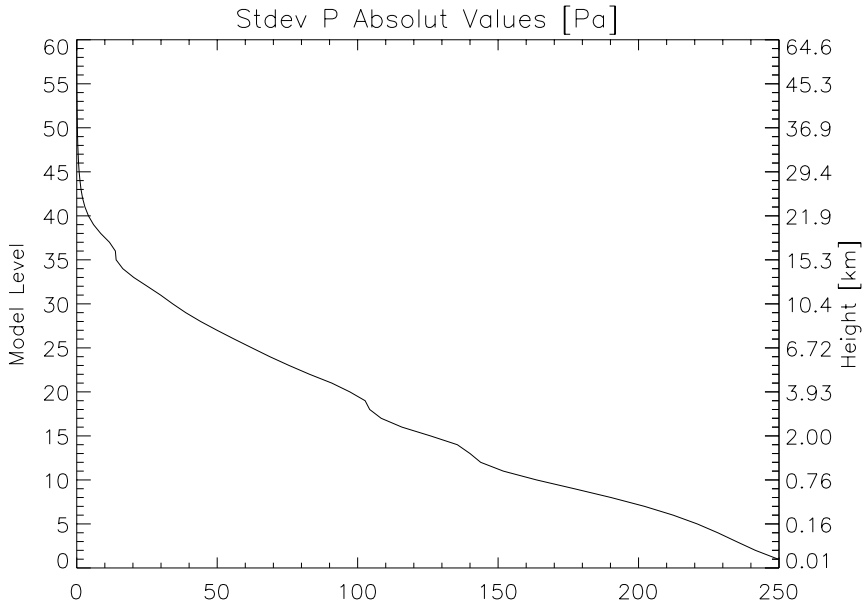

Global mean derived pressure standard deviation in absolute values [Pa].

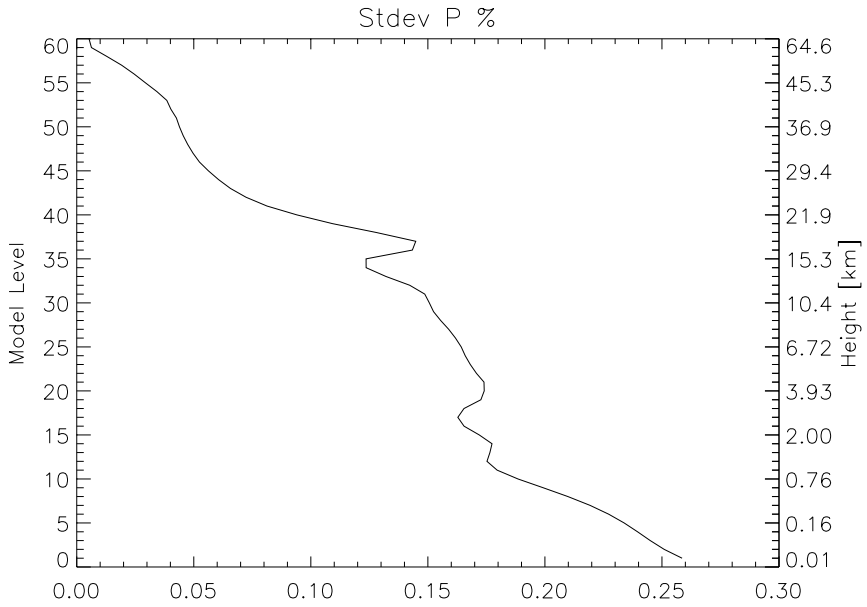

Global mean derived pressure standard deviation in relative values [%].

Figure 4.8: Global mean derived pressure standard deviation.

Derived Refractivity Standard Deviation

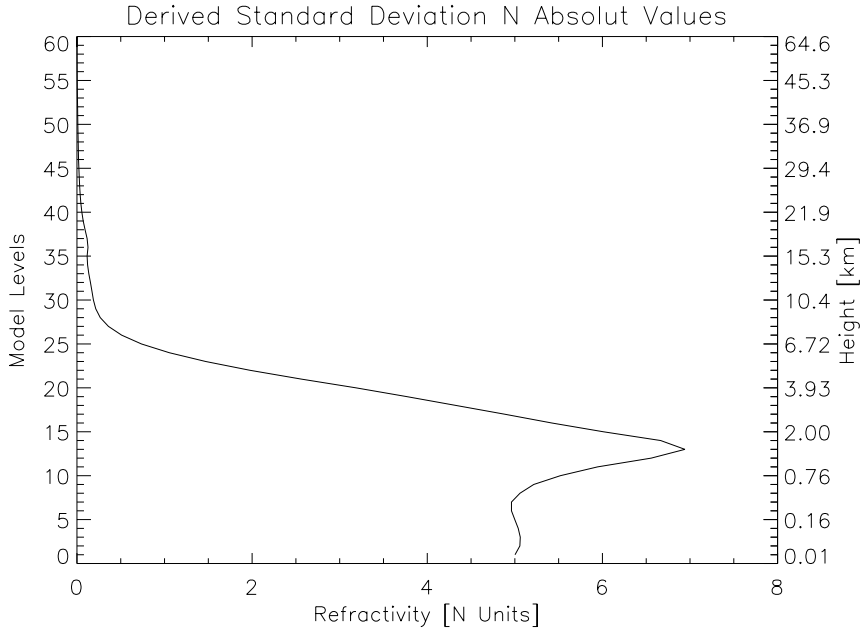

Global mean derived refractivity standard deviation in N units.

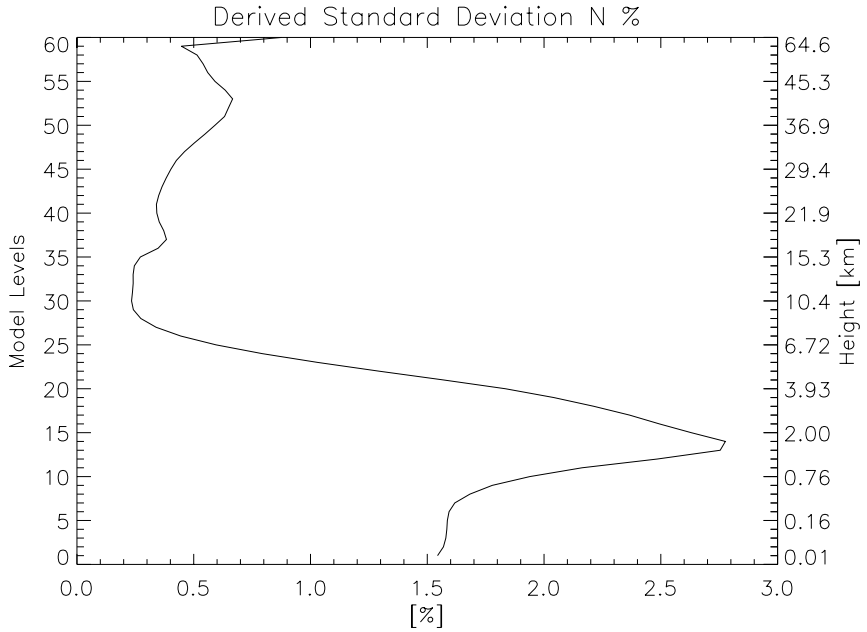

Global mean derived refractivity standard deviation in relative values.

Figure 4.9: Global mean derived refractivity standard deviation.

Finally σ_N is given by the square root of the variance

$$\sigma_N = \sqrt{\sigma_N^2} \ . \tag{4.42}$$

The derived refractivity standard deviation (cf. Fig. 4.9) is dominated by the temperature error over ~ 18 km due to the the marginal water vapor content of the atmosphere above the tropopause.

Vertical Error Correlation

The vertical correlation of σ_N is derived by a weighted average of the ECMWF temperature ($\mathrm{Corr}_V\_T_{i,j}$) and specific humidity ($\mathrm{Corr}_V\_q_{i,j}$) correlations. To calculate the weighting factors, the fraction of the combined temperature and surface pressure variance of the total refractivity variance σ_N^2 and the fraction of the specific humidity variance were calculated separately. The correlation matrix was calculated by:

$$\mathrm{Corr}_V\_N_{i,j} = \frac{\sigma_{T,p_i}^2}{\sigma_{N_i}^2} \cdot \mathrm{Corr}_V\_T_{i,j} + \frac{\sigma_{q_i}^2}{\sigma_{N_i}^2} \cdot \mathrm{Corr}_V\_q_{i,j} \tag{4.43}$$

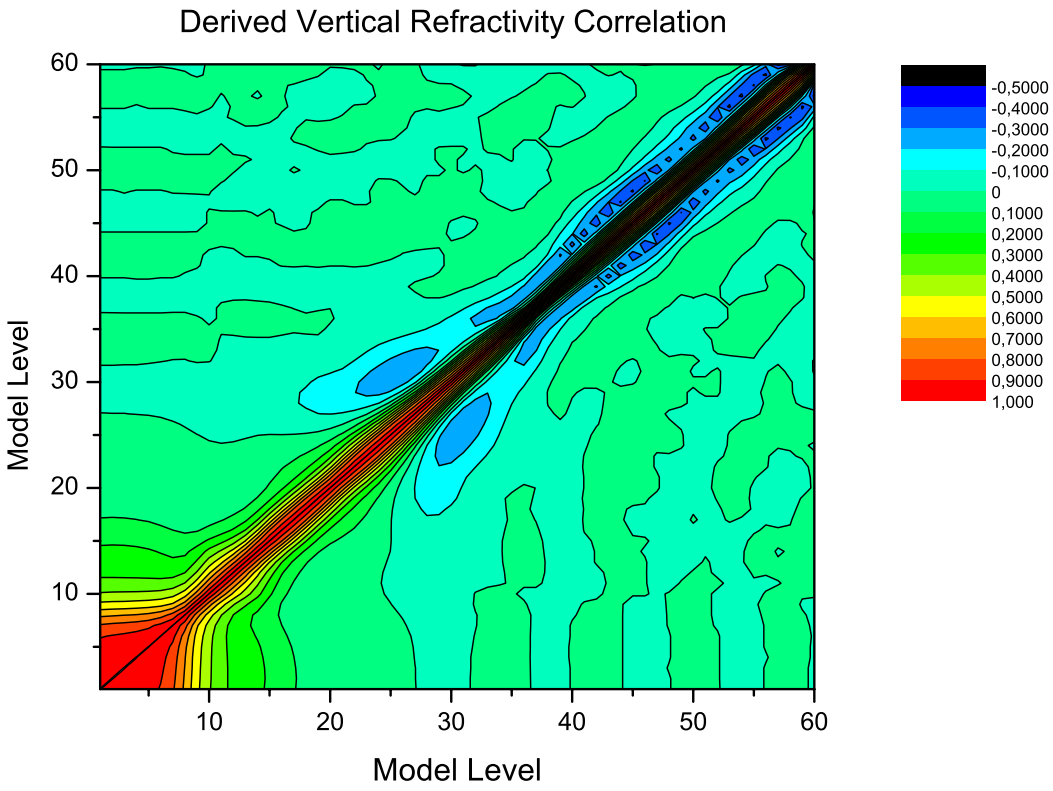

Figure 4.10: Derived vertical correlation of background refractivity errors, L60.

Horizontal Error Correlation

The horizontal correlation of σ_N is derived the same way as the vertical one by a weighted average of the ECMWF temperature ($\mathrm{Corr}_H\_T_{i,j}$) and specific humidity ($\mathrm{Corr}_H\_q_{i,j}$) correlations. To calculate the weighting factors, the fraction of the combined temperature and surface pressure variance of the total refractivity variance σ_N^2 and the fraction of the specific humidity variance were calculated separately. The correlation matrix was calculated by

$$\mathrm{Corr}_H\_N_{i,j} = \frac{\sigma_{T,p_i}^2}{\sigma_{N_i}^2} \cdot \mathrm{Corr}_H\_T_{i,j} + \frac{\sigma_{q_i}^2}{\sigma_{N_i}^2} \cdot \mathrm{Corr}_H\_q_{i,j} \ . \tag{4.44}$$

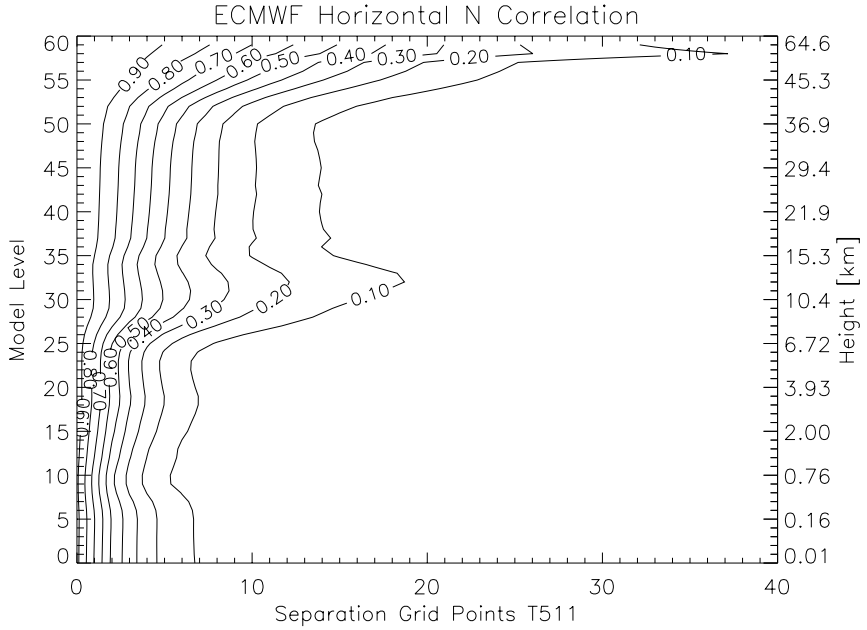

Figure 4.11: Derived horizontal correlation of background refractivity errors.

4.8 Control Space Transformations

The principles of 3D-Var are briefly described in Chapter 2. For a model state $\mathbf{x}$ with n degrees of freedom minimization of the cost function requires $O(n^2)$ calculations [*F. Bouttier* (1999)], thus becomes prohibitively expensive for usual ns. One practical solution to this problem is to perform the minimization in a control variable space $\mathbf{v}$ given by

$$\mathbf{x} = \boldsymbol{U}\mathbf{v} \ .$$

The transform U has to be chosen in a way that

$$\mathbf{B} = \boldsymbol{U}\boldsymbol{U}^T \ , \tag{4.45}$$

is approximately satisfied. In the control space $\mathbf{v}$ the number of required minimization calculations is reduced from $O(n^2)$ to $O(n)$. Furthermore by using the transform Eq. 4.45, the background error covariance matrix becomes $\mathbf{B}_v = \mathbf{I}$, hence effectively preconditioning the problem. $\mathbf{I}$ denotes the identity matrix, $\mathbf{B}_v$ the vertical background covariance matrix. In terms of increments the control variable transform can be written as

$$\mathbf{x}' = \boldsymbol{U}\mathbf{v} \ .$$

The transformation

$$\mathbf{v} = \boldsymbol{U}^{-1}\mathbf{x}'$$

can be specified in different ways. The definition must provide a way to break down the atmospheric state $\mathbf{x}$ into uncorrelated but physically realistic error modes which can be *penalized* in J_b according to their estimated error magnitude.

4.8.1 Vertical Control Variable Transform

The vertical transform serves to project control variables from model levels onto the weighted eigenvectors of the vertical component of the background error covariance matrix

$$\mathbf{B}_v = \overline{\epsilon_v \epsilon_v^T} \ . \tag{4.46}$$

Eq. 4.46 considers the vertical transformation of v at a single horizontal location. For practical reasons approximations must be made like the use of climatological eigenvectors and eigenvalues and the averaging over a geographical domain of these structures. At the moment global means are used, derived from error characteristics provided by ECMWF.

General Formulation of $\boldsymbol{U}_v$

The vertical covariance matrix $\mathbf{B}_v$ is given as $K \times K$ positive-definite symmetric matrix where K is equal the number of vertical levels. These are properties which allow to perform an eigendecomposition

$$\begin{aligned} \mathbf{B}_v &= \boldsymbol{P}^{-1}\mathbf{E}\boldsymbol{\Lambda}\mathbf{E}^T\boldsymbol{P}^{-1} \ , \\ &= \boldsymbol{P}\widehat{\mathbf{B}}_v\boldsymbol{P}^{-1} \ . \end{aligned} \tag{4.47}$$

The inner product $\boldsymbol{P}$ defines a weighted error $\widehat{\epsilon_v} = \boldsymbol{P}\epsilon_v$ which may be used to allow for variable model level thickness or introduce synoptic dependencies. In the current version this option is not used. The columns of the matrix $\mathbf{E}$ are the K eigenvectors $\mathbf{e}(m)$ of $\widehat{\mathbf{B}}_v$ which obey the orthogonality relationship

$$\mathbf{E}\mathbf{E}^T = \mathbf{I} \ .$$

The diagonal matrix $\boldsymbol{\Lambda}$ contains the K eigenvalues $\lambda(m)$. With this standard theory it is possible to define a transform $\boldsymbol{U}_v$ between variables $v(k)$ on model levels k and their projection $v(m)$ onto vertical modes m defined by

$$\mathbf{B}_v = \boldsymbol{U}_v\boldsymbol{U}_v^T \ . \tag{4.48}$$

If one compares Eq. 4.47 and Eq. 4.48 it is possible to derive

$$\begin{aligned} \mathbf{v} &= \boldsymbol{U}_v \mathbf{v}_v \\ &= \boldsymbol{P}^{-1} \mathbf{E} \boldsymbol{\Lambda}^{\frac{1}{2}} \mathbf{v}_v \ . \end{aligned} \tag{4.49}$$

If Eq. 4.49 is inserted into the control variable space form of the background error cost function

$$J_b = \frac{1}{2} \mathbf{v}_v^T \mathbf{B}_v^{-1} \mathbf{v} \ ,$$

which gives

$$\begin{aligned} J_b &= \frac{1}{2} \mathbf{v}_v^T \mathbf{v}_v \\ &= \frac{1}{2} \sum_m \mathbf{v}_v(m)^2 \ , \end{aligned} \tag{4.50}$$

and for the gradient

$$\bigtriangledown_v J_b = \mathbf{v}_v. \tag{4.51}$$

As can be seen easily there are several effects of the $\boldsymbol{U}_v$ transform.

- The projection onto uncorrelated eigenvectors of $\mathbf{B}_v$ leads to very significant CPU savings as can be seen via Eq. 4.50 in the calculation of the background cost function and in its adjoint (gradient) calculations.
- The scaling by the square root of the eigenvalues $\lambda^{\frac{1}{2}}(m)$ serves as a preconditioner.
- The eigenvectors are ordered by the size of their respective eigenvalues what means $\lambda(1)$ is the dominant structure and $\lambda(k)$ essentially contains low amplitude noise. This ordering can be used to filter vertical grid scale noise which reduces CPU still further by neglecting small-scale eigenvalue structures, which contribute little to the total error.

Approximated Eigenstructures

Assuming a single column model, with knowledge of the background covariance matrix and hence the eigenvectors and eigenvalues the $\boldsymbol{U}_v$ transform Eq. 4.49 is an efficient means of reducing CPU without any loss of information. In reality the background covariance matrix is not exactly known, so approximations have to be made. Furthermore our application is 3D-Var were averaging is necessary compared to the 1D-Var case. At the moment global mean error structures are used, resulting from the global mean error structures provided by ECMWF. Absolute temperature standard deviations are converted to relative values by the use of a global mean temperature profile calculated from the background. The specific humidity is transformed to *LOG* space before any other transformation, what means that the minimization takes place in a transformed *LOG* space (the same applies for the refractivity only scheme). The fractional errors applied in the calculation of the covariance matrix are the global means provided by ECMWF.

4.8.2 Horizontal Control Variable Transform

A recursive filter (RF) is used to represent the horizontal component of the background error covariance matrix. The implementation is based on the description of RFs in [*Lorenc* (1992)].

4.8.3 Recursive Filters

RF Basic Algorithm

The basic algorithm for a recursive filter is quite simple. The RF is presented with an initial function A_j at gridpoints j where $1 \leq j \leq J$. A single pass of the of the RF consists of an initial smoothing from *left* to *right*

$$B_j = \alpha B_{j-1} + (1-\alpha)A_j \text{ for } j = 1...J \ , \tag{4.52}$$

followed by another pass from *right* to *left*

$$C_j = \alpha C_{j+1} + (1-\alpha)B_j \text{ for } j = J...1 \ . \tag{4.53}$$

The application of the RF in each direction is performed to ensure zero phase change. So a 1-pass filter is defined as a single application of Eq. 4.52 and Eq. 4.53. A N-pass RF is defined by N sequential applications.

RF Boundary Conditions

Eq. 4.52 and Eq. 4.53 are used to compute recursively the RF response at all points $j = 2 : J-1$ interior to the boundary. Explicit boundary conditions are required to specify the response at points $j = 1$ and J. If there is a limited area and thus a *real* boundary a method of Hayden & Purser [*Hayden and Lorenc* (1995)] can be used to specify boundary conditions which assume a given decay-tail outside the domain. This technique assures that the response to observations near the boundary is equivalent to the response within the center of the domain. The boundary conditions for B_1 and C_{J+1} depend on the particular number of passes p of the filter in *opposite directions*. Assuming no previous pass of the left moving filter ($p = 0$) we have

$$B_1 = (1-\alpha)A_1 \ . \tag{4.54}$$

Following one pass of the filter in the opposite direction the $p = 1$ boundary condition is

$$(C_J, B_1) = \frac{1-\alpha}{(1-\alpha^2)^2}\left[(B_J, A_1) - \alpha^3(B_{J-1}, A_2)\right] \ . \tag{4.55}$$

Hayden & Purser [*Hayden and Lorenc* (1995)] suggest to use the $p = 2$ boundary condition also for $p > 2$. In our application there is no *real* boundary but the boundary conditions for B_1 and C_{J+1} still have to be defined

$$B_1 = \alpha A_J + (1-\alpha)A_1 \ , \tag{4.56}$$

and

$$C_J = \alpha B_1 + (1-\alpha)B_J \ . \tag{4.57}$$

Matching of RF Output and Analytical Functions

The smoothing operations performed by the RF algorithm are related to certain analytical functions. In particular, for $N = 2$, the RF output approximates a second order autoregressive (SOAR) function

$$\mu_s(r) = \left(1 + \frac{r}{s}\right) e^{-\frac{r}{s}} \ . \tag{4.58}$$

In the limit $N \to \infty$ it can be shown that the RF output tends to a Gaussian function

$$\mu_g(r) = \exp\left[-\frac{1}{2}\left(\frac{r}{2s}\right)^2\right] \tag{4.59}$$

where r is distance and s is a characteristic length scale. The α is calculated as

$$\frac{\alpha}{(1-\alpha)^2} = \frac{1}{2E} \ , \tag{4.60}$$

where

$$E = \frac{N(\triangle x)^2}{4s^2} \ . \tag{4.61}$$

The definition of E is in this particular case the same for the SOAR and the Gaussian function. This arises from the particular scaling of the Gaussian function given by equation 4.59. $\triangle x$ denotes the grid spacing, N and s are also known parameters, thus E can be calculated from Eq. 4.61. α can be calculated as follows

$$\alpha = 1 + E - \sqrt{E(E+2)} \ . \tag{4.62}$$

This approach is matching the large-scale response of the RF that of a SOAR for $N = 2$ and approaches that of a Gaussian for increasing N. The matching of the large scale response to analytical SOAR and Gaussian functions serves the definition of α via Eq. 4.62. It is also required that the RF conserves the background error variance, for the zero distance case. The calculation of this scaling factor S is realized as the inverse of the zero distance response of a 1D N - pass RF to a delta function. A two dimensional N - pass RF is realized by performing N applications of multiple 1D RF's in one direction followed by the multiple application of 1D RF's in the orthogonal direction. α and E are calculated in the same way as in the 1 dimensional case, however the RF output has to be scaled by S^2 instead of S which is defined as in the one dimensional case.

Transform To Non Dimensional Space

Due to the fact that $\triangle x$ is not uniform over the grid domain, the two dimensional field must be transformed to a non dimensional space prior to the filter procedure. This transform is realized as an inner product which is defined as

$$\frac{\text{Increment in Control Space}}{\sqrt{\text{Grid Box Area}}} \ . \tag{4.63}$$

The grid box area is calculated by subtraction of fractions of ellipsoid areas between the equator and the pole and subsequent division by the number of longitudes. The ellipsoid (WGS84) areas are calculated by

$$\begin{aligned}\text{Ellipsoid Area} = 2\pi\,(r_{\text{Equator}} + z)^2 \cdot (&0.996647190 \cdot \sin(\text{Lat}) - 0.001116660 \\ &\sin(3.0 \cdot \text{Lat}) + 1.68880838^{-6} \cdot \sin(5.0 \cdot \text{Lat}) - 2.70005436^{-9} \\ &\sin(7.0 \cdot \text{Lat}) + 4.41731436^{-12} \cdot \sin(9.0 \cdot \text{Lat}))\ ,\end{aligned} \tag{4.64}$$

where z denotes the height over the reverence ellipsoid [*Lauf* (1983)].

RF Representation of Background Error Covariances

The control variable transform uses the identity

$$\mathbf{B} = \boldsymbol{U}\boldsymbol{U}^T\ , \tag{4.65}$$

to define a transform $\mathbf{x}' = \boldsymbol{U}\mathbf{v}$ which relates preconditioned control variables $\mathbf{v}$ to analysis increments in $\mathbf{x}'$ in model space. The horizontal component $\boldsymbol{U}_h$ defined by

$$\mathbf{B}_h = \boldsymbol{U}_h \boldsymbol{U}_h^T\ , \tag{4.66}$$

is realized by scaled recursive filters. The RF has to be applied in a non dimensional space

$$\widehat{\mathbf{v}} = P_x^{\frac{1}{2}}\mathbf{v}\ ,$$

where the scaling factor P_x contains the grid box area as described above. The relation between model and non dimensional space background error covariance matrix $\widehat{\mathbf{B}}$ is given as

$$\mathbf{B} = P_x^{-\frac{1}{2}}\widehat{\mathbf{B}}P_x^{-\frac{1}{2}}\ . \tag{4.67}$$

The comparison between Eq. 4.65 and Eq. 4.67 indicates that the horizontal component of the control variable transform $\boldsymbol{U}_h$ relating model space control variables $\mathbf{v}$ to model space analysis variables $\mathbf{x}$ via $\mathbf{x} = \boldsymbol{U}_h\mathbf{v}$ can be represented by using a recursive filter $\widehat{R}$ in non dimensional space as

$$\mathbf{x}' = \sigma_b P_x^{-\frac{1}{2}}\widehat{R}P_x^{-\frac{1}{2}}\mathbf{v}\ . \tag{4.68}$$

When the two dimensional recursive filter $\widehat{R}$ is applied only $\frac{N}{2}$ passes are performed, as indicated in Eq. 4.66 the other $\frac{N}{2}$ passes are performed by the adjoint transform [*Barker* (1999)].

4.9 Horizontal Background Error Covariances

As recursive filters approximate analytical functions it naturally occurs to be difficult to match them with statistically derived correlation function. Nevertheless it is possible to archive a quite good agreement with the ECMWF provided horizontal correlations.

4.9.1 Horizontal Refractivity Error Correlation

In the case of refractivity the horizontal correlation is derived as shown in Eq. 4.44. The representation as a function of the type Eq. 4.59 is reasonable accurate as you can see comparing the Fig. 4.11 and Fig. 4.12. To achieve this match of correlation functions some experiments to find the optimal characteristic length scale for each model level are necessary. At this point it is possible to calculate the optimal filter coefficients. As shown in Fig. 4.11 and Fig. 4.12, the filter reproduces the analytical correlation function well, the slightly expanded horizontal correlation is intentional.

4.9.2 Horizontal Temperature Error Correlation

The horizontal temperature correlation (cf. Fig. 4.13) realized as an analytical function of the type Eq. 4.59 reproduces the ECMWF provided correlation (Fig. 4.4) with sufficient accuracy, the slightly expanded correlation is as in the case of refractivity intentional. The filter (cf. Fig. 4.13) approximates the correlation function well.

4.9.3 Horizontal Specific Humidity Error Correlation

The horizontal specific humidity correlation (cf. Fig. 4.14) realized as an analytical function of the type Eq. 4.59 reproduces the ECMWF provided correlation (cf. Fig. 4.6) accurate enough, but is smother over the vertical dimension. The broader correlation is intentional and is slightly expanded in the filter realization of the correlation function (cf. Fig. 4.14).

4.9.4 Horizontal Surface Pressure Error Correlation

Due to the steep descent of the original ECMWF provided surface pressure correlation (cf. Fig. 4.7) and the short correlation length, it is impossible to realize a similar smooth correlation function, due to the limited number of grid points, either with an analytical function of the type 4.59 (cf. Fig. 4.15) nor with the filter approximation (cf. Fig. 4.15). Concerning the limited influence of the highly accurate surface pressure fields this realization of the correlation function is precise enough.

Horizontal Refractivity Error Correlation Realized as Function and Filter

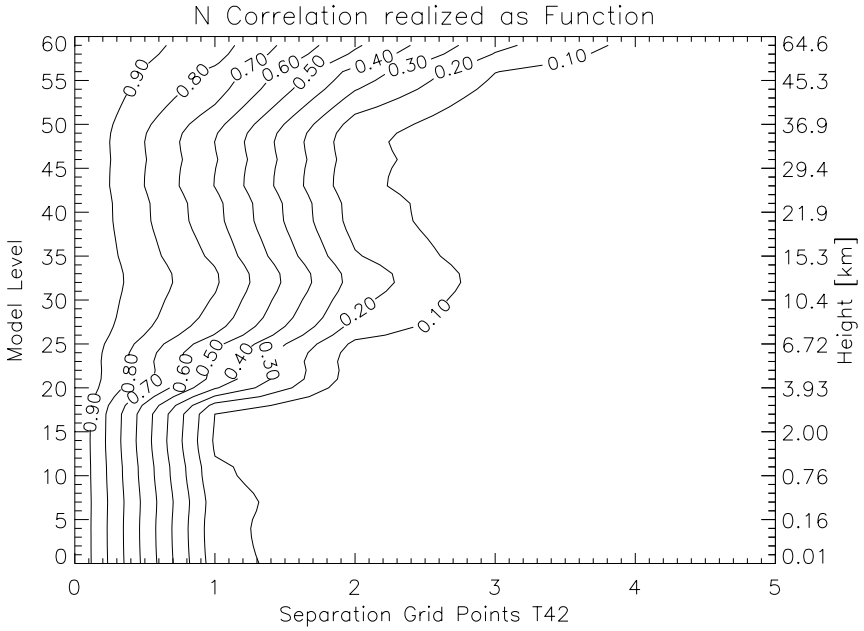

Derived horizontal correlation of background refractivity errors realized as function.

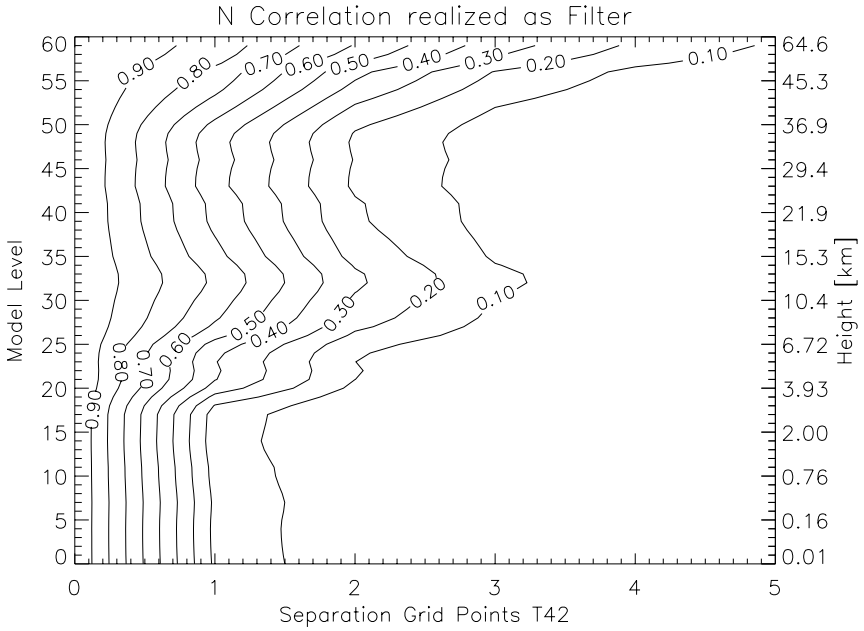

Derived horizontal correlation of background refractivity errors realized as filter.

Figure 4.12: Horizontal correlations of refractivity errors realized as function and filter.

Horizontal Temperature Error Correlation Realized as Function and Filter

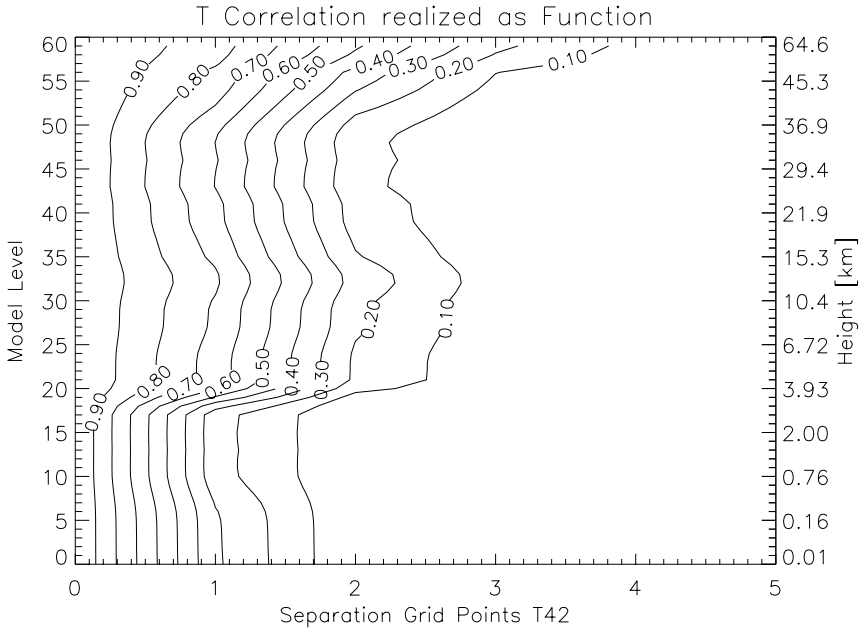

Horizontal correlation of background temperature errors realized as function.

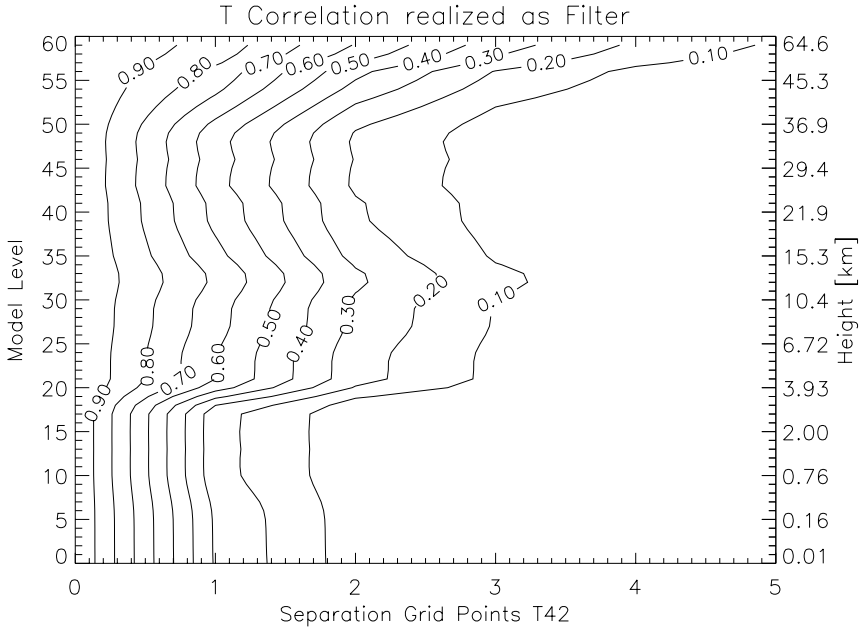

Horizontal correlation of background temperature errors realized as filter.

Figure 4.13: Horizontal correlations of temperature errors realized as function and filter.

Horizontal Specific Humidity Error Correlation Realized as Function and Filter

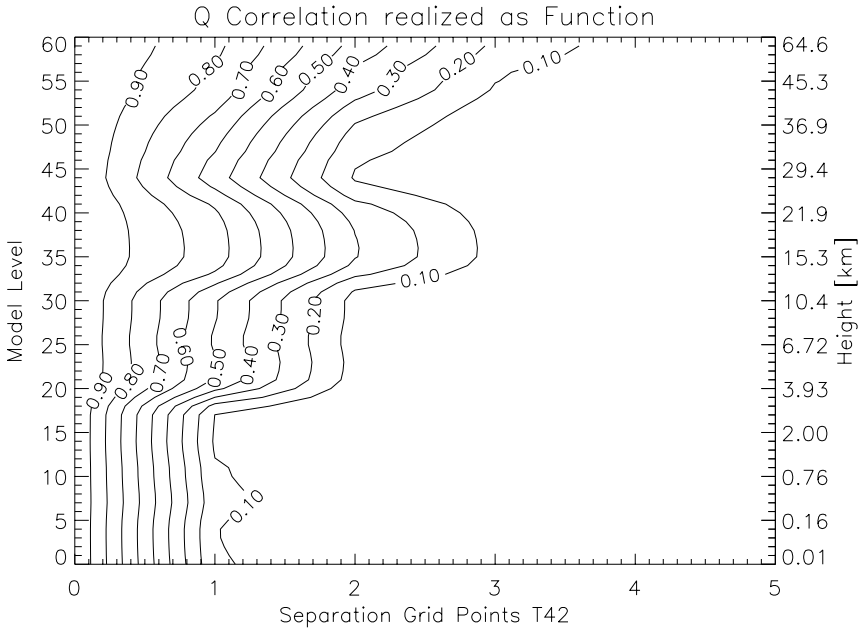

Horizontal correlation of background specific humidity errors realized as function.

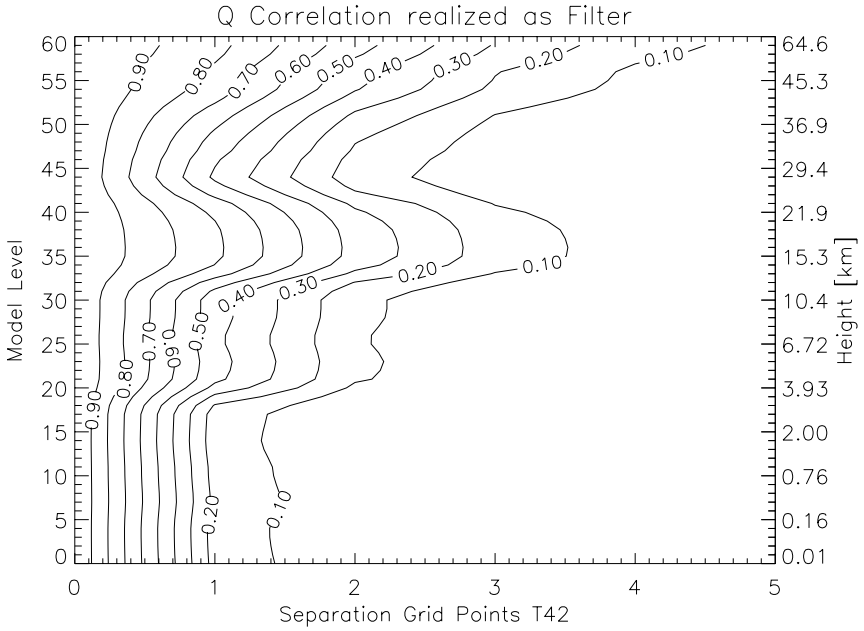

Horizontal correlation of background specific humidity errors realized as filter.

Figure 4.14: Horizontal correlations of specific humidity errors realized as function and filter.

Horizontal Surface Pressure Error Correlation Realized as Function and Filter

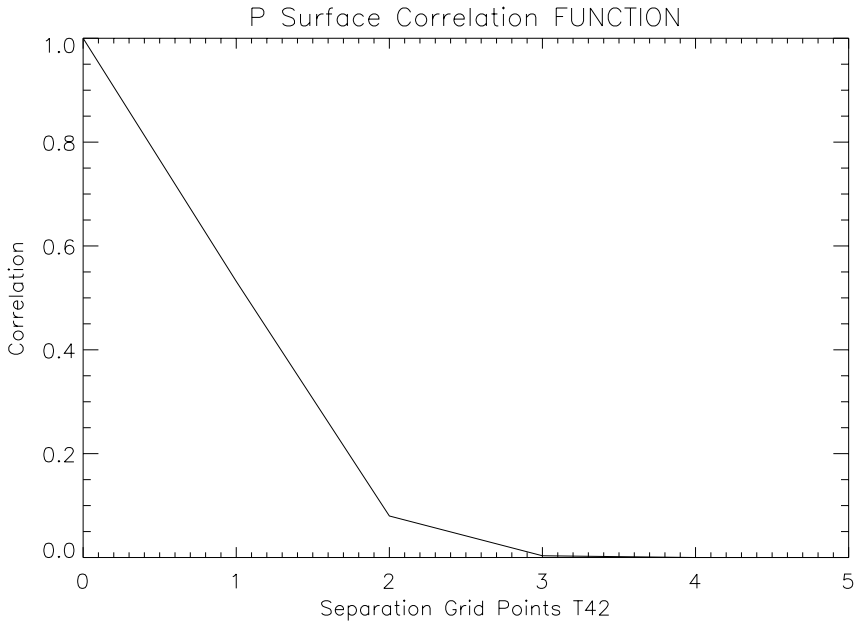

Horizontal correlation of background surface pressure errors realized as function.

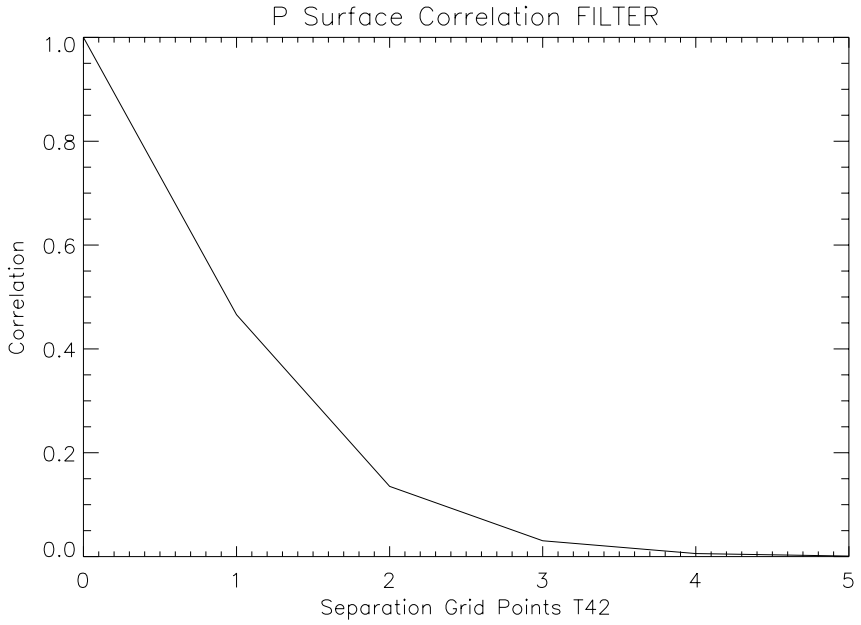

Horizontal correlation of background surface pressure errors realized as filter.

Figure 4.15: Horizontal correlations of surface pressure errors realized as function and filter.

4.10 The Minimization Algorithm

The L-BFGS-B algorithm is a limited memory algorithm (L) for solving large nonlinear optimization problems subject to simple bounds on the variables. It is based on the Broyden-Fletcher-Goldfarb-Shanno Method (BFGS), which is from the class of Quasi-Newton methods, the most common. BFGS uses the following basic update for A_i

$$A_{i+1} = A_i + \frac{s_i s_i^T}{s_i^T v_i} + \frac{A_i v_i v_i^T}{v_i^T A_i v_i} + \left(v_i^T A_i v_i\right) \cdot u_i u_i^T \ , \tag{4.69}$$

with

$$u_i = \frac{s_i}{s_i^T} - \frac{A_i v_i}{v_i^T A_i v_i} \ , \tag{4.70}$$

where $s_i = x_{i+1}$ and $v_i = \bigtriangledown f_{i+1} - \bigtriangledown f_i$. For a symmetric positive definite matrix A_i the matrix A_{i+1} is also symmetric positive definite, and thus the Quasi-Newton condition is fulfilled.

This version was chosen to be able to apply simple bounds within the assimilation framework (denoted by the B). This option is currently not used. It is intended for problems in which information on the Hessian matrix is difficult to obtain or for large dense problems. L-BFGS-B can also be used for unconstrained problems, as currently in our application, and in this case performs similarly to its predecessor algorithm L-BFGS (Harwell routine VA15). The algorithm is implemented in Fortran 77 [*Byrd et al.* (1994)], [*Dong and Nocedal* (1989)].

5

Verification by Assimilation of Simulated Data

5.1 Assimilation of Derived Measurement Profiles

5.1.1 Test Bed Setup

Out of the ECMWF analysis background fields profiles are calculated with the observation operators of the assimilation system. This profiles are perturbed by the error patterns method. In total 800 profiles consisting of 38400 single refractivity observations (48 per profile) are used.

Error Patterns

To generate a test setup it is assumed that the vertical covariance matrices of the observations $\mathbf{O}_v$ and the background $\mathbf{B}_v$ are known. The formulation of $\mathbf{B}$ is the same as used in the assimilation scheme and takes here only vertical correlations into account [*Rodgers* (2000)]. The basic principle is shown by way of example $\mathbf{B}_v$. Any covariance matrix $\mathbf{B}_v$ can be decomposed as

$$\mathbf{B}_v = \sum_j e_j e_j^T \ , \tag{5.1}$$

where

$$e_j = \sqrt{\lambda_j}\mathbf{l}_j \ , \tag{5.2}$$

these e_j are denoted as *error patterns* which can be regarded as eigenvectors $\mathbf{l}_j$ scaled by the eigenvalues λ_j of $\mathbf{B}_v$. The random error of the background state vector $\mathbf{x}_B$ can be expressed as

$$\epsilon_x = \sum_j a_j e_j \ , \tag{5.3}$$

where the a_j are normally distributed random deviates with unit variance. To generate a disturbed background field consistent with $\mathbf{B}_v$ we simply have to add ϵ_x to the *true* state vector $\mathbf{x}_B$.

Validation of Error Patterns

A way to verify the implementation of this *error patterns method* itself is the reconstruction of the original covariance matrices by

$$\mathbf{B}_{v_r} = \frac{1}{n} \sum_i \epsilon_{x_i} \epsilon_{x_i}^T \ , \tag{5.4}$$

where n denotes the number of individual vertical profiles and $\mathbf{B}_{v_r}$ the reconstructed vertical covariance matrix. In our case of a T42L60 grid 8192 vertical profiles were used. As can be seen in lower panel Fig. 5.2 the original vertical covariance matrix (upper panel Fig. 5.2) is very accurately reconstructed.

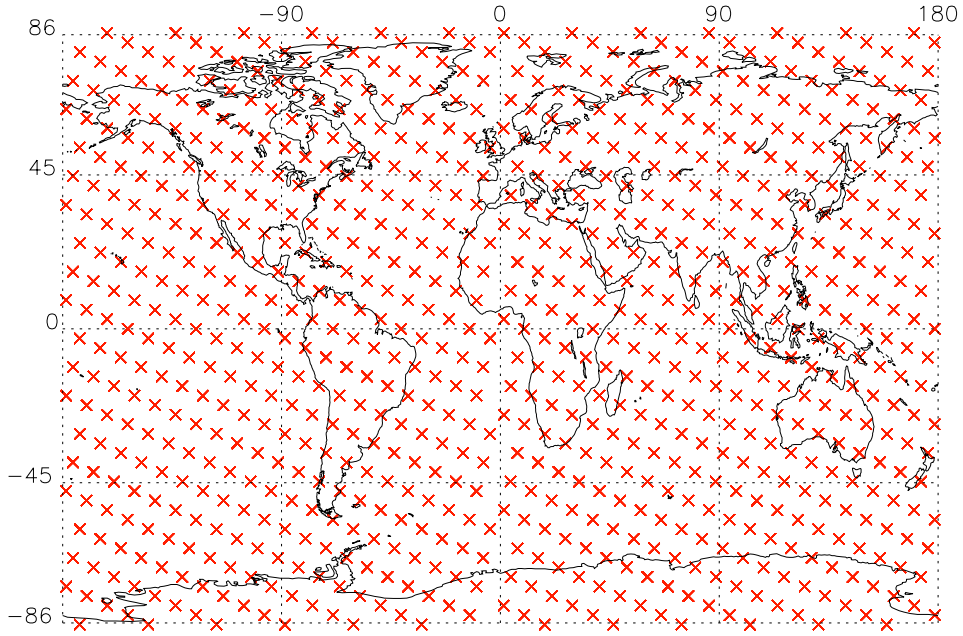

Figure 5.1: Geolocation of 800 synthetic profiles interpolated from the refractivity background.

5.1.2 Validation of the Refractivity Background Assimilation Scheme

To perform assimilation experiments 800 global evenly distributed (see Fig. 5.1) measurements profiles out of 8192 synthetic profiles were used. To derive this test sample the assimilation operators were used, which makes the system intrinsically consistent. As atmospheric input data ECMWF analysis fields were used (12 UTC analysis, 2003.01.03). One has to be aware that bugs in the implementation of the operators can not be found within this kind of test. The emphasis is placed on the vertical covariance matrices, because within the assimilation framework the control space transformations depend on the vertical background covariance matrices. On the other hand it is difficult to apply this method within a recursive filter framework, like the realization of the horizontal background covariance matrices.

Validation Vertical Refractivity Background Error Covariance Matrix

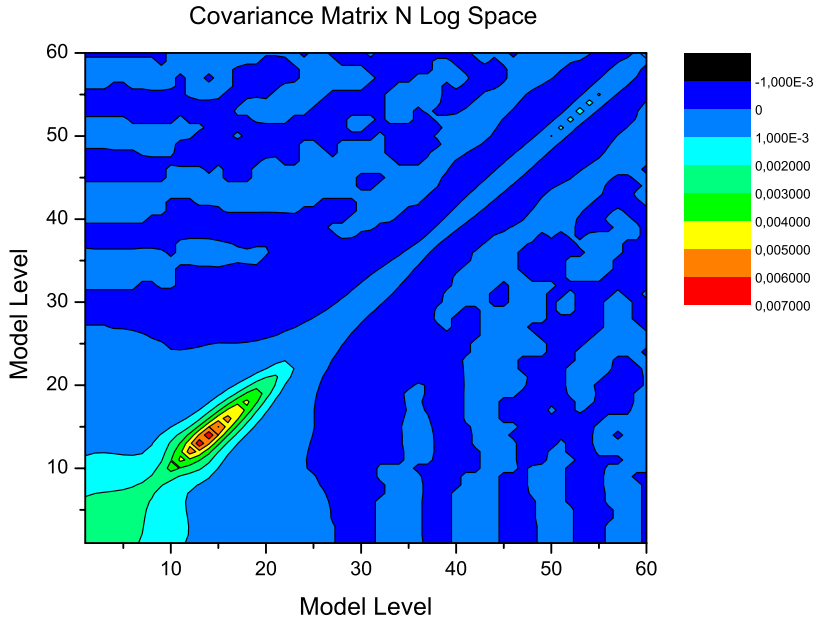

Derived vertical refractivity error covariance matrix in Log space, L60.

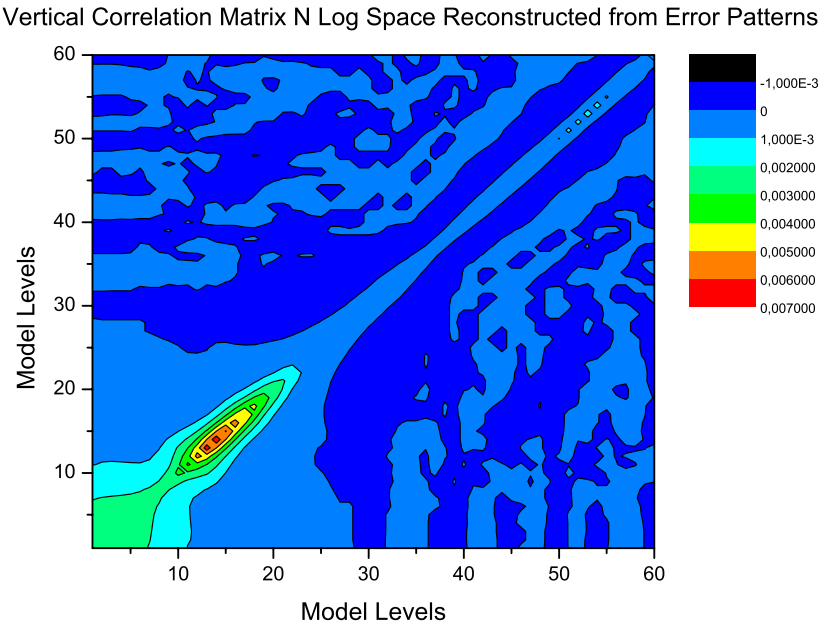

Derived vertical refractivity error covariance matrix in Log space reconstructed from error patterns, L60.

Figure 5.2: Validation of error patterns implementation by reconstructing the vertical refractivity error covariance matrix.

Validation Refractivity Background Standard Deviation and Bias

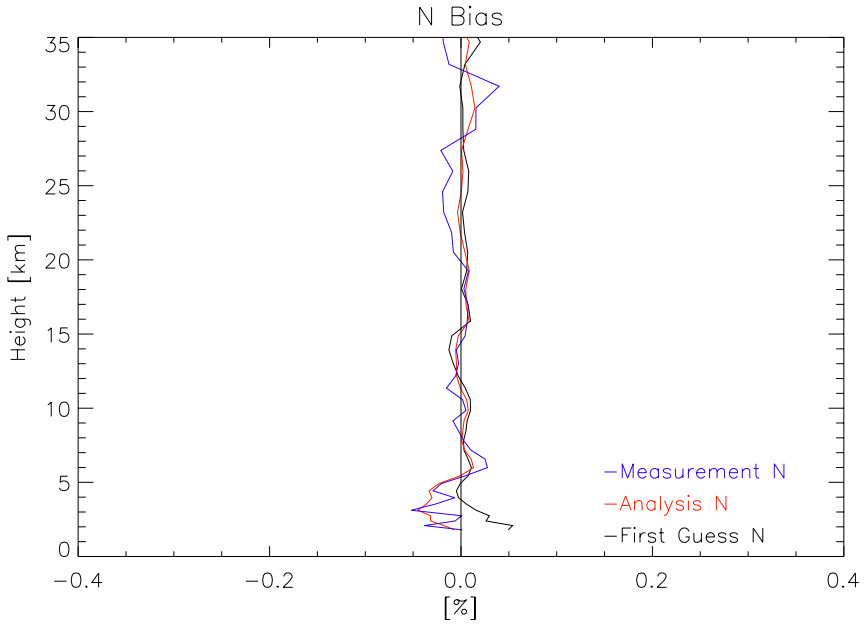

Refractivity bias of disturbed background, measurements and analysis.

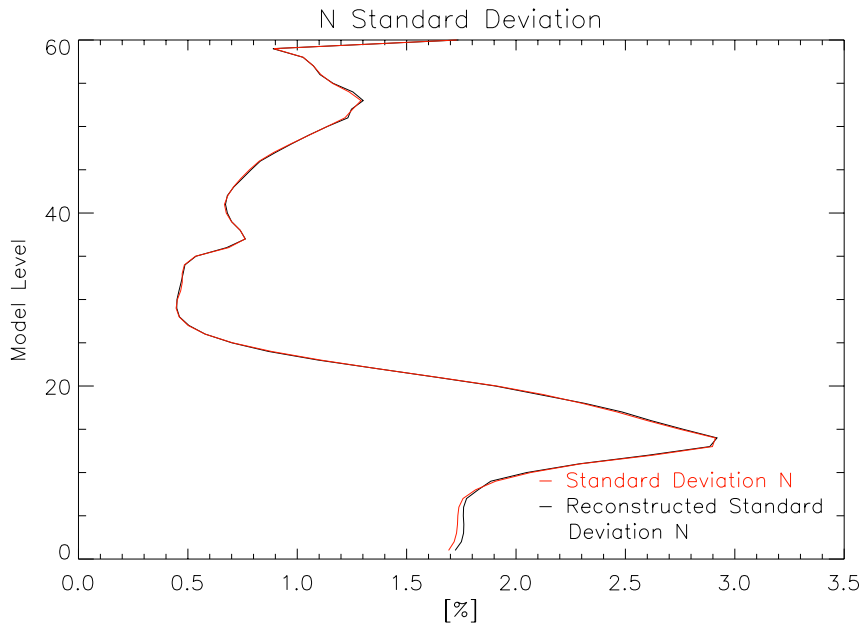

Comparison refractivity standard deviation and refractivity standard deviation reconstructed from error patterns.

Figure 5.3: Validation of error patterns implementation by reconstructing the refractivity standard deviation and calculating the bias.

As can be seen in Fig. 5.2, it is possible to reconstruct the original vertical refractivity covariance matrix using Eq. 5.4. Secondly, the disturbed background (denoted as first guess) is virtually bias free (upper panel Fig. 5.3), and it is possible to reconstruct the refractivity standard deviation accurately. The refractivity standard deviations and the vertical correlation matrix used for this check are equivalent to the error characteristics described at Section 4.7.2.

Validation of Observation Standard Deviation

The same procedure as for the background was applied to the measurement profiles. To reconstruct the vertical covariance matrix 8192 profiles were used. As can be seen in the lower panes Fig. 5.3 the disturbed measurement profiles are bias free. For the relative standard deviation at the tropopause height y a value of 0.2% was chosen (cf. Section 4.6). Like for the background standard deviation, the measurement standard deviation can be reconstructed very accurately (Fig. 5.4). The validation of the vertical error covariance matrix (miscellaneous measurement profiles are assumes to be horizontally uncorrelated) can be seen in Fig. 5.5. The inaccuracy within the reconstruction is due to noise caused by small numbers (exponential drop off), nevertheless the diagonal and main off diagonal elements are reconstructed exactly.

These checks ensure a correct implementation, resulting in a background and measurement profiles, which are disturbed in a way matching the error covariance matrices within the assimilation framework.

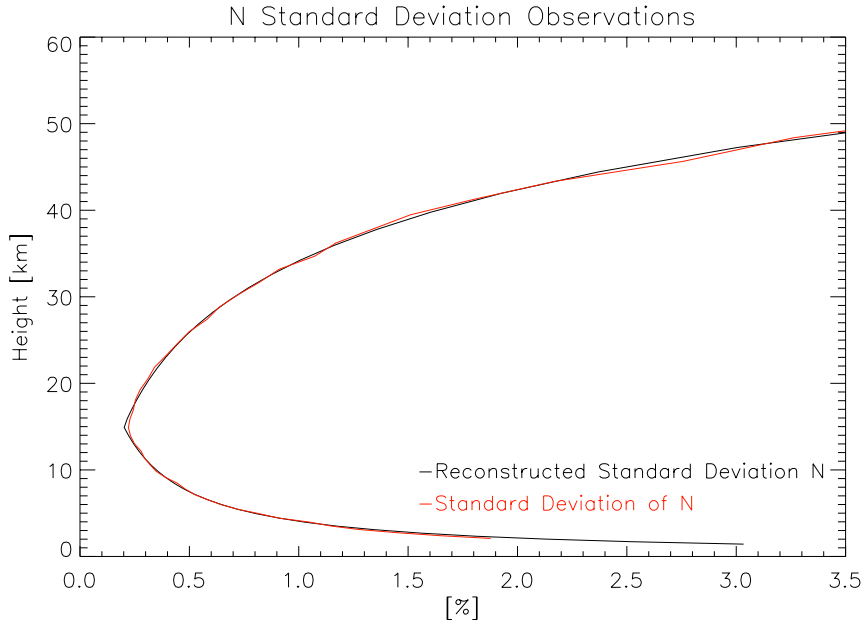

Figure 5.4: Comparison of standard deviation of the observations and of the reconstructed standard deviation.

Validation Vertical Refractivity Observation Error Covariance Matrix

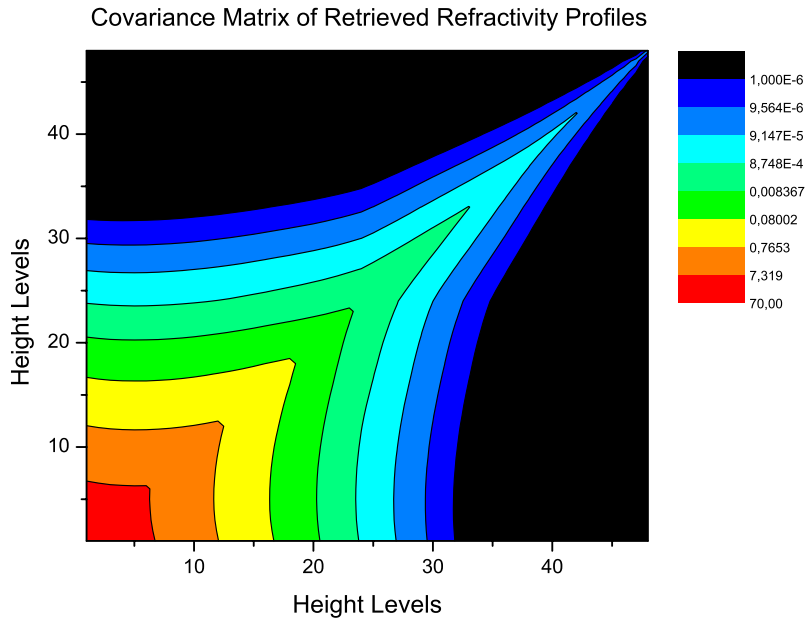

Vertical observation error covariance matrix.

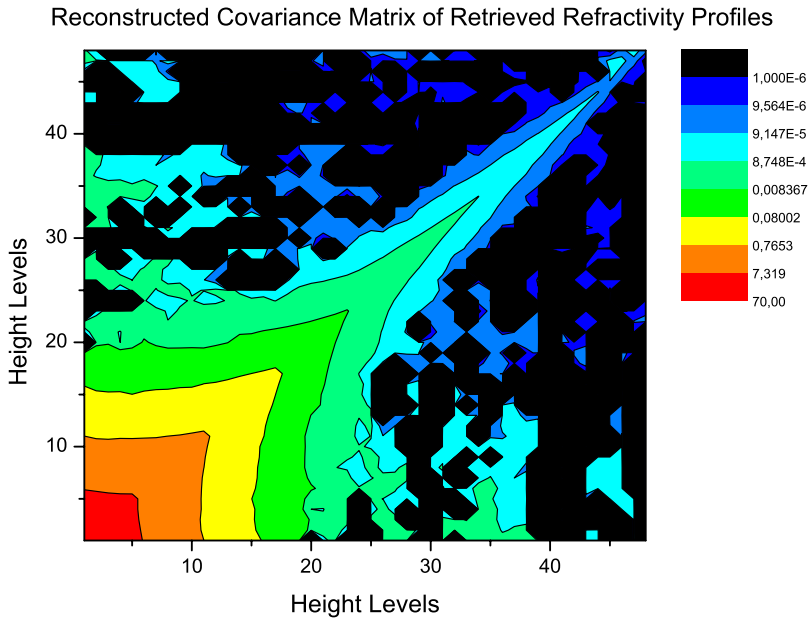

Vertical observation error covariance matrix reconstructed from error patterns.

Figure 5.5: Validation of the error patterns implementation by reconstructing the vertical observation error covariance matrix.

5.1.3 Assimilation Experiments Using a Refractivity Background

The assimilation experiments showed the expected improvement of the first guess. Due to the excellent posed problem (in fact the correct covariance matrices are known) the convergence behavior of the cost function was excellent (cf. Section 5.4.1). The outcome of the assimilation itself is shown in Fig. 5.6. The analysis standard deviation at observation location is systematically better than the standard deviation of the first guess, which is plotted once calculated at the grid point location and once at the observation location (where the standard deviation is significantly smaller due to the averaging nature of the interpolation procedure). Fig. 5.3, upper panel shows that no bias is introduced in the analysis through the assimilation process.

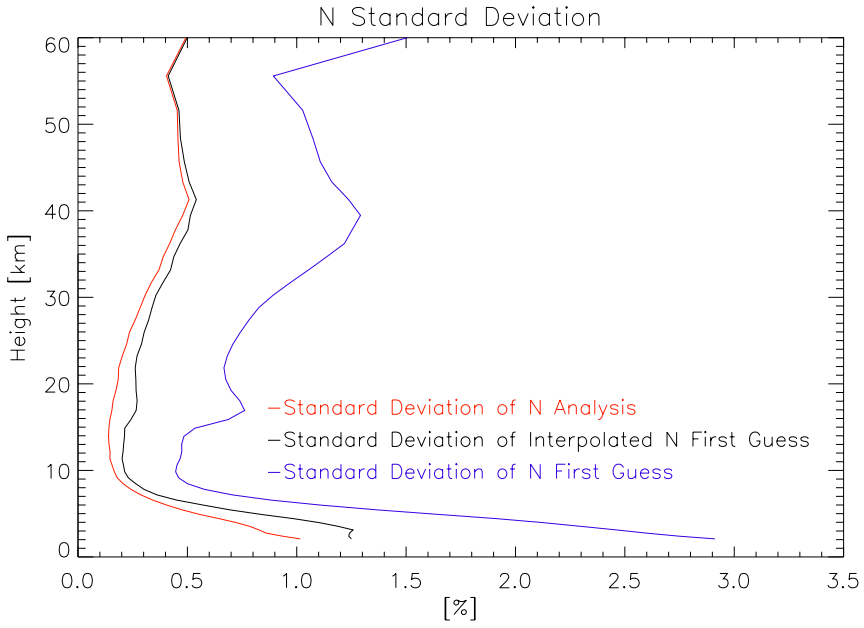

Figure 5.6: Comparison of standard deviation of refractivity first guess, analysis, and first guess interpolated at observation location.

5.1.4 Validation of Temperature, Specific Humidity, and Surface Pressure Background Assimilation Scheme

In principal, the same procedure as in the refractivity only case was applied. Within the error patterns framework a linear approximation concerning the errors is used, which is, in the specific humidity case (relative standard deviations up to $\sim 50\%$, see Fig. 4.5), not longer valid. Tests proofed that the use of the error patters method concerning specific humidity is futile, without restrictions, making the whole procedure unfit for specific humidity. Nevertheless the same tests as for refractivity were applied for temperature. The original correlation matrix is reconstructed closely (Fig. 5.7), and the reconstructed standard deviation is basically the same as the original input. The used error characteristics for the background temperature are described in Section 4.7.

Validation Vertical Temperature and Specific Humidity Background Error Covariance Matrices

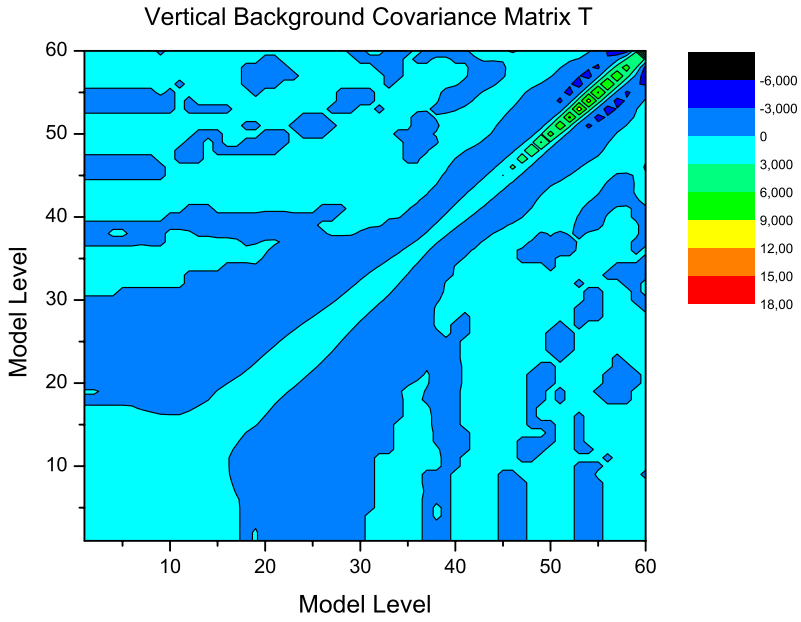

Vertical background temperature error covariance matrix, L60.

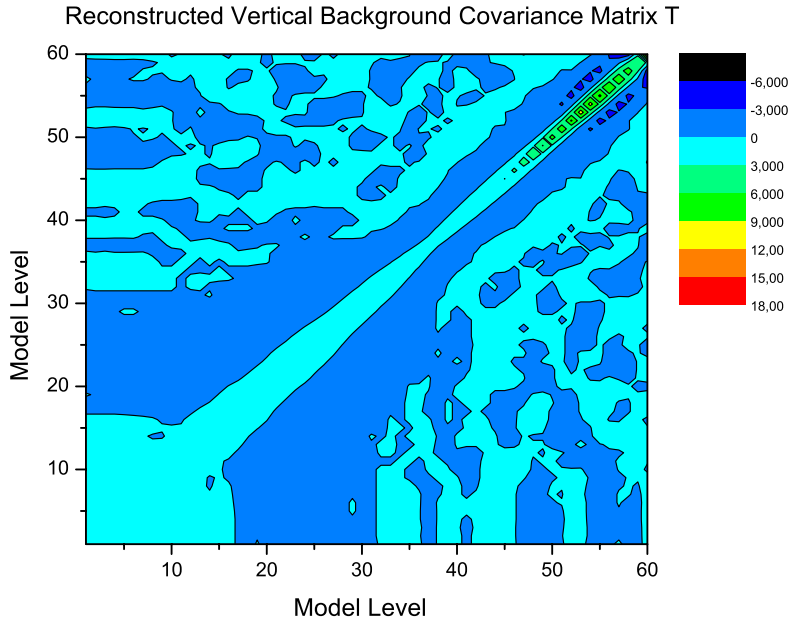

Vertical background temperature error covariance matrix temperature reconstructed from error patterns, L60.

Figure 5.7: Validation of the vertical temperature background error covariance matrix.

Validation Temperature Background Standard Deviation

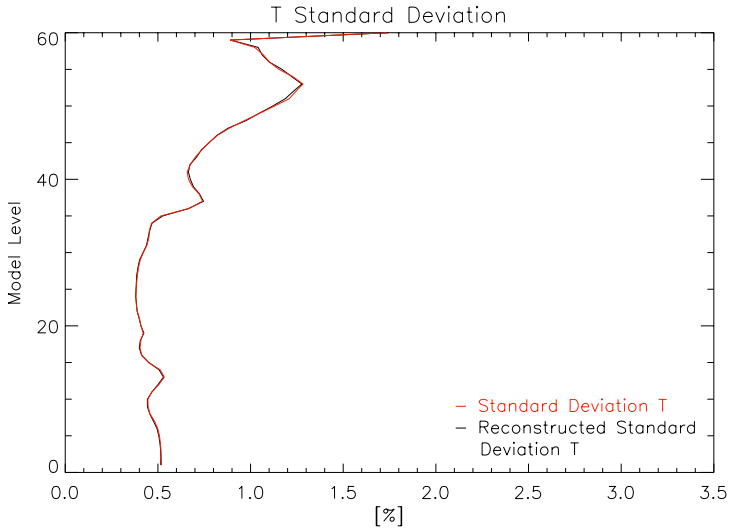

Figure 5.8: Comparison of temperature standard deviation and temperature standard deviation from error patterns reconstructed.

Full assimilation experiments using the error patterns method are not applicable within the temperature, specific humidity and surface pressure 3D-Var framework due to the specific problems concerning the standard deviation of specific humidity (cf. Section 5.3.1).

5.2 Assimilation of Raytraced Measurement Profiles

5.2.1 Test Bed Setup

To generate a realistic test sample of RO measurements, within a controlled environment, the GNSS End To End Simulator EGOPS [*Kirchengsat et al.* (2002)] was used. As timeframe for the simulation the 03.01.2003 was chosen. An original CHAMP TLE from this day was used as input to calculate the CHAMP like LEO satellite orbits, starting from 00:00 UTC the simulation was lasting for 24 hours. To simulate the GNSS satellite constellation appropriate GPS TLE's for this timeframe were used. Assuming a GRASS like receiver on-board the CHAMP like LEO satellite, the 24 hour simulation period translates into 245 occultation events. Out of this 24 hour data set occultations within a $+3/-3$ hour time window around 12:00 UTC were used for the validation runs.

Validation Occultations

In practice some of the simulated events are rejected (e.g. they are too short) during the further processing. After the retrieval procedure 242 occultations were left for the 24 hour period. From these simulated events, 61 were compatible with the assimilation time window. The number of single observations within a profile is about 300 - 400

which exceeds the number of vertical levels (60) of the background by far. During a preprocessing step the number of observations within one profile is reduced. To find the optimal number of measurements between 2.5 and 35 km and to determine the best suited averaging procedure some separate experiments were performed.

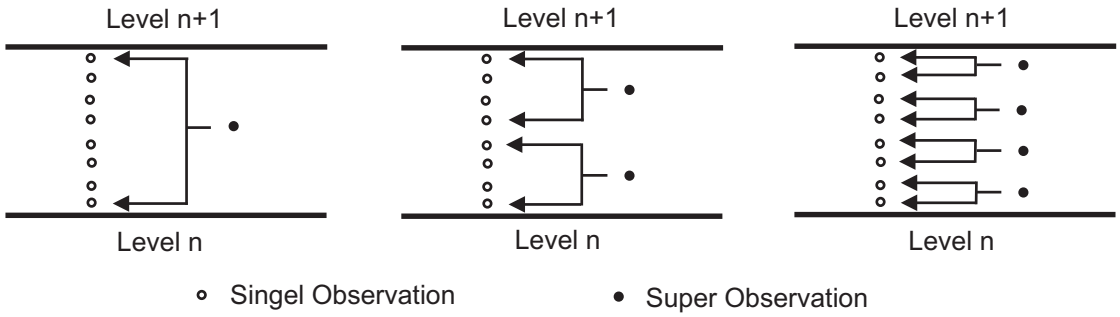

Figure 5.9: Interpolated measurement distributions 1, 2 and 4 measurements.

During the preprocessing the number of measurements is reduced by averaging, taking the background grid into account. To find an optimal setup three distributions of so called *super observations* as shown in Fig. 5.9, were tested, using 61 raytraced profiles corresponding to the $+3/-3$ hour time window around 12:00 UTC. The linear averaging procedure takes the spacing of the background levels into account which is derived from the mean global vertical grid, and is performed in measurement and in *LOG* space.

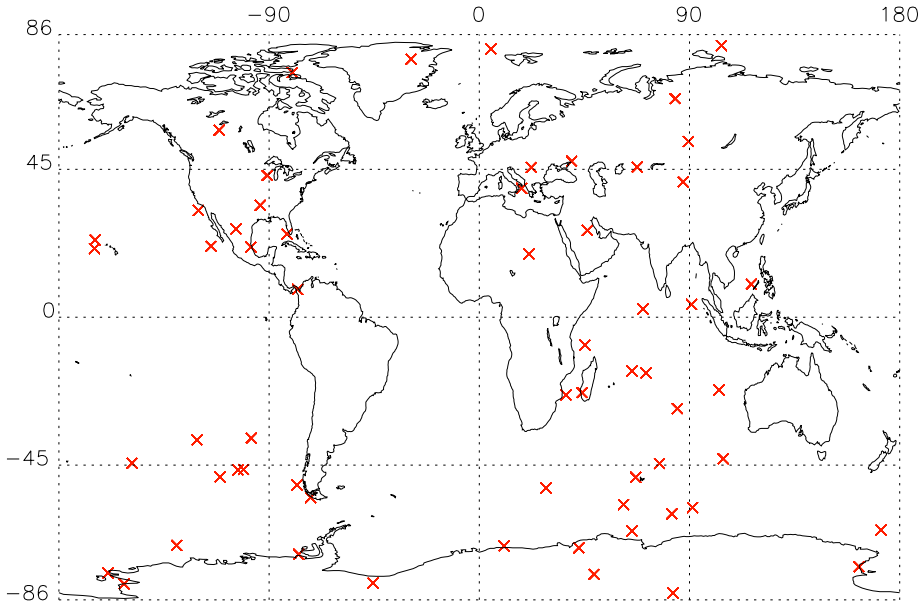

Figure 5.10: Distribution of the 61 raytraced measurement profiles within the 6 hour assimilation window around 12:00 UTC 03.01.2003.

Bias of Measurements, First Guess and Analysis, Measurements Linear Interpolated, Linear Observation Interpolation Operator in LOG Space

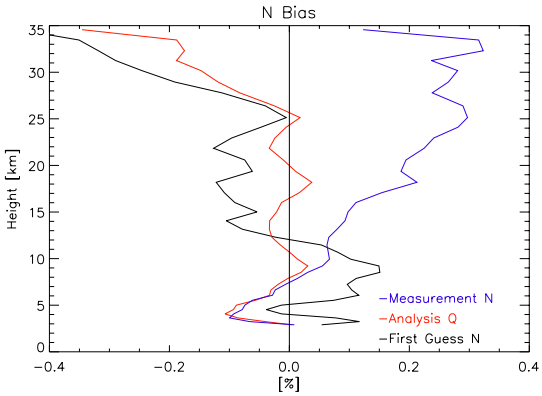

Measurement distribution 1.

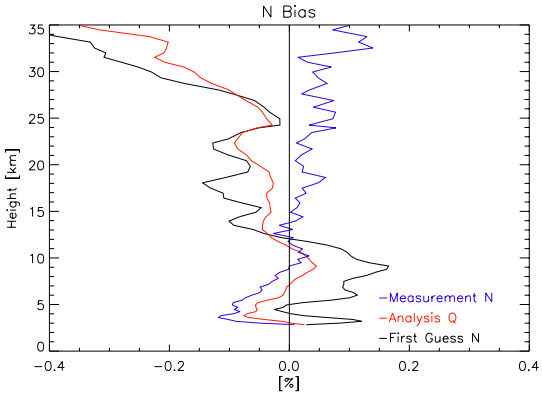

Measurement distribution 2.

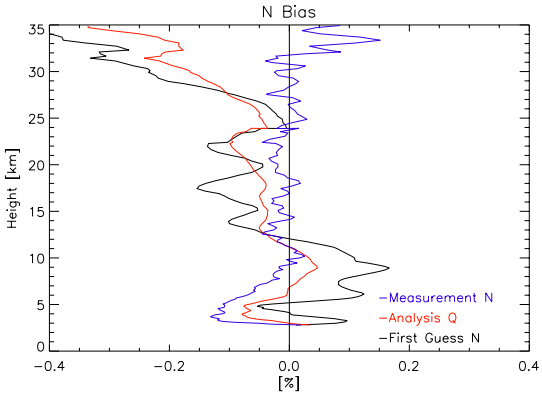

Measurement distribution 4.

Figure 5.11: Bias of measurements, first guess and analysis, linear interpolation operator.

Bias of Measurements, First Guess and Analysis, Measurements Linear Interpolated in LOG Space, Linear Observation Interpolation Operator in LOG Space

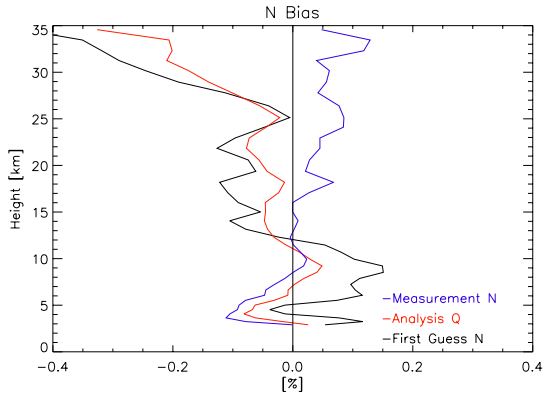

Measurement distribution 1.

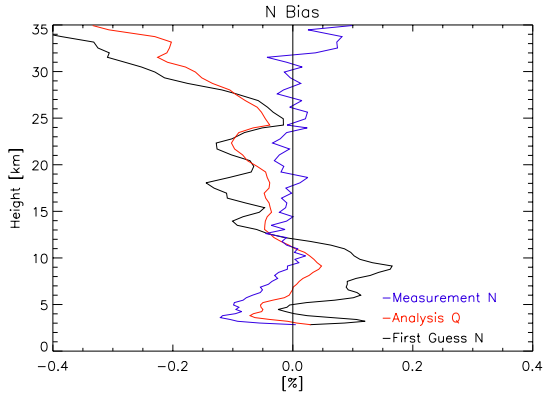

Measurement distribution 2.

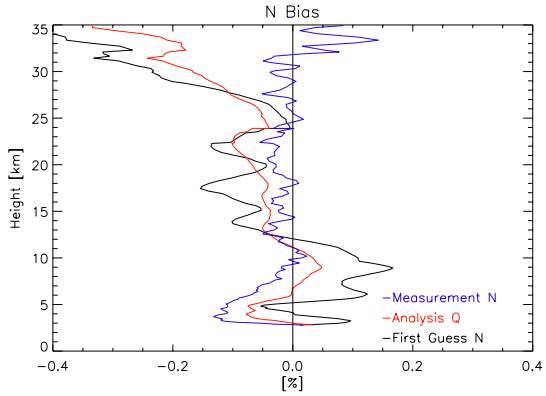

Measurement distribution 4.

Figure 5.12: Bias of measurements, first guess and analysis, linear interpolation operator in LOG space.

Bias of Measurements, First Guess and Analysis, Measurements Linear Interpolated in LOG Space, Cubic Spline Interpolation Operator

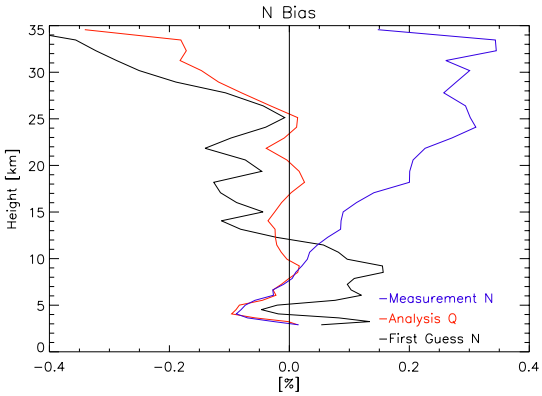

Measurement distribution 1.

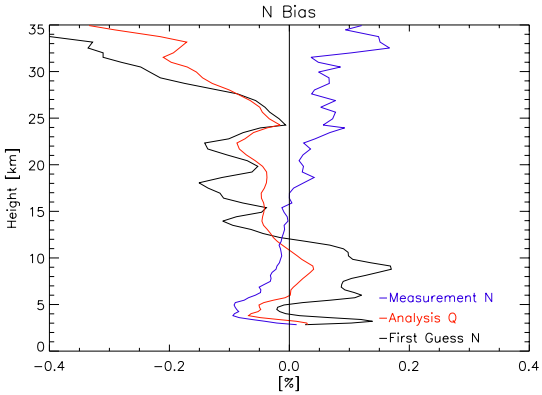

Measurement distribution 2.

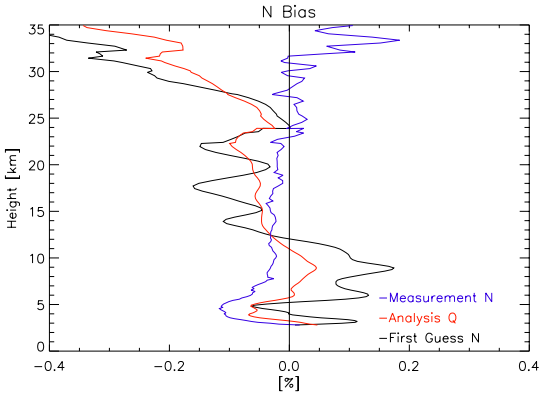

Measurement distribution 4.

Figure 5.13: Bias of measurements, first guess and analysis, measurements linear interpolated, cubic spline interpolation operator.

Bias of Measurements, First Guess and Analysis, Measurements Linear Interpolated in LOG Space, Cubic Spline Observation Interpolation Operator in LOG Space

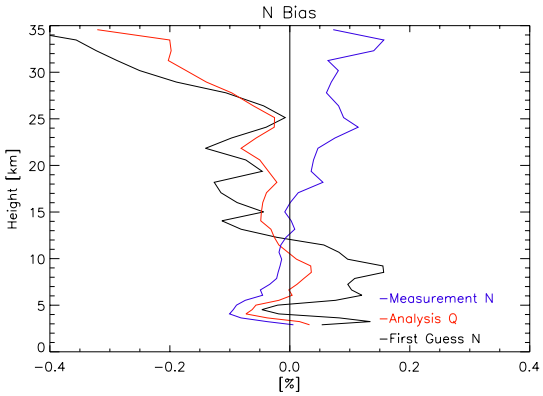

Measurement distribution 1.

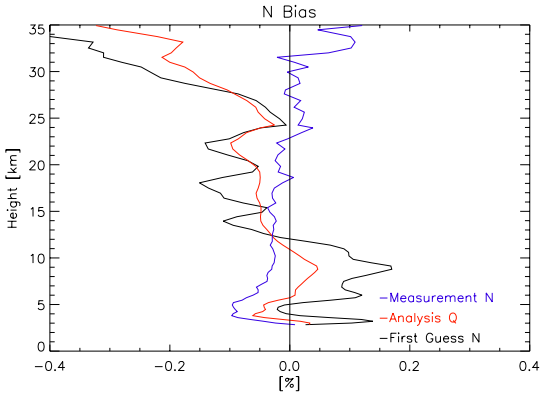

Measurement distribution 2.

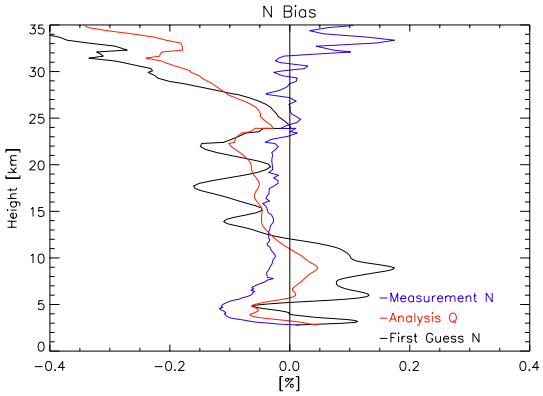

Measurement distribution 4.

Figure 5.14: Bias of measurements, first guess and analysis, measurements linear interpolated in LOG space, cubic spline interpolation operator in LOG space.

Due to accuracy considerations strictly only observations between 2.5 km and 35 km are chosen to enter the assimilation procedure. Fore more details concerning the error characteristics of RO measurements cf. [*Steiner and Kirchengast* (2004)]. As can be seen in Fig. 5.11 linear interpolation is not appropriate, it introduces a significant bias. Fig. 5.12 shows the improvement of applying the averaging procedure in *LOG* space. Furthermore the Fig. 5.13 and 5.14 show that concerning the bias, the linear vertical observation operator and the cubic spline vertical interpolation operators, both in *LOG* space, are equivalent within the assimilation system. The comparisons of different measurement distributions suggest to use two measurements between two vertical background levels linear interpolated in *LOG* space. Nevertheless one observation per vertical interval would be desirable to cut down computing time, but introduces within this observation preprocessing setup an unacceptable bias. This problem could be solved by using more sophisticated interpolation algorithms, taking the non equidistant nature of the vertical grid better into account. Further on measurement distribution 2 was used for the simulated measurements as well as for the real CHAMP data.

Validation Background

As background for the assimilation procedure, the corresponding ECMWF T42L60 12:00 UTC 48 hour forecast was selected. Calculations showed that the 48 hour forecast - corresponding analysis differences agrees not perfect, but acceptable with the error characteristics provided by ECMWF. To validate the results the valid 12:00 UTC ECMWF analysis was compared with the assimilation output. The temperature standard deviation used to calculate the temperature background covariance matrix and to derive the refractivity error characteristics was taken times two to achieve realistic errors, otherwise the error characteristics are conform to the formulations in Chapter 4.

5.2.2 Refractivity Assimilation

The following plots are showing standard deviations of first guess, measurements and resulting analysis of the assimilation experiments. Two different vertical interpolation operators were used (as in the bias calculations before), which are described in detail in Section 4.5.3. Spikes in the measurement standard deviation as in Fig. 5.15 can be attributed to outliers within the raytraced measurements (compare with Fig. 5.16). These outliers were not removed by a quality control on purpose to study their impact within the assimilation procedure. The Fig. 5.15 shows a significant improvement of the standard deviation due to the assimilation procedure. A smoothing effect is also clearly visible if you compare the analysis standard deviation with first guess and measurement standard deviation, furthermore the system is somewhat robust against outliers. Comparing the results of the assimilation procedures using the linear and cubic spline interpolation operators in *LOG* space (cf. Fig. 5.15) are showing no significant advantage of a certain vertical interpolation operator. Comparing the results shown in Fig. 5.16 also shows no special benefit concerning the accuracy of one or the other observation operator. The assimilation procedure itself improves the first guess significant, as can be seen in the Fig. 5.15 and Fig. 5.16.

Standard Deviation for Refractivity Assimilation Experiments Linear and Cubic Spline Vertical Observation Interpolation Operator in LOG Space

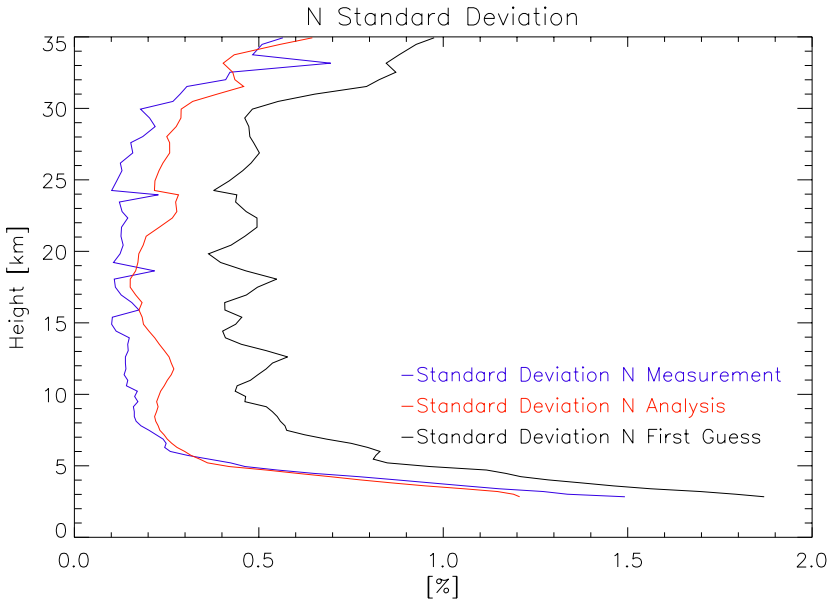

Standard deviations of the analysis using the linear interpolation operator in LOG space.

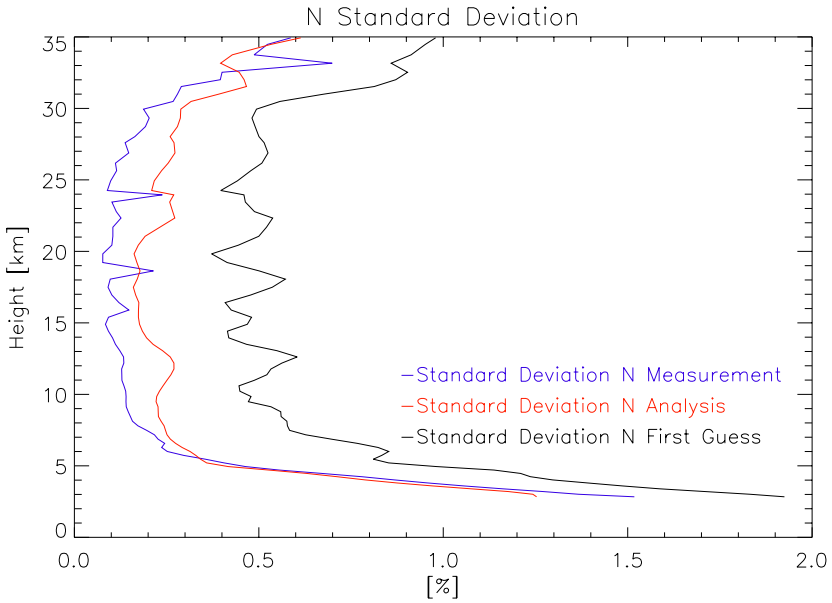

Standard deviations of the analysis using the cubic spline interpolation operator in LOG space.

Figure 5.15: Standard deviation for refractivity assimilation experiments linear vertical and cubic spline interpolation operator in LOG space.

Scatter Plots for Refractivity Assimilation Experiments Linear and Cubic Spline Vertical Observation Interpolation Operator in LOG Space

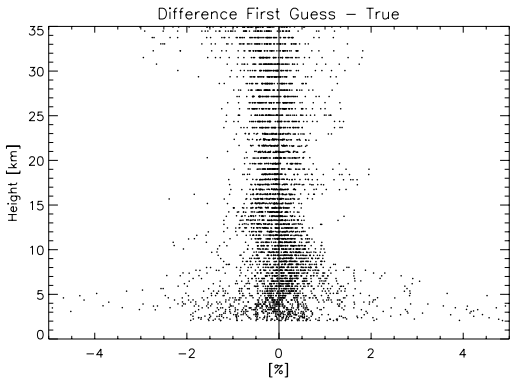

Linear interpolation in LOG space.

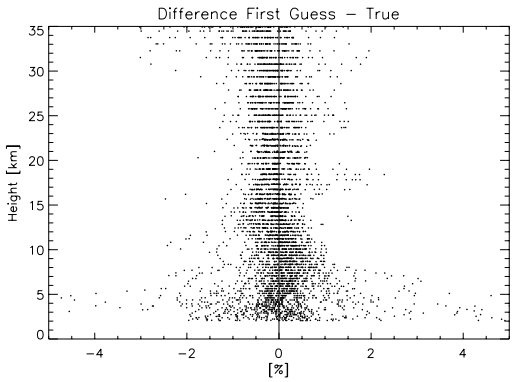

Cubic spline interpolation in LOG space.

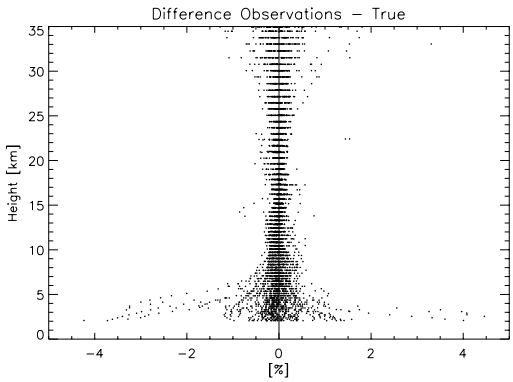

Linear interpolation in LOG space.

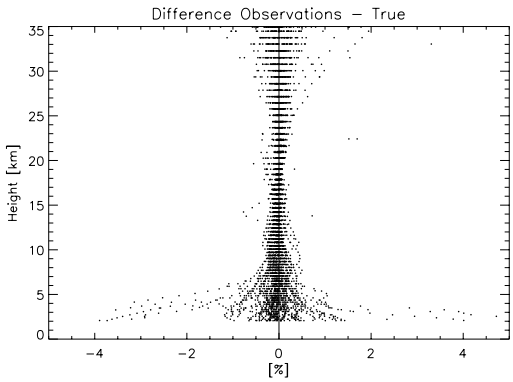

Cubic spline interpolation in LOG space.

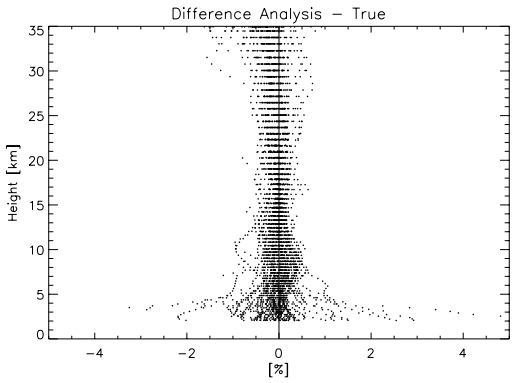

Linear interpolation in LOG space.

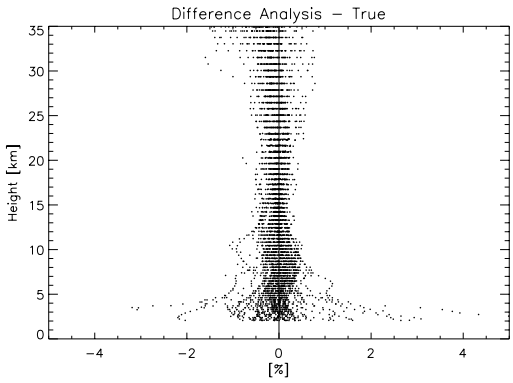

Cubic spline interpolation in LOG space.

Figure 5.16: Comparison assimilation results using linear interpolation operator and cubic spline interpolation operator in LOG space.

5.2.3 Temperature, Specific Humidity, and Surface Pressure Assimilation

Temperature, Specific Humidity, and Surface Pressure Assimilation at Refractivity Level

Comparing Fig. 5.17 with Fig. 5.15 shows the equivalence of both assimilation schemes at refractivity level. That means that at the chosen background resolution the difference introduced by calculating the refractivity at the background grid points and interpolating a refractivity field at the location of the observation, or interpolating background temperature, specific humidity and pressure at the observation location and then calculating the resulting refractivity, doesn't introduce significant deviations. This is true for the present setup, but one has to be aware of its dependents on grid resolution and interpolation strategy.

Basically both experiments (refractivity assimilation and temperature specific humidity and surface pressure assimilation at refractivity level) show very similar results, proving a certain robustness of the implementation, and the interpolation operators. There is also a limited capability to cope with outliers (cf. Fig. 5.17 and Fig. 5.18, for example outlier around $\sim$ 24 km) which is true at refractivity level, and there is no visible advantage of one or the other vertical interpolation scheme. The assimilation results are comparable to the refractivity only assimilation scheme, improving the first guess as can be seen in the Fig. 5.19 and 5.20.

Temperature, Specific Humidity, and Surface Pressure Assimilation

Temperature One of the stand out features of Fig. 5.19 is the sharp spike of the temperature analysis standard deviation around $\sim$ 24 km, which is caused by two observation outliers which are clearly visible in Fig. 5.20. Other than in the refractivity cases, where the effects of these outliers were somewhat damped, the influence on the temperature analysis are substantial. This difference stems from the different background error covariances. Which accentuates the importance of rigorous quality control of the observations, used within the assimilation framework. As in the refractivity case, the first guess is improved significantly by the assimilation procedure, as can be seen in the Fig. 5.17 and 5.18.

Specific Humidity If you take a look at Fig. 5.22 the most striking feature is the tremendous scatter of the specific humidity (X-axis $\pm$100%) which results in a standard deviation up to $\sim$ 85% (cf. Fig. 5.21). The other feature is the sharp decrease of variation around $\sim$ 18 km due to the strong decline of water vapor content above the tropopause, which means that at higher altitude the refractivity is dominated by the temperature. Even though the uncertainties concerning the specific humidity are huge, the assimilation framework deals quite successfully with this matter, it is possible to reduce the peaks of the standard deviation considerable as can be seen in Fig. 5.21. The analysis standard deviation follows closely the principal features of the standard deviation of the first guess, but at lower magnitude up to an altitude of $\sim$ 15 km, where both quantities become nearly equal. The reason is as mentioned before the marginal water vapor content of the atmosphere above the tropopause.

Standard Deviation for TQP Assimilation Experiments at Refractivity Level Linear and Cubic Spline Vertical Observation Interpolation Operator in LOG Space

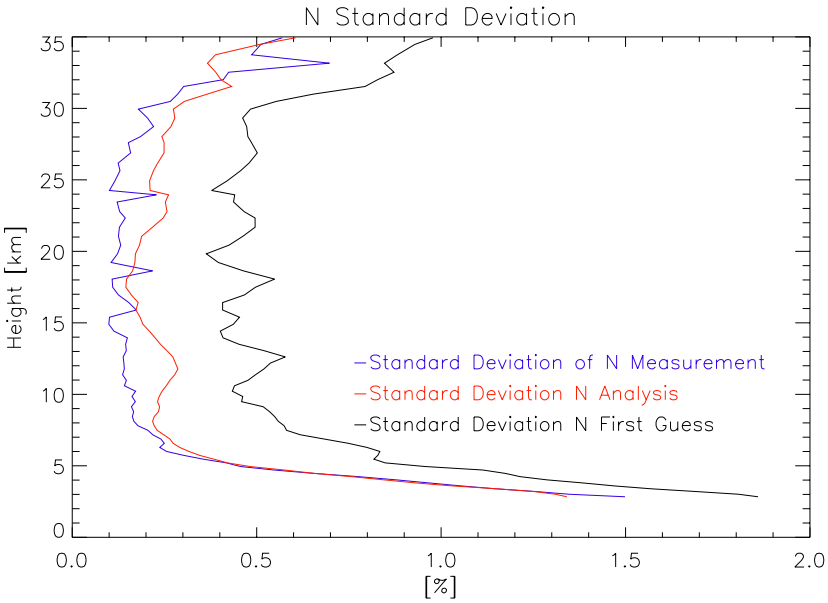

Standard deviations of the analysis using the linear interpolation operator in LOG space.

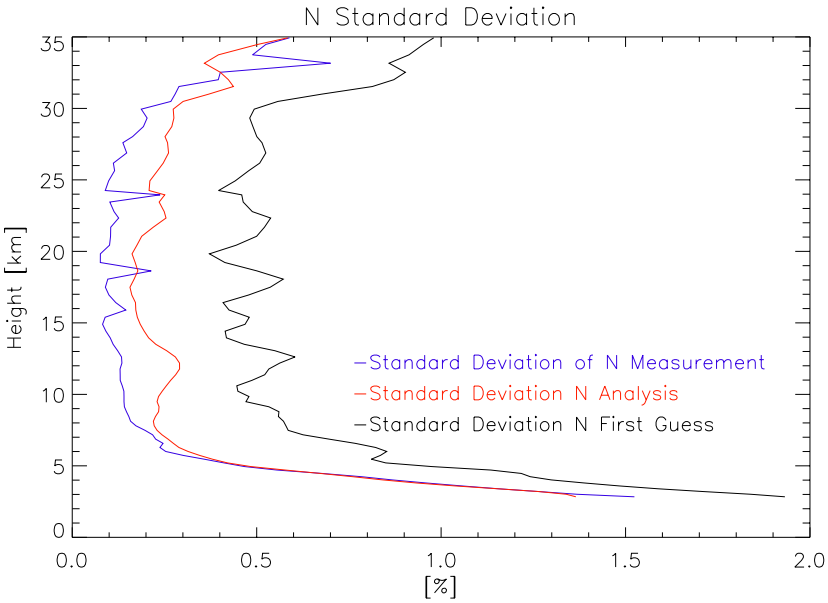

Standard deviations of the analysis using the cubic spline interpolation operator in LOG space.

Figure 5.17: Standard deviation for TQP assimilation experiments linear vertical and cubic spline interpolation operator in LOG space.

Scatter Plots for TQP Assimilation Experiments at Refractivity Level Linear and Cubic Spline Vertical Observation Interpolation Operator in LOG Space

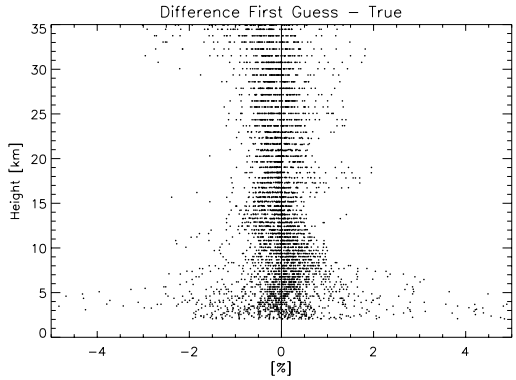

Linear interpolation in LOG space.

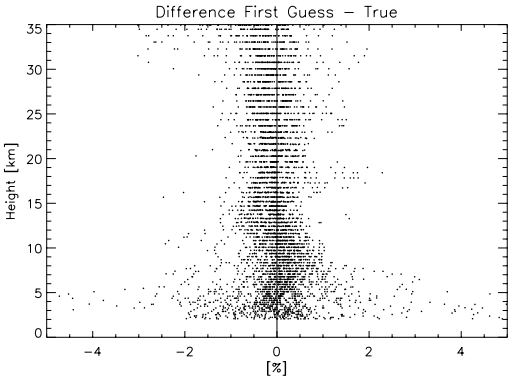

Cubic spline interpolation in LOG space.

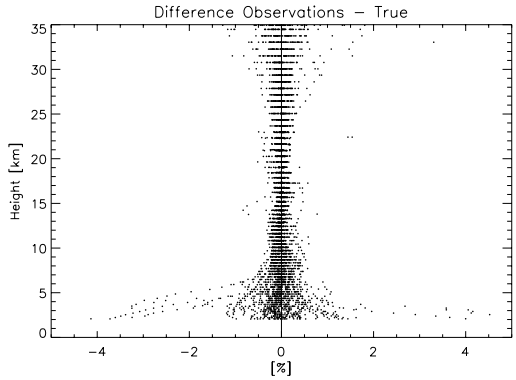

Linear interpolation in LOG space.

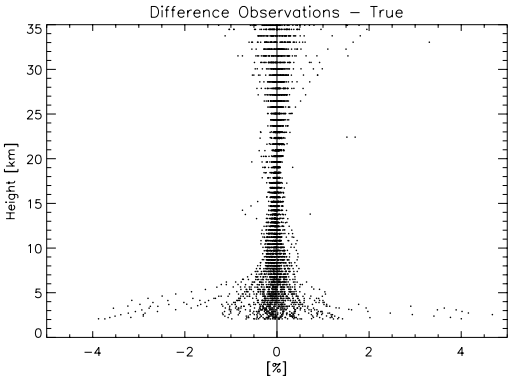

Cubic spline interpolation in LOG space.

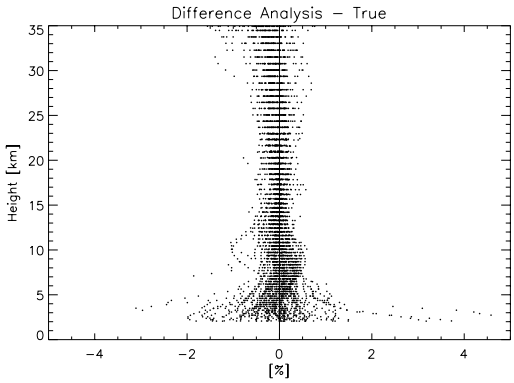

Linear interpolation in LOG space.

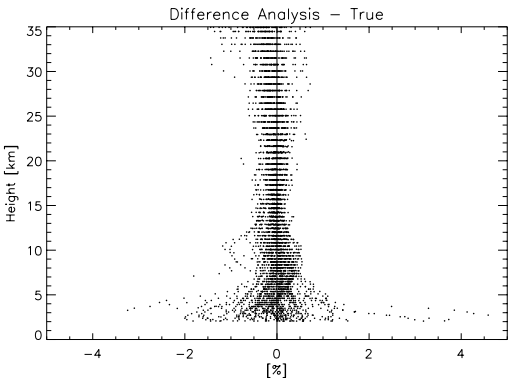

Cubic spline interpolation in LOG space.

Figure 5.18: Scatter plots for TQP assimilation experiments at refractivity level linear vertical and cubic spline interpolation operator in LOG space.

Standard Deviation for TQP Assimilation Experiments for Temperature Linear and Cubic Spline Vertical Observation Interpolation Operator in LOG Space

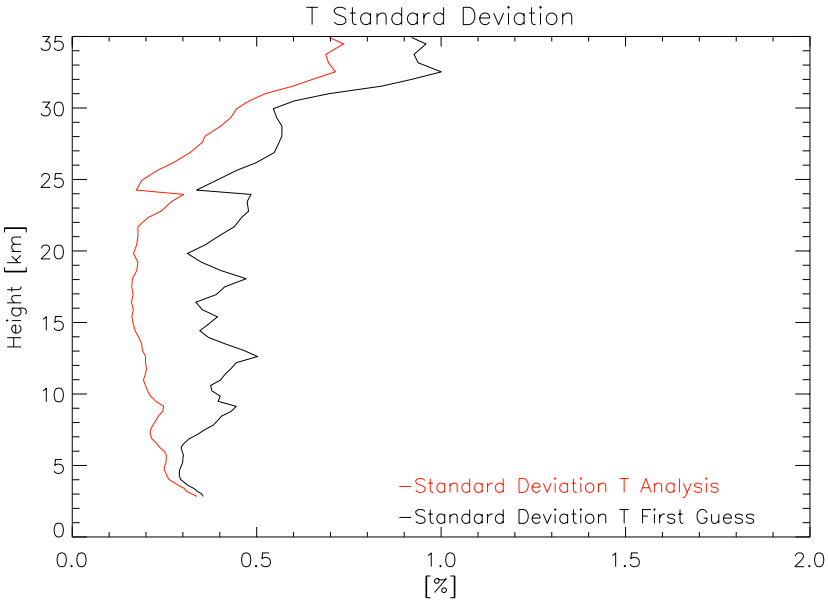

Standard deviations for assimilation using the linear interpolation operator in LOG space.

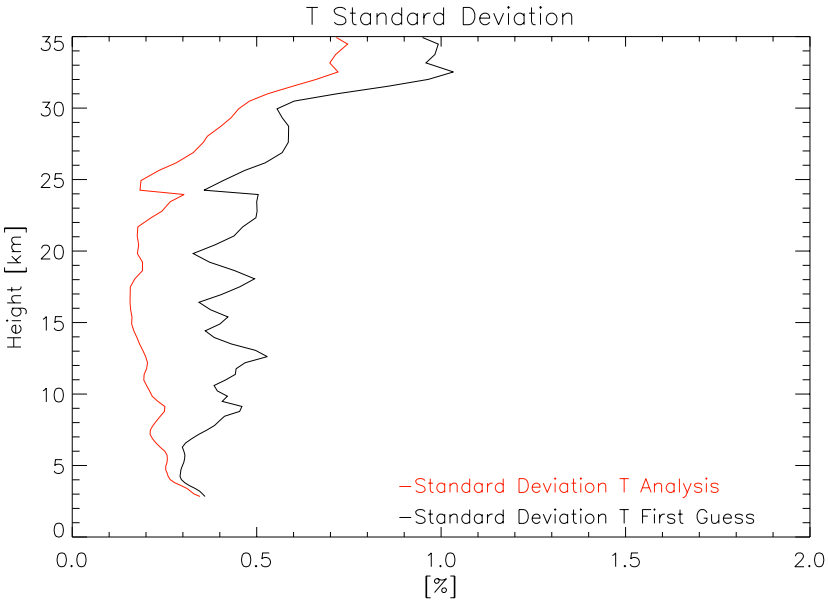

Standard deviations for assimilation using the cubic spline interpolation operator in LOG space.

Figure 5.19: Standard deviation for TQP assimilation experiments for temperature linear vertical and cubic spline interpolation operator in LOG space.

Scatter Plots for TQP Assimilation Experiments for Temperature Linear and Cubic Spline Vertical Observation Interpolation Operator in LOG Space

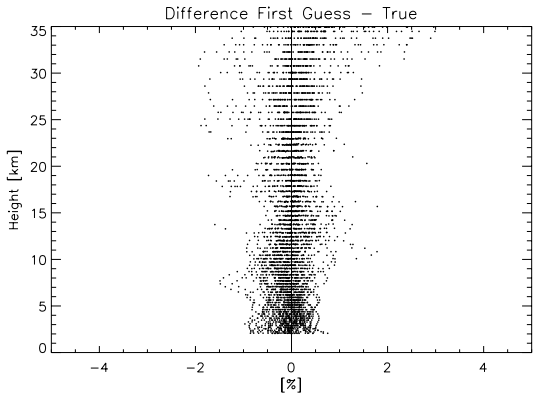

Linear interpolation in LOG space.

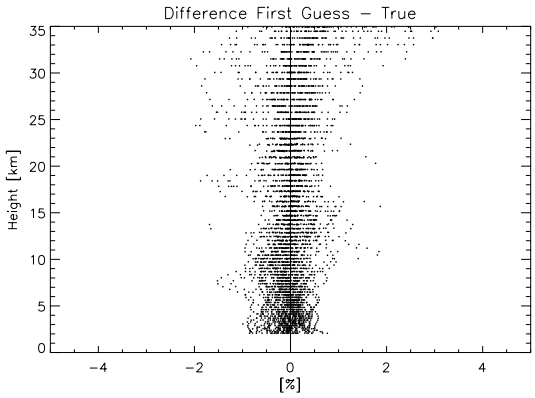

Cubic spline interpolation in LOG space.

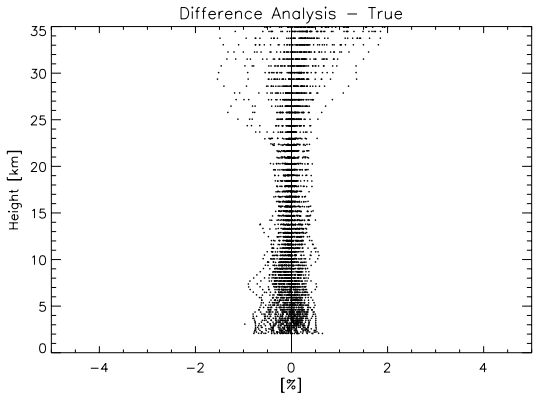

Linear interpolation in LOG space.

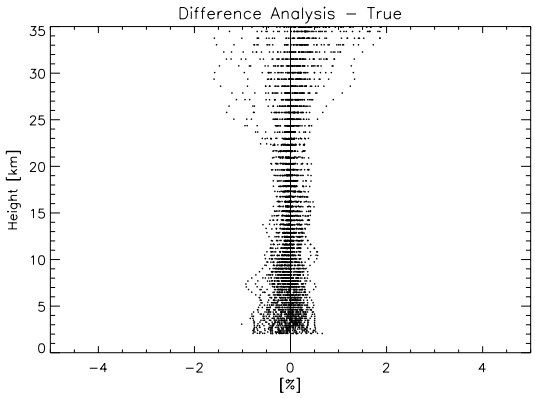

Cubic spline interpolation in LOG space.

Figure 5.20: Scatter plots for TQP assimilation experiments for temperature linear vertical and cubic spline interpolation operator in LOG space.

Surface Pressure In general the surface pressure is assumed to be well known and a global mean standard deviation of 250 Pa translates assuming the standard surface pressure of 1013.25 hPa into a relative standard deviation of roughly $\sim 0.25\%$. The surface pressure is coupled via the vertical coordinate operator with the vertical pressure grid (Section 4.5.3). In the Fig. 5.23 and 5.24, the mean tangent points of the occultations are depicted as crosses. The result is somewhat undetermined, showing alterations of the surface pressure around $\sim 0.20\%$. On the other hand there are several vertical levels between the surface and the observation cutoff height of 2.5 km, which are still influenced by the vertical background error covariance matrices.

Standard Deviation for TQP Assimilation Experiments for Specific Humidity Linear and Cubic Spline Vertical Observation Interpolation Operator in LOG Space

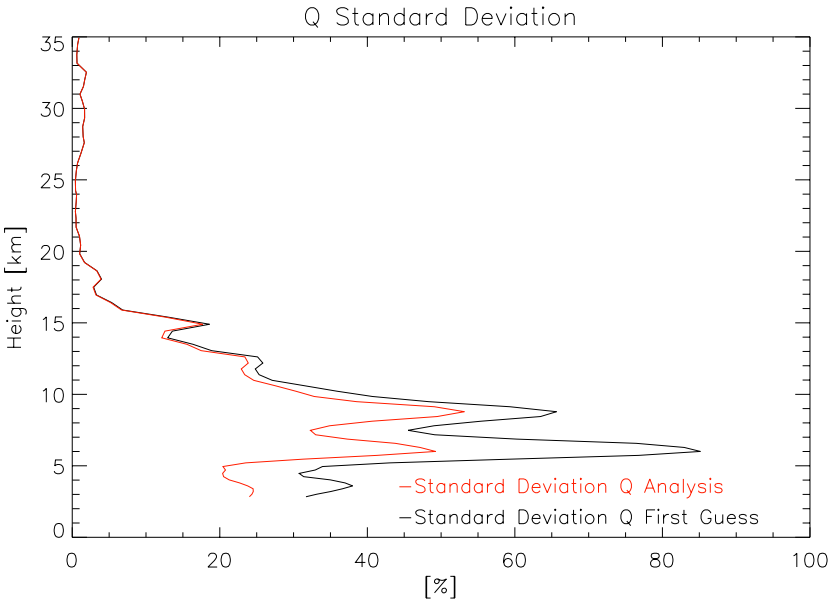

Standard deviations for assimilation using the linear interpolation operator in LOG space.

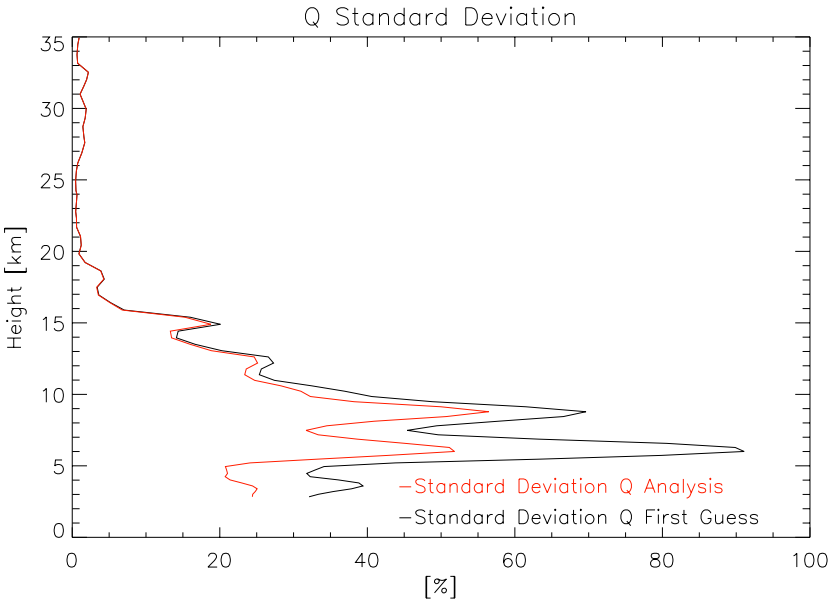

Standard deviations of the analysis using the cubic spline interpolation operator in LOG space.

Figure 5.21: Standard deviation for TQP assimilation experiments for specific humidity linear vertical and cubic spline interpolation operator in LOG space.

Scatter Plots for TQP Assimilation Specific Humidity Linear and Cubic Spline Vertical Observation Interpolation Operator in LOG Space

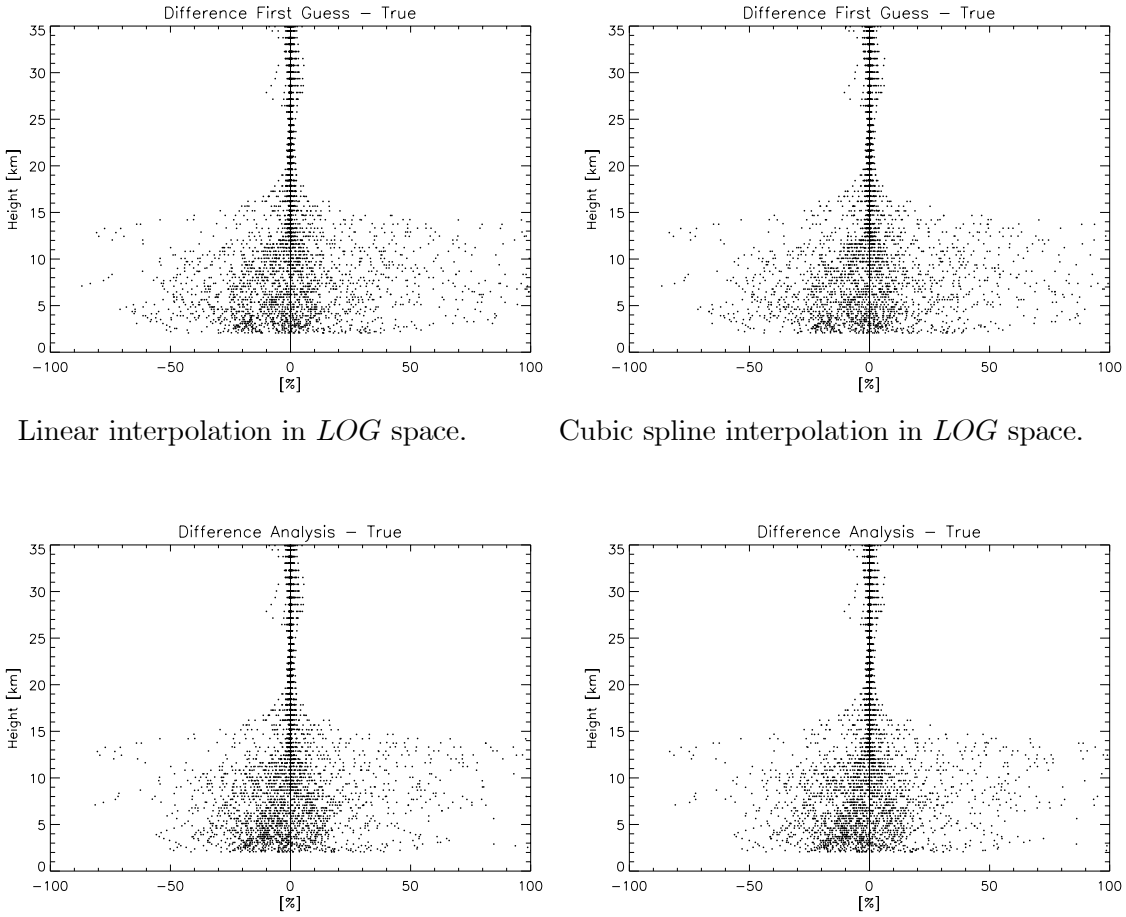

Linear interpolation in LOG space. Cubic spline interpolation in LOG space.

Linear interpolation in LOG space. Cubic spline interpolation in LOG space.

Figure 5.22: Scatter plots for TQP assimilation experiments for specific humidity linear vertical and cubic spline interpolation operator in LOG space.

Recursive Filter Impact

The horizontal background covariance matrices are realized as recursive filters (described in detail in Section 4.8.2). This horizontal slices are showing the spreading of information, introduced into the system via observations for refractivity, temperature and specific humidity. For surface pressure no special plots are shown, but the plots on the next pages, depicting the increments, are giving an idea of the horizontal spread of information. Model level 21 roughly corresponds to a height of 5 km, level 31 to a height of roughly 12 km.

Plots for TQP Assimilation Surface Pressure Linear Vertical Observation Interpolation Operator in LOG Space

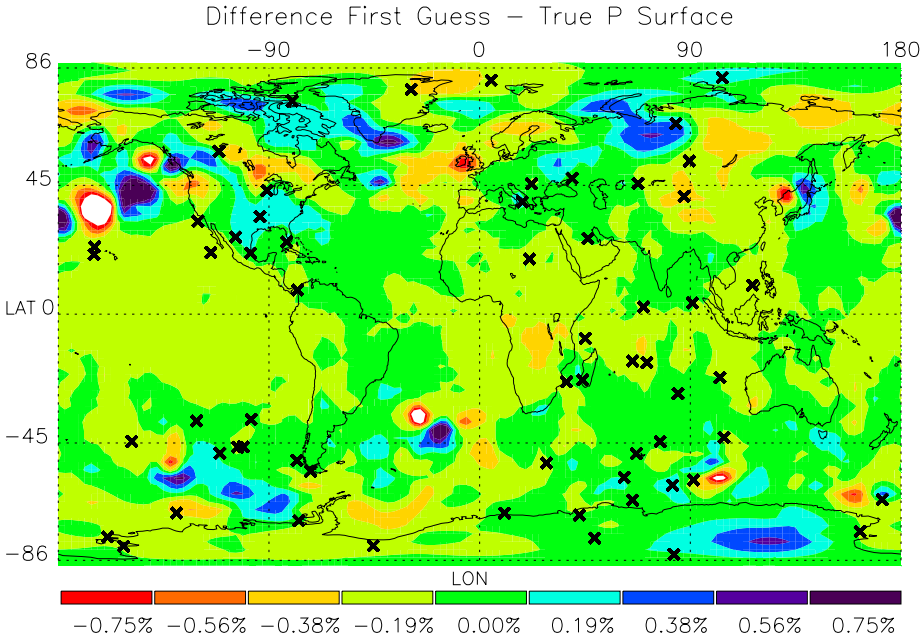

Linear interpolation in LOG space.

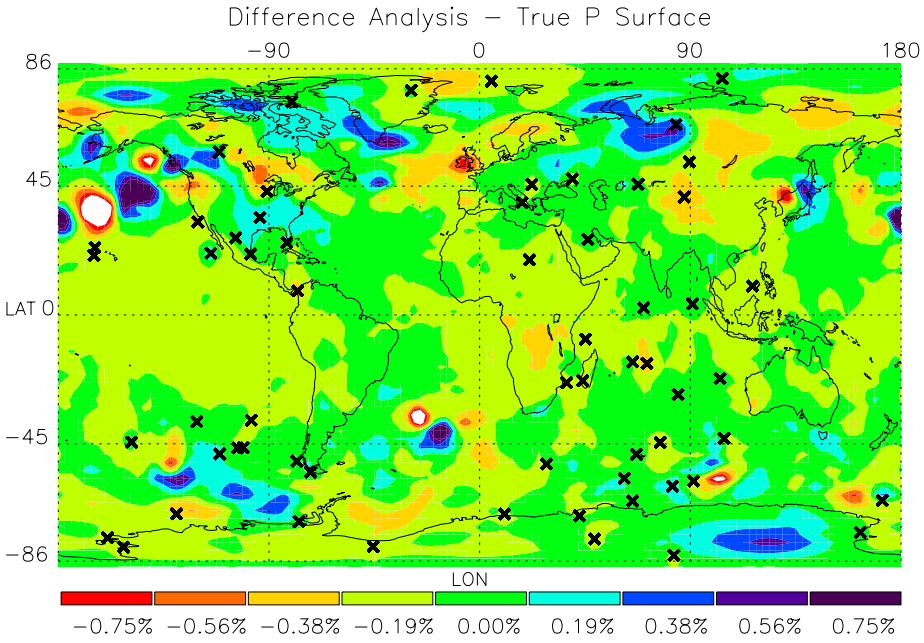

Linear interpolation in LOG space.

Figure 5.23: Surface pressure plots for TQP assimilation experiments linear vertical interpolation operator in LOG space.

Plots for TQP Assimilation Surface Pressure Cubic Spline Vertical Observation Interpolation Operator in LOG Space

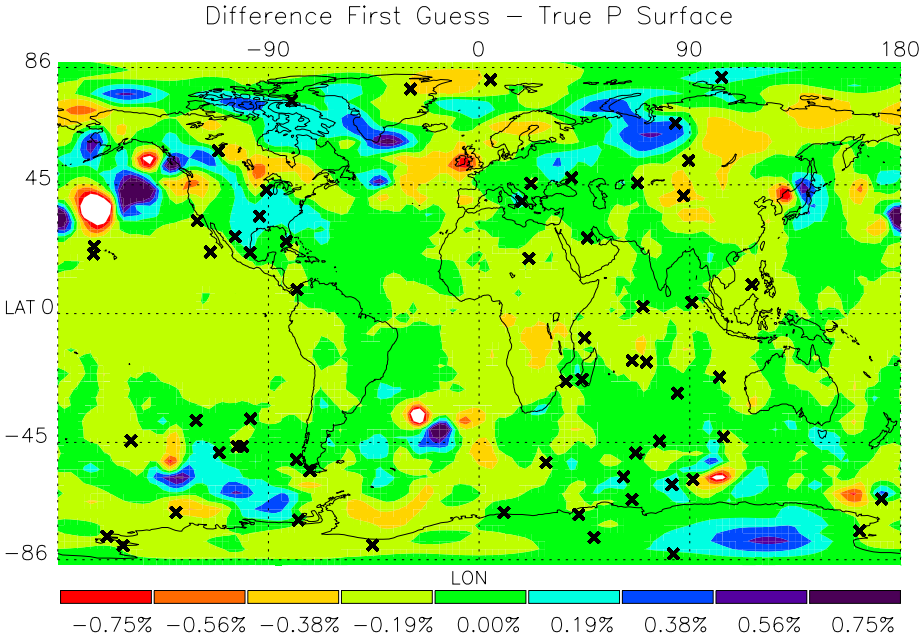

Cubic spline interpolation in LOG space.

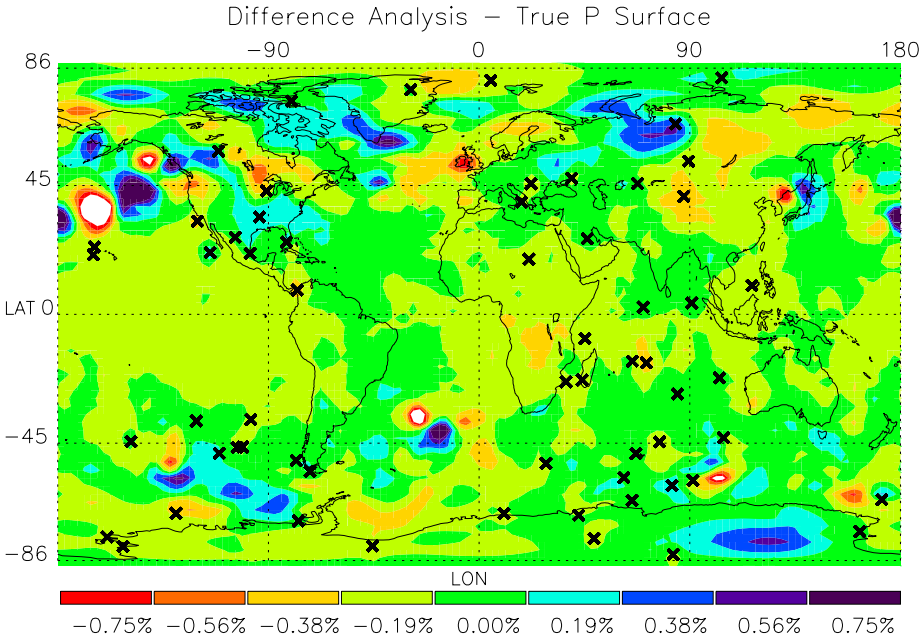

Cubic spline interpolation in LOG space.

Figure 5.24: Surface pressure plots for TQP assimilation experiments cubic spline interpolation operator in LOG space.

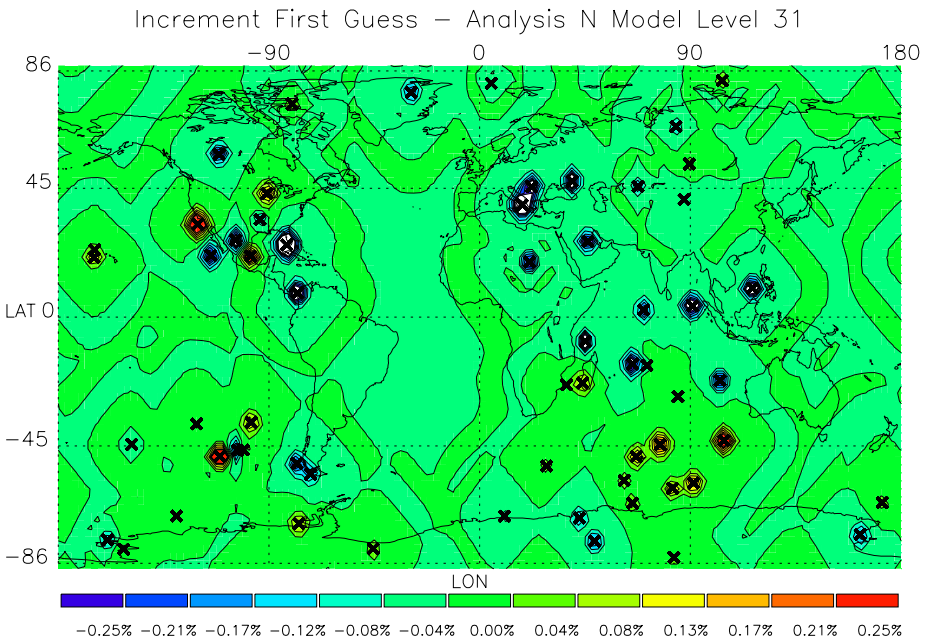

Figure 5.25: Analysis increment to show the influence of the horizontal correlation realized as recursive filter for refractivity, model level 31 corresponds to $\sim$ 12 km.

As to be expected the effects are limited to the observation location. Comparing Fig. 5.25 with upper plot Fig. 5.26 shows the anti correlation between temperature and refractivity. Both slices are collocated, depicting the same observations. Increase in refractivity is mirrored by a decrease in temperature and vice versa.

5.3 Summary Verification

5.3.1 Summary Error Patterns

The test runs concerning the assimilation experiments using the error patterns method delivered the anticipated results. The convergence behavior will be discussed in the next Section of this Chapter. The correct application of errors onto the background and observations was validated. Full assimilation runs were conducted using only vertical correlations within the refractivity framework. Within the temperature, specific humidity and surface pressure framework, limited experiments were run owing to the specific humidity error characteristics. Nevertheless are these experiments suggesting a certain independence of separate atmospheric parameters, indicating a particular robustness which stems from isolated flaws within specific parameters.

5.3.2 Summary Raytraced Measurements

The assimilation of the quite realistic raytraced profiles, also shows some promising results, in improving consistently the first guess.

Recursive Filter Impact for Temperature and Specific Humidity

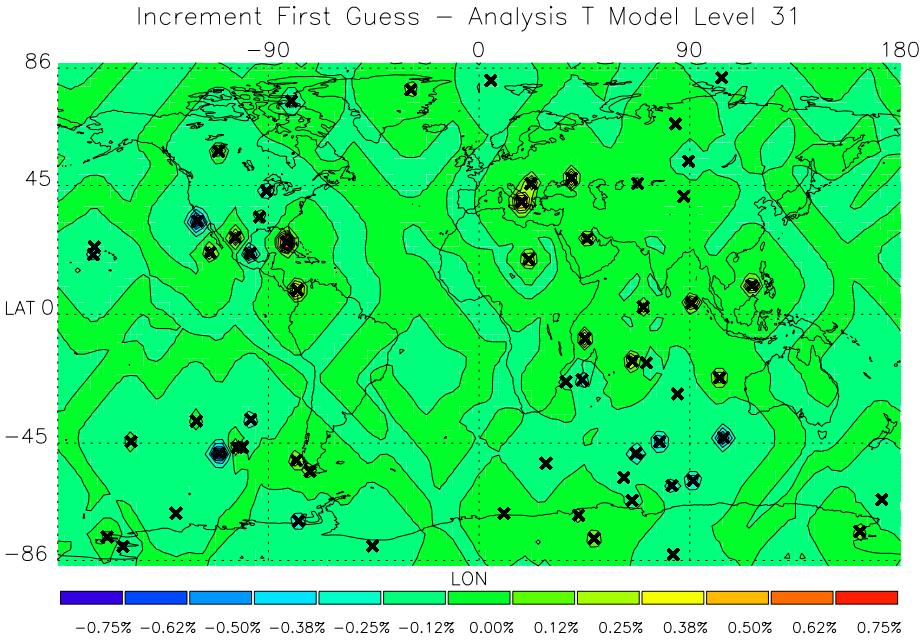

Analysis increment to show the influence of the horizontal correlation realized as recursive filter for temperature, model level 31, $\sim$ 12 km.

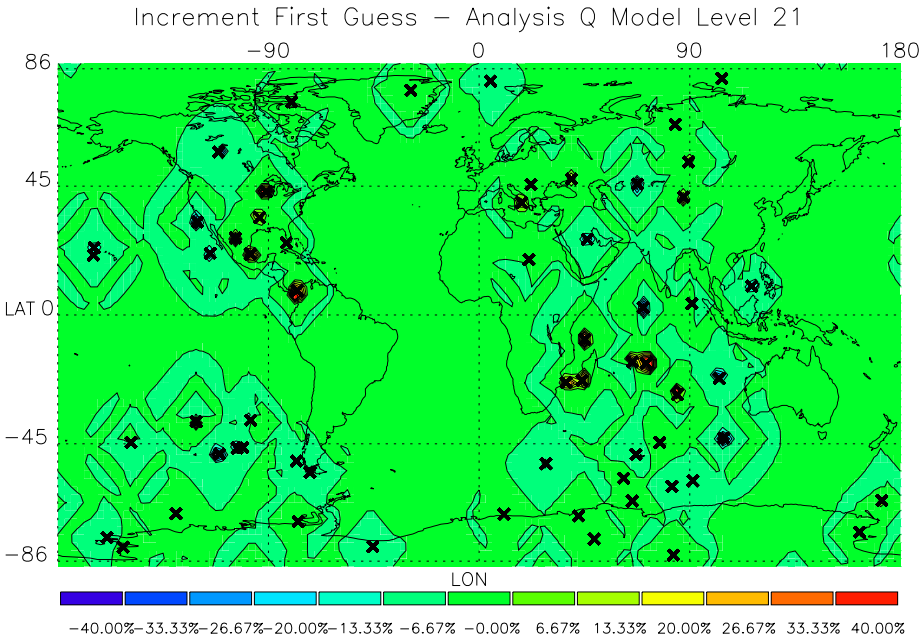

Analysis increment to show the influence of the horizontal correlation realized as recursive filter for specific humidity, level 21, $\sim$ 5 km.

Figure 5.26: Horizontal spreading of information for temperature and specific humidity by RF filters.

The experiments were run twice, using once the linear vertical observation interpolation operator and once the cubic spline version, both in *LOG* space. As can be seen in all the figures there is no significant advantage of one or the other version neither concerning the overall accuracy nor the bias of the interpolation in a statistical way.

5.4 Convergence Behavior

The assimilation procedure is an iterative process, were suitable aboard or convergence condition have to be defined. The used minimization algorithm (Section 4.10) offers a broad variety of options to define a convergence condition. The criteria to stop the iteration has also to take computing time into account, so at least the process should be able to deliver results in real time. It is also vital to distinguish between an *iteration* which means a new atmospheric state is found and a so called *simulation* which just means an evaluation of cost function and gradient. To find a new state several simulations may be necessary. The better posed the problem is, the easier is it to find a new state.

5.4.1 Assimilation experiments using error patterns

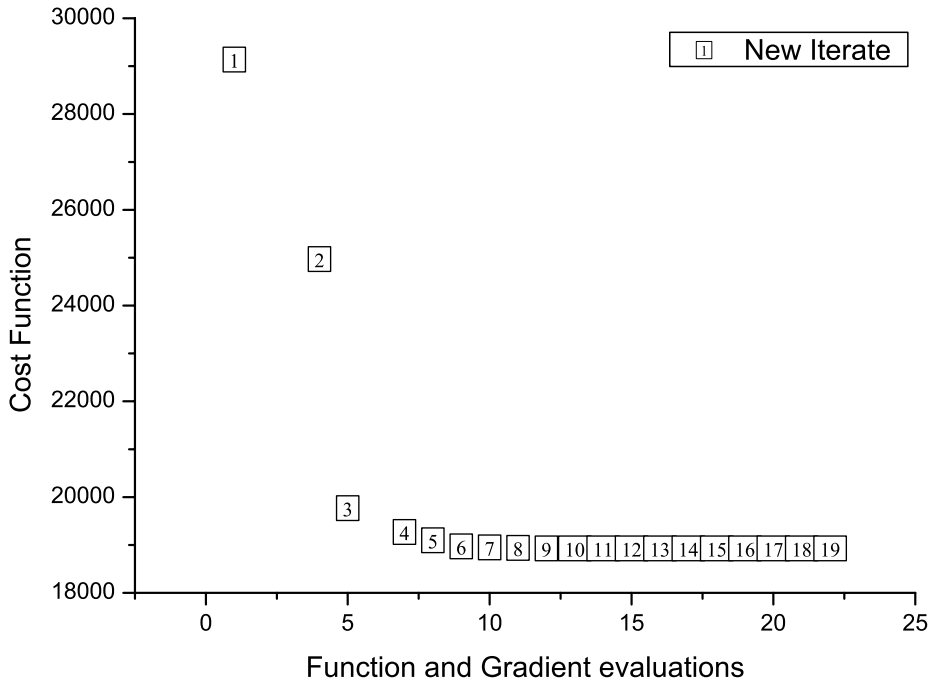

Figure 5.27: Convergence bahavior during refractivity assimilation experiment using error patterns.

As to be expected, the refractivity assimilation experiment based on error pattern (cf. Section 5.1.2) is a well posed problem. The excellent convergence behavior is shown in

Fig. 5.27. 22 cost function and gradient evaluations are necessary to get 19 new iterates. It is clearly visible, that the most significant reduction of the cost function only requires 6 iterations. Another minor step is achieved after 9 iterations, from iteration 9 to 19 the change of the cost function is from 18970 to 18930, which is completely negligible for the accuracy of the analysis. This result is purely theoretical but it suggests that within a more realistic setup an abort condition for the minimization cycle has to be defined.

5.4.2 Assimilation Experiments using Raytraced Measurements

Refractivity Assimilation

Using more realistic assumptions concerning measurement and background data, namely using raytraced profiles and realistic error characteristics, the convergence behavior differs. The first iterations are showing again the most significant reduction of the cost function, but there is a second significant step after 17 iterations (which translates into 29 cost function and gradient evaluations). The problem is less well posed as can be easily seen if you compare new iterates versus cost function and gradient evaluations (32 new iterates require 77 evaluations of cost function and gradient). Nevertheless it seems appropriate to cut down the number of iterates to reduce computing time. A reasonable value would be 35 cost function and gradient evaluations, the gain of accuracy within the analysis due to further minimization cycles is marginal. Till iteration 20 the behavior of the two different observation operators conducting the vertical interpolation is negligible, further on the cubic spline version finds more solutions ending up with 32 iterations after 77 cost function and gradient evaluations compared to 21 iterations after 56 cost function and gradient evaluations. This difference occurs at a stage of the minimization at which no advantage for one or the other method concerning the overall accuracy is apparent (cf. Fig. 5.28).

Temperature, Specific Humidity and Surface Pressure Assimilation

Finally using the full version of the assimilation framework, updating temperature, specific humidity and surface pressure fields directly, the convergence behavior is somewhat smoother than in the refractivity case. The development of the total cost function still shows a sharp bend around evaluation 30, but it is significant smoother than in the refractivity only case. The results also suggest that a reasonable aboard condition for the minimization cycles might be 30-35 cost function and gradient evaluations. Which would be the best trade off between accuracy and computing time with a certain *safety* margin. Within this assimilation framework, the two different vertical interpolation observation operators perform equivalent (cf. Fig. 5.29).

5.4.3 Conclusion Concerning the Vertical Interpolation Operator

From this trial run no advantage of the cubic spline interpolation scheme can be conducted (cf. also Section 5.3.1). It is suggested to use the simple linear interpolation scheme in LOG space to increase the overall system performance concerning computing time.

Refractivity Assimilation Convergence Behavior

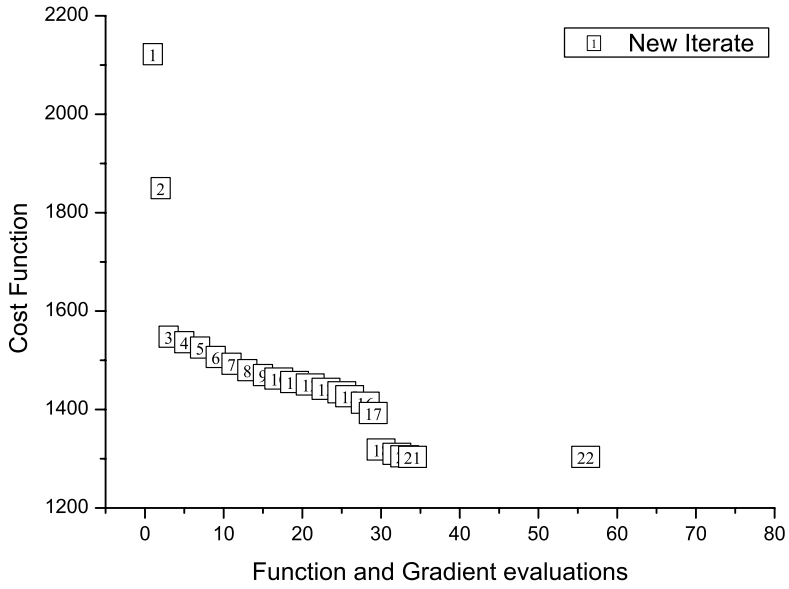

Convergence bahavior linear observation interpolation operator in *LOG* space.

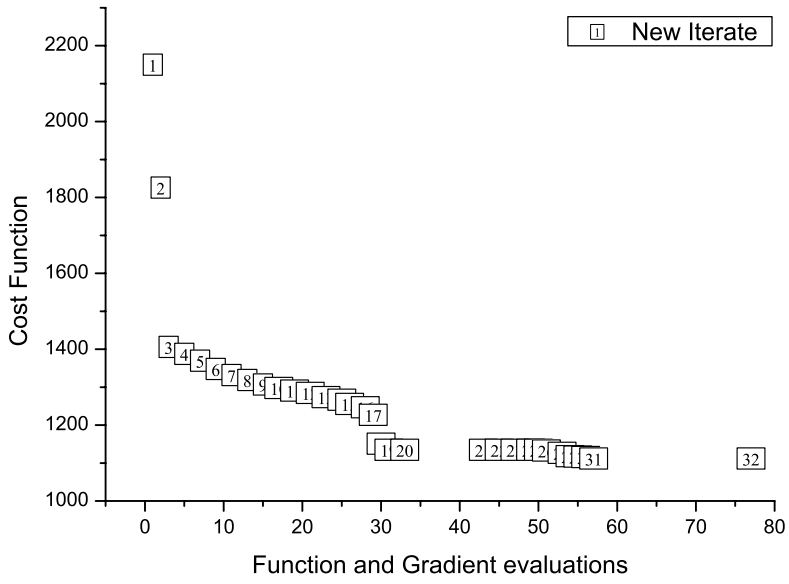

Convergence bahavior cubic spline observation interpolation operator in *LOG* space.

Figure 5.28: Convergence bahavior of refractivity assimilation experiments using ray traced profiles.

Temperature, Specific Humidity, and Surface Pressure Assimilation Convergence Behavior

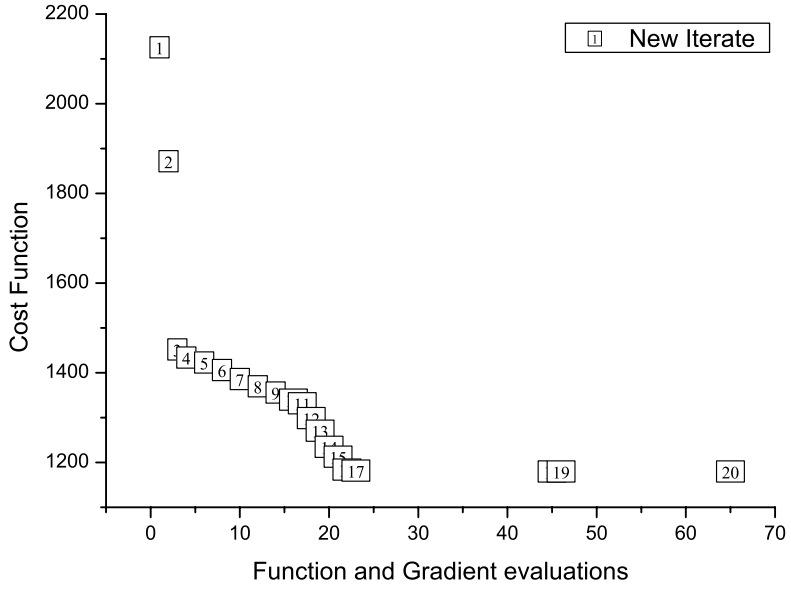

Convergence bahavior linear observation interpolation operator in LOG space.

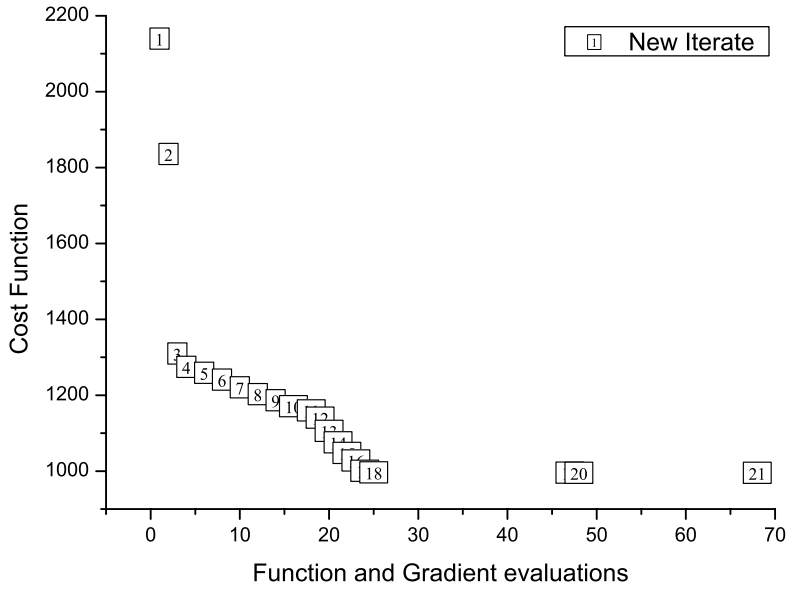

Convergence bahavior cubic spline observation interpolation operator in LOG space.

Figure 5.29: Convergence bahavior of temperature, specific humidity, and surface pressure assimilarion experiments using ray traced profiles.

6

Experiments Using CHAMP Data

To perform the first experiments assimilating CHAMP data the summer season 2003 was chosen. Day 225 was selected to perform the first assimilation of 24 hours of CHAMP occultations. For the global distribution of this 142 RO profiles cf. Fig. 3.4. The first experiments where conducted with the ±3 hour assimilation time window around 12 UTC. The global measurement distribution for this six hour period is shown in Fig. 6.1.

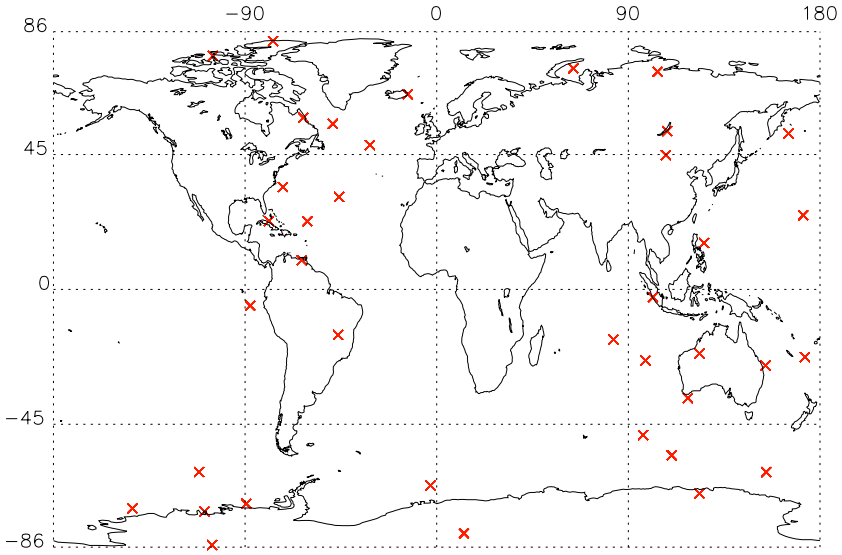

Figure 6.1: Global distribution of 38 RO profiles from the six hour assimilation window around 12 UTC from day 225 of 2003.

For the relative observation standard deviation a value of 0.4% [*Steiner* (2004)] was chosen within this assimilation runs (cf. Fig. 4.6). The number of cost function and gradient evaluations was limited to 101. For this test case again both assimilation schemes using the two vertical interpolation operators where used. The corresponding ECMWF analysis fields served as first guess. As with the raytraced profiles only observations between 2.5

km and 35 km were used. Prior to the assimilation procedure a data thinning step is applied to reduce the number of observations within one profile to a configuration denoted as measurement distribution 2 (cf. Subsection 5.2.1). Within this preprocessing step, data flagged as suspicious is also rejected, so only already quality controlled observations can enter the assimilation process. Due to the fact that compared to the validation runs, the *true* is not known, and thus a *standard deviation* can not be derived, the terms *mean statistical deviation* and *mean bias* are used, for the real data error statistics (comparison against ECMWF).

6.1 Experiments ± 3 Hour Assimilation Window Around 12 UTC Day 225 Year 2003

This CHAMP measurement sample was chosen, to conduct the first assimilation runs with real data. It consists of 38 profiles, containing 2278 single observations. As to expect from such a limited sample the distribution is not global even. About one third of the profiles are between a latitude of -45° and -90° which can be seen in Fig. 6.1. This generates an interesting effect, which will be explained in the next sections.

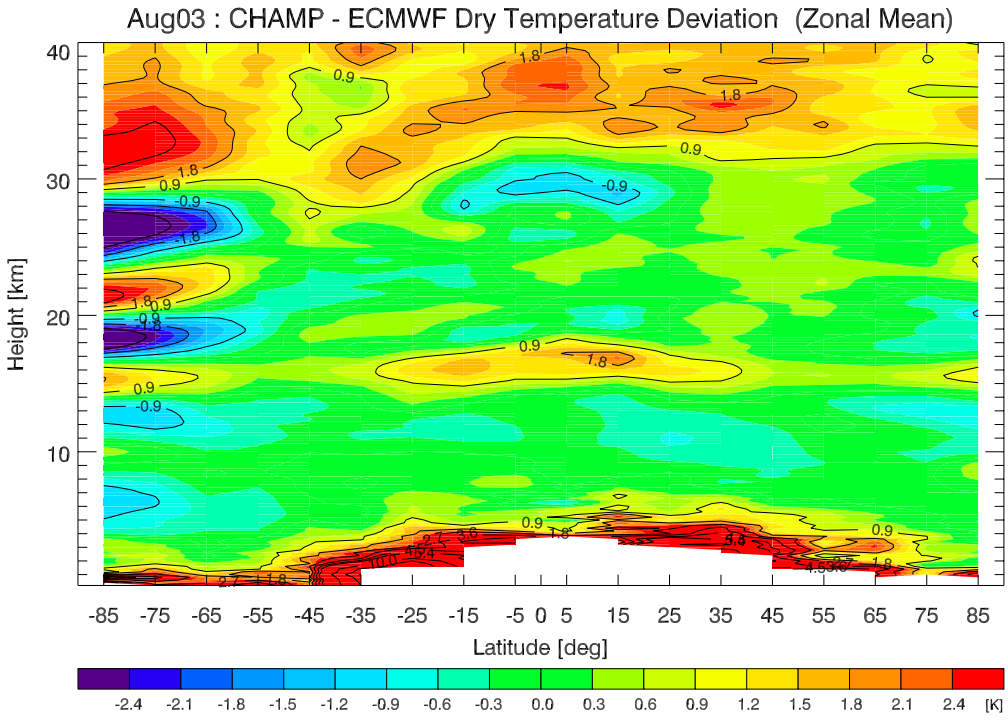

Figure 6.2: August mean increment 2003 RO derived dry temperature - ECMWF seasonal mean analysis (courtesy M. Borsche, IGAM/UniGraz).

6.1.1 Refractivity Assimilation

The Figs. 6.3 are showing a significant 0.4% systematic deviation of the CHAMP measurements, which is only slightly propagated into the analysis, a fact which is also clearly visible. This effect stems from the different statistical weights of observations and background. The effect of the observations onto the first guess at the observation location is about $\sim 0.25\%$ which can be seen in the Figs. 6.4. This first results suggest to apply a correction of the observation prior to assimilation. The Figs. 6.19 indicate some *wave like* vertical structure, which can be probably explained by the numerical representation of the polar vortex within the ECMWF model. A comparison of a seasonal mean dry temperature map derived from CHAMP data with the corresponding seasonal mean of ECMWF shows some interesting features, which indicates that the *wave like* vertical structure stems from the background, as can be seen in Fig. 6.2. At the southern high latitudes the wave like structures are clearly apparent at temperature level, which translates above the tropopause (with pressure) quite directly into refractivity. An assumption which is confirmed in Subsection 6.9.2 (cf. Fig. 6.57).

6.1.2 Temperature, Specific Humidity, and Surface Pressure Assimilation

Temperature, Specific Humidity, and Surface Pressure Assimilation at Refractivity Level

The same procedure as in the refractivity only case was applied. The tests are showing equivalent results like in Subsection 5.2.3. At refractivity level both assimilation schemes show very similar results. The same applies for the two realizations of the vertical interpolation operator, which behave the same at refractivity level, concerning the systematic deviation (cf. Fig. 6.17) and mean deviation from the first guess after the assimilation (cf. Fig. 6.18). In general the real CHAMP measurements behave similar to the simulated data (cf. Subsection 5.2.1, except the standard deviation, and surprisingly a smoother convergence behavior see Section 6.3), so also the systematic deviation of 0.4% is present. This proofs the realistic setup of the EGOPS system concerning the raytraced measurements.

Temperature, Specific Humidity, and Surface Pressure Assimilation

Temperature Fig. 6.9 shows the mean deviation of temperature between first guess and analysis. Within this two plots a difference between the two interpolation operators can be seen. The features of the mean deviations are nearly identical, but the magnitude depends on the used vertical interpolation operator. The cubic spline version applies a somewhat bigger correction to the first guess (cf. Fig. 6.10), an effect which is more pronounced with altitude. In Fig. 6.10 the *wave like* vertical structure is even more pronounced than in Fig. 6.19, which indicates, that this effect is temperature driven. This features are also visible within the zonal mean temperature analysis of August 2003 (cf. Fig. 6.56, upper panel), but at a much smaller level (the assimilation result depicts temperature compared to dry temperature in Fig. 6.58). Within the TQP assimilation scheme the information content of the refractivity observations is somewhat diluted by being segmented into temperature, specific humidity, and surface pressure, via local pressure. So the increments of each separate variable are quite small, visible in the temperature (cf. Fig. 6.56 upper panel).

Mean Bias of Refractivity Assimilation Experiments Linear and Cubic Spline Vertical Observation Interpolation Operator in LOG Space Using CHAMP Data

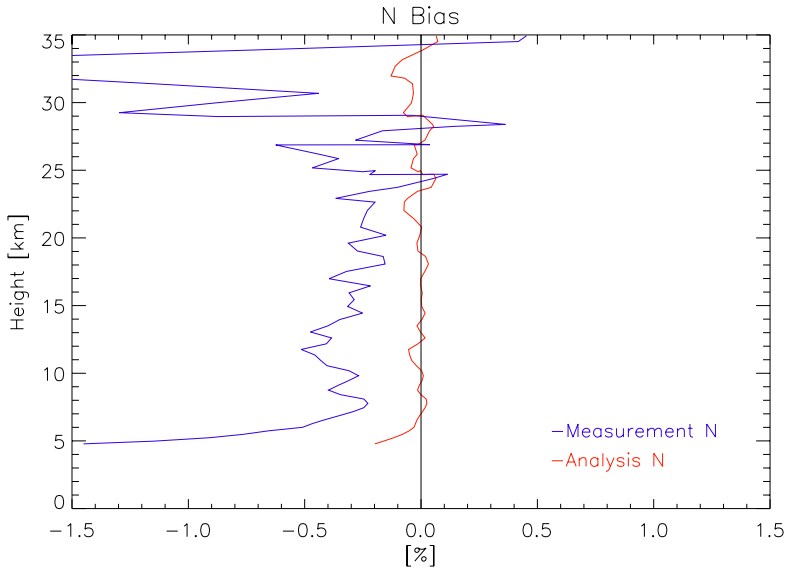

Mean bias of refractivity analysis and observations using the linear interpolation operator in LOG space.

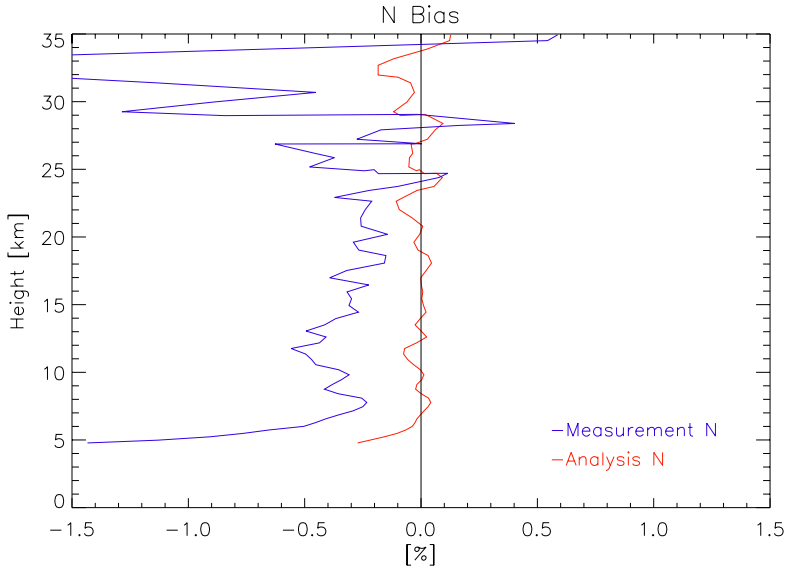

Mean bias of refractivity analysis and observations using the cubic spline interpolation operator in LOG space.

Figure 6.3: Mean bias of refractivity assimilation experiments linear vertical and cubic spline interpolation operator in LOG space using CHAMP data.

Mean Statistical Deviation from First Guess for Refractivity Assimilation Experiments Linear and Cubic Spline Vertical Observation Interpolation Operator in LOG Space Using CHAMP Data

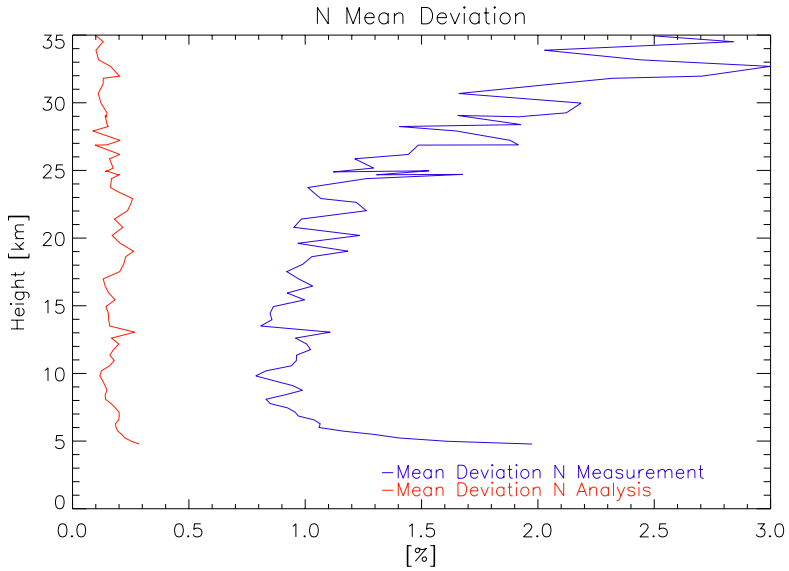

Mean statistical deviations for the refractivity analysis and observations using the linear interpolation operator in LOG space.

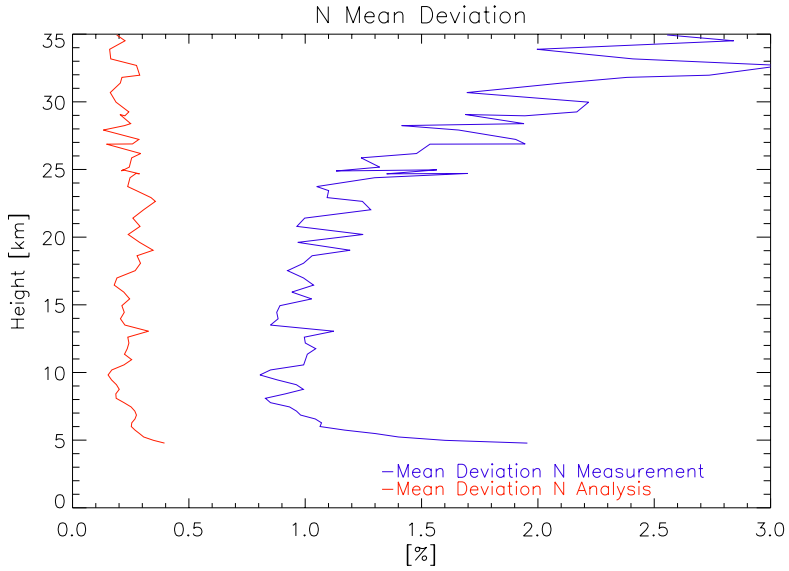

Mean statistical deviations for the refractivity analysis and observations using the cubic spline interpolation operator in LOG space.

Figure 6.4: Mean statistical deviation from first guess for refractivity assimilation experiments linear vertical and cubic spline interpolation operator in LOG space using CHAMP data.

Scatter Plots for Refractivity Assimilation Experiments Linear and Cubic Spline Vertical Observation Interpolation Operator in LOG Space Using CHAMP Data

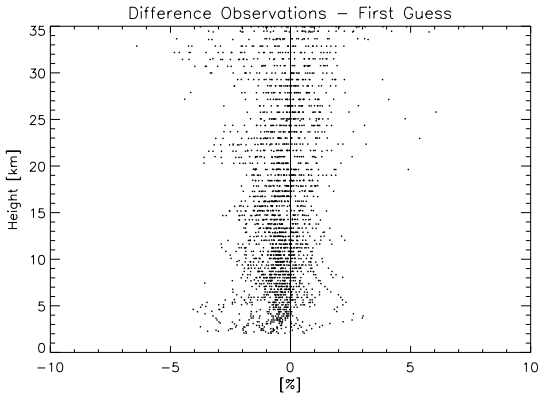

Linear interpolation in LOG space.

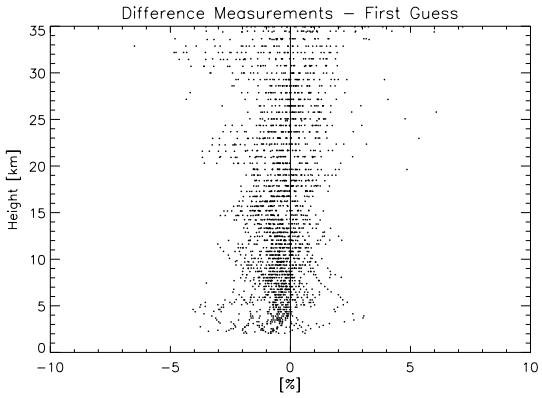

Cubic spline interpolation in LOG space.

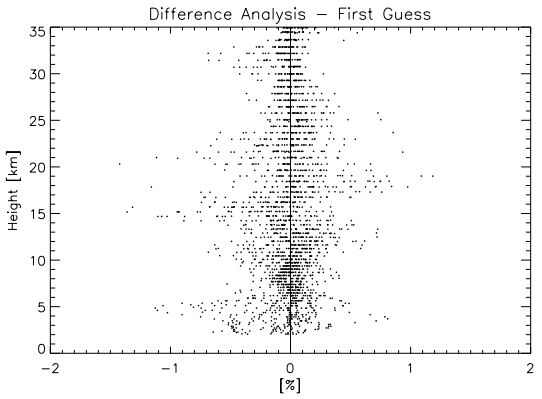

Linear interpolation in LOG space.

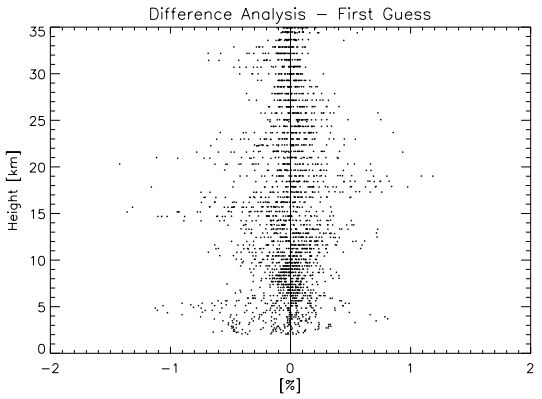

Cubic spline interpolation in LOG space.

Figure 6.5: Scatter plots for refractivity assimilation experiments for linear vertical and cubic spline interpolation operator in LOG space using CHAMP data.

Specific Humidity

The mean deviation of the specific humidity analysis compared with the first guess (Fig. 6.11), shows a deviation of $\sim 7\%$ for the linear interpolation operator and $\sim 9.5\%$ for the cubic spline version, showing the same general features, but again slightly more impact of the cubic spline interpolation scheme onto the analysis is apparent (an effect which is also visible in Fig. 6.12). No *wave like* vertical structures are immediate apparent, proving the temperature dependence of this phenomenon.

Mean Bias of TQP Assimilation Experiments at Refractivity Level Linear and Cubic Spline Vertical Observation Interpolation Operator in LOG Space Using CHAMP Data

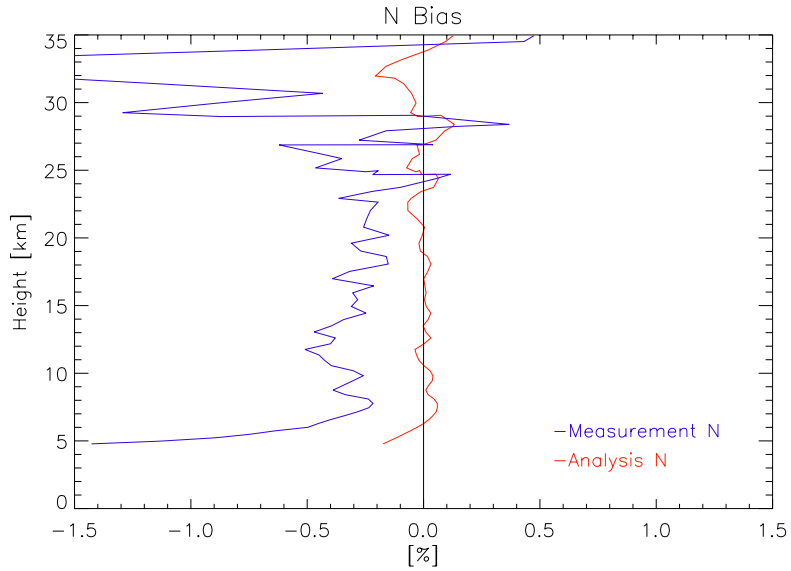

Mean bias of refractivity analysis and observations using the linear interpolation operator in LOG space.

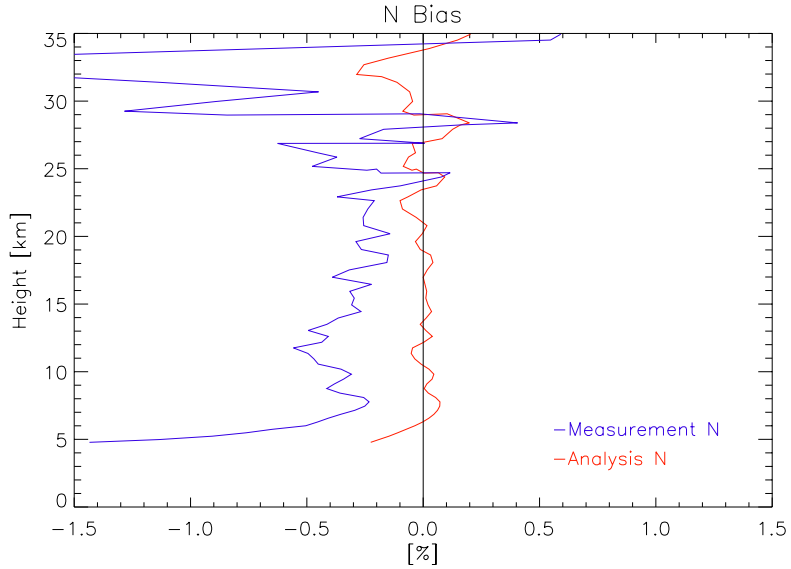

Mean bias of refractivity analysis and observations using the cubic spline interpolation operator in LOG space.

Figure 6.6: Mean bias of TQP assimilation experiments at refractivity level linear vertical and cubic spline interpolation operator in LOG space using CHAMP data.

Mean Statistical Deviation from First Guess for TQP Assimilation Experiments at Refractivity Level Linear and Cubic Spline Vertical Observation Interpolation Operator in LOG Space Using CHAMP Data

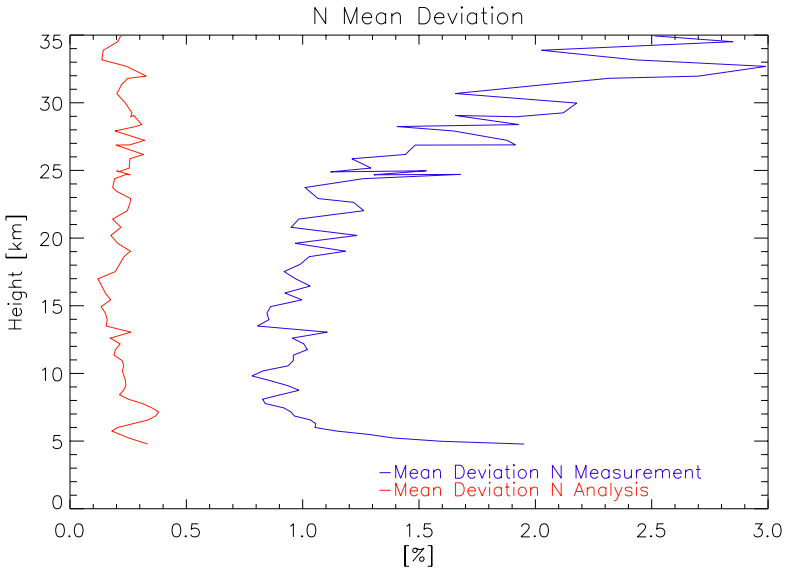

Mean statistical deviations for refractivity and observations using the linear interpolation operator in LOG space.

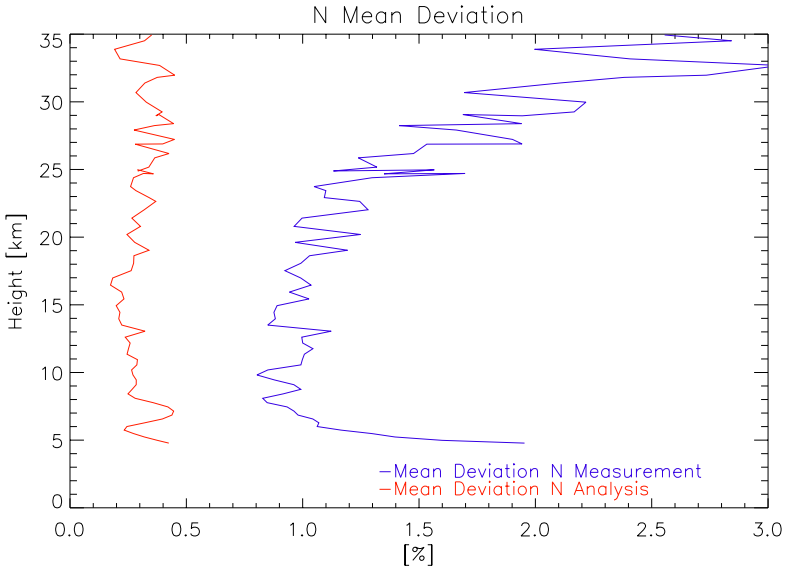

Mean Statistical deviations for refractivity and observations using the cubic spline interpolation operator in LOG space.

Figure 6.7: Mean statistical deviation from first guess for TQP assimilation experiments at refractivity level linear vertical and cubic spline interpolation operator in LOG space using CHAMP data.

Scatter Plots for TQP Assimilation Experiments at Refractivity Level Linear and Cubic Spline Vertical Observation Interpolation Operator in LOG Space Using CHAMP Data

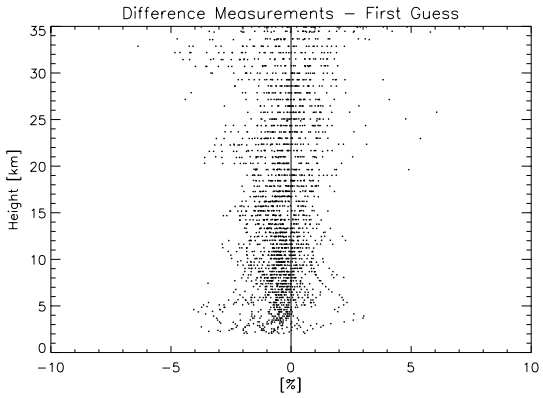

Linear interpolation in LOG space.

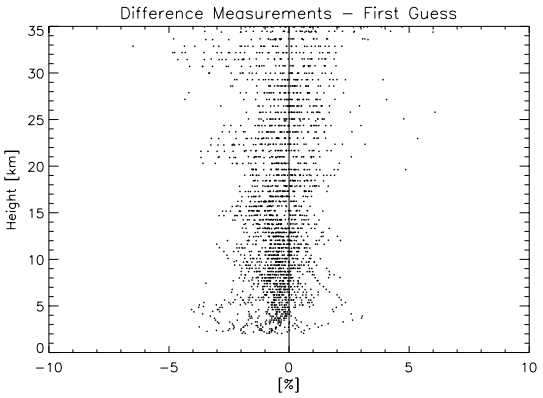

Cubic spline interpolation in LOG space.

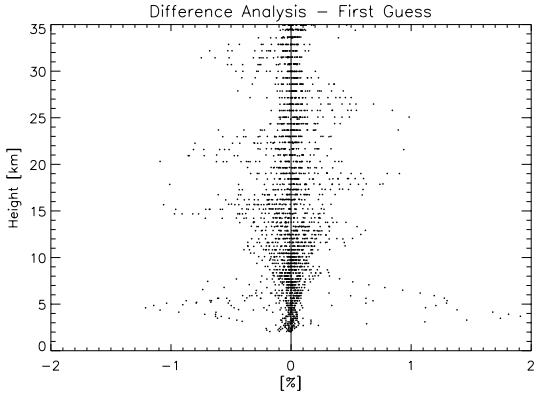

Linear interpolation in LOG space.

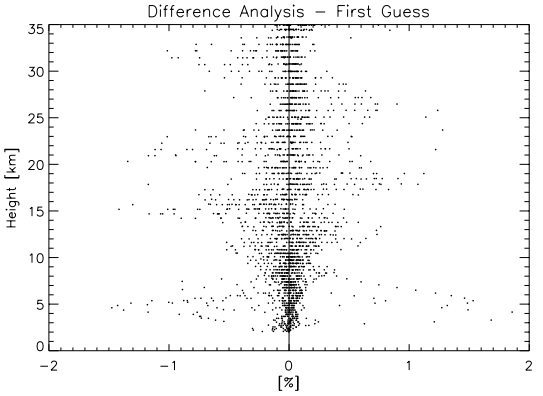

Cubic spline interpolation in LOG space.

Figure 6.8: Scatter plots for TQP assimilation experiments at refractivity level for linear vertical and cubic spline interpolation operator in LOG space using CHAMP data.

Surface Pressure

As you can see in Fig. 6.13, the surface pressure increment is marginal, which basically mirrors that the surface pressure is assumed to be known to a high degree of accuracy. It is interesting to mention that the corrections of the first guess are predominantly negative (as the whole analysis introduces a slightly negative correction to large areas). Furthermore it is clearly visible that the corrections to the first guess are somewhat larger if the cubic spline interpolation operator is used (lower panel Fig. 6.13), but the overall tendency to a negative correction of the first guess is again apparent.

Mean Statistical Deviation for TQP Assimilation Experiments for Temperature Linear and Cubic Spline Vertical Observation Interpolation Operator in LOG Space Using CHAMP Data

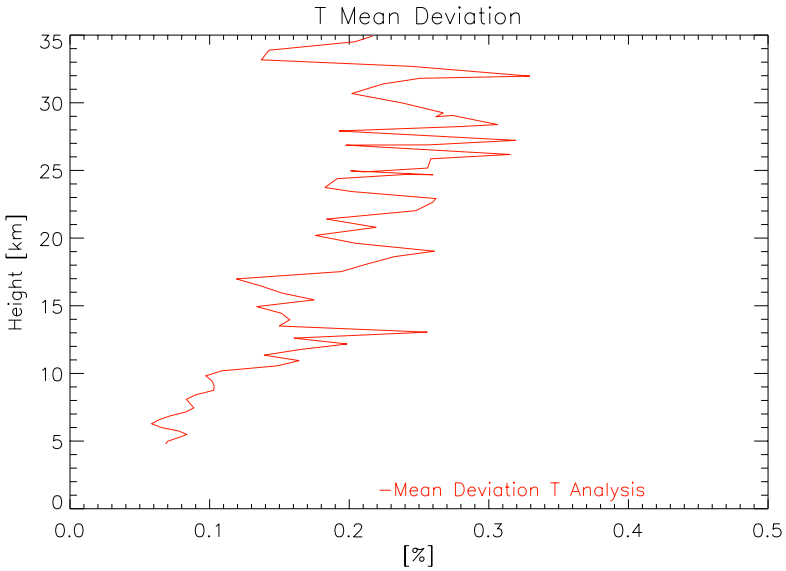

Mean statistical deviations for the temperature analysis using the linear interpolation operator in LOG space.

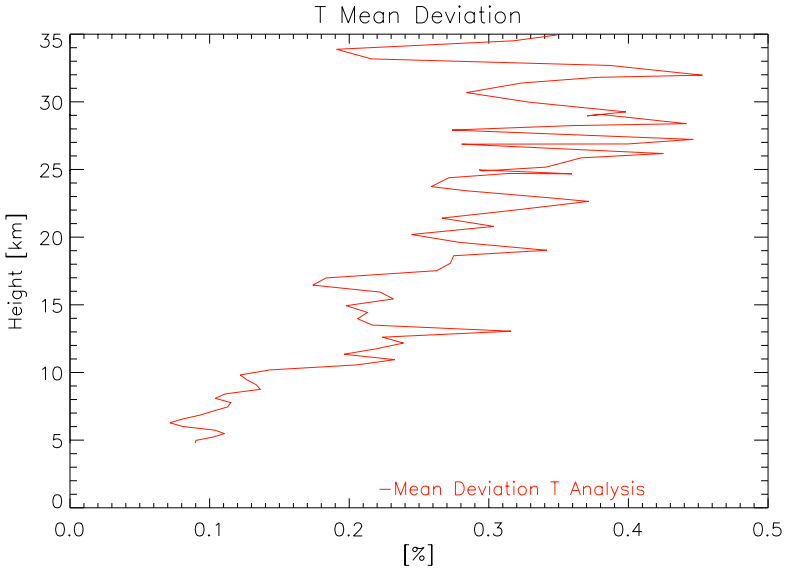

Mean statistical deviations for the temperature analysis using the cubic spline interpolation operator in LOG space.

Figure 6.9: Mean statistical deviation for TQP assimilation experiments for temperature linear vertical and cubic spline interpolation operator in LOG space using CHAMP data.

Scatter Plots for TQP Assimilation Experiments for Temperature Linear and Cubic Spline Vertical Observation Interpolation Operator in LOG Space Using CHAMP Data

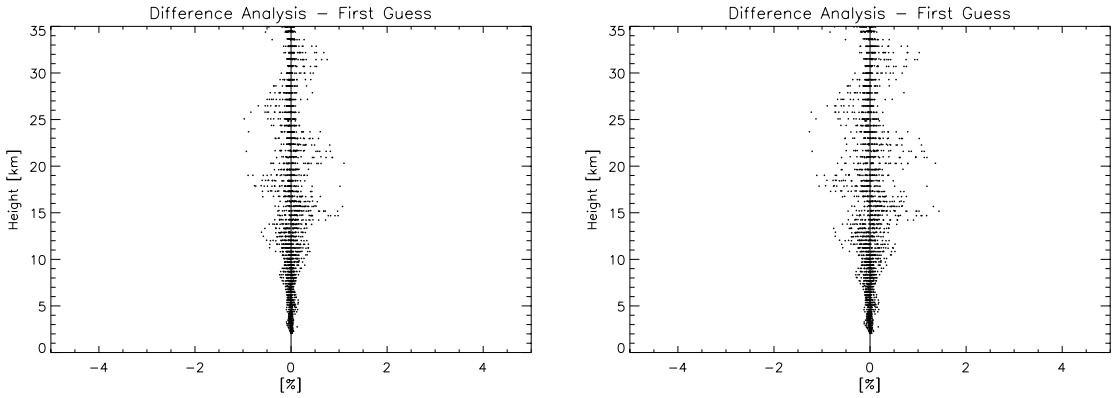

Linear interpolation in LOG space. Cubic spline interpolation in LOG space.

Figure 6.10: Scatter plots for TQP assimilation experiments for temperature linear vertical and cubic spline interpolation operator in LOG space using CHAMP data.

Summary

At the moment CHAMP profiles provided *as they are*, are showing a significant systematic deviation of $\sim 0.4\%$. This deviation occurs consistently within the refractivity only assimilation and the TQP scheme and is not introduced by the data preprocessing procedures (data thinning cf. Section 5.2.1). Within a further preprocessing step, the observations have to be corrected for this deviation, prior to assimilation. On the other hand you have to be aware that a *real* true is not existing (the observations are compared with ECMWF analysis fields, which might be biased themselves). Still, due to accuracy considerations, this refractivity bias of radio occultation measurements against ECMWF analysis, stems most likely from the retrieval procedure, which is consistently approved by independent analyses [*Gobiet and Kirchengast* (2004b)], [*Ao et al.* (2003)], as will be seen later (see conclusions), this problem has to be tackled at retrieval level. To correct for this deviation is a justified measure, and has to be seen only as a first step, which is done for the further experiments. A new version of the retrieval algorithm should solve this problem, and introduce also other enhancements (cf. Section 6.10.5). The *wave like* structures stem from the background which was already mentioned, and their origin is most likely in the ECMWF model representation of the polar vortex.

Mean Statistical Deviation for TQP Assimilation Experiments for Specific Humidity Linear and Cubic Spline Vertical Observation Interpolation Operator in LOG Space Using CHAMP Data

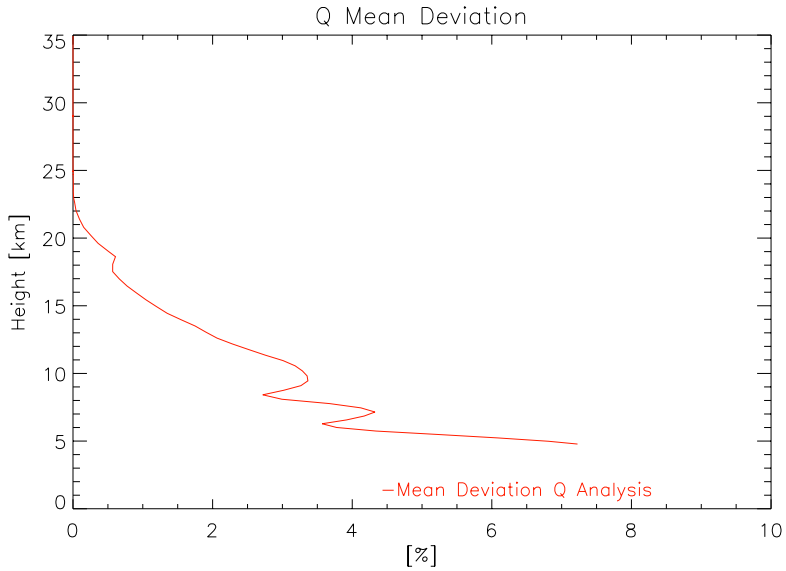

Mean statistical deviation for the specific humidity analysis using the linear interpolation operator in LOG space.

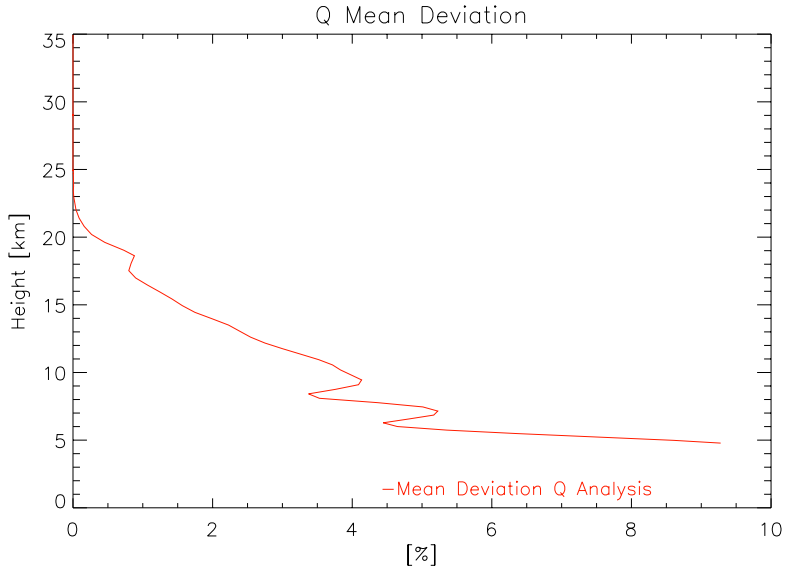

Mean statistical deviation for the specific humidity analysis using the cubic spline interpolation operator in LOG space.

Figure 6.11: Mean statistical deviations for TQP assimilation experiments for specific humidity linear vertical and cubic spline interpolation operator in LOG space using CHAMP data.

Scatter Plots for TQP Assimilation Experiments for Specific Humidity Linear and Cubic Spline Vertical Observation Interpolation Operator in LOG Space Using CHAMP Data

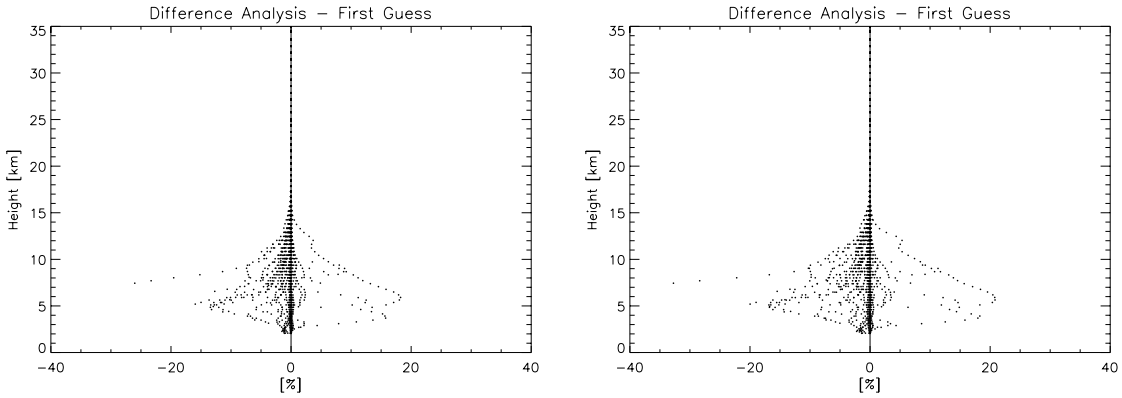

Linear interpolation in LOG space. Cubic spline interpolation in LOG space.

Figure 6.12: Scatter plots for TQP assimilation experiments for specific humidity linear vertical and cubic spline interpolation operator in LOG space using CHAMP data.

Plots for TQP Assimilation Surface Pressure Linear Vertical Observation Interpolation Operator in LOG Space

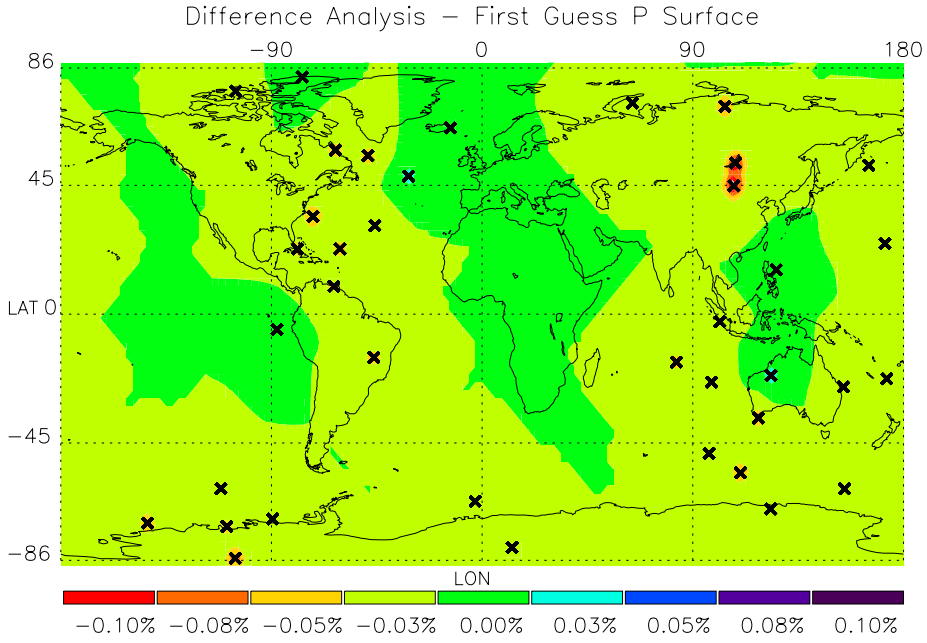

Linear interpolation in LOG space.

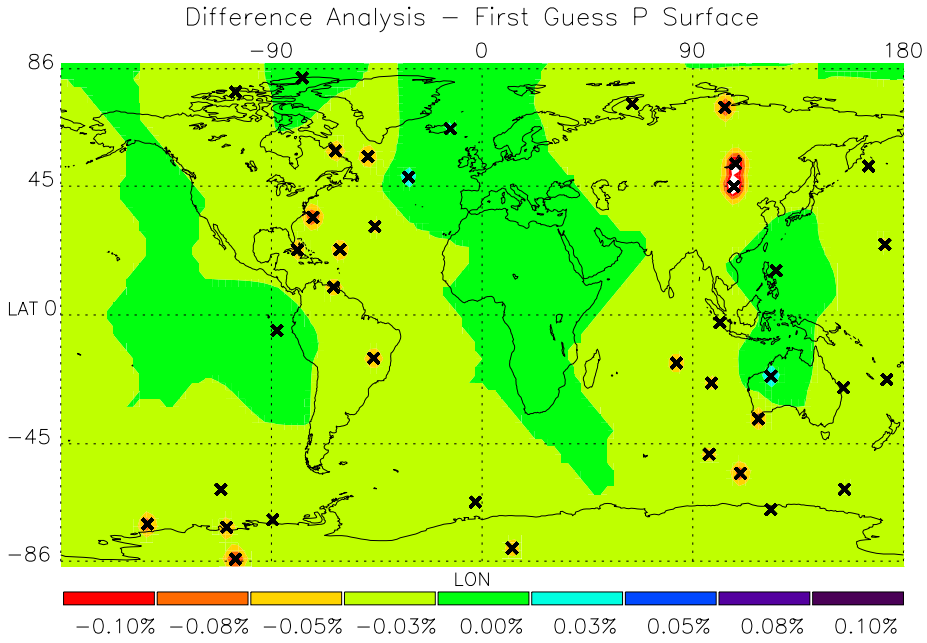

Cubic spline interpolation in LOG space.

Figure 6.13: Surface pressure plots for TQP assimilation experiments linear and cubic spline vertical interpolation operator in LOG space.

6.2 Corrected Runs ±3 Hour Assimilation Window Around 12 UTC Day 225 Year 2003

The same assimilation runs as in Section 6.1 were conducted, except that a 0.4% correction for the systematic deviation was applied to the observations prior to the assimilation.

6.2.1 Corrected Refractivity Assimilation

The result of the applied correction can be seen in Fig. 6.14, where the measurement deviation is even a little bit *over estimated* for this observation sample, and the analysis is virtually bias free now. This is also reflected in the slightly reduced mean deviation of the measurements, but leaving the mean analysis deviation nearly unchanged (Fig. 6.15). Within the scatter plots a significant change of the analysis increments occurs for the linear interpolation operator in *LOG* space. Comparing Figs. 6.16 and Figs. 6.19 it is immediate apparent, that especially below 5 km the increment is observably reduced in the bias corrected run.

6.2.2 Corrected Temperature, Specific Humidity, and Surface Pressure Assimilation

Corrected Temperature, Specific Humidity, and Surface Pressure Assimilation at Refractivity Level

The results are equivalent to the refractivity only assimilation runs and the same conclusions can be drawn (cf. Figs. 6.17, 6.18 and 6.19).

Corrected Temperature, Specific Humidity, and Surface Pressure Assimilation

Temperature There is no significant impact of the bias correction onto the temperature increments (compare Fig. 6.9, and Fig. 6.20), also the scatter plots are quasi identical (cf. Fig. 6.10, and Fig. 6.21)

Specific Humidity The comparison of Fig. 6.11 and Fig. 6.22 shows a slight reduction of the specific humidity increment below 5 km and a slight increase of the increment up to an altitude of 23 km within the bias corrected assimilation results. A tendency which is also visible in Fig. 6.12 and Fig. 6.21.

Surface Pressure The increment of the bias corrected analysis (Fig. 6.24) compared to the non corrected one (Fig. 6.13) is even smaller. Larger areas are not altered by the assimilation procedure at all.

Mean Bias of Corrected Refractivity Assimilation Experiments Linear and Cubic Spline Vertical Observation Interpolation Operator in LOG Space Using CHAMP Data

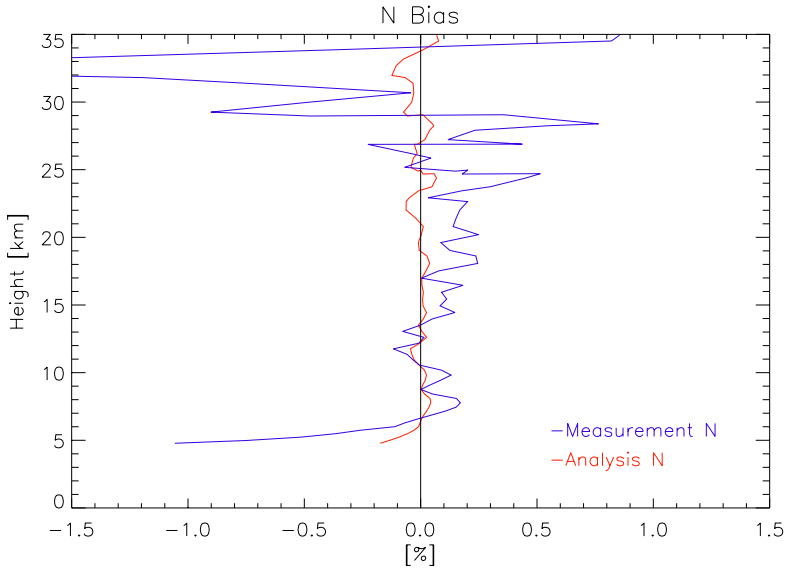

Mean bias of refractivity analysis and observations using the linear interpolation operator in LOG space.

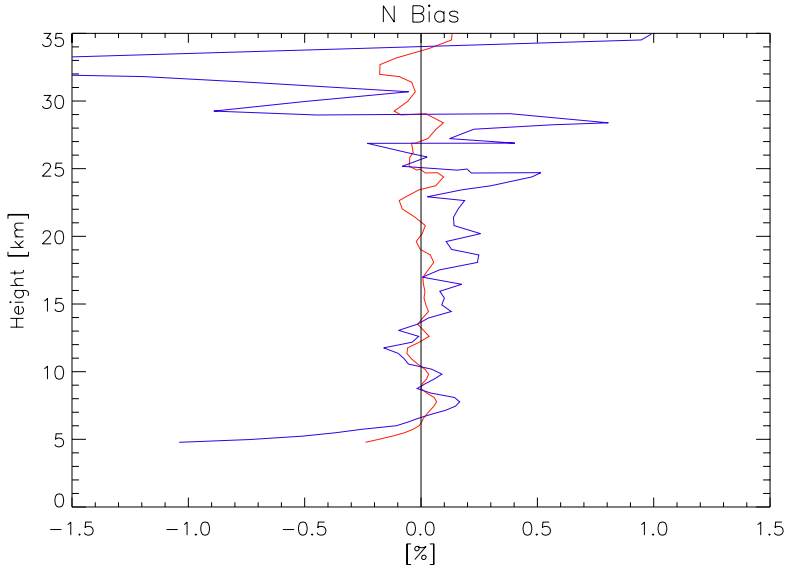

Mean bias of refractivity analysis and observations using the cubic spline interpolation operator in LOG space.

Figure 6.14: Mean bias of bias corrected refractivity assimilation experiments linear vertical and cubic spline interpolation operator in LOG space using CHAMP data.

Mean Statistical Deviation from First Guess for Corrected Refractivity Assimilation Experiments Linear and Cubic Spline Vertical Observation Interpolation Operator in LOG Space Using CHAMP Data

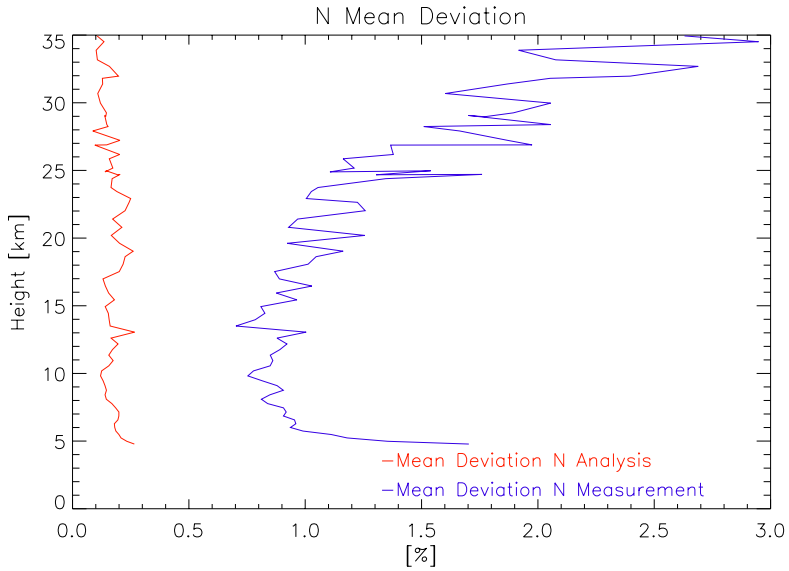

Mean Statistical deviations for the refractivity analysis and observations using the linear interpolation operator in LOG space.

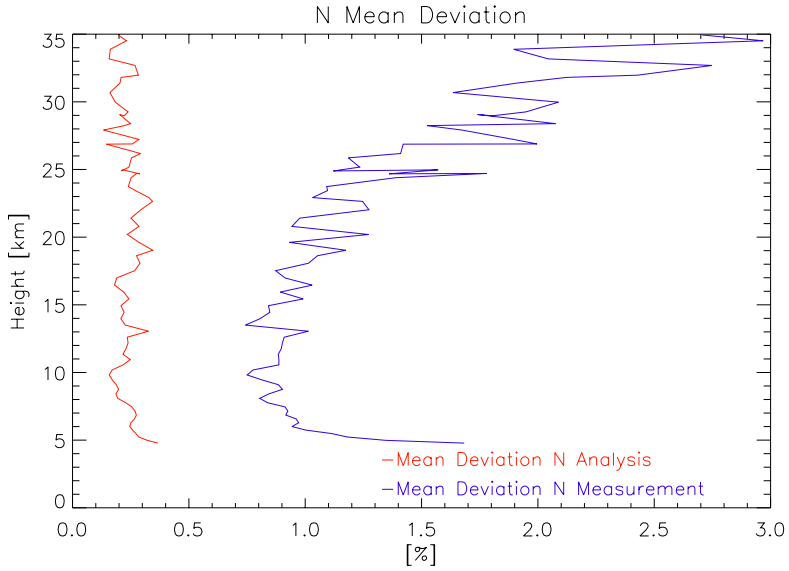

Mean statistical deviations for the refractivity analysis and observations using the cubic spline interpolation operator in LOG space.

Figure 6.15: Mean statistical deviations from first guess for bias corrected refractivity assimilation experiments linear vertical and cubic spline interpolation operator in LOG space using CHAMP data.

Scatter Plots for Corrected Refractivity Assimilation Experiments Linear and Cubic Spline Vertical Observation Interpolation Operator in LOG Space Using CHAMP Data

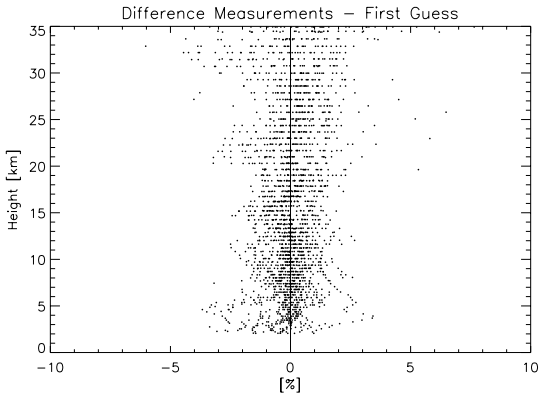

Linear interpolation in LOG space.

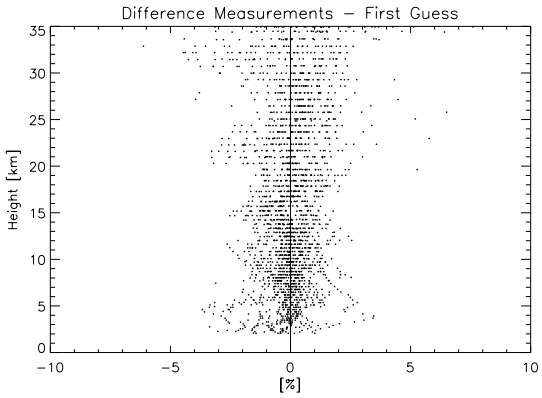

Cubic spline interpolation in LOG space.

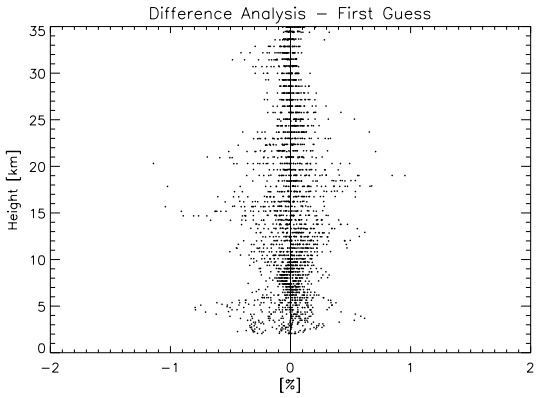

Linear interpolation in LOG space.

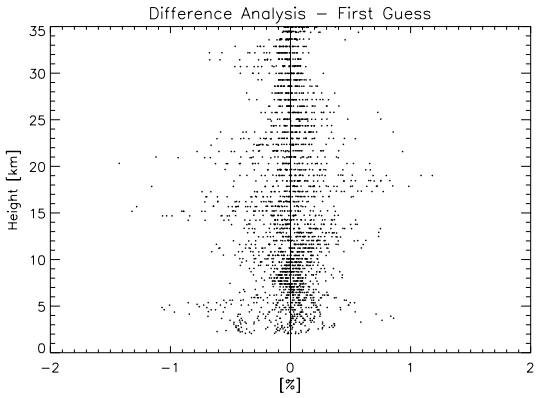

Cubic spline interpolation in LOG space.

Figure 6.16: Scatter plots for bias corrected refractivity assimilation experiments for linear vertical and cubic spline interpolation operator in LOG space using CHAMP data.

Summary As to be expected, the systematic measurement deviation is removed by the correction, which leaves the analysis virtually bias free. But a general correction of 0.4% is just a first step, but not appropriate for all observation samples (see for example Fig. 6.33, plots A and C). This problem has to be solved at retrieval level. The mean deviation of the measurements is slightly reduced, which has no significant impact onto the analysis increments at refractivity level. It is interesting, that the bias correction has nearly no impact onto the temperature analysis increments, but there is a slight increase of the increment within the specific humidity analyses and a slight decrease of the surface pressure increment (which is in general at a very low level).

Mean Bias of Corrected TQP Assimilation Experiments at Refractivity Level Linear and Cubic Spline Vertical Observation Interpolation Operator in LOG Space Using CHAMP Data

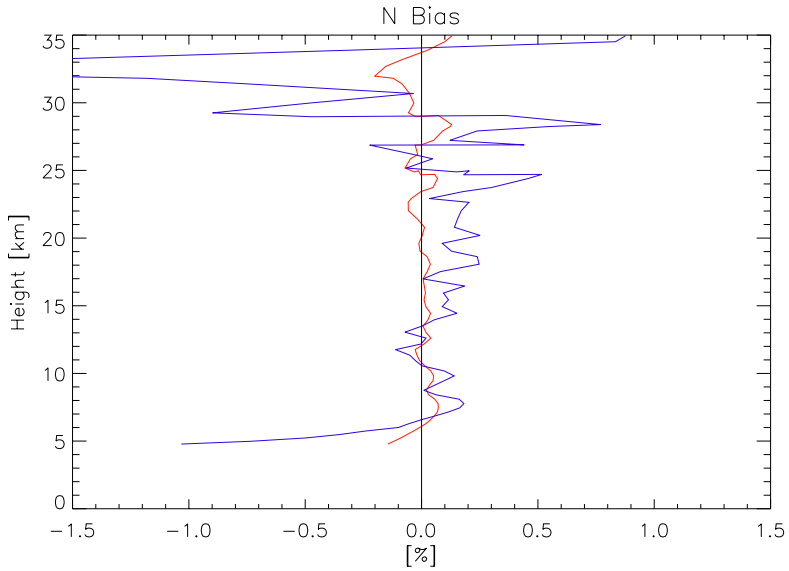

Mean bias of the refractivity and observations using the linear interpolation operator in LOG space.

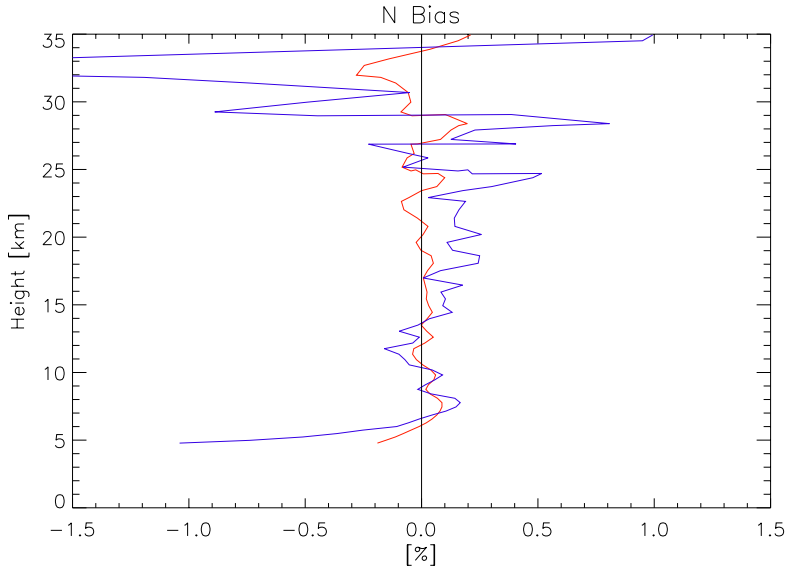

Mean bias of the refractivity and observations using the cubic spline interpolation operator in LOG space.

Figure 6.17: Mean bias of for for TQP assimilation experiments at refractivity level linear vertical and cubic spline interpolation operator in LOG space using CHAMP data.

Mean Statistical Deviation from First Guess for Corrected TQP Assimilation Experiments at Refractivity Level Linear and Cubic Spline Vertical Observation Interpolation Operator in LOG Space Using CHAMP Data

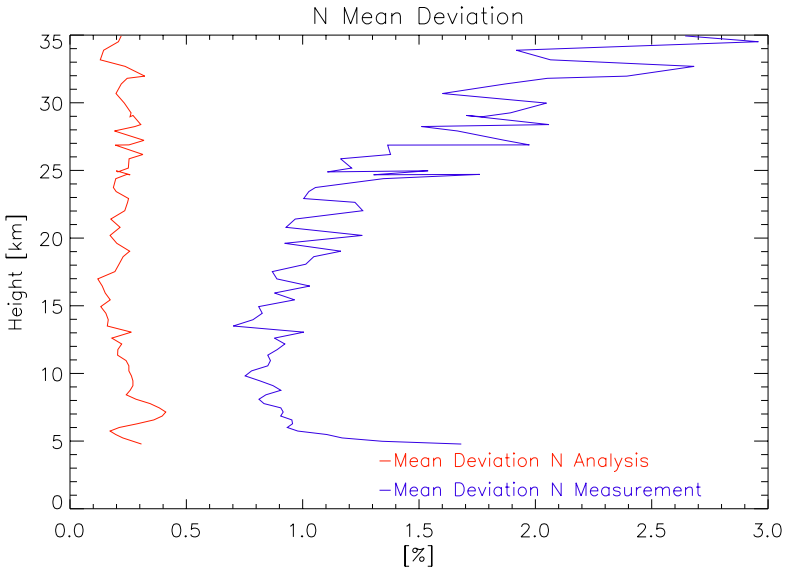

Mean statistical deviations for the refractivity and observations using the linear interpolation operator in LOG space.

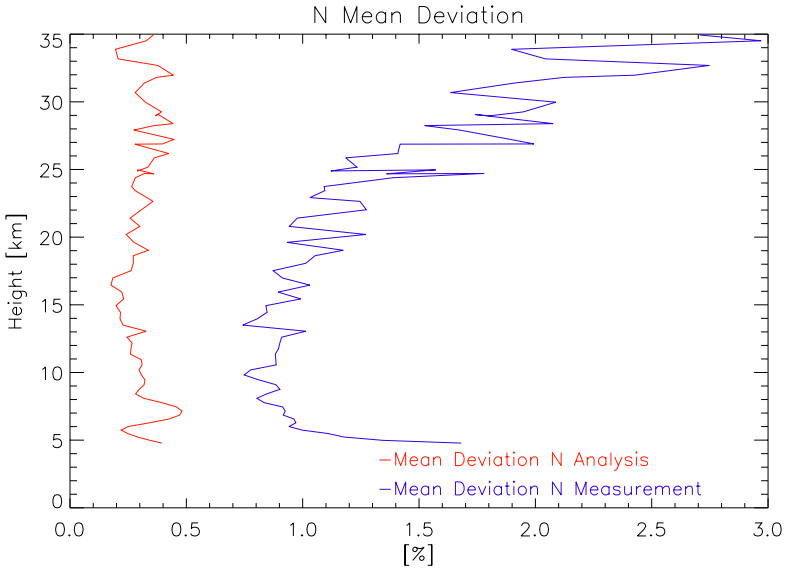

Mean statistical deviations for the refractivity and observations using the cubic spline interpolation operator in LOG space.

Figure 6.18: Mean statistical deviation from first guess for TQP assimilation experiments at refractivity level linear vertical and cubic spline interpolation operator in LOG space using CHAMP data.

Scatter Plots for Corrected TQP Assimilation Experiments at Refractivity Level Linear and Cubic Spline Vertical Observation Interpolation Operator in LOG Space Using CHAMP Data

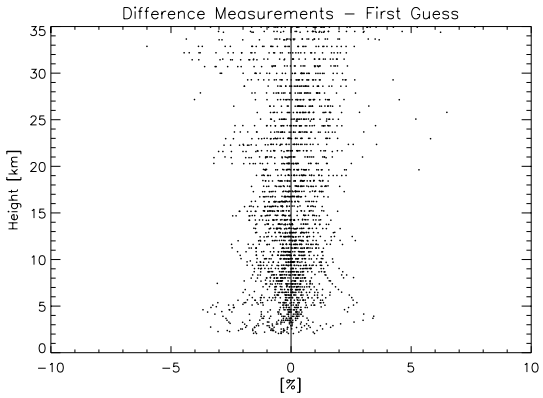

Linear interpolation in LOG space.

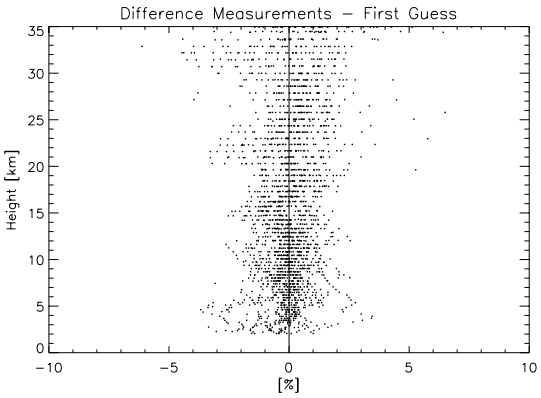

Cubic spline interpolation in LOG space.

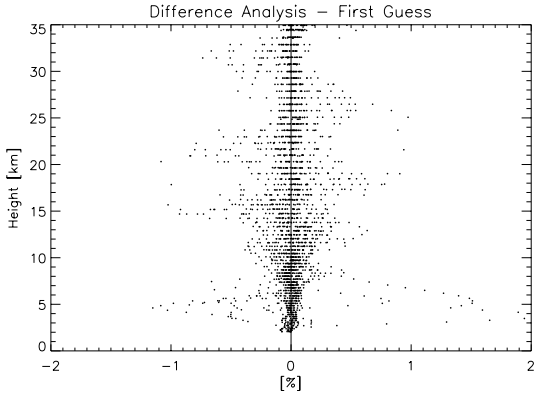

Linear interpolation in LOG space.

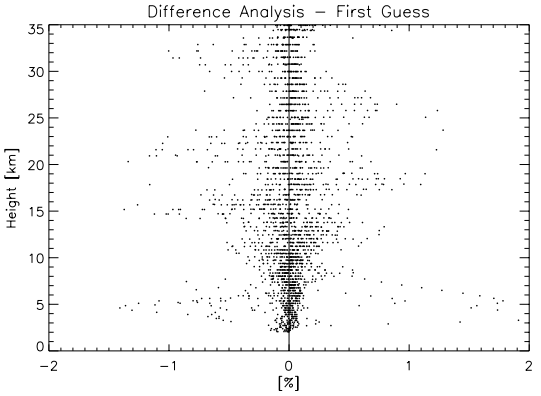

Cubic spline interpolation in LOG space.

Figure 6.19: Scatter plots for TQP assimilation experiments at refractivity level for linear vertical and cubic spline interpolation operator in LOG space using CHAMP data.

Mean Statistical Deviation for Corrected TQP Assimilation Experiments for Temperature Linear and Cubic Spline Vertical Observation Interpolation Operator in LOG Space Using CHAMP Data

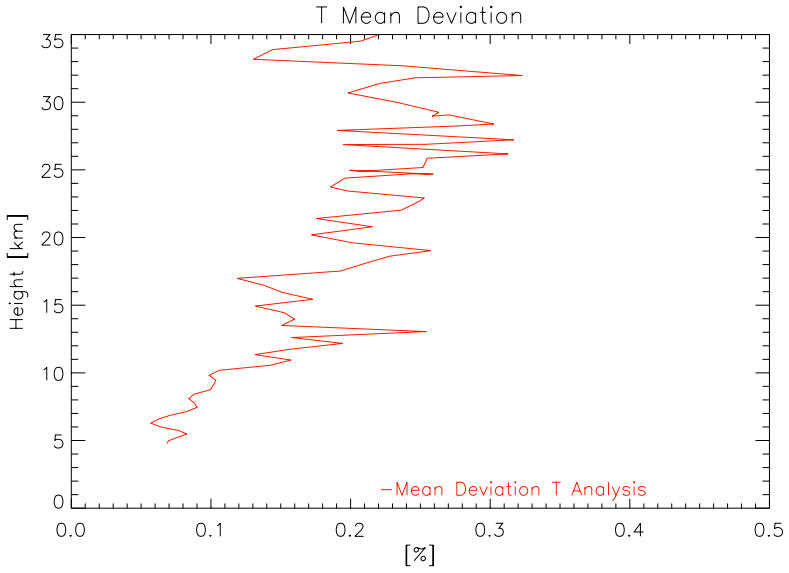

Mean statistical deviations for the temperature analysis using the linear interpolation operator in LOG space.

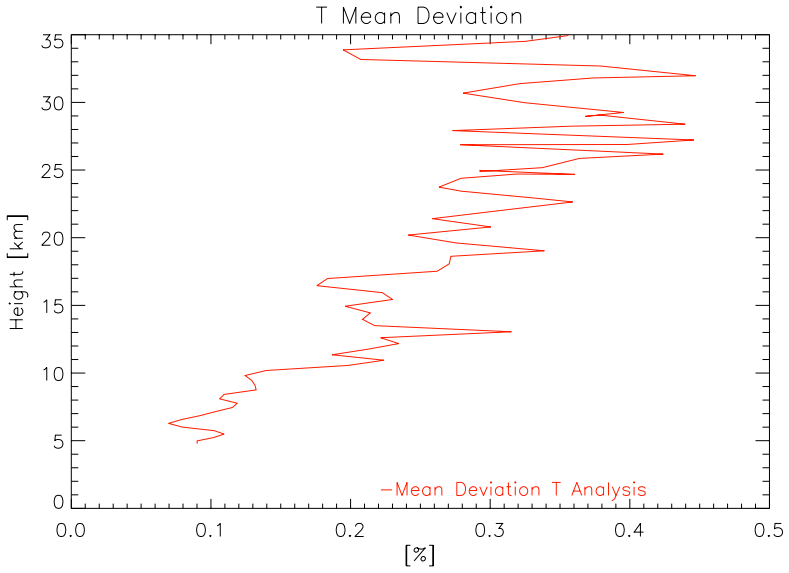

Mean statistical deviations for the temperature analysis using the cubic spline interpolation operator in LOG space.

Figure 6.20: Mean statistical deviation for TQP bias corrected assimilation experiments for temperature linear vertical and cubic spline interpolation operator in LOG space using CHAMP data.

Scatter Plots for Corrected TQP Assimilation Experiments for Temperature Linear and Cubic Spline Vertical Observation Interpolation Operator in LOG Space Using CHAMP Data

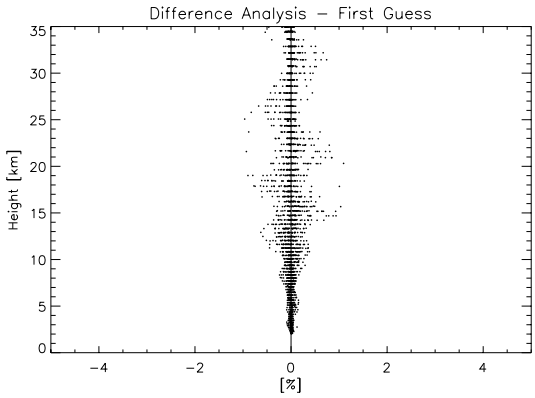

Linear interpolation in LOG space.

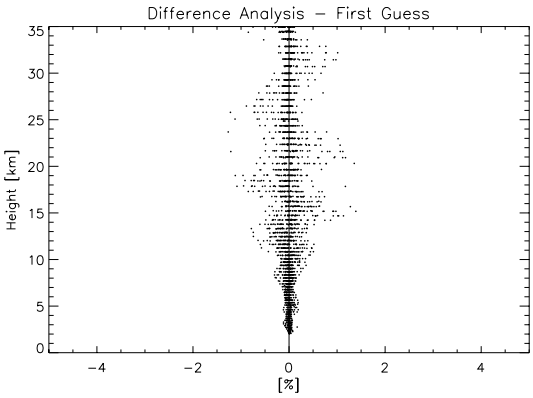

Cubic spline interpolation in LOG space.

Figure 6.21: Scatter plots for TQP bias corrected assimilation experiments for temperature linear vertical and cubic spline interpolation operator in LOG space using CHAMP data.

Mean Statistical Deviation for Corrected TQP Assimilation Experiments for Specific Humidity Linear and Cubic Spline Vertical Observation Interpolation Operator in LOG Space Using CHAMP Data

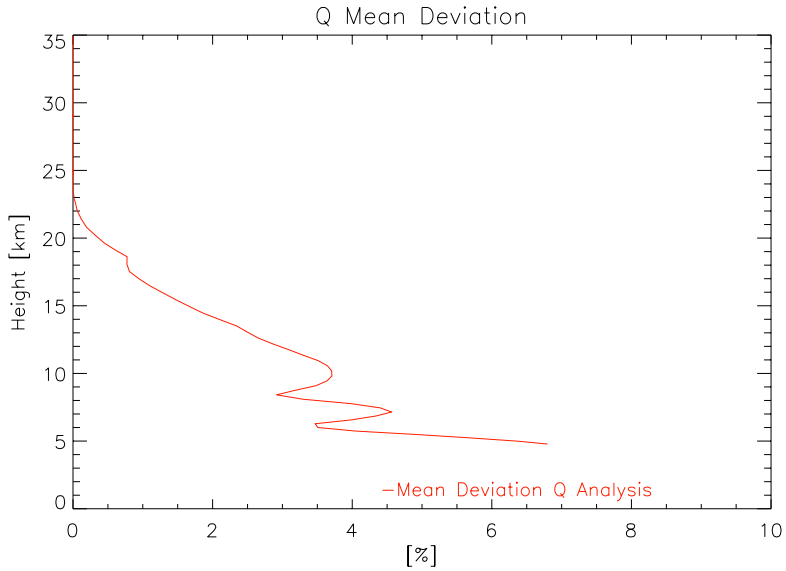

Mean statistical deviations for the specific humidity analysis using the linear interpolation operator in LOG space.

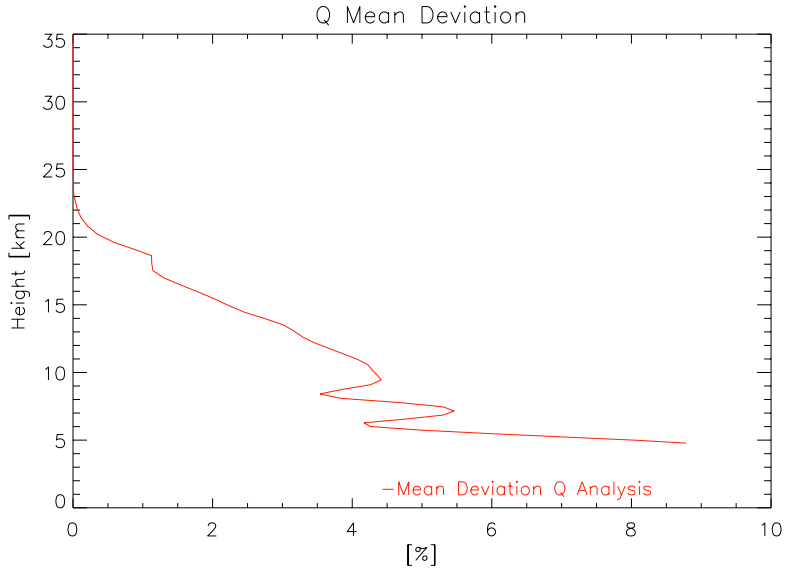

Mean statistical deviations for the specific humidity analysis using the cubic spline interpolation operator in LOG space.

Figure 6.22: Mean statistical deviation for TQP bias corrected assimilation experiments for specific humidity linear vertical and cubic spline interpolation operator in LOG space using CHAMP data.

Scatter Plots for Corrected Assimilation TQP Experiments for Specific Humidity Linear and Cubic Spline Vertical Observation Interpolation Operator in LOG Space Using CHAMP Data

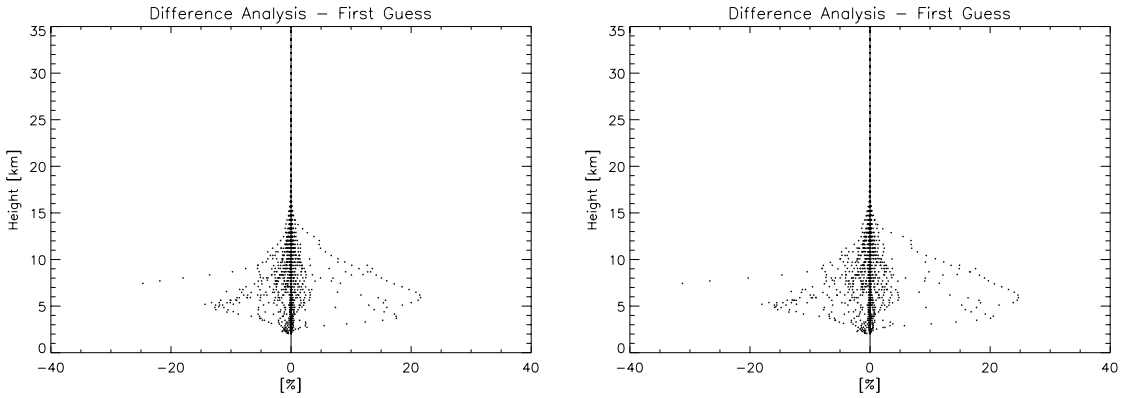

Linear interpolation in LOG space. Cubic spline interpolation in LOG space.

Figure 6.23: Scatter plots for TQP bias corrected assimilation experiments for specific humidity linear vertical and cubic spline interpolation operator in LOG space using CHAMP data.

Plots for Corrected TQP Assimilation Surface Pressure Linear Vertical Observation Interpolation Operator in LOG Space

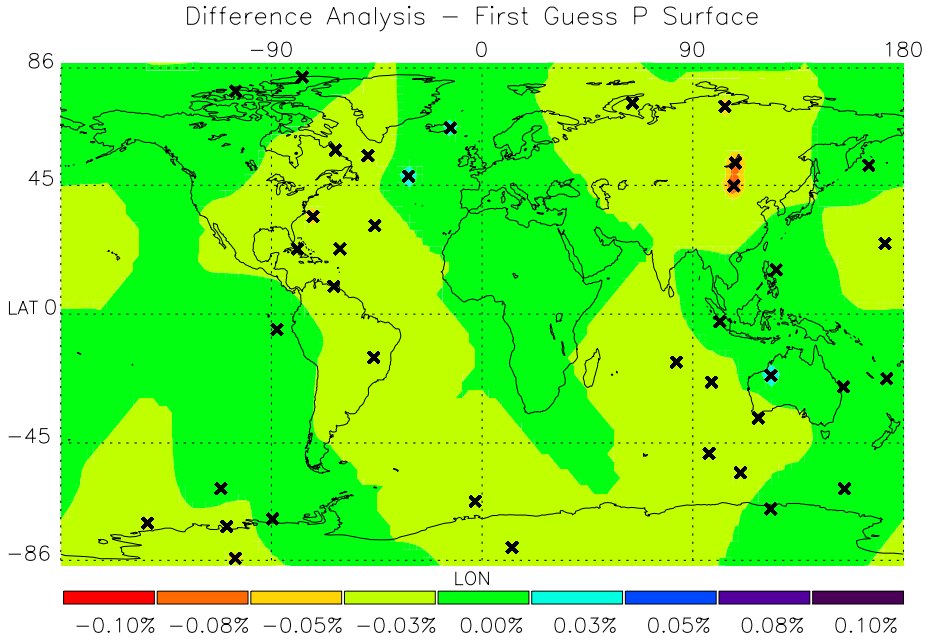

Linear interpolation in LOG space.

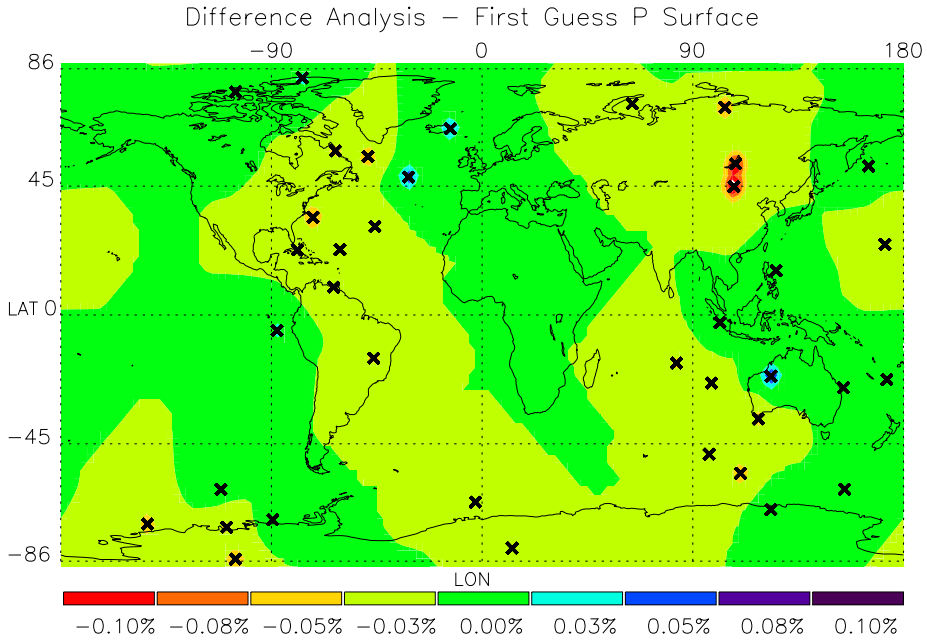

Cubic spline interpolation in LOG space.

Figure 6.24: Surface pressure plots for TQP bias corrected assimilation experiments linear and cubic spline vertical interpolation operator in LOG space.

6.3 Convergence Behavior of Real CHAMP Data

The convergence behavior of real CHAMP data is analyzed to derive some appropriate abort conditions during the minimization cycles, to enhance the computational feasibility. Compared to the raytraced observations (cf. Subsection 5.4.2), the real data seems to *converge* faster, which significantly reduces computational time. The conclusions drawn in Subsection 5.4.2 concerning the abort conditions have to be reconsidered.

6.3.1 Convergence Behavior of the Refractivity Assimilation Scheme

The convergence behavior for the refractivity assimilation is slightly different for the two interpolation operators (cf. Fig. 6.25). The scheme using cubic spline interpolation in the vertical dimension finds more new solutions, but at a level of very small increments, which is in general comparable to the results using raytraced observations (cf. Subsection 5.4.2). Performance considerations would suggest to stop the iteration cycle after 15 cost function and gradient evaluations, taking a conservative safety margin of 5 additional cost function and gradient evaluations into account we end up with a maximum of 20 simulations. This abort condition would apply for either interpolation schemes.

6.3.2 Convergence Behavior of the Temperature, Specific Humidity, and Surface Pressure Assimilation Scheme

In principle the same as was said in the refractivity only assimilation case applies. The number of new iterates is even bigger for the framework using the cubic spline interpolation operator, again like in the simulated case (cf. Subsection 5.4.2), but at a level of very small increments (cf. Fig. 6.26). A reasonable abort condition would be again to stop the iteration cycle after 15 cost function and gradient evaluations plus a safety margin of 5 simulations, which translates into approximately 5 to 6 new iterates.

6.4 Convergence Behavior of Corrected CHAMP Data

The convergence behavior is not influenced significantly by the correction. This applies for both, the refractivity only and the temperature, specific humidity, and surface pressure assimilation schemes for either interpolation operators (cf. Fig. 6.27 and Fig. 6.28). The same recommendation concerning the abort conditions as in Section 6.3 should be used.

Refractivity Assimilation Convergence Behavior for CHAMP Data (as is)

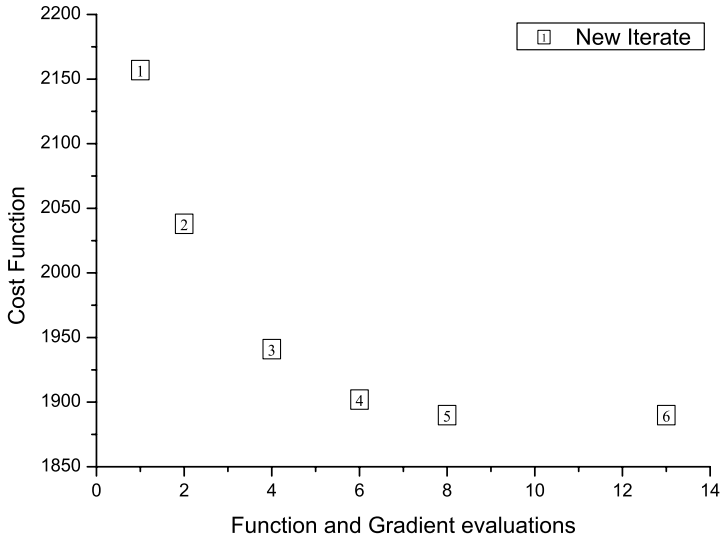

Convergence bahavior linear observation interpolation operator in LOG space.

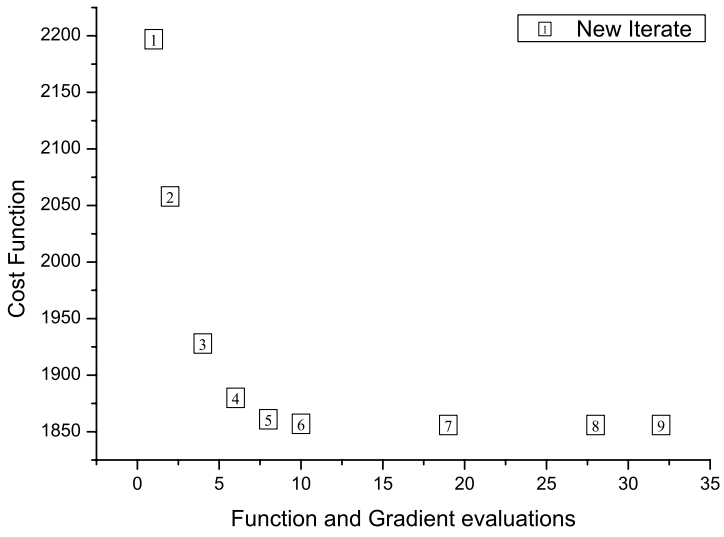

Convergence bahavior cubic spline observation interpolation operator in LOG space.

Figure 6.25: Convergence bahavior of refractivity assimilation experiment using real CHAMP data (no corrections).

Temperature, Specific Humidity, and Surface Pressure Assimilation Convergence Behavior for CHAMP data (as is)

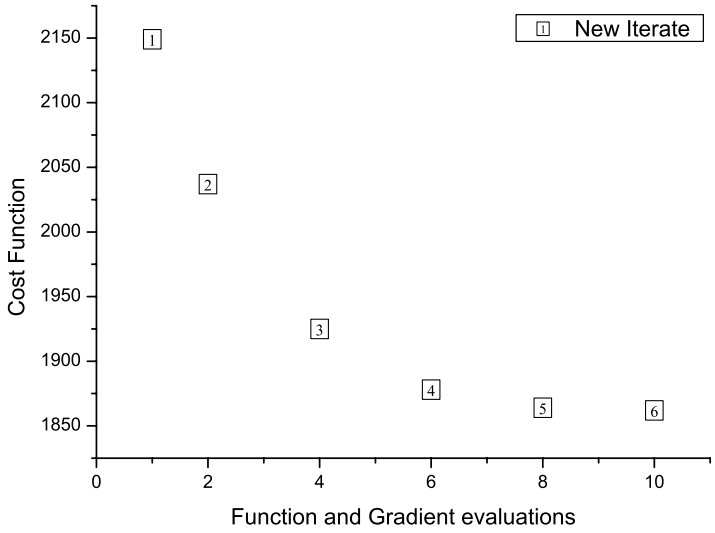

Convergence bahavior linear observation interpolation operator in LOG space.

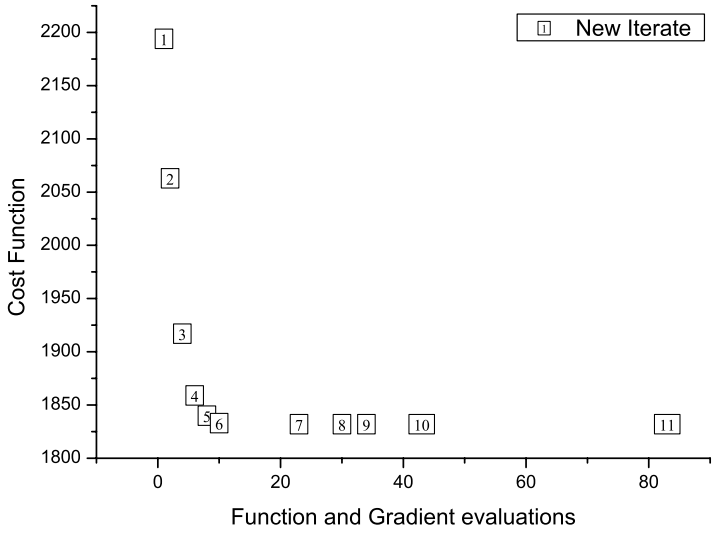

Convergence bahavior cubic spline observation interpolation operator in LOG space.

Figure 6.26: Convergence bahavior of temperature, specific humidity and surface pressure assimilation experiment using real CHAMP data (no corrections).

Refractivity Assimilation Convergence Behavior for CHAMP Data (corrected)

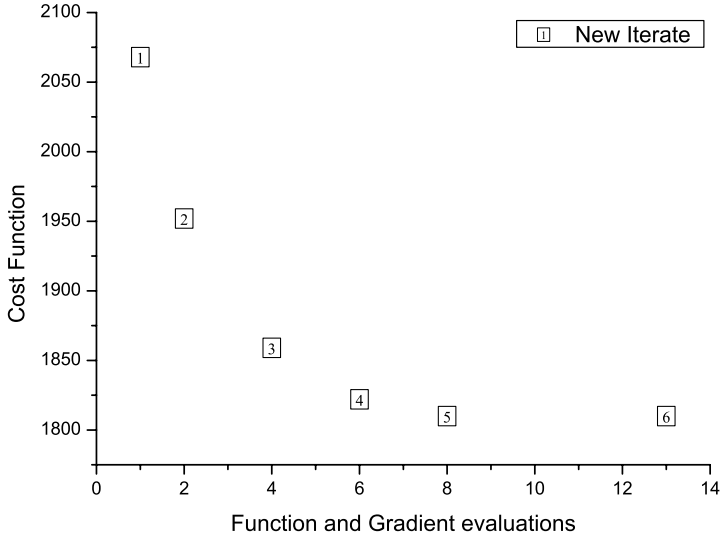

Convergence bahavior linear observation interpolation operator in LOG space.

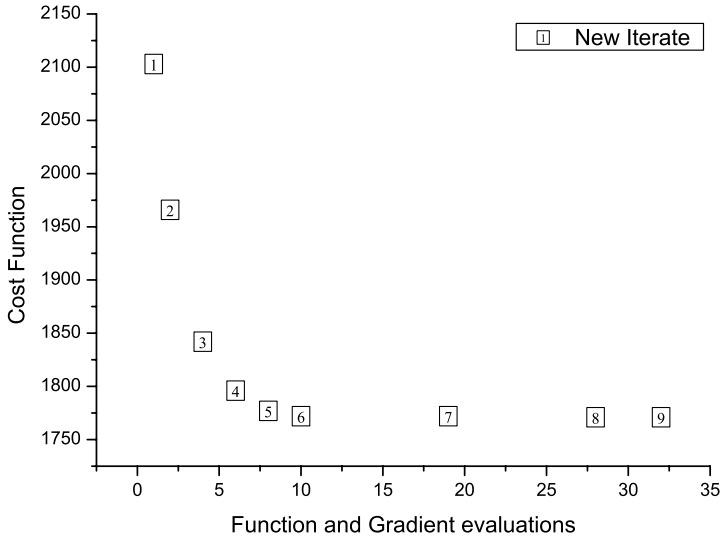

Convergence bahavior cubic spline observation interpolation operator in LOG space.

Figure 6.27: Convergence bahavior of refractivity assimilation experiment using real CHAMP data (bias corrected).

Temperature, Specific Humidity, and Surface Pressure Assimilation Convergence Behavior for CHAMP data (corrected)

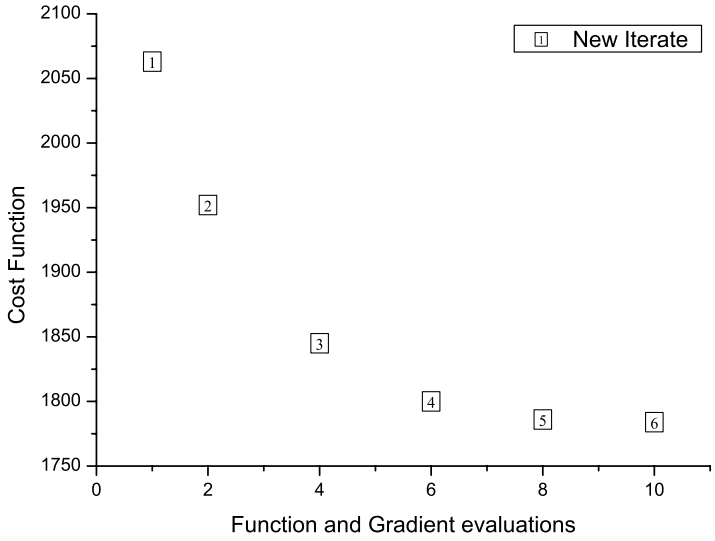

Convergence bahavior linear observation interpolation operator in LOG space.

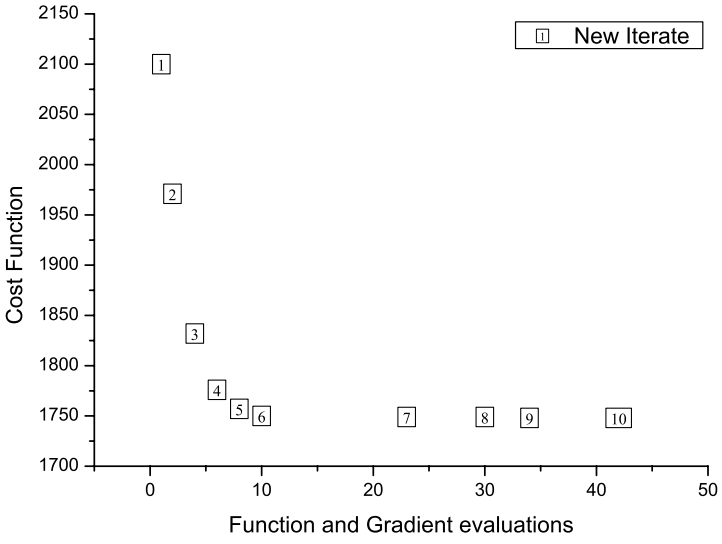

Convergence bahavior cubic spline observation interpolation operator in LOG space.

Figure 6.28: Convergence bahavior of temperature, specific humidity and surface pressure assimilarton experiment using real CHAMP dat (bias corrected).

6.5 Experiments Around 00, 06, 18, 00 UTC Day 225 and 226 Year 2003

For the following experiments corrected observations were used. Furthermore only the linear interpolation operator in *LOG* space was considered. Used error characteristics where the same as in Section 6.1. This setup could be considered as a first quasi operational version of the assimilation scheme.

6.5.1 Experiments ± 3 Hour Assimilation Window Around 00 UTC Day 225 Year 2003

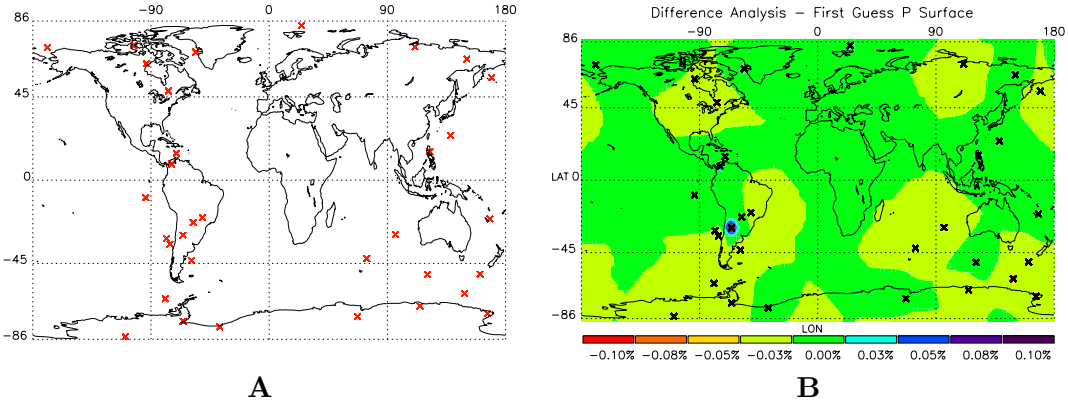

Figure 6.29: Plot A depicts the global distribution of RO profiles, plot B the analysis increments of the surface pressure.

- Plot **A** Fig. 6.30: Refractivity assimilation N mean bias analysis (red), observations (blue); Fig. 6.31: Refractivity assimilation observations - first guess N
- Plot **B** Fig. 6.30: Refractivity assimilation N mean statistical deviation; Fig. 6.31: Refractivity assimilation analysis - first guess N
- Plot **C** Fig. 6.30: TQP assimilation N mean bias analysis (red), observations (blue); Fig. 6.31: TQP assimilation observation - first guess N
- Plot **D** Fig. 6.30: TQP assimilation N mean statistical deviation; Fig. 6.31: TQP assimilation analysis - first guess N
- Plot **E** Fig. 6.30: TQP assimilation T mean statistical deviation analysis; Fig. 6.31: TQP assimilation analysis - first guess T
- Plot **F** Fig. 6.30: TQP assimilation Q mean statistical deviation analysis; Fig. 6.31: TQP assimilation analysis - first guess Q

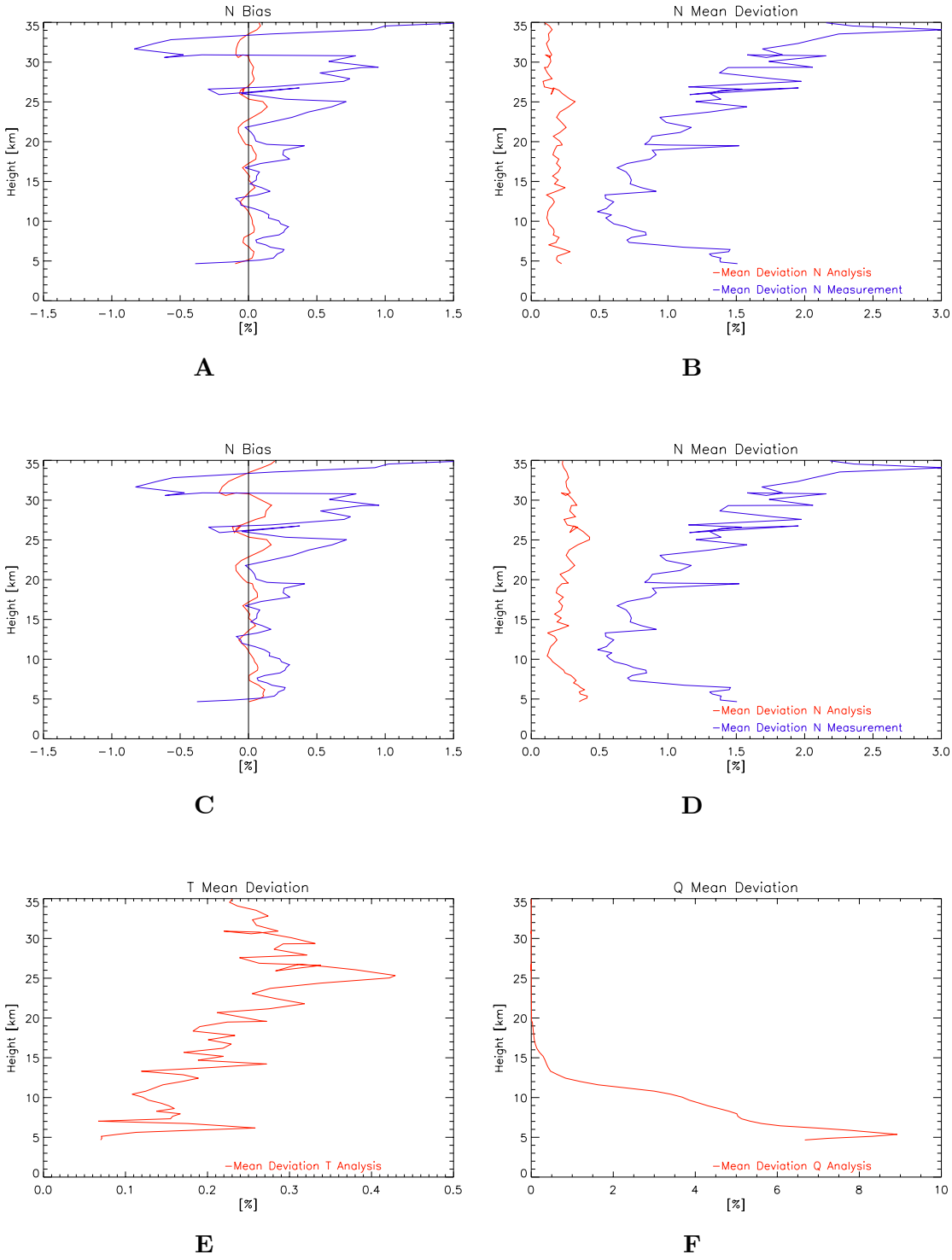

Figure 6.30: Mean bias and mean statistical deviation plots, day 225 00 UTC 2003.

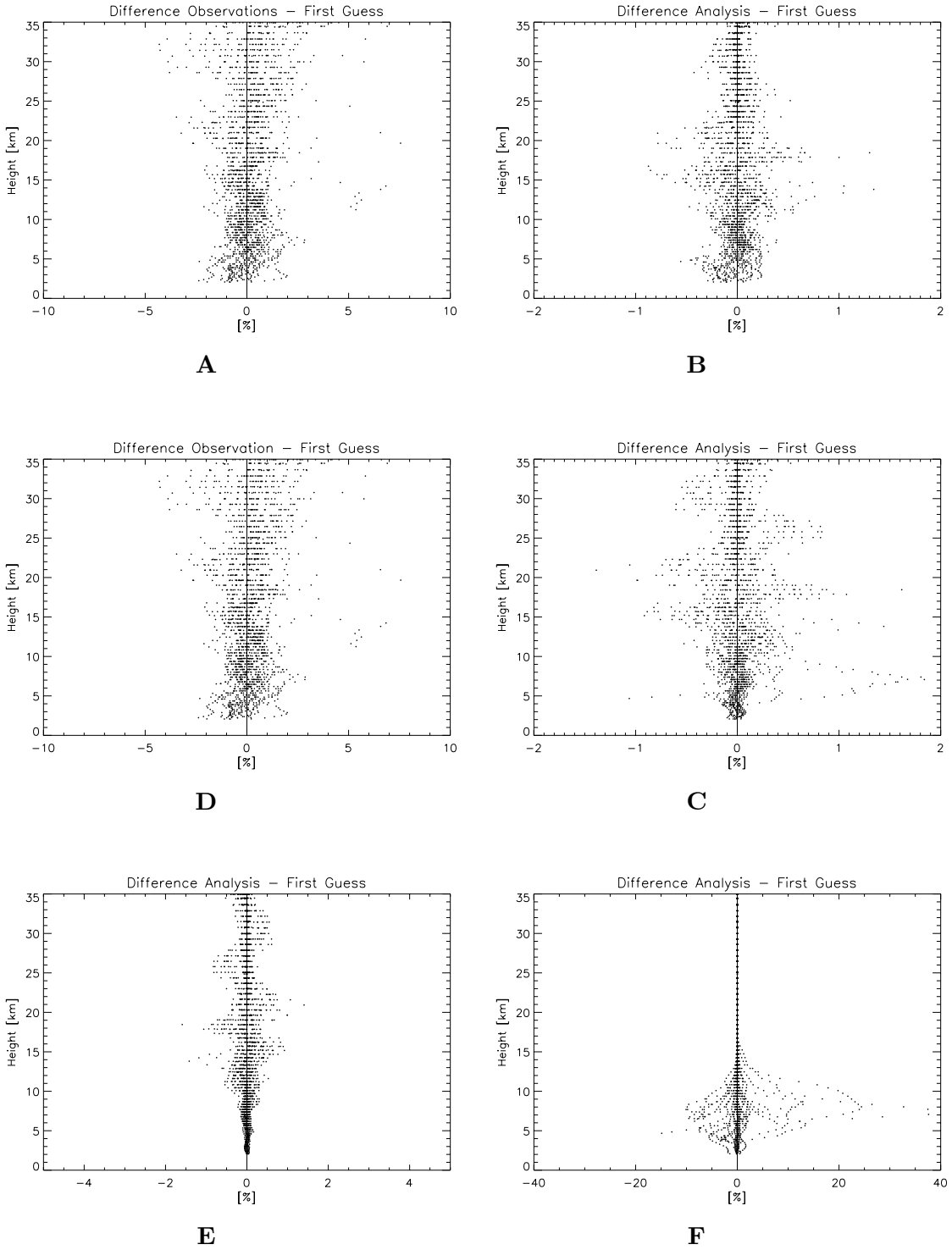

Figure 6.31: Scatter plots for N and TQP assimilation schemes, day 225 00 UTC 2003.

6.5.2 Experiments ±3 Hour Assimilation Window Around 06 UTC Day 225 Year 2003

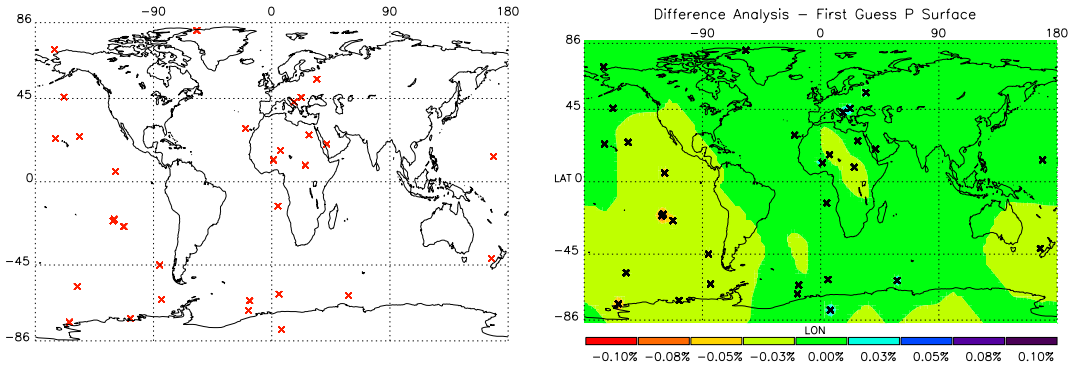

Figure 6.32: Plot A depicts the global distribution of RO profiles, plot B the analysis increments of the surface pressure.

- Plot **A** Fig. 6.33: Refractivity assimilation N mean bias analysis (red), observations (blue); Fig. 6.34: Refractivity assimilation observations - first guess N

- Plot **B** Fig. 6.33: Refractivity assimilation N mean statistical deviation; Fig. 6.34: Refractivity assimilation analysis - first guess N

- Plot **C** Fig. 6.33: TQP assimilation N mean bias analysis (red), observations (blue); Fig. 6.34: TQP assimilation observation - first guess N

- Plot **D** Fig. 6.33: TQP assimilation N mean statistical deviation; Fig. 6.34: TQP assimilation analysis - first guess N

- Plot **E** Fig. 6.33: TQP assimilation T mean statistical deviation analysis; Fig. 6.34: TQP assimilation analysis - first guess T

- Plot **F** Fig. 6.33: TQP assimilation Q mean statistical deviation analysis; Fig. 6.34: TQP assimilation analysis - first guess Q

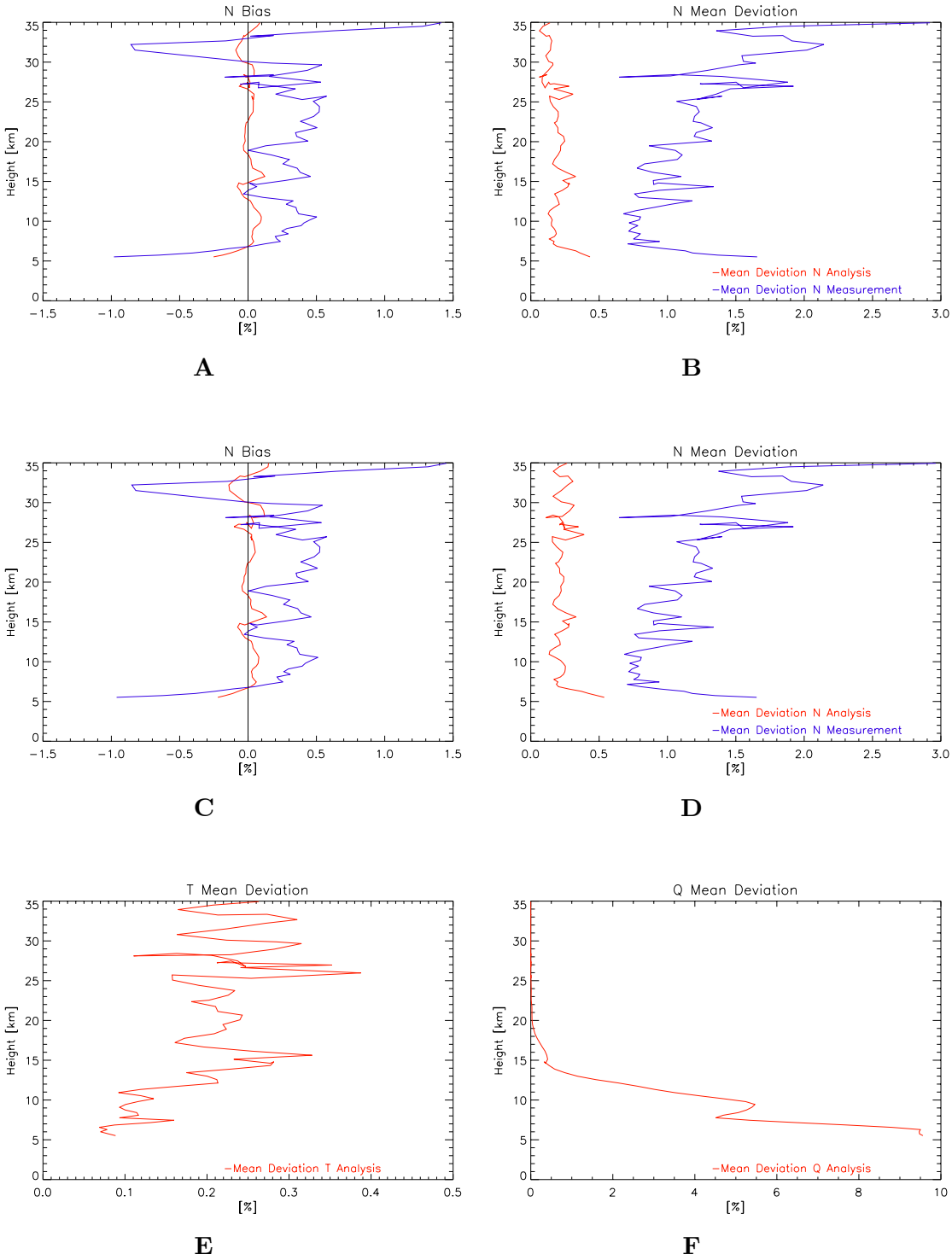

Figure 6.33: Mean bias and mean statistical deviation plots, day 225 06 UTC 2003.

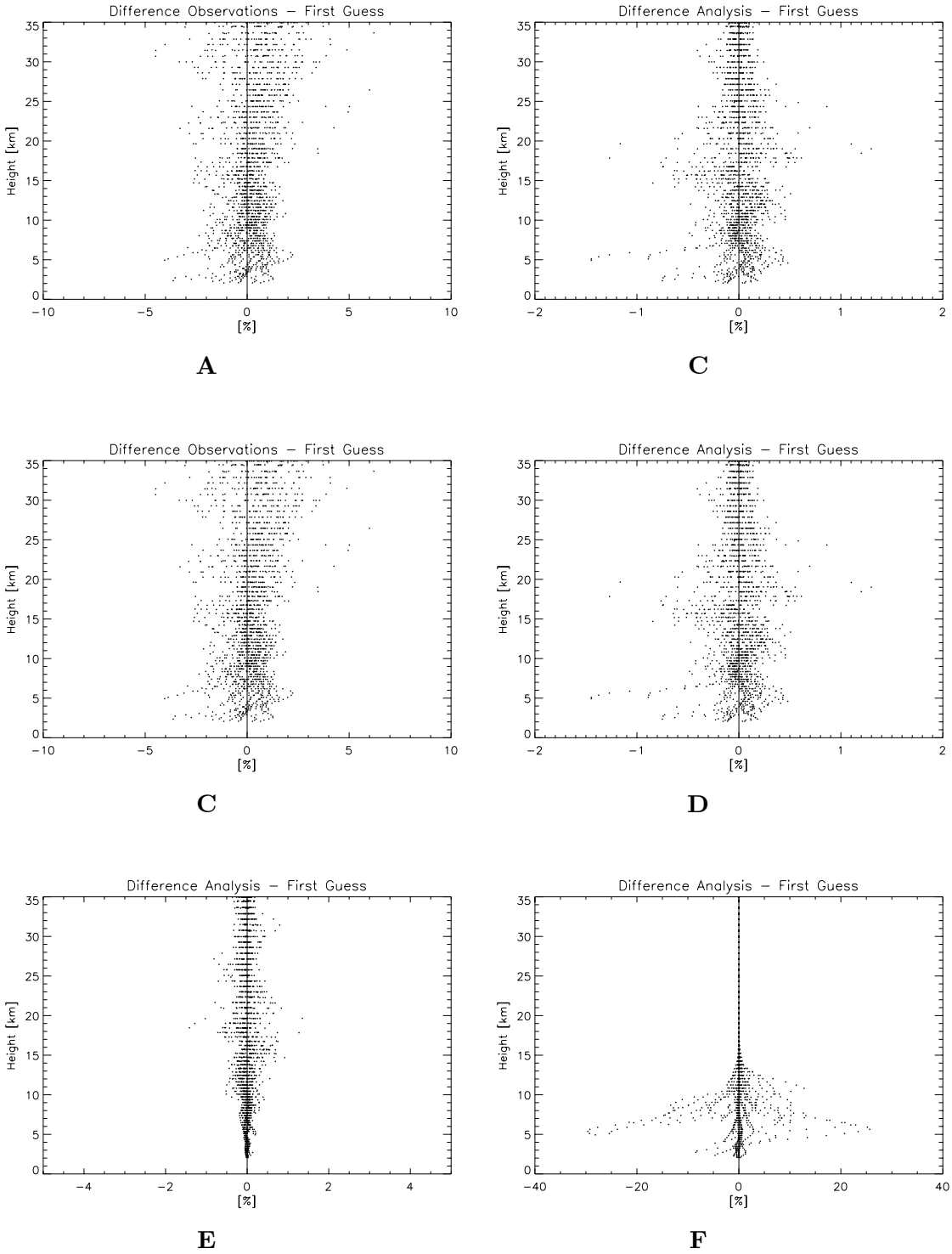

Figure 6.34: Scatter plots for N and TQP assimilation schemes, day 225 06 UTC 2003.

6.5.3 Experiments ±3 Hour Assimilation Window Around 18 UTC Day 225 Year 2003

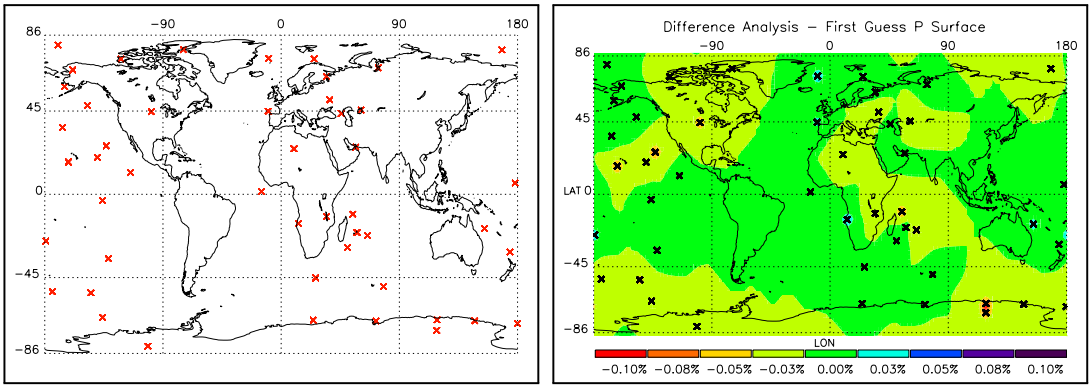

Figure 6.35: Plot A depicts the global distribution of RO profiles, plot B the analysis increments of the surface pressure.

- Plot **A** Fig. 6.36: Refractivity assimilation N mean bias analysis (red), observations (blue); Fig. 6.37: Refractivity assimilation observations - first guess N

- Plot **B** Fig. 6.36: Refractivity assimilation N mean statistical deviation; Fig. 6.37: Refractivity assimilation analysis - first guess N

- Plot **C** Fig. 6.36: TQP assimilation N mean bias analysis (red), observations (blue); Fig. 6.37: TQP assimilation observation - first guess N

- Plot **D** Fig. 6.36: TQP assimilation N mean statistical deviation; Fig. 6.37: TQP assimilation analysis - first guess N

- Plot **E** Fig. 6.36: TQP assimilation T mean statistical deviation analysis; Fig. 6.37: TQP assimilation analysis - first guess T

- Plot **F** Fig. 6.36: TQP assimilation Q mean statistical deviation analysis; Fig. 6.37: TQP assimilation analysis - first guess Q

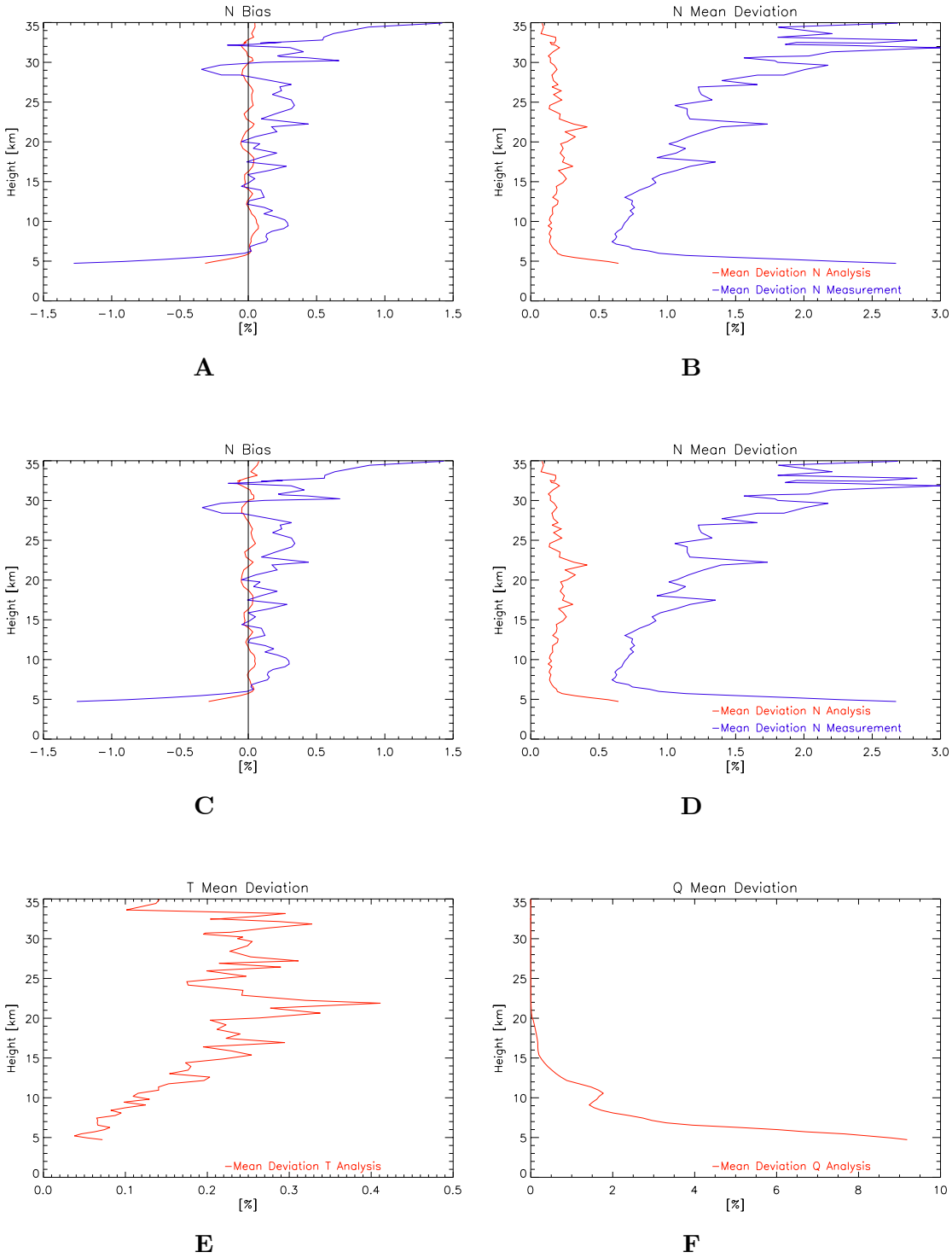

Figure 6.36: Mean bias and mean statistical deviation plots, day 225 18 UTC 2003.

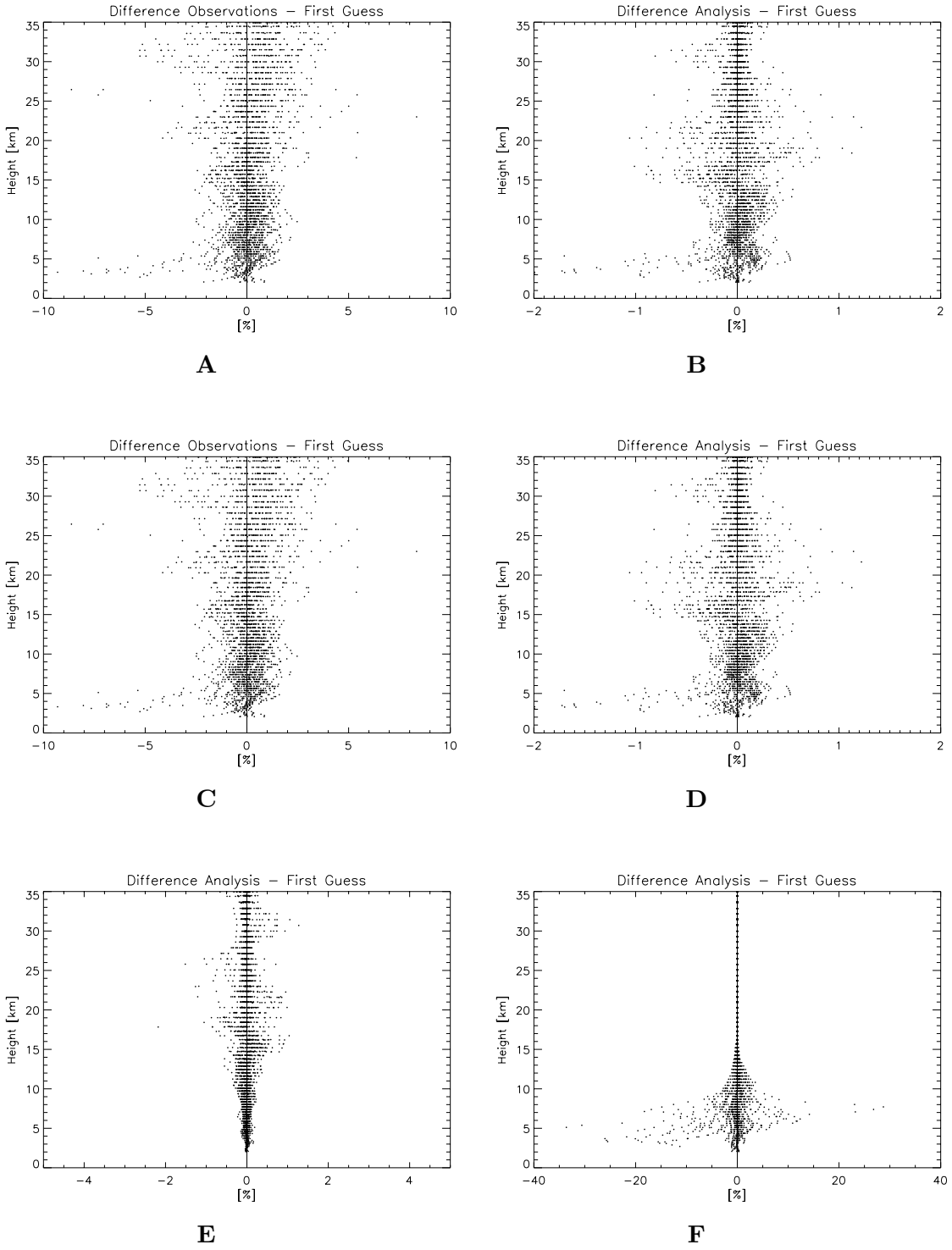

Figure 6.37: Scatter plots for N and TQP assimilation schemes, day 225 18 UTC 2003.

6.5.4 Experiments ± 3 Hour Assimilation Window Around 00 UTC Day 226 Year 2003

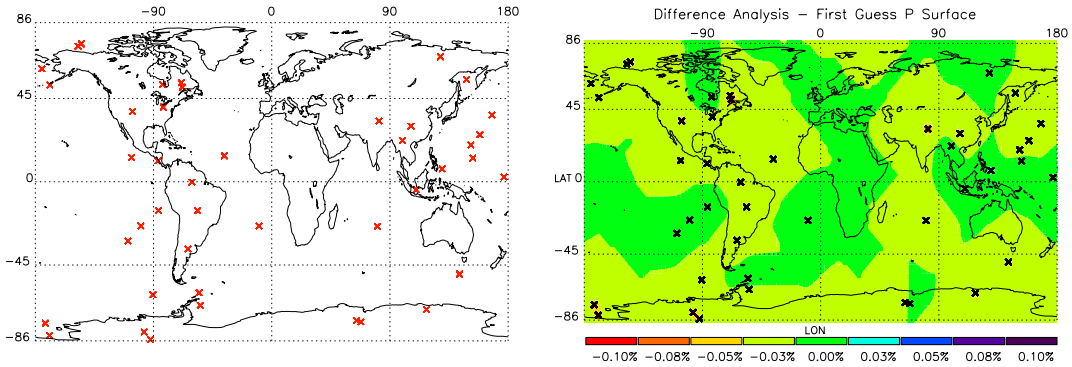

Figure 6.38: Plot A depicts the global distribution of RO profiles, plot B the analysis increments of the surface pressure.

- Plot **A** Fig. 6.39: Refractivity assimilation N mean bias analysis (red), observations (blue); Fig. 6.40: Refractivity assimilation observations - first guess N

- Plot **B** Fig. 6.39: Refractivity assimilation N mean statistical deviation; Fig. 6.40: Refractivity assimilation analysis - first guess N

- Plot **C** Fig. 6.39: TQP assimilation N mean bias analysis (red), observations (blue); Fig. 6.40: TQP assimilation observation - first guess N

- Plot **D** Fig. 6.39: TQP assimilation N mean statistical deviation; Fig. 6.40: TQP assimilation analysis - first guess N

- Plot **E** Fig. 6.39: TQP assimilation T mean statistical deviation analysis; Fig. 6.40: TQP assimilation analysis - first guess T

- Plot **F** Fig. 6.39: TQP assimilation Q mean statistical deviation analysis; Fig. 6.40: TQP assimilation analysis - first guess Q

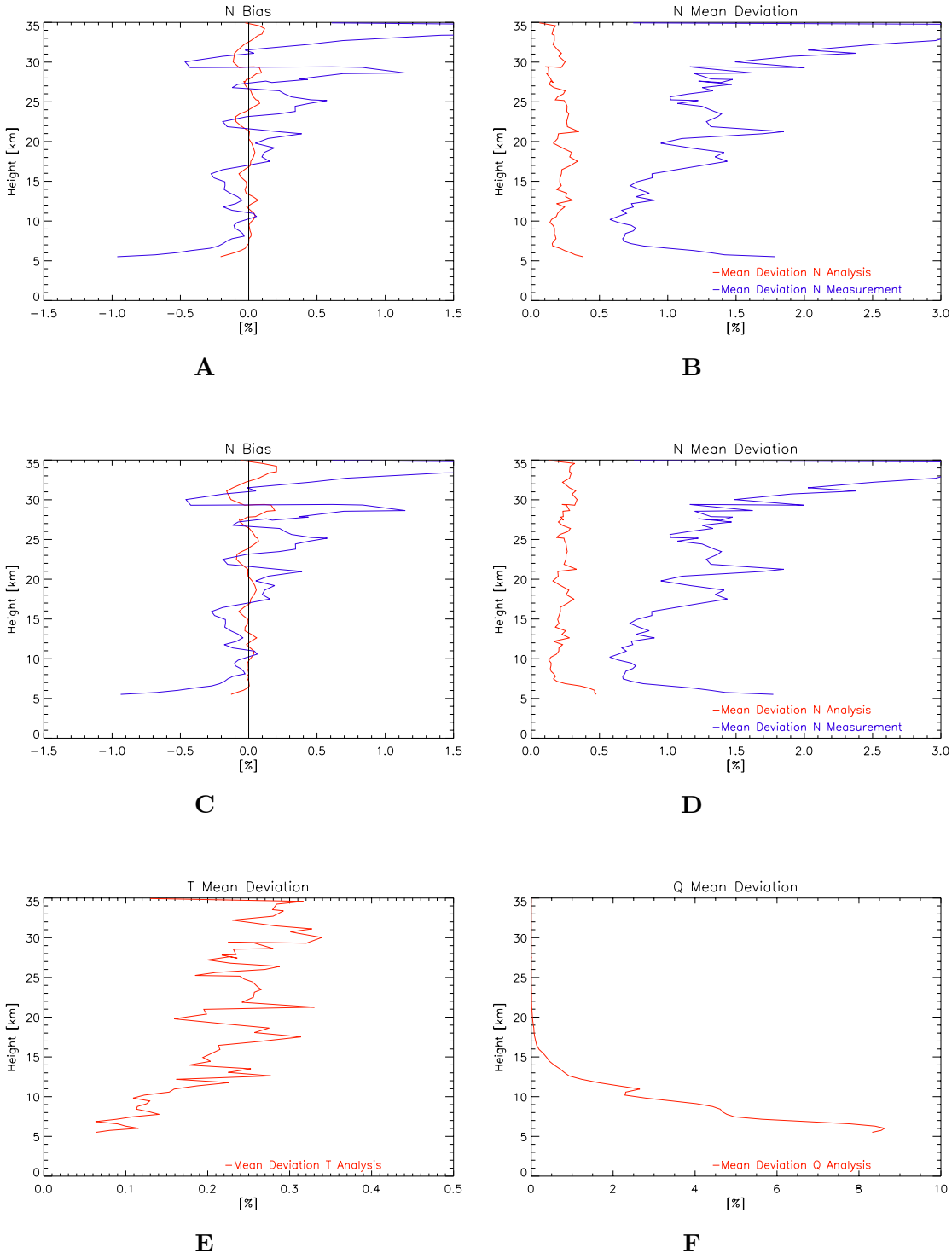

Figure 6.39: Mean bias and mean statistical deviation plots, day 226 00 UTC 2003.

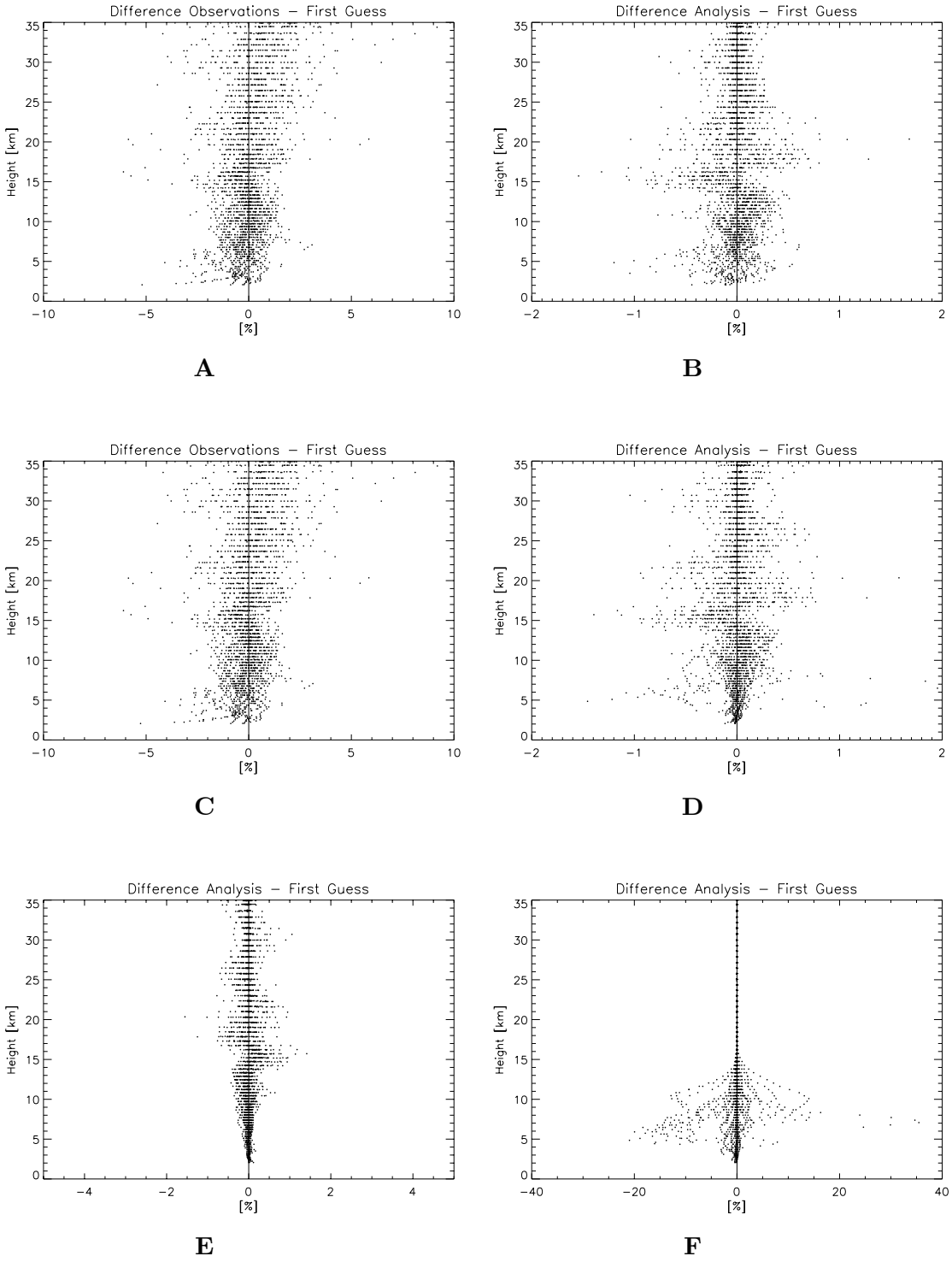

Figure 6.40: Scatter plots for N and TQP assimilation schemes, day 226 00 UTC 2003.

6.6 Observation Statistics

UTC	Profiles	Observations	Profiles Assim.	Observations Assim.
00	40	18157	33	2011
06	38	16958	31	1807
12	44	21591	38	2278
18	55	24523	48	2939
00	54	23421	43	2503

Table 6.1: Observation statistics for the 24 hour test case day 225 year 2003.

Tab. 6.1 shows the number of observations in detail. The test cases were effectively five 6 hour time windows around the ECMWF analysis times 00, 06, 12, 18 and 00 UTC. This means that the first six hour window already starts on day 224 at 21:00 (for the 00 UTC time layer) and the last six hour window ends on day 226 03:00 (for the consecutive 00 UTC time layer of day 226). The difference between profiles and profiles assimilated stems from the rejection of profiles flagged as suspicious (different codes indicate the possible problem during the retrieval). Observations assimilated indicates the number of single observations entering the analysis after the rejection of suspicious data and the data thinning procedure (cf. Section 5.2.1) and possible rejection due to problems with the orography. In total 193 profiles containing 11538 single observations were processed.

6.7 Convergence Statistics

Assimilation Window	Mode	Iterations	Simulations	Abort Criteria
Day 225 00 UTC	N	6	50	5
	TQP	14	97	5
Day 225 06 UTC	N	14	94	4
	TQP	15	96	5
Day 225 12 UTC	N	6	53	5
	TQP	6	50	5
Day 225 18 UTC	N	14	94	4
	TQP	12	100	5
Day 226 00 UTC	N	14	101	4
	TQP	9	71	5

Table 6.2: Convergence bahavior of test assimilation windows.

In Tab. 6.2 the convergence behavior of all runs (corrected, linear interpolation operator in *LOG* space) is shown, were in the column *aboard criteria* the number of iteration after 15 cost function and gradient evaluations are shown. The general abort criteria was 101 cost function and gradient evaluations. This criteria was only once reached, the minimization cycle was mostly aborted by an intrinsic condition, which stops the iteration after 20 cost function and gradient evaluations without finding a new iterate. This can be

caused by errors in cost function or gradient evaluation, or if rounding errors dominate the computation. A close look at the cost function reductions confirms the assumption of Section 6.3. These results are somewhat dependent on the dimensions of the background grid and the number of observations, the conclusions concerning the convergence behavior, drawn here are only valid for similar assimilation setups.

6.8 Assimilation Results for August 2003

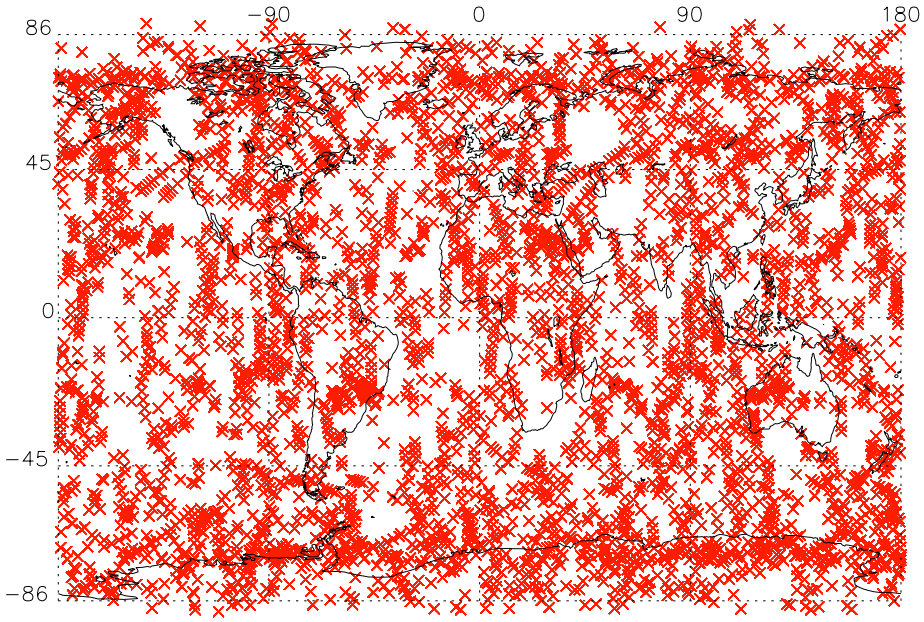

Figure 6.41: Geolocation of 4482 occultation profiles used within the assimilation experiment covering August 2003.

For this quasi operational run, every day of August 2003, divided into four assimilation windows of 6 hours was processed. This translates in total into 31 independent time slices, around 00, 06 12 and 18 UTC, delivering 124 analyses. The global distribution of the 4482 CHAMP RO profiles is depicted in Fig. 6.41, which translate in 245220 single observations. As lower cut off height 5 km was chosen as the previous results suggest. The data quality degrades below 5 km rapidly which can be seen in many plots of the previous Section. The problem has to be solved at retrieval level (wave optics methods, see conclusions), to be able to effectively use observations below 5 km. The analysis fields were averaged separately for every time layer and in addition a total monthly mean was derived by averaging the time layer means. These averaged fields were compared with the corresponding monthly mean analysis of ECMWF. This procedure was applied for the refractivity and the temperature, specific humidity, and surface pressure assimilation schemes. The minimization process was stopped after 20 cost function and gradient evaluation, leaving some safety margin (cf. Section 6.7), which means that about 5 to 6 successful iterations were conducted for every assimilation time window.

6.8.1 Refractivity Assimilation Results for August 2003

For this quasi operational assimilation run the refractivity only assimilation scheme was used on a beowulf cluster, processing 12 time layers in parallel.

Refractivity Assimilation Increments for August 2003 Model Level 21

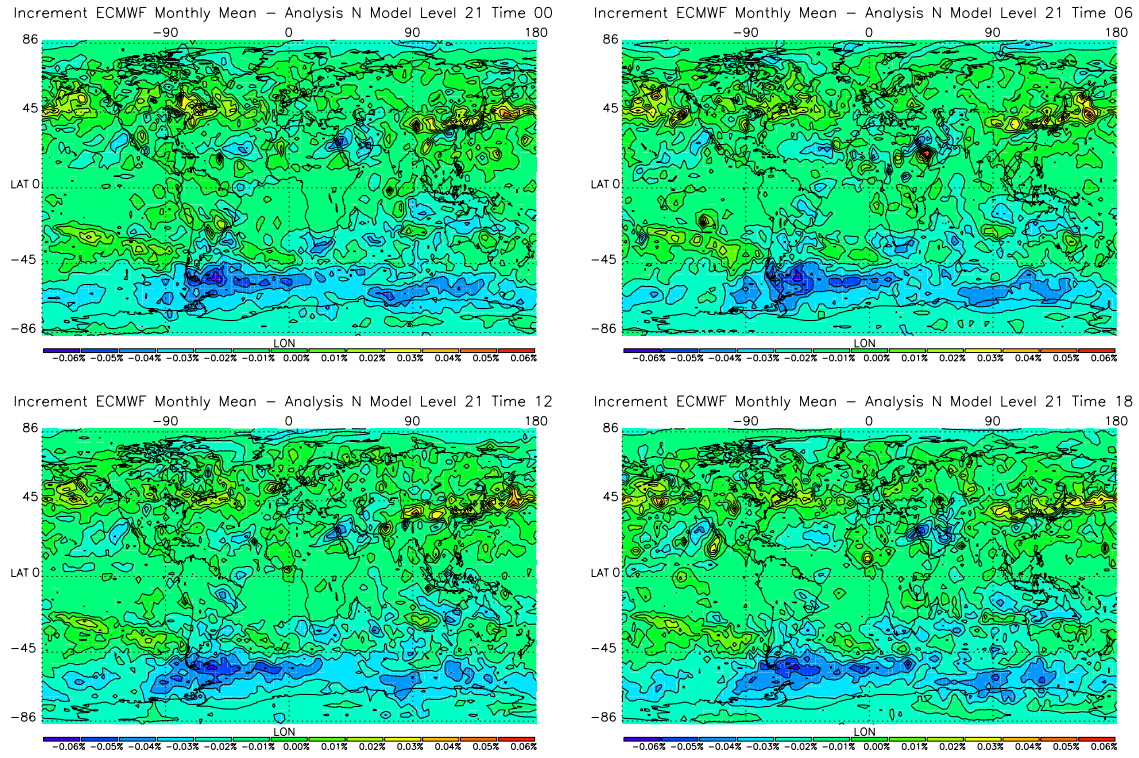

Figure 6.42: Increments of the refractivity assimilation of August 2003 between analysis and ECMWF monthly mean for the time layers 00, 06, 12, and 18 UTC at model level 21, which corresponds to a height of approximatly 5 km.

Refractivity In Fig. 6.42 the refractivity increments for model level 21 corresponding to a height of $\sim$ 5 km are depicted. The increments are generally at a quite low level, but the most significant feature is the negative increment over the southern hemisphere at high latitudes and a slightly positive increment in the northern hemisphere around a latitude of 45°, apparent within all time layers. This feature is also clearly apparent at model level 31 (cf. Fig. 6.43), which corresponds roughly to a height of $\sim$ 12 km. Within this layer an additional negative refractivity increment over the northern hemisphere at high latitudes appears, similar to the southern hemisphere. The appearance of the increments is consistent within all time layers. At model level 40 (cf. Fig. 6.44), corresponding to a height of $\sim$ 20 km, the features over the northern hemisphere vanish, the negative increment over the southern high latitudes are even more pronounced. The refractivity increments at the upper model levels are smoother,

Refractivity Assimilation Increments for August 2003 Model Level 31

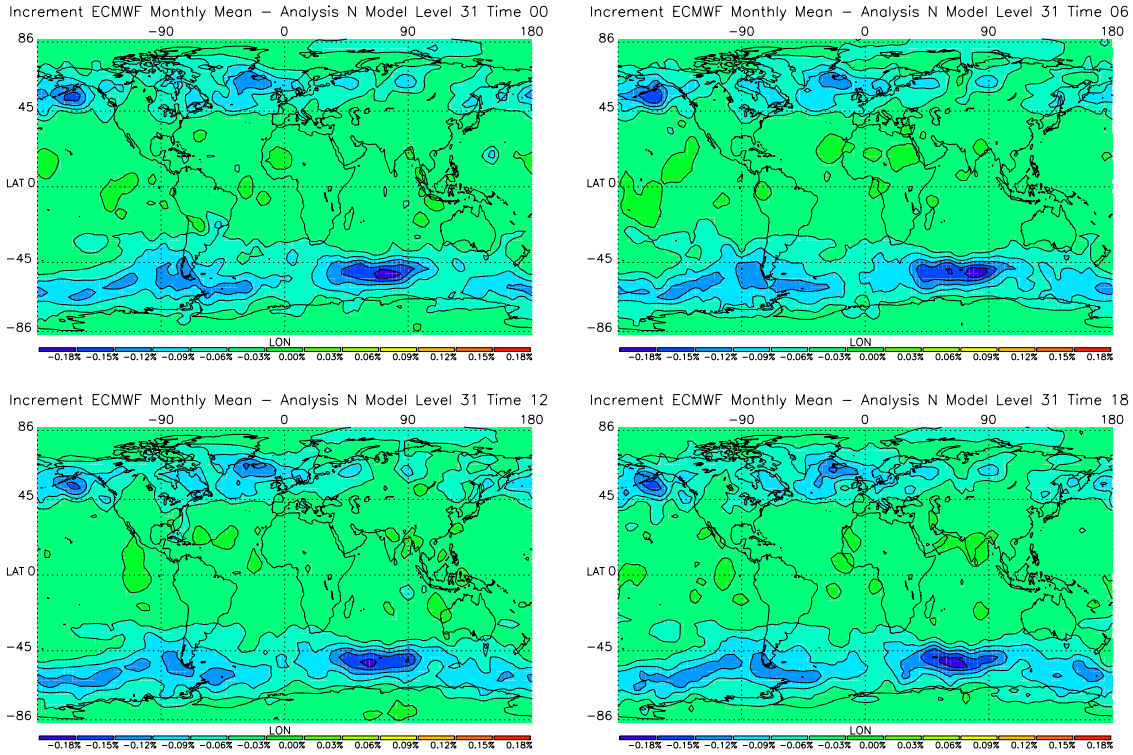

Figure 6.43: Increments of the refractivity assimilation of August 2003 between analysis and ECMWF monthly mean for the time layers 00, 06, 12, and 18 UTC at model level 31, which corresponds to a height of approximatly 12 km.

due to the fact of the extremely low water vapor content, which induces lower refractivity gradients. This reduces significantly the local variability of the refractivity gradient. One has to be aware of the different scaling of the plots. At model level 40 the most significant impact ($\sim 0.3\%$) of RO data onto the refractivity field derived from the ECMWF monthly mean temperature, specific humidity, and surface pressure fields can be seen. Taking the total monthly mean of August 2003 (which means an average over all time layers) for the model levels 21, 31 and 40 shows no surprising results (cf. Fig. 6.45). The results are consistent with the increments of the single time layers, the features are smoother and more pronounced. The most prominent feature is the negative refractivity increment over the high latitudes of the southern hemisphere. A result which is somewhat mirrored in the RO-only climatologies (cf. Subsection 1.2.3). The magnitude of the increment increases systematically with altitude. Over the southern high latitudes the strongest signal appears, within all levels, getting more significant with altitude. An interesting feature is that the impact around the equator is quite low even at model level 21, which is clearly visible within the separate time layers, and even more clearly in the total global mean.

Refractivity Assimilation Increments for August 2003 Model Level 40

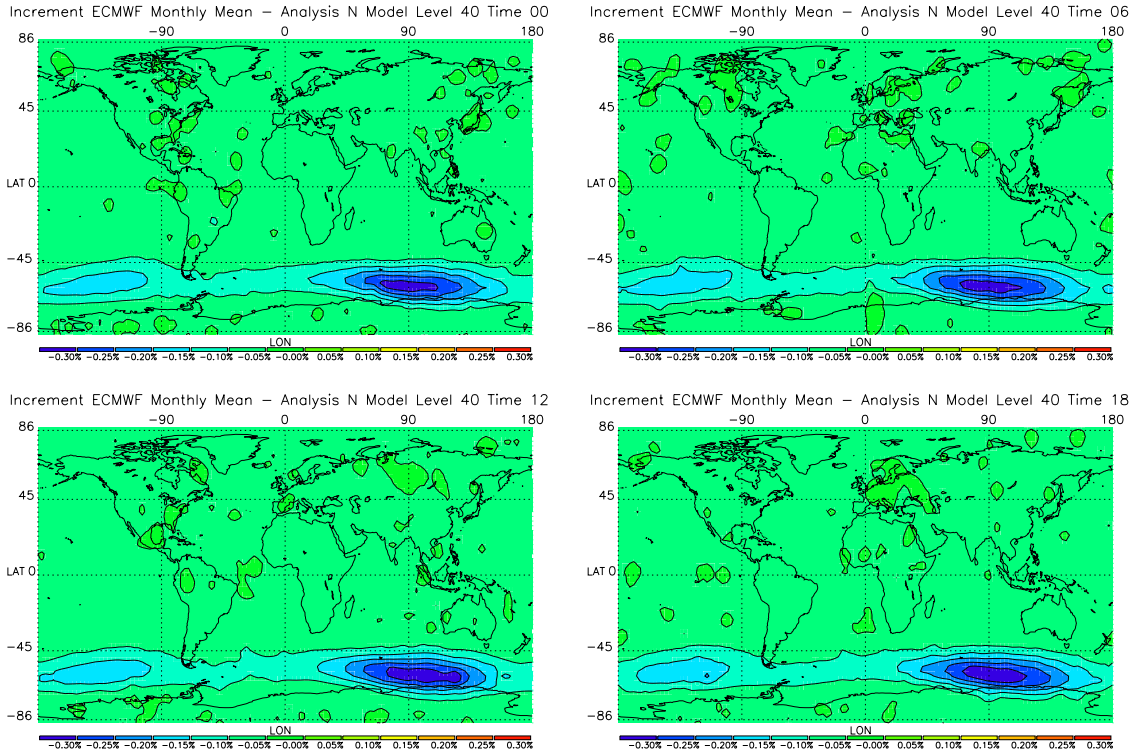

Figure 6.44: Increments of the refractivity assimilation of August 2003 between analysis and ECMWF monthly mean for the time layers 00, 06, 12, and 18 UTC at model level 40, which corresponds to a height of approximatly 20 km.

If the overall impact is compared with the geolocation of the measurements, a consistent picture is shown were increments only appear at locations with a systematic deviation of the measurements from the background. Non persistent deviations are vanishing within the monthly mean fields, delivering a neutral result. As the RO observations are an independent source of information, this results indicate a systematic deviation within certain regions of the ECMWF analysis fields. The error structure of monthly and seasonal mean analysis fields is believed to be bias driven[1]. A bias within the RO data themselves (cf. Subsection 6.1.1) cannot be excluded from the considerations, and improved retrieval algorithms are expected soon, but the applied correction prior to assimilation, seems to be appropriate as a first step. A systematic deviation introduced by the observations would be expected to be globally evenly distributed (cf. geolocation of observations Fig. 6.41). This not being the case, strengthens the suspicion of a systematic deviation within certain regions of the ECMWF background data. This result is roughly consistent with the intercomparison of the seasonal mean RO-only based climatologies of dry temperature with the corresponding ECMWF fields (cf. Fig. 6.2).

[1] Eric Anderson, ECMWF Reading, U.K., pers. communication, 2003.

Total Refractivity Assimilation Increments for August 2003

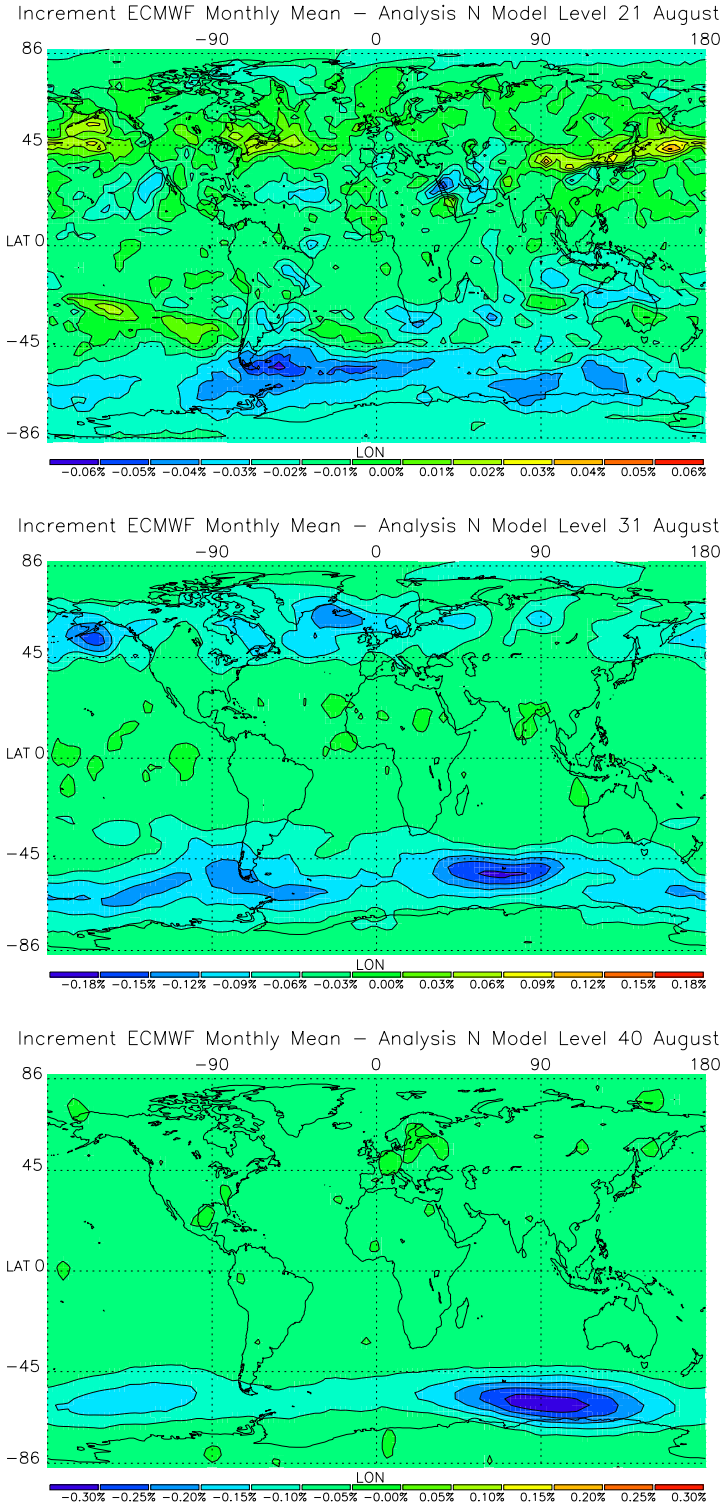

Figure 6.45: Increment of the total refractivity assimilation (mean of all time layers) August 2003 for the model levels 21 ($\sim$ 5 km), 31 ($\sim$ 12 km) and 40 ($\sim$ 20 km), different scaling of plot contours (Level 31/40 three/five times the contour spacing of Level 21).

6.8.2 Temperature, Specific Humidity, and Surface Pressure Assimilation Results for August 2003

For this quasi operational assimilation run the temperature, specific humidity, and surface pressure assimilation scheme was used on a beowulf cluster, processing 12 time layers in parallel.

Temperature Assimilation Increments for August 2003 Model Level 21

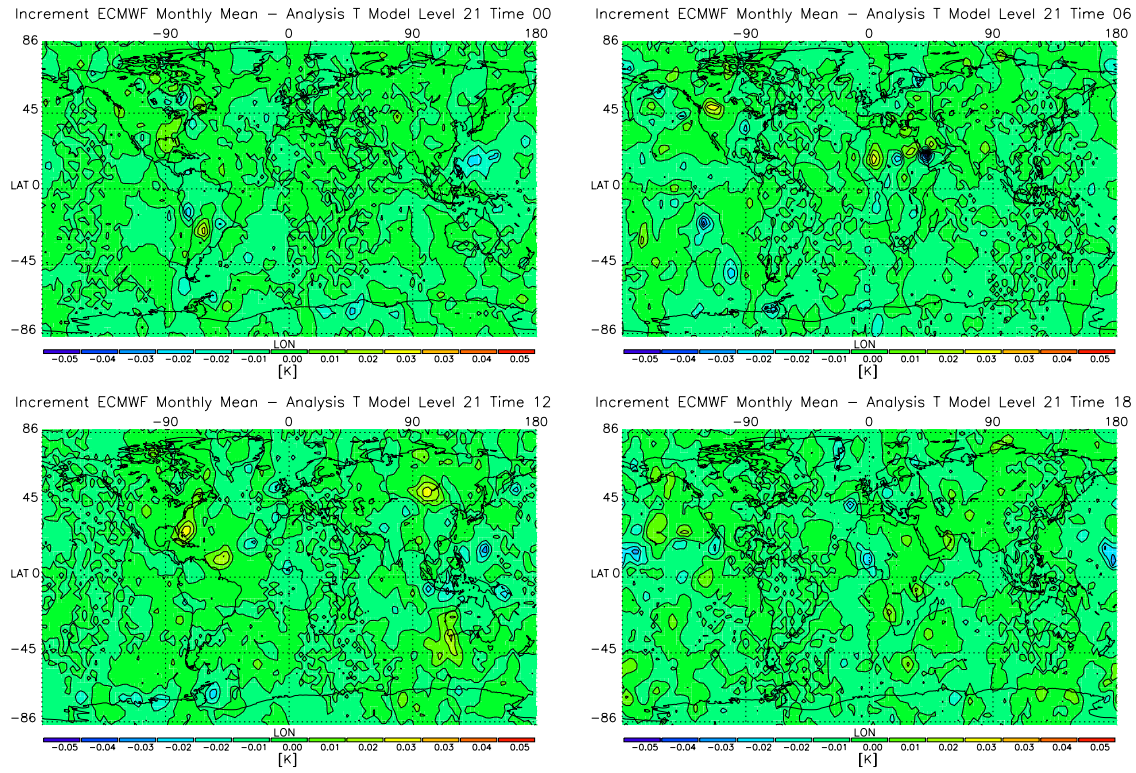

Figure 6.46: Increments of the temperature assimilation of August 2003 between analysis and ECMWF monthly mean for the time layers 00, 06, 12, and 18 UTC at model level 21, which corresponds to a height of approximatly 5 km.

Temperature In Fig. 6.46 the temperature increments for model level 21 corresponding to a height of $\sim$ 5 km are shown. The monthly mean increments are quite marginal at temperature level, for every time layer, showing no significant features. This effect stems from the spread of observational information into temperature, specific humidity, and surface pressure increments. The situation is similar for model level 31 ($\sim$ 12 km, cf. Fig. 6.47), but increments seem to be cumulated over the continents, and model level 40 ($\sim$ 20 km cf. Fig. 6.48), where increments appear especially at southern high latitudes. The increments are at a low level and show at level 31 and level 40 some isolated patterns. Like in the refractivity case, some interesting features are visible within the zonal mean of the temperature analysis, which will be shown later (cf. Fig. 6.57). The same applies for

the total mean temperature increment (cf. Fig. 6.49), which is for every model level at a very low magnitude, but shows at southern high latitudes at level 40 a significant negative deviation (order of 0.1 K).

Temperature Assimilation Increments for August 2003 Model Level 31

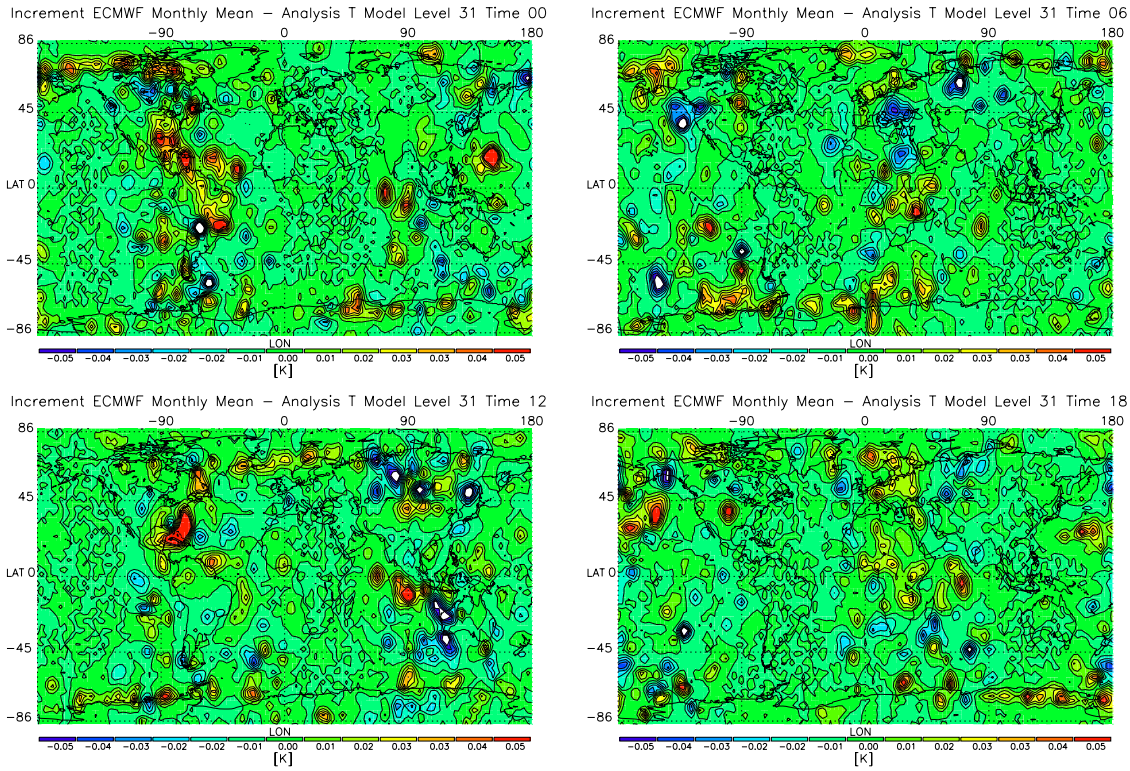

Figure 6.47: Increment of the temperature assimilation of August 2003 between analysis and ECMWF monthly mean for the time layers 00, 06, 12, and 18 UTC at model level 31, which corresponds to a height of approximatly 12 km.

Specific Humidity The specific humidity is showing quite substantial increments at model level 21 ($\sim$ 5 km, cf. Fig. 6.50), without any specific global pattern. Looking at model level 31 ($\sim$ 12 km, cf. Fig. 6.51), the similar picture appears, at a lower level of increments, but showing a significant signal, consistent within all time layers over the Mediterranean sea, which also appears consistently in Fig. 6.52 middle panel. For the total global mean the increment is slightly reduced (cf. Fig. 6.52) due to the averaging process, which indicates the low stability of the atmospheric specific humidity. For the total mean, also model level 40 ($\sim$ 20 km) is depicted, showing virtually no increment, as against model level 21 and 31, highlighting the absence of humidity at atmospheric layers exceeding the tropopause. As in the temperature case, a zonal monthly mean will be shown later, which will highlight the low increment around the equator.

Temperature Assimilation Increments for August 2003 Model Level 40

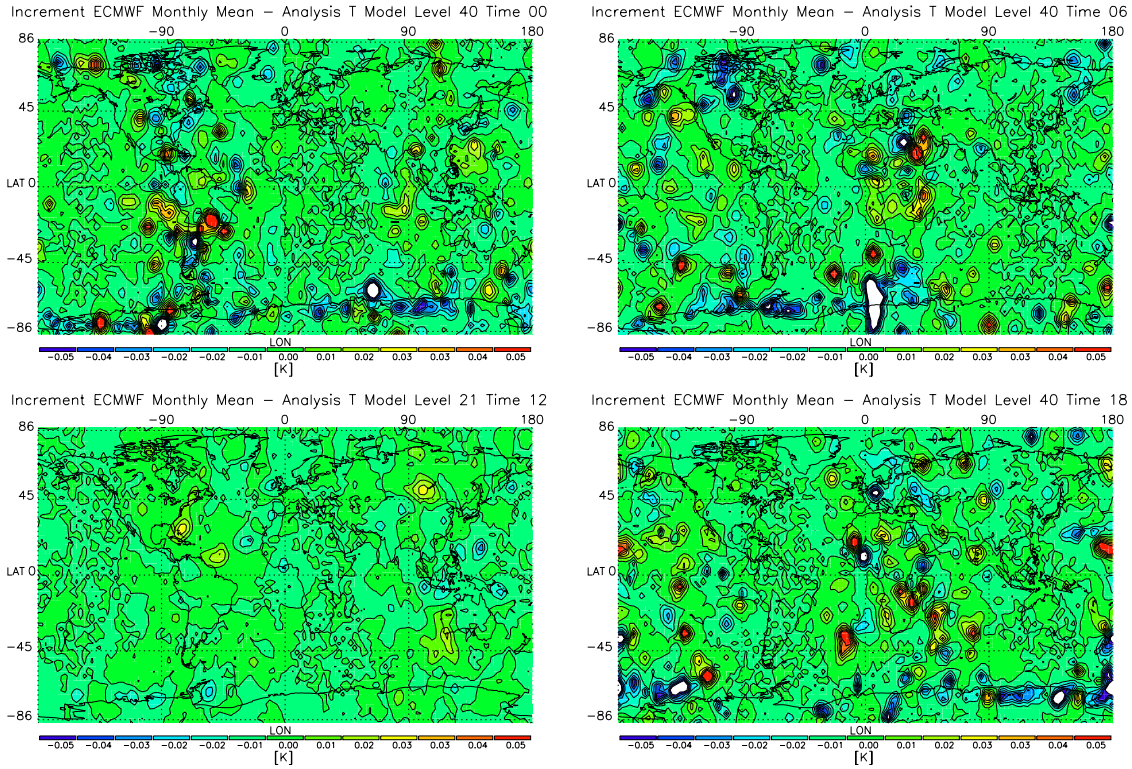

Figure 6.48: Increment of the temperature assimilation of August 2003 between analysis and ECMWF monthly mean for the time layers 00, 06, 12, and 18 UTC at model level 40, which corresponds to a height of approximatly 20 km.

Surface Pressure The surface pressure analysis again shows small increments, as to be expected (assumed relative global surface pressure standard deviation $\sim 0.25\%$), which are consistent within all time layers. The total mean surface pressure of August also shows no unexpected increments . The overall increment is slightly negative with a pattern around the mid latitudes with unaltered surface pressure. The most significant pattern appears at the southern high latitudes, this is also true for the total monthly mean of the surface pressure, showing no significant deviations from the increments of the single time slices. This increment at the southern high latitudes agrees especially well with the refractivity increments as can be seen in Fig. 6.45. A significant portion of the observation increment is attributed to the local pressure and propagated via the adjoint operators down to the surface pressure grid.

Compared to the refractivity only assimilation scheme, the impact of the temperature, specific humidity, and surface pressure assimilation is somewhat limited. Especially at the upper model levels like model level 40 one would expect a more significant impact concerning the temperature background, due to the absence of humidity,

Total Temperature Assimilation Increments for August 2003

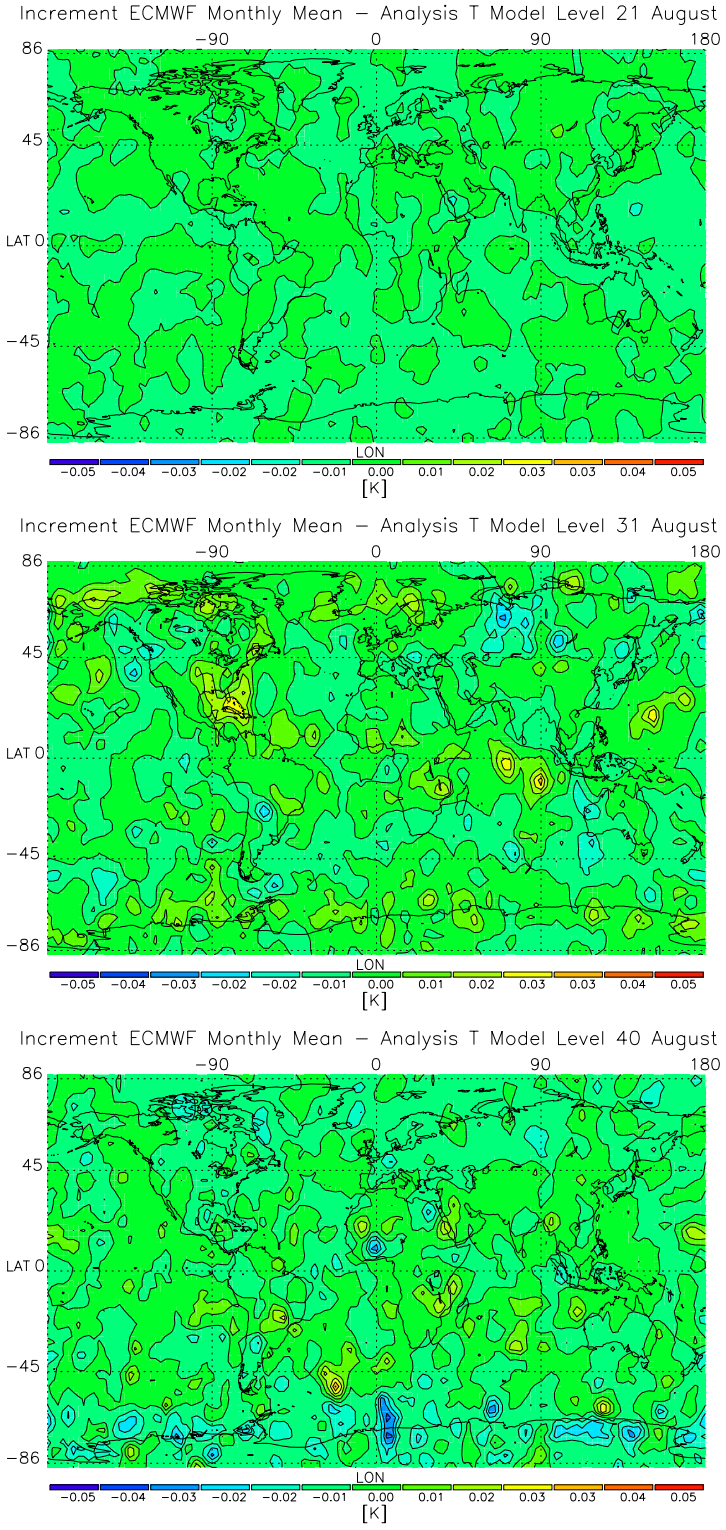

Figure 6.49: Increment of the total temperature assimilation (mean of all time layers) August 2003 for the model levels 21 ($\sim$ 5 km), 31 ($\sim$ 12 km) and 40 ($\sim$ 20 km).

Specific Humidity Assimilation Increments for August 2003 Model Level 21

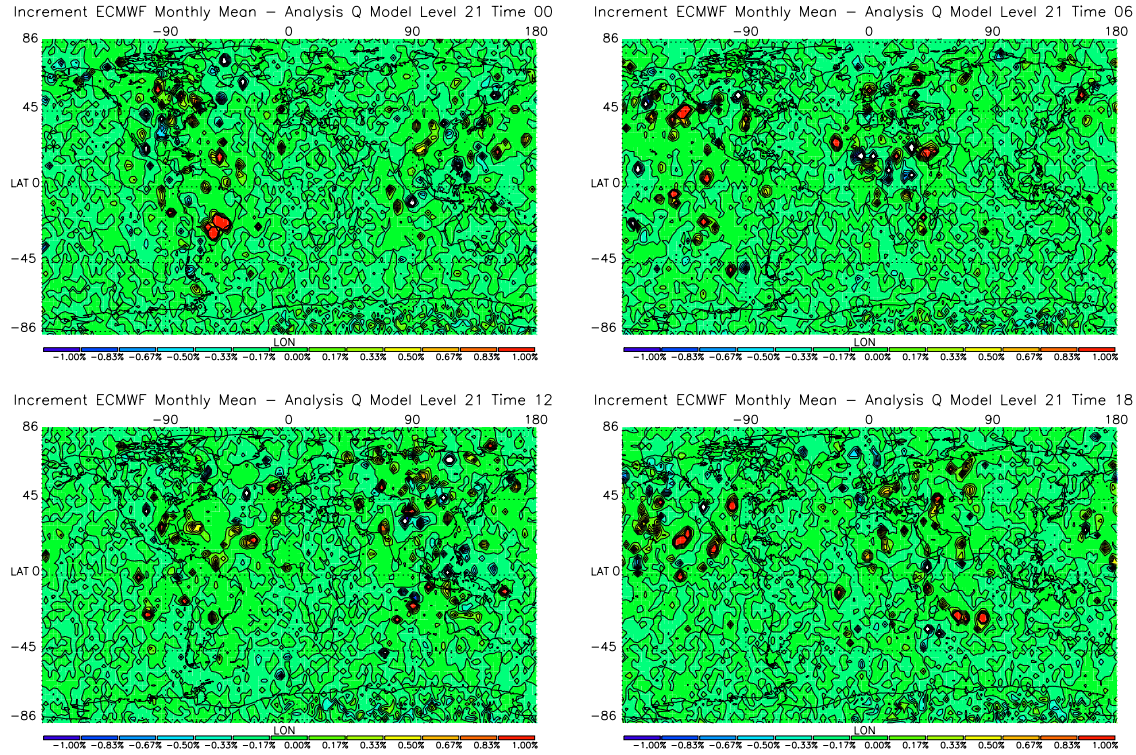

Figure 6.50: Increment of the specific humidity assimilation of August 2003 between analysis and ECMWF monthly mean for the time layers 00, 06, 12, and 18 UTC at model level 21, which corresponds to a height of approximatly 5 km.

the correction should be applied mainly to the temperature background and the pressure field, which is subsequently propagated down to the surface pressure. The significant features apparent in the refractivity analysis at the southern high latitudes, are apparent in the temperature analysis only at a marginal level. As mentioned above a significant part of the introduced information seems to be attributed to the pressure grid and is subsequently propagated to the surface pressure. Nevertheless the temperature increment pattern is consistent with the refractivity only analysis increment, which can be seen at zonal mean level. The temperature increment at zonal mean level perfectly agrees with the increment of the from temperature, specific humidity, and surface pressure analyses recalculated refractivity field.

Specific Humidity Assimilation Increments for August 2003 Model Level 31

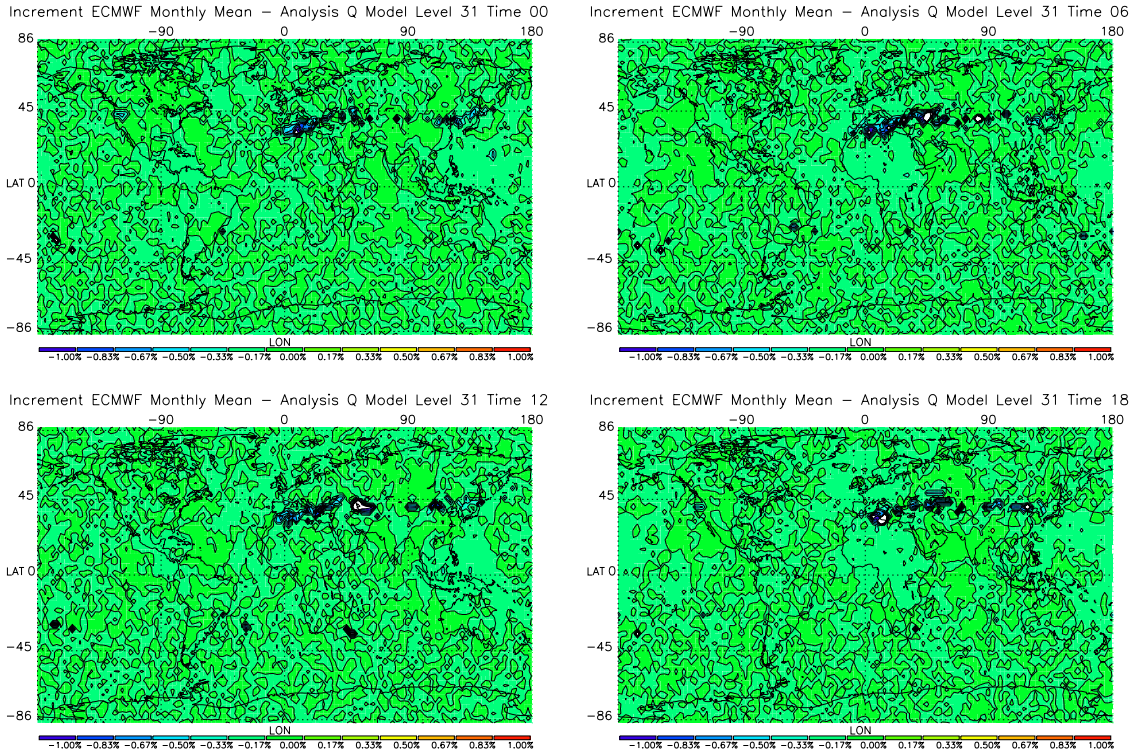

Figure 6.51: Increment of the specific humidity assimilation of August 2003 between analysis and ECMWF monthly mean for the time layers 00, 06, 12, and 18 UTC at model level 31, which corresponds to a height of approximatly 12 km.

Specific Humidity Assimilation Increments for August 2003

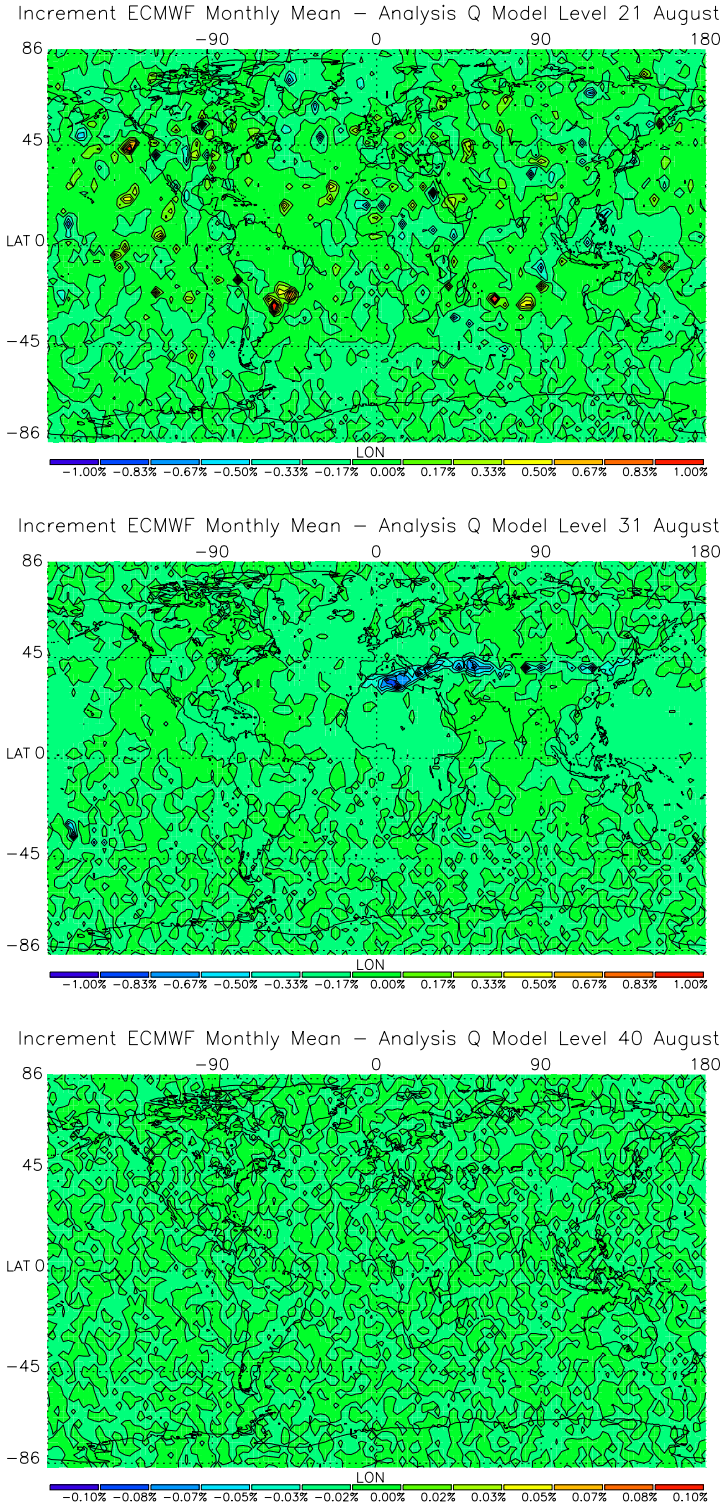

Figure 6.52: Increment of the total specific humidity assimilation (mean of all time layers) August 2003 for the model levels 21 ($\sim$ 5 km), 31 ($\sim$ 12 km) and 40 ($\sim$ 20 km), different scaling of Level 40 plot (10 times less spacing than Level 21 and Level 31 plots, respectively).

Surface Pressure Assimilation Increments for August 2003

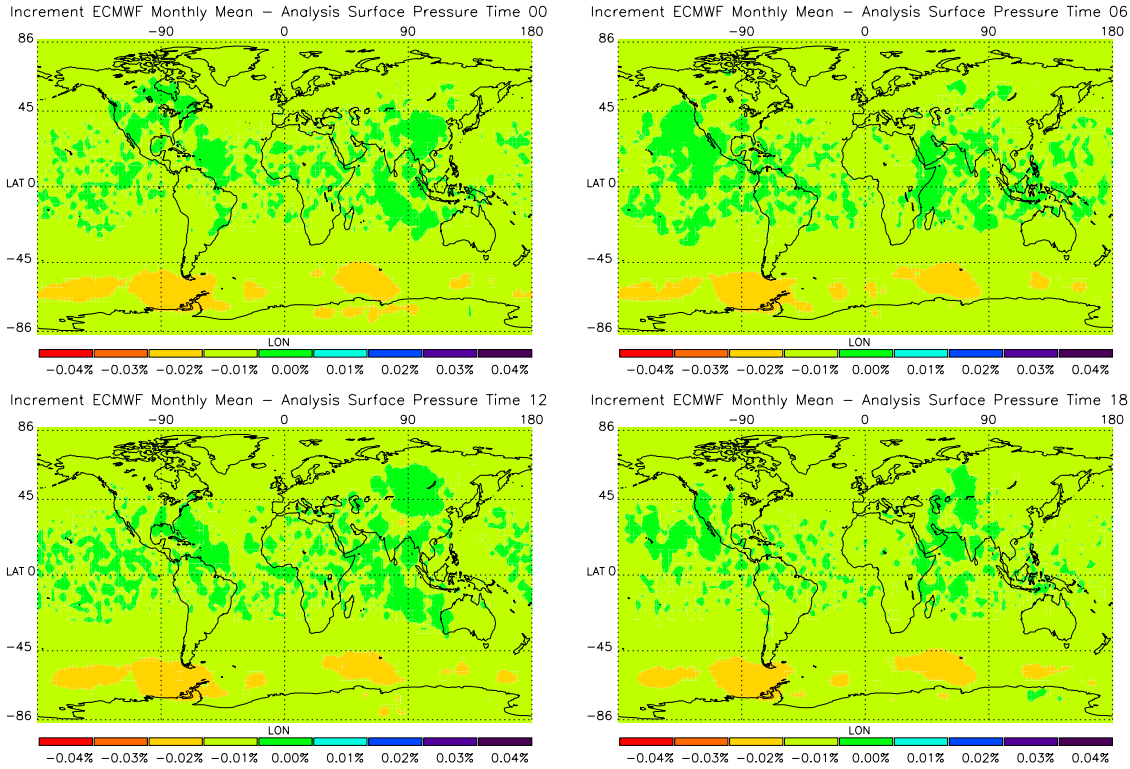

Figure 6.53: Increment of the surface pressure assimilation of August 2003 between analysis and ECMWF monthly mean for the time layers 00, 06, 12, and 18 UTC.

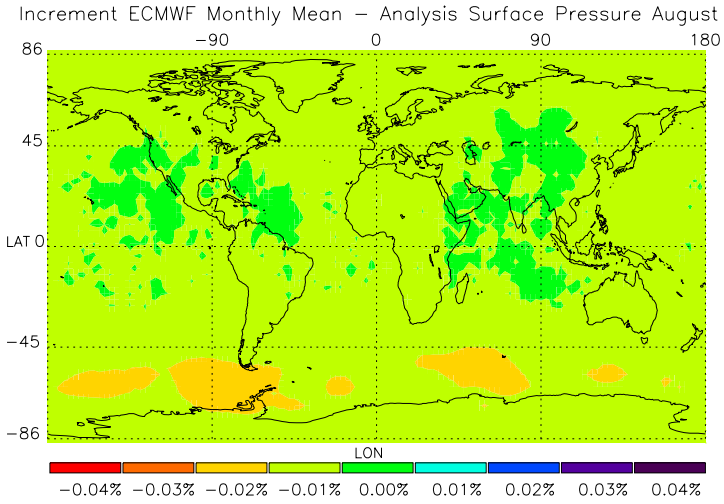

Figure 6.54: Increment of the total surface pressure assimilation (mean of all time layers) August 2003.

6.9 Zonal Means

From the total monthly analyses of August 2003, zonal means were calculated.

6.9.1 Zonal Mean Refractivity

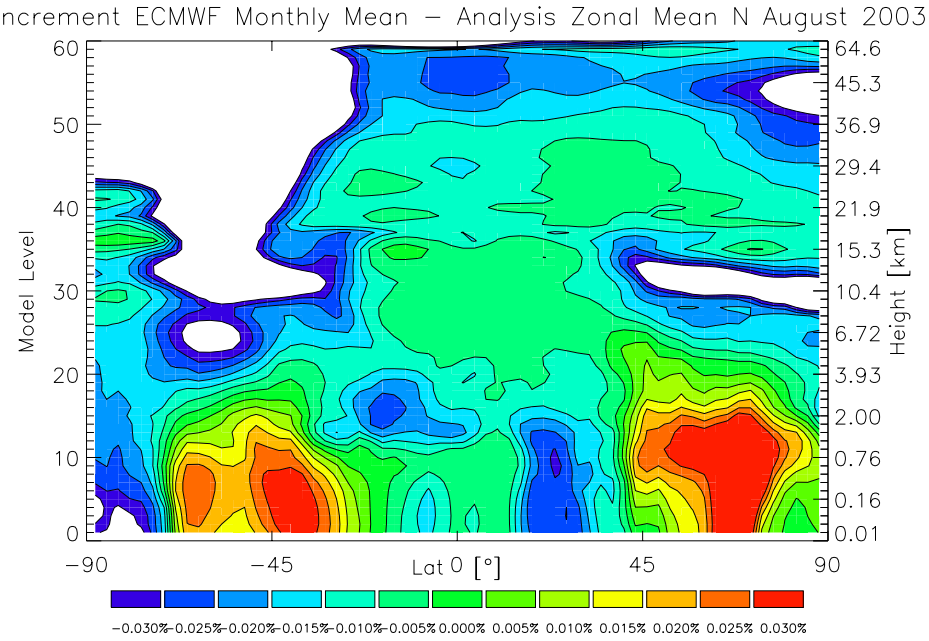

Figure 6.55: Zonal mean increment refractivity calculated from the total mean analysis of August 2003 and the corresponding ECMWF analysis.

Finally the zonal mean from the total monthly mean analysis of the refractivity was calculated. The zonal mean Fig. 6.55 shows a very significant feature between model level 50 and 60 where in fact no direct observations can cause an impact (cut off height is 35 km due to accuracy considerations), but of course these levels are coupled with the lower parts of the atmosphere via the vertical error covariance matrices (cf. Fig. 4.10). The features around level 40 are clearly visible within the horizontal slice in Fig. 6.45, there is also a slight hint of the negative increment at the northern high latitudes around model level 31, also clearly visible in Fig. 6.45. Except from the significant increment between model level 50 and 60 the refractivity field calculated from the temperature, specific humidity, and surface pressure analyses (cf. Fig. 6.57) is showing similar features, at different magnitude. Wave like structures are also apparent over the southern hemisphere at high latitudes. An other feature is the strong negative increment at norther heigh latitudes around 10 km, which is mirrored in Fig. 6.57 upper panel to a minor degree. The increment in the refractivity only case is stronger pronounced and less smooth, especially below some 10 km due to the water vapor content within the troposphere.

6.9.2 Zonal Mean Temperature and Specific Humidity

Zonal Mean Temperature and Specific Humidity

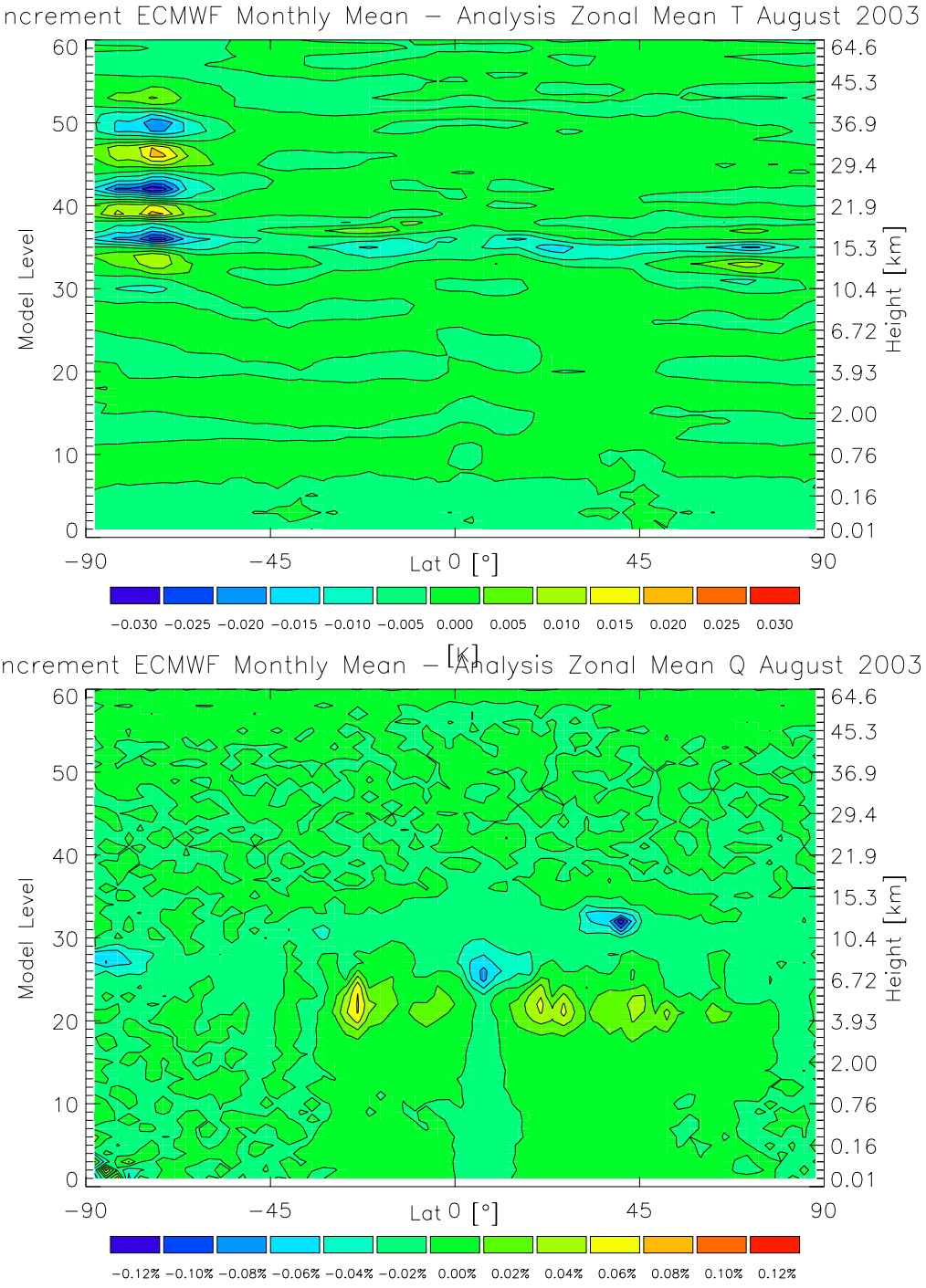

Figure 6.56: Zonal mean increment of total temperature (lower panel) and specific humidity (upper panel) assimilation to ECMWF August 2003.

Zonal Mean Temperature and Refractivity Increment

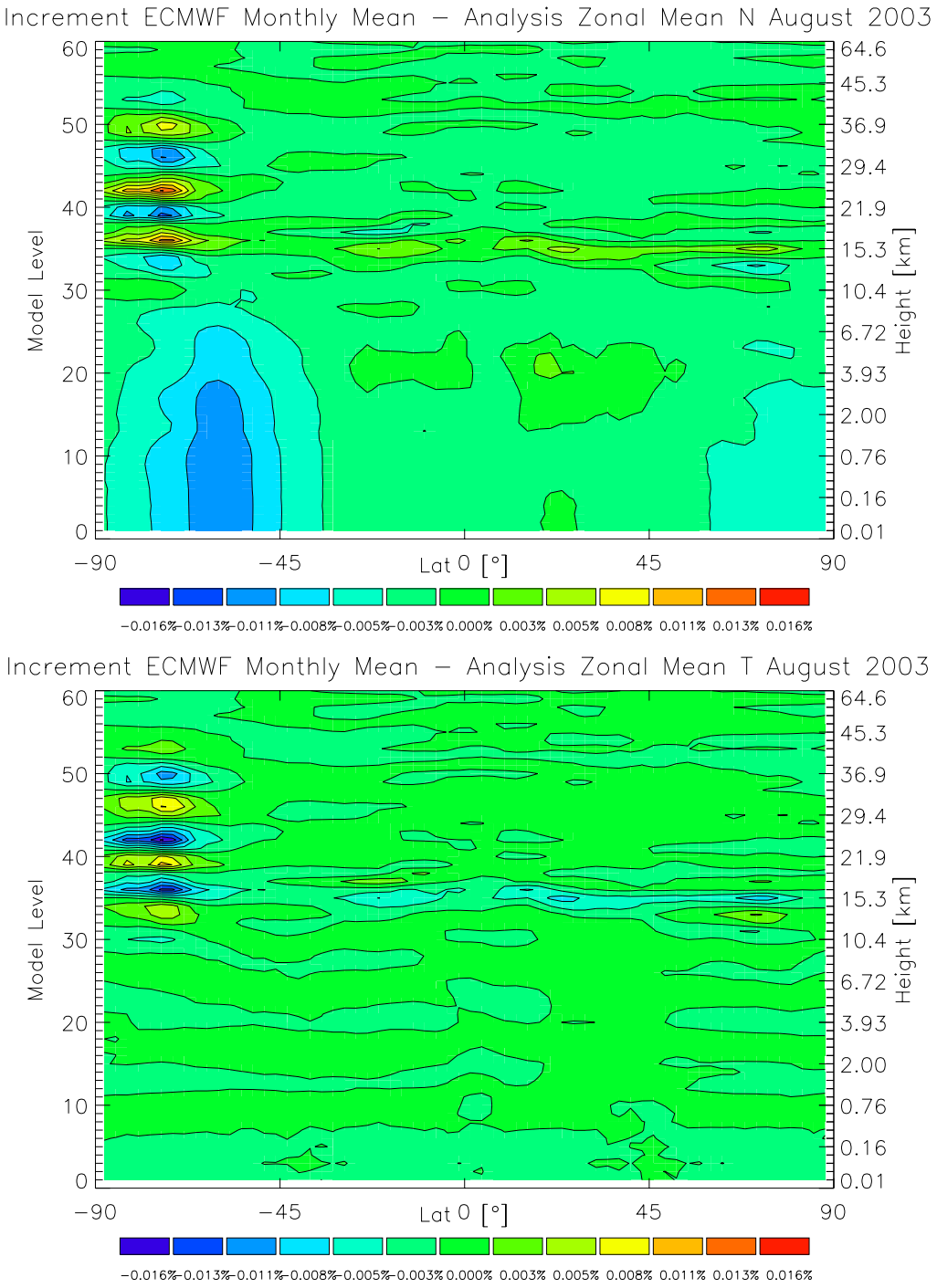

Figure 6.57: Zonal mean increment of temperature assimilation (lower panel) and from temperature, specific humidity and surface pressure analyses derived refractivity (upper panel) to the corresponding ECMWF fields, August 2003.

Zonal Mean Temperature Analysis and RO only Dry Temperature Climatology

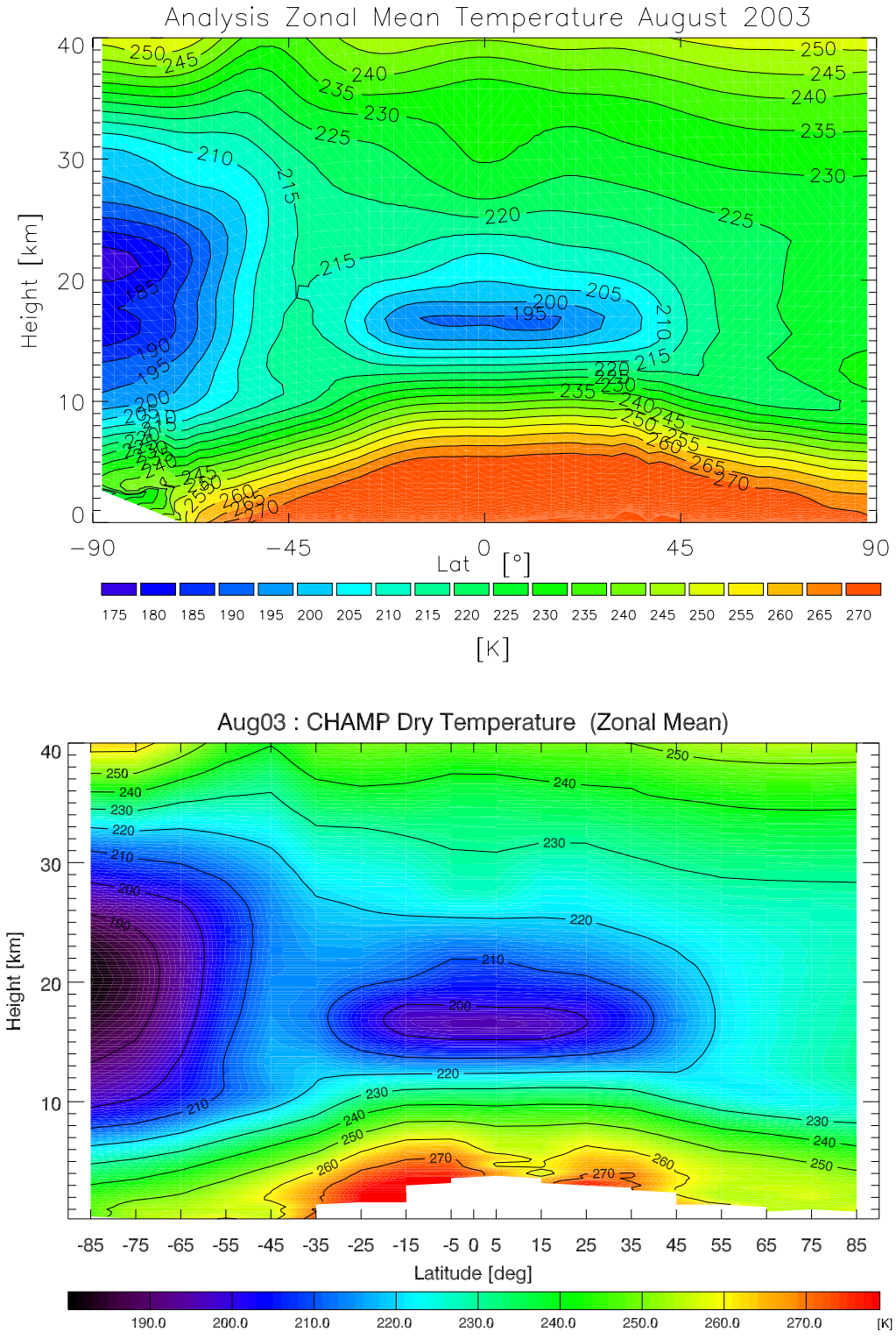

Figure 6.58: Zonal mean temperature analysis and RO only dry temperature climatology, August 2003, lower plot (courtesy M. Borsche, IGAM/UniGraz).

The zonal mean temperature increment shows a consistent pattern compared to the increment of the CHAMP RO only climatologies (cf. Fig. 6.2) compared to ECMWF (cf. Fig. 6.56, upper panel). The specific humidity shows some interesting patterns around the equator shifted to the northern hemisphere, and around the tropopause height. The most interesting feature is shown in Fig. 6.57, which depicts the relative refractivity increment (upper plot) and the relative temperature increment (lower plot), showing their close agreement, spatially and concerning the magnitude, and sign.

6.10 Conclusion

The standard deviation at the observation locations is lesser than at the background grid points, due to the averaging nature of the interpolation processes. For the observation error characteristics a conservative approach was chosen. As the observations are averaged during the preprocessing step, their standard deviation should be reduced compared to the original observations within the profiles. The error characteristics currently used within the assimilation framework is more conservative that of the unprocessed original observations.

6.10.1 Systematic Deviation

Plots A and C of Fig. 6.30 indicate a problem concerning the correction of the systematic deviation of the input data. As can be seen the deviation correction seems to be overestimated by $\sim 0.15\%$ for this set of observations. The same applies even more significant for plots A and C of Fig. 6.33, and less pronounced for plots A and C of Fig. 6.36. For the other time slices the correction seems to be appropriate. An improved retrieval algorithm is foreseen, which should solve this problem.

6.10.2 Refractivity Analysis

The increment is calculated at observation locations, compared to the monthly mean studies, where the whole field increments are analyzed. The overall increment at refractivity level seems to be consistently $\sim 0.25\%$ for all assimilation time windows for the refractivity-only system. The results of all five time windows are quite comparable, there are no significant patterns within single time slices.

6.10.3 Temperature, Specific Humidity, and Surface Pressure Analysis

The overall increment at refractivity level seems to be consistently $\sim 0.25\%$ for all assimilation time windows for the temperature, specific humidity, and surface pressure scheme, which is comparable to the refractivity-only system. The temperature increments are $\sim 0.10\%$ in the troposphere, increasing to $\sim 0.2\%$ at higher altitudes (cf. Figs. 6.30, 6.33, 6.36, 6.39 panels E). As in the refractivity case the increment is calculated at observation location. Like in the refractivity case the results of all five assimilation time windows are quite comparable, there are no significant patterns within single time slices.

6.10.4 Monthly Mean

The monthly mean analysis allows to compare the full average field increments, the number of observations (in our case 245220) and their global coverage are sufficient. As a future perspective seasonal means will introduce roughly three times as many observations, further increasing the impact onto the background. Additional RO data from GRACE and GRAS on METOP as well as COSMIC will soon vastly increase impacts.

Monthly Mean Refractivity Analysis

The refractivity analysis shows some significant patterns, especially at the high latitudes of the souther hemisphere. A similar feature appears around model level 31 ($\sim$ 12 km) over the northern high latitudes, the features are in general showing an increasing magnitude with height.

The refractivity analysis shows a significant increment between the monthly mean analysis and the corresponding ECMWF fields at refractivity level, consistent at all time layers and within the total monthly mean. The most striking feature is the negative increment at the southern high latitudes. The zonal mean of the total monthly mean analysis also offers interesting insights into the vertical structure of the increments.

Monthly Mean Temperature, Specific Humidity, and Surface Pressure Analysis

The clearly visible increment between monthly mean analysis and the corresponding ECMWF fields at refractivity level, are not that significantly apparent within the increments of the temperature, specific humidity, and surface pressure fields. Nevertheless they are present, at a smaller magnitude, as clearly visible within the zonal mean plots.

The monthly zonal mean increment between analysis and ECMWF shows quite significant patterns over the southern hemisphere at high latitudes (cf. Fig. 6.56, upper plot), which agree very well with the increments of RO-only climatologies and ECMWF (cf. Fig. 6.2). This result is also mirrored in the well reconstructed increment pattern of the zonal mean refractivity field calculated from temperature, specific humidity, and surface pressure slices and compared to the corresponding refractivity field derived from the monthly mean ECMWF fields (cf. Fig. 6.57). The plot shows the excellent agreement between the temperature and refractivity increments, depicting that an increase of temperature brings forth a decrease in refractivity and vice versa, as should be the case. The plot also shows that the refractivity is dominated by the temperature above the tropopause due to the marginal water vapor content at high altitudes. Within the troposphere, the strong temperature signature of the refractivity is diluted by the influence of water vapor (compare Fig. 6.57), where part of the negative increment below model level 40 should also be attributed to the surface pressure increment. The absolute temperature analysis of the total zonal monthly mean and the corresponding RO-only climatology are shown in Fig. 6.58, showing both the same principal features.

The specific humidity increments are showing a decline in magnitude with increase of the altitude, an effect which is clearly to be expected. At model level 40 ($\sim$ 20 km), far above the tropopause the increment oscillates around zero which can be contributed to numerical *noise* (cf. Fig. 6.52). Again a more significant pattern can be seen within the plots of the zonal mean (cf. Fig. 6.56, lower panel).

The total monthly mean of the surface pressure shows only at the southern high latitudes a significant signal, the overall correction is slightly negative with some unaltered regions mainly at mid latitudes. These surface pressure increments is specially consistent compared to the spatial location of the refractivity and temperature increments (cf. Figs. 6.54, 6.45 and 6.49).

6.10.5 Alternative Background Data

As an alternative approach concerning the choice of the first guess, short range forecasts and the corresponding error characteristics should be taken into consideration. This could be a better choice of first guess data for climate monitoring applications and impact studies should be conducted in future.

Conclusions

Overview

During the development of the 3D-Var system introduced in this study, several technical and principal problems occurred. Addressing the technical issues, most of them could be solved in a convenient way. Concerning computational feasibility, for example it turned out that a severe reduction of cost function and gradient evaluations is not spoiling the analysis results (cf. Section 6.3), cutting down computation time tremendously. By processing the whole set of CHAMP observations from August 2003 the computational feasibility, on a small Linux cluster was proven. Using the described setup, the average six hour assimilation time window takes about one hour to be processed using the refractivity analysis setup and about three hours using the full temperature, specific humidity, and surface pressure formulation. Using a Linux cluster with six nodes, every node equipped with 2 processors (i.e. 1.8 GHz CPUs), the 31 days of August where processed within about 45 hour computational time.

Due to the quite accurate first guess, the corrections, applied through the observations to the background fields are fairly small. This is to be expected, so increments of the mean data fields as a whole should be studied at a monthly or seasonal mean basis. This also serves the foreseen application of the system, which is to conduct studies of long term variability and climate change. Using only CHAMP data, at least one month of observations should be used, to achieve enough global coverage and data density.

As a derivation of the error characteristics of the RO-only based global climatologies is on-going currently, it is difficult to specify error characteristics of the mean analysis fields of ECMWF. It is assumed that these errors are bias driven, but they are not sufficiently characterized yet. On the other hand we believe that apart from the small systematic deviation in our current CHAMP data, the error characteristics of RO data have a sound foundation to serve as unbiased observations between 5 and 35 km, and the assumptions made within this work are quite conservative.

Concerning CHAMP data improved retrieval algorithms are expected soon (with the perspective of a removal of the systematic deviation), for now the applied correction is sufficient, however for the geolocation, instead of a mean tangent point of the profile the mean real position of the single observations would be preferable due to the smearing characteristics of the RO profiles, an improvement which is currently under development. The system is ready for geopotential as alternative vertical coordinate, which is probably the better choice and should be tested in future.

Assimilation creating full monthly or seasonal mean climatologies would give valu-

able insight into the increments of ECMWF mean analysis fields, and would allow valuable insights into possible bias characteristics. As mentioned above, the error characteristics of the mean analysis fields of ECMWF are not sufficiently characterized yet, but the derivation of the monthly mean test analysis of August 2003 proved that the approach of processing every single time layer of one month using the appropriate observations to derive the total monthly mean analysis adequate. As can be seen in the analysis of the real CHAMP data, observations below $\sim$ 5 km are problematic. As a first approach it was found better to use this limit as cut off height for the observations, which was done in the processing of the August 2003 analysis. Advanced retrieval techniques like wave optics are able to cope with the problems occurring in the lower troposphere and hence are superior to geometric optics below about 5 km [*Gorbunov* (2002)], [*Hocke et al.* (1999)], [*Sokolovskiy* (2003)], [*Jensen et al.* (2003)], [*Beyerle et al.* (2003)]. Future RO data products will take advantage of the improved retrieval techniques and thus deliver high quality observations down into the lower troposphere at least to the top of the planetary boundary layer.

Outlook

A short term outlook was already given in the previous section concerning mainly improvements of retrieval algorithms [*Gobiet and Kirchengast* (2004a)]. Here a longer term outlook will be given concerning new instruments and background data. Furthermore, direct improvements of the assimilation scheme itself will be discussed at the end of this section.

Better error characteristics of new generation receivers like GRAS (0.2% compared to 0.4%, see Subsection 3.2.5) will increase the increments and lead to climatologies of even better accuracy. With the new missions en route the global coverage will be better within 24 hours leading to more impact on the data fields as a whole (see COSMIC subsection 3.2.5). Independent validation against for example collocated RAOB data will be easier due to the increased number of observations and intervalidation of the different systems will allow to even better specify the error characteristics of RO observations. With the availability of GRAS data, the first checks concerning the change of increments due to the expected data quality of GRAS occultations could be conducted. In this context, the possibility of direct comparison of collocated CHAMP and GRAS profiles to compare the receiver performance will be very useful.

Within the control space transformation framework (cf. Section 4.8) it is possible to filter vertical grid-scale, low amplitude noise from the system by neglecting small-scale structures which contribute little to the total error (this step would also reduce computing time). The inner product $\boldsymbol{P}$, which defines a weighted error (see Eq. 4.47) could be also used to introduce further dependencies into the vertical transform. The foreseen upgrade to L90 of ECMWF will enhance the resolution of vertical atmospheric structures, especially around the tropopause height and can be handled without problems (except a linear increase of computing time). The system itself is fit for any horizontal or vertical resolution (tested for T21L60 and T42L60), the limit is mainly the available computing power. As mentioned in Subsection 3.1.1, the T42L60, or in future the T42L90 resolution, fits best on the one hand the spatial characteristics of RO observations (cf. Section 3.2),

and on the other hand the climatological applications. Another interesting option will be the use of forecasts (with adopted error characteristics) as first guess to conduct impact studies (cf. 6.10.5).

Since the observations are preprocessed, and a kind of *super observations* is used within the assimilation framework, the assumptions used for the observational error within the assimilation experiments are currently very conservative. The standard deviation of the observations should be reconsidered and partially reduced in the future, which will affect directly the analysis increments.

Using global mean background covariance matrices as a first step was acceptable, but the use of geographically dependent error characteristics will be clearly more appropriate in the future Furthermore as the plots in Chapter 6 clearly indicate (and in more detail the work of Andreas Gobiet), there are some deficiencies in the background temperature fields at high latitudes during the winter in the southern hemisphere. This indicates that also introduction of a seasonal dependency will be valuable in order to get a more realistic representation of the background errors[2]. Overall, it is satisfactory to see that the basis laid with the developments of this work finds many promising opportunities for future advancements and climatological applications.

[2]Andreas Gobiet IGAM/UniGraz, AUT, pers. communications 2004

A

Constants

k_1	=	77.60	[K/hPa]	Empirical Constant Thayer Formula & Smith Weintraub
k_2	=	70.40	[K/hPa]	Empirical Constant Thayer Formula & Smith Weintraub
k_3	=	373900.00	[K^2/hPa]	Empirical Constant Thayer Formula & Smith Weintraub
A	=	6.02214×10^{23}	[mol^{-1}]	Avogadro Number
R	=	8.3145	[Pa·m^3/K·mol]	Universal Gas Constant
R_{Dry}	=	287.06	[J/K·Kg]	Dry Air Gas Constant
R_{WatVap}	=	461.52	[J/K·Kg]	Water Vapor Gas Constant
m_A	=	28.964	[kg/kmol]	Molar Mass of Dry Air
m_W	=	18.015	[kg/kmol]	Molar Mass of Water Vapor
g_{Mean}	=	9.80665	[m·s^{-1}]	Mean Acceleration of Gravity
r_{Mean}	=	6371.0	[Km]	Mear Radius of Earth
r_{Pol}	=	6356.752314	[Km]	Polar Radius of Earth
r_{Equ}	=	6378.137	[Km]	Equatorial Radius of Earth
M^*	=	6.022140×10^{26}	[$Kmol^{-1}$]	Kilo Mol
$Earth\_Flattening$	=	$\frac{r_{Equ}}{r_{Pol}} - r_{Equ}$	[km]	Earth Flattening
J_2	=	1.08263×10^{-3}		GRS-80 zonal coefficient
g_{Equ}	=	9.7803	[m·s^{-1}]	Acceleration of Gravity at Equator

Table A.1: Relevant constants

B

Notation

$\mathbf{x}_t$	:	True State of the Atmosphere	Dimension n
$\mathbf{x}_b$	:	Background Model State	Dimension n
$\mathbf{x}_a$	:	Analysis Model State	Dimension n
$\mathbf{y}$	:	Observation Vector	Dimension p
H	:	Observation Operator	Dimension $n \rightarrow p$
$\mathbf{H}$	:	Linear Observation Operator	Dimension $n \rightarrow p$
$\mathbf{B}$	:	Background Covariance Matrix	Dimension $n \times n$
$\mathbf{R}$	:	Observation Covariance Matrix	Dimension $p \times p$
$\mathbf{A}$	:	Analysis Covariance Matrix	Dimension $n \times n$
$\mathbf{K}$	:	Gain Matrix	Dimension $n \times n$
$\mathbf{I}$	:	Identity Matrix	
J_b	:	Background Cost Function	
J_o	:	Observation Cost Function	
J	:	Total Cost Function	
$\mathbf{v}$	:	Background State Vector in Control Space	Dimension n
$\mathbf{E}$	:	Matrix Containing Eigenvectors (Columns)	Dimension $n \times n$
U	:	Control Space Transformation Operator	
λ	:	Eigenvalues	
P	:	Inner Product	
z	:	Geometric Height	
ϕ	:	Geopotential Height	
φ	:	Latitude	
λ	:	Longitude	
σ	:	Standard Deviation	

Table B.1: Notation-Major symbols

C

List of Acronyms

ECMWF	:	European Center for Medium Range Weather Forecast
CHAMP	:	Challanging Mini Satellite Payload
RO	:	Radio Occultation
LEO	:	Low Earth Orbit Satellite
MEO	:	Medium Earth Orbit Satellite
GEO	:	Geo Stationary Orbit Satellite
TEC	:	Total Electron Content
GFZ	:	Geo Forschungszentrum Potsdam
3D-VAR	:	Three Dimensional Variational Data Assimilation
4D-VAR	:	Four Dimensional Variational Data Assimilation
pdf	:	Probability Density Function
BLUE	:	Best Linear Unbiased Estimator
TL	:	Tangent Linear
AD	:	Adjoint
IFS	:	ECMWF Integrated Forecast System
TLE	:	Two Line Element
COSMIC	:	Constellation Observing System for Meteorology, Ionosphere & Climate
CIRA	:	Cospar International Reference Atmosphere
COSPAR	:	Comite on Space Research
MSISE	:	Mass Spectrometry Incoherent Scatter (Extended)
RAOB	:	Radio (Balloon) Observations
MIPAS	:	Michelson Interferometer for Passive Atmospheric Sounding
PCA	:	Principal Component Analysis
ICA	:	Independent Component Analysis
GFZ	:	Geo Forschungs Zentrum Potsdam
DMI	:	Danish Meteorological Institute
ENVISAT	:	Enviroment Satellite
ERA40	:	ECMWF Re-Analysis 40
GRAS	:	GNSS Receiver for Atmospheric Sounding
GNSS	:	Global Navigation Satellite System

WMO	:	Word Meteorological Organization
WCRP	:	World Climate Research Program
ECHAM5	:	European Center Hamburg Model 5
METOP	:	Metorological Operational Satellite
EPS	:	Eumetsat Polar System
SAF	:	Satellite Application Facility
WRF	:	Weather Research and Forecasting Model
MM5	:	Mesoscale Model 5
GENESIS	:	GPS Environmental & Earth Science Information System
IPCC	:	Intergovernmental Panel on Climate Change
GCM	:	Global Circulation Model
NWP	:	Numerical Wather Prediction
OI	:	Optimal Interpolation
RF	:	Recursive Filter
INRIA	:	Institut National de Recherche en Informatique et en Automatique
r.m.s.	:	Root Mean Sqare
NASA	:	National Aironautics and Space Administration
NOAA	:	National Ocean and Athmospheric Administration
UCAR	:	University Cooperation for Atmospheric Research
CDAAC	:	COSMIC Data Analysis and Archive Center
GPS	:	Global Positioning System
SOAR	:	Second Order Autoregressive Function
FGAT	:	First Guess at Appropriate Time
ESA	:	European Space Agency
NCEP	:	National Climate and Environmental Prediction
BFGS	:	Broyden-Fletcher-Goldfarb-Shanno Methode
NPOESS	:	National Polar Orbiting Environmental Satellite System
GPSOS	:	GPS Occultation Sensor

D

Namelist Program

- UTref

  Time layer of grib-file to be used, Options: 00, 06, 12, 18

- gribfile

  Name of input grib-file

- inputmes

  Name of input measurement file

- input_stdev_T

  Name of input temperature standard deviation file

- input_stdev_Q

  Name of input specific humidity standard deviation file

- input_corr_T

  Name of input vertical temperature correlation file

- input_corr_T_H

  Name of input horizontal temperature correlation file

- input_corr_Q

  Name of input vertical specific humidity correlation file

- input_corr_Q_H

  Name of input horizontal specific humidity correlation file

- input_corr_Psur

  Name of input horizontal surface pressure correlation file

- output_path
  Absolute path to write output files
- input_grib_path
  Absolute path to grib files
- input_obs_path
  Absolute path to observation files
- input_errors_path
  Absolute path error characteristic files
- Switch_background_error_model
  Define used background error model, Options: 1, 2, 3 (Standard choice)
- Switch_background_corr_model
  Define used background correlation (vertical) model, Options: 1 Gauss like drop off, 2 correlations from input files (Standard choice)
- Switch_filter_response_test
  Trigger filter test output, Options: 0 (Standard choice),1
- Filter_pass
  Define number of filter passes, Options: 4, 6 (Standard choice)
- Switch_deltaN_Calculation 0 (Standard choice), 1 (use TLM)
- switch_Interpol_operator_ad_test
  Trigger test of adjoint interpolation operator, Options: 0 (Standard choice),1
- switch_operator_tlm_test
  Trigger test of tangent linear interpolation operator, Options: 0 (Standard choice),1
- switch_operator_ad_test
  Trigger test of adjoint observation operator, Options: 0 (Standard choice),1
- gridX
  Longitude dimension of background grid , Options: 64, 128 (Standard choice)
- gridY
  Latitude dimension of background grid , Options: 21, 64 (Standard choice)
- gridZ
  Number of vertical levels of background grid 60 (Standard choice)
- Stdev_Psur
  Surface pressure standard deviation 250 Pa (Standard choice)

- corr_length_N

  Correlation lenght for Switch_background_corr_model = 1, 5.0 (Standard choice)

- rel_error_N

  Relative standard deviation for Switch_background_error_model = 1, 3.0 (Standard choice)

- corr_length_Q

  Correlation lenght for Switch_background_corr_model = 1, 3.0 (Standard choice)

- rel_error_Psur

  Relative standard deviation for Switch_background_error_model = 1, 3.0 (Standard choice)

- corr_length_Psur

  Correlation lenght for Switch_background_corr_model = 1, 3.0 (Standard choice)

- rel_error_Q

  Relative standard deviation for Switch_background_error_model = 1, 22.0 (Standard choice)

- corr_length_T

  Correlation lenght for Switch_background_corr_model = 1, 3.0 (Standard choice)

- rel_error_T

  Relative standard deviation for Switch_background_error_model = 1, 1.0 (Standard choice)

- methode 3 (Standard choice), (1,2 *Not Operational*)

- Nformula

  Define formula to calculate refractivit *Obsolet*

- switch_calc_BH_BV

  Devine used correlations Options: 1 vertical & horizonta (Standard choice), 2 only , 3 only

- termination_criteria

  Define termination criteria for minimisation cycle Options 1 defined by max_iteration (Standard choice), 2 defined by min_cost_diff, 3 defined by max_grad

- mmax

  Parameter for minimisation routine 21 (Standard choice)

- max_iteration

  Defines maximal number of cost function and gradient evaluations, 20 (Standard choice for operational use)

- min_const_unconst

  Constrained or unconstrained minimisation *Not Operational*

- max_grad

  Minimal projected gradient to abord minimisation 1.0^{-10} (Standard choice)

- min_cost_diff

  Minimal cost function difference to abord minimisation 10.0 (Standard choice)

- VInterpolation

  Choice of vertical interpolation *Not Operational*

- Switch_Quality

  Activate quality check of observations Options 0, 1 *Not Operational*

- Switch_H_geopot_P

  Define vertical coordinate grid Options 1 geometric height (Standard choice), 2 geopotential height, 3 pressure levels (*Not Operational*)

- Switch_BV_mean_all

  Use global mean vertical standard deviations or every single profile Options 1 mean (Standard choice) , 2 all profiles

- Assim_mod

  Defines used assimilation mode, Options: 1 N to N assimilation, 2 N to TQP assimilation

- Switch_recalculate_Zdim

  Update vertical grid after every recalculation of background fields Options 0 no (Standard choice), 1 yes

- Switch_transforms

  Turn on/off control space transformations Options 0 on, 1 off *Not Operational*

- Switch_obs_corr

  Define vertical observation covariance model Options: 1 linear model, 2 realistc model (Standard choice)

- Convergece_Constant

  Used for abort condition 1.0D-5 (Standard choice)

- gridZ_start_N

  Define first vertical background level 1 (Standard choice)

- gridZ_start_T

  Define first vertical background level 1 (Standard choice) *Not Operational*

- gridZ_start_Q

  Define first vertical background level 1 (Standard choice) *Not Operational*

- gridZ_start_P

  Define first vertical background level 1 (Standard choice) *Not Operational*

- gridZ_end_N

  Define last vertical background level 60 (Standard choice)

- gridZ_end_T

  Define last vertical background level 60 (Standard choice) *Not Operational*

- gridZ_end_Q

  Define last vertical background level 60 (Standard choice) *Not Operational*

- gridZ_end_P

  Define last vertical background level 60 (Standard choice) *Not Operational*

- gridZ_level_P

  Define last vertical background surface pressure level 1 (Standard choice)

- corr_levela

  To define simple linear correlation model 15.0 (Standard choice)

- corr_levelb

  To define simple linear correlation model 60.0 (Standard choice)

- corr_length_o_levela

  To define simple linear correlation model 2.0 (Standard choice)

- corr_length_o_levelb

  To define simple linear correlation model 1.0 (Standard choice)

- Y_tropo

  Relative standard deviation at tropopause height 0.4 (Standard choice for CHAMP data)

- X_tropo

  Tropopause height 15 km (Standard choice for CHAMP data)

- a2

  Parameter for observation error covariance calculations 4.4610 (Standard choice for CHAMP data)

- a4

  Scale height for the error increase over the stratosphere 11.9 (Standard choice for CHAMP data)

- LevelA_quality
  Not Used
- LevelB_quality
  Not Used
- LevelC_quality
  Not Used
- LevelD_quality
  Not Used
- ErrorlevelA_quality
  Not Used
- ErrorlevelB_quality
  Not Used
- ErrorlevelC_quality
  Not Used
- ErrorlevelD_quality
  Not Used
- Errorlevel_constant_quality
  Not Used
- quality_parameter_mes
  Factor to multiply measurement increment in quality check *Not Operational*
- quality_parameter_bac
  Factor to multiply background increment in quality check *Not Operational*
- LevelA
  Height level for linear observation error model, 0.0 (Standard choice)
- LevelB
  Height level for linear observation error model, 10.0 (Standard choice)
- LevelC
  Height level for linear observation error model, 35.0 (Standard choice)
- LevelD
  Height level for linear observation error model, 60.0 (Standard choice)
- ErrorlevelA
  Relative standard deviation for linear observation error model, 3.0 (Standard choice)

- ErrorlevelB

  Relative standard deviation for linear observation error model, 0.20 (Standard choice)

- ErrorlevelC

  Relative standard deviation for linear observation error model, 0.20 (Standard choice)

- ErrorlevelD

  Relative standard deviation for linear observation error model, 3.50 (Standard choice)

- Errorlevel_constant

  Relative standard deviation for linear observation error model, 0.20 (Standard choice)

- LOV

  Not Used

E

Program Flow Chart

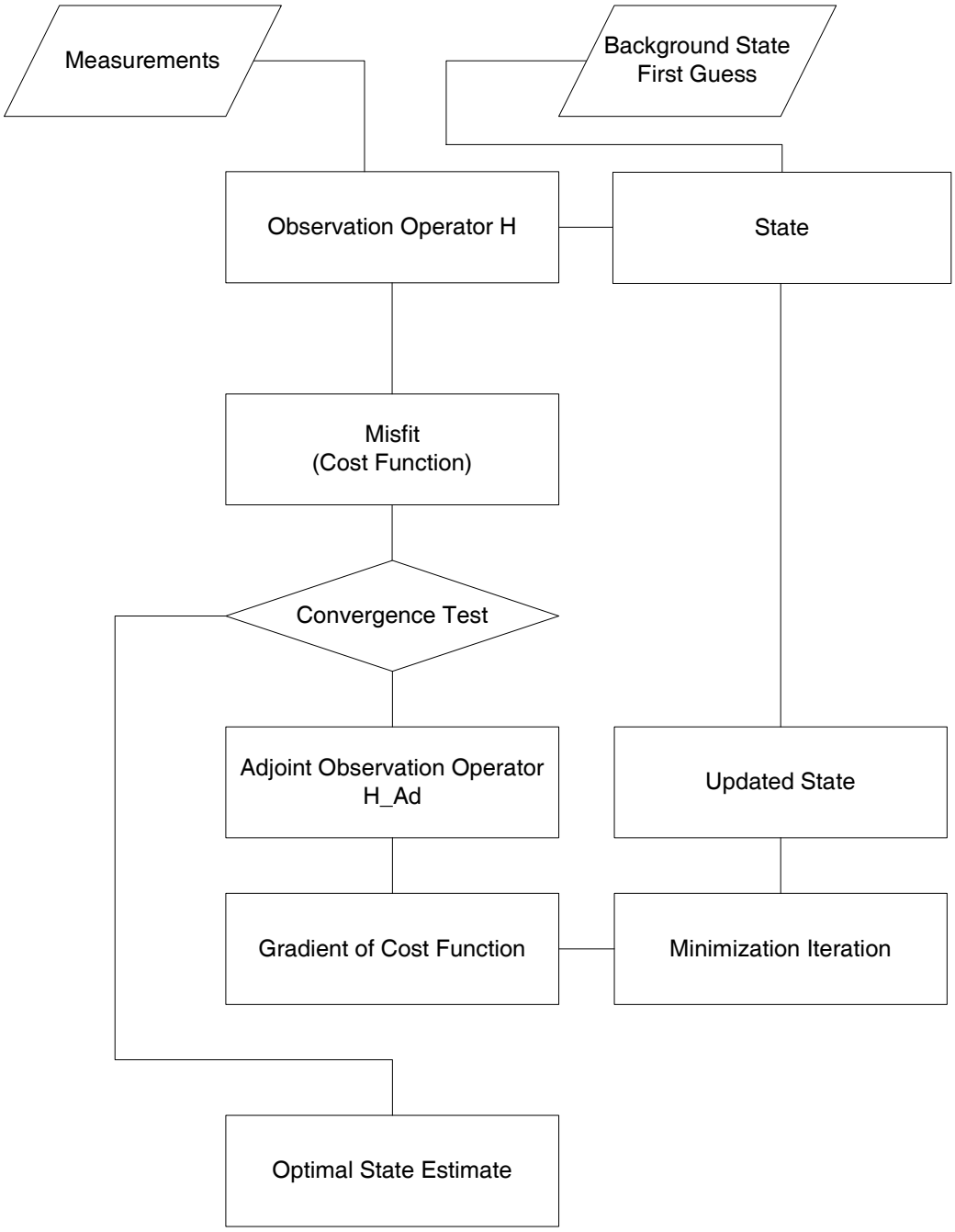

Figure E.1: Principal program flow chart

F

Useful Links

ESA	:	www.esa.int
ECMWF	:	www.ecmwf.int
EUMETSAT	:	www.eumetsat.int
TAPENADE Ad Compiler	:	www-sop.inria.fr/tropics/tapenade.html
Adjoint Compiler	:	www.autodiff.org
DMI	:	www.dmi.dk
MPI Hamburg	:	www.mpimet.mpg.de
Lexikon der Fernerkundung	:	www.fe-lexikon.info
WMO	:	www.wmo.int
Data Assimilation Research Center	:	darc.nerc.ac.uk
Weather Research and Forecasting Model	:	wrf-model.org
MM5 Assimilation Homepage	:	www.mmm.ucar.edu/3dvar/
Geospatial Information	:	earth-info.nga.mil/
CHAMP Homepage	:	op.gfz-potsdam.de/champ/index_CHAMP.html
GENESIS	:	www-genesis.jpl.nasa.gov
Earth Observation Handbook	:	
Numerical Recipies	:	www.nr.com
IPCC	:	www.ipcc.ch/
Ad Copmpiler	:	www.fastopt.de
JPL Genessis Page	:	www-genesis.jps.nasa.gov

List of Figures

List of Tables

References

[*Ao et al.* (2003)] Ao, C. O., T. K. Meehan, G. A. Hall, A. J. Mannuci, and G. Beyerle, Bias in GPS Occultaion Retrivals, *J. Geophys. Res.*, *108(D18)*, 4547, 2003.

[*Barker* (1999)] Barker, D., A general formulation for 3DVAR control variables, 1999.

[*Beyerle et al.* (2003)] Beyerle, G., J. Wickert, T. Schmidt, and C. Reigber, Atmospheric sounding by GNSS radio occultation: An analysis of negative refractivity bias using CHAMP observations, *J. Geophys. Res.*, 2003.

[*Burroughs* (2001)] Burroughs, W. J., *Climate Change A Multidicciplinary Approach*, Cambridge University Press, 2001.

[*Byrd et al.* (1994)] Byrd, R. H., L. Peihuang, J. Nocedal, and Z. Ciyou, A Limited Memory Algorithm for Bound Constrained Optimization, *Tech. rep.*, Northwestern University, 1994.

[*Dong and Nocedal* (1989)] Dong, L. C., and J. Nocedal, On the Limited Memory BFGS Methode for Large Scale Optimisation, *Mathematical Programming*, *5*, 503–528, 1989.

[*ECMWF* (2004a)] ECMWF, IFS Documentation, CY28r1, *Tech. rep.*, ECMWF, 2004a.

[*ECMWF* (2004b)] ECMWF (Ed.), *Recent Developments in Data Assimilation for Atmosphere and Ocean, Seminar Proceedings*, ECMWF, 2004b.

[*Edwards and Pawlak* (2000)] Edwards, P. G., and D. Pawlak, Metop: The space segment for Eumetsats Polar System, *ESA Bulletin 102*, pp. 6–18, 2000.

[*EUMETSAT* (2003)] EUMETSAT (Ed.), *2nd GRAS SAF User Workshop, Workshop Proceedings*, vol. EUM P 40, EUMETSAT, 2003.

[*F. Bouttier* (1999)] F. Bouttier, P. C., *Data Assimilation Concepts and Methodes, Meteorological Training Course Lecture Series*, 1999.

[*Fjeldbo et al.* (1971)] Fjeldbo, G. F., V. R. Eshleman, and A. J. Kliore, The Neutral Atmosphere of Venus as Studied with the Mariner V Radio Occultation Experiments, *Astron. J.*, *76*, 123–140, 1971.

[*Foelsche et al.* (2003)] Foelsche, U., G. Kirchengast, and A. K. Steiner, Global climate monitoring based on CHAMP/GPS radio occultation data, in *First CHAMP Mission Results for Gravity, Magnetic and Atmospheric Studies*, edited by C. Reigber, H. Lühr, and P. Scheintzer, pp. 397–407, Springer, 2003.

[*Gobiet and Kirchengast* (2004a)] Gobiet, A., and G. Kirchengast, Advancements of Global Navigation Satellite System Radion Occultation Retrieval in the Upper Stratosphere for Optimal Climate Monitoring Utility, *J. Geophys. Res.*, *109*, 2004a.

[*Gobiet and Kirchengast* (2004b)] Gobiet, A., and G. Kirchengast, Advancement of GNSS Radio Occultation Retrival in the Upper Stratosphere, in *1st International Workshop on Occultations for probing Atmosphere and Climate*, edited by G. Kirchengast, U. Foelsche, and A. K. Steiner, Springer, 2004b.

[*Gobiet et al.* (2004)] Gobiet, A., A. K. Steiner, C. Retscher, U. Foelsche, and G. Kirchengast, Algorithms Validation Based on CHAMP/GPS Data, *Tech. rep.*, Inst. for Geophys., Asrophys., and Metorol., Univ. of Graz, Austria, 2004.

[*Gorbunov* (2002)] Gorbunov, M. E., Canonical transform methode for processing radio occultation data in the lower troposphere, *Radio Sci.*, *37(5)*, 1057, 2002.

[*Gorbunov and Gurvich* (1998)] Gorbunov, M. E., and A. S. Gurvich, Microlab-1 Experiment: Multipath effects in the lower troposphere, *J. Geophys. Res.*, *103, D12*, 13,819–13,826, 1998.

[*Gorbunov and Kornblueh* (2003)] Gorbunov, M. E., and L. Kornblueh, Principles of variational assimilation of GNSS radio occultation data, *Tech. Rep. Report No.350*, Max-Plank-Institut für Meteorologie, Hamburg, 2003.

[*Gorbunov and Sokolovskiy* (1993)] Gorbunov, M. E., and S. V. Sokolovskiy, Remote sensing of refractivity from space for global observations of atmospheric parameters, *Tech. rep.*, Max Planck Institute for Meteorology, Hamburg, 1993.

[*Gorbunov et al.* (1996)] Gorbunov, M. E., S. Sokolovskiy, and L. Bengtsson, Space refractivity tomography of the atmosphere: Modeling of direct and invers problems, *Tech. rep.*, Max Planck Institute for Meteorology, Hamburg, 1996.

[*Hayden and Lorenc* (1995)] Hayden, C. M., and A. C. Lorenc, Recursive filter for objective analysis of meteorological fields. Applications to NESDIS operational processing, *J. Appl. Meteor.*, *34*, 3–15, 1995.

[*Hedin* (1991)] Hedin, A. E., Extension of the MSIS thermosphere model into the middle and lower atmosphere, *J. Geophys. Res.*, *96*, 1159–1172, 1991.

[*Hocke* (1997)] Hocke, K., Inversion of GPS meteorology data, *Annales. Geophysicae*, *15*, 443–450, 1997.

[*Hocke et al.* (1999)] Hocke, K., A. Pavelyev, O. I. Yakovlev, L. Barthes, and N. Jakowski, Radio occultation data analysis by the radioholographic methode, *J. Atmos. Terr. Phys.*, *61*, 1169–1177, 1999.

[*Hollingsworth and Lönnberg* (1986)] Hollingsworth, A., and P. Lönnberg, The statistical structure of short-range forecast errors as determined from radiosonde data. PartI: The wind field., *Tellus*, *38A*, 111–136, 1986.

[*Houghton et al.* (2001)] Houghton, J. T., Y. Ding, D. J. Griggs, M. Noguer, P. J. van der Linden, X. Dai, K. Maskell, and C. A. Johnson (Eds.), *Climate Change – The Scientific Basis*, Cambridge University Press, 2001.

[*INRIA* (2002)] INRIA, Software TAPENADE INRIA 2002, version 2.0, *Tech. rep.*, Domaine de Voluceau, Rocquencourt - BP 105, 78153 Le Chesnay Cedex, FRANCE, 2002.

[*Jakowski et al.* (2004)] Jakowski, N., S. Heise, A. Wehrenpfennig, and K. Tsybulya, *Ionospheric Radio Occultation Measurements and Space Weather*, pp. 383–392, in [*Kirchengast et al.* (2004)], 2004.

[*Jensen et al.* (2003)] Jensen, A. S., H.-H. Benzon, and A. Nielsen, Full spectrum inversion of radio occultation signals, *Radio Sci.*, *18(3)*, 1159, 2003.

[*Kalnay* (2003)] Kalnay, E., *Atmospheric Modeling, Data Assimilation and Predictability*, Cambridge University Press, 2003.

[*Kirchengast et al.* (2004)] Kirchengast, G., U. Foelsche, and A. Steiner (Eds.), *Occultations for Probing Atmosphere and Climate*, Springer, 2004.

[*Kirchengsat et al.* (2002)] Kirchengsat, G., J. Fritzer, and J. Ramsauer, End-toEnd GNSS Occultation Performance Simulator Version4 (EGOPS4) Software User Manual (Overview and Reference Manual), *Tech. rep.*, Inst. for Geophys., Asrophys., and Metorol., Univ. of Graz, Austria, 2002.

[*Kozo* (1997)] Kozo, N. (Ed.), *Data Assimilation in Meteorology and Oceanography: Theory and Practice, Special Issue of the Journal of the Meteorological Society of Japan*, vol. 75,1B, Meteorological Society of Japan, 1997.

[*Kursinski et al.* (1997)] Kursinski, R. E., G. A. Hajj, J. T. Schofield, R. P. L. K., and R. Hardy, Observing Eart's atmosphere with radio occultation measurements using the Global Positioning System, *J. Geophys. Res.*, *120*, 23,429–23,465, 1997.

[*Kursinski et al.* (1996)] Kursinski, R. E., et al., Initial results of radio occultation observations of Earth's atmosphere using the Global Positioning System, *Science*, *271*, 1107–1110, 1996.

[*Lauf* (1983)] Lauf, G. B., Geodesy and Map Projections, *TAFE Publications Unit*, 1983.

[*Lorenc* (1992)] Lorenc, A. C., Analysis methodes for numerical weather prediction, *Qart. J. Ray. Meteor. Soc.*, *112*, 1177–1194, 1992.

[*Malberg* (2002)] Malberg, H., *Meteorologie und Klimatologie*, Springer, 2002.

[*Nichols* (2003)] Nichols, N. K., *Data Assimilation: Aims and Basic Concepts*, pp. 9–20, in [*Swinbank et al.* (2003)], 2003.

[*Parrish and Derber* (1992)] Parrish, D., and J. C. Derber, The National Meteorological's Cenetrspectral statistical interpolation analysis system, *Monthly Weather Review*, *120*, 1747–1763, 1992.

[*Person* (2003)] Person, A., *User Guide to ECMWF Forecast Products*, 2003.

[*Press et al.* (1987)] Press, W. H., B. P. Flannery, S. A. Teukolsky, and W. T. Vetterling (Eds.), *Numerical Recipes, The Art of Scientific Computing*, Cambridge University Press, 1987.

[*Raith* (1997)] Raith, W. (Ed.), *Bergmann-Schaefer – Erde und Planeten*, Walter de Gruyter, 1997.

[*Randel et al.* (2002)] Randel, W., M. L. Chanic, and C. Michaut, SPARC intercomparison of middel atmosphere climatologies, *Tech. rep.*, WCRP 116, 2002.

[*Rees* (1988)] Rees, D., PartI: Thermosphere Model, *Adv. Space Res.*, *8*, 1988.

[*Reigber et al.* (1995)] Reigber, C., P. Schwinzer, and A. Kohlhase, CHAMP - A challenging micro satellite payload for geophysical research and application, Feasibility study for DARA, Final report, *Tech. rep.*, Geo Forschungs Zentrum Potsdam, Germany, 1995.

[*Reigber et al.* (2003)] Reigber, C., H. Lühr, and P. Scheintzer (Eds.), *First CHAMP Mission Results for Gravity, Magnetic and Atmospheric Studies*, Springer, 2003.

[*Rodgers* (2000)] Rodgers, C. D., *Inverse Methods for Atmospheric Sounding: Theory and Practice*, World Scientific, 2000.

[*Roeckner et al.* (2003)] Roeckner, E., et al., The Atmospheric General Circulation Model ECHAM5 PartI, *Tech. Rep. Report No.349*, Max-Plank-Institut für Meteorologie, Hamburg, 2003.

[*Salby* (1996)] Salby, M. L., *Fundamentals of Atmospheric Physics*, Academic Press, 1996.

[*Sokolovskiy* (2003)] Sokolovskiy, S. V., Effects of superrefraction on inversions of radio occultation signals in the lower troposphere, *Radio Sci.*, *38(3)*, 1058, 2003.

[*Sokolovskiy and Hunt* (1996)] Sokolovskiy, S. V., and D. Hunt, Statistical Optimisation Approach for GPS/Met Data Inversions, paper presented at the URSI GPS/Met Workshop, Tucson, Arizona, in *URSI GPS/Met Workshop*, 1996.

[*Steiner* (2004)] Steiner, A. K., Error Analyses of Refractivity Profiles Retrieved from CHAMP Radio Occultation Data, *Tech. Rep. Scientific Report 04-02*, Danish Meteorological Institute, 2004.

[*Steiner and Kirchengast* (2004)] Steiner, A. K., and G. Kirchengast, *Ensamble-Based Analysis of Errors in Atmospheric Profiles Retrieved from GNSS Occultation Data*, pp. 149–160, in [*Kirchengast et al.* (2004)], 2004.

[*Swinbank et al.* (2003)] Swinbank, R., V. Shutayaev, and W. Lahoz (Eds.), *Data Assimilation for the Earth System, Nato Science Series*, Kluwer Academic Publishers, 2003.

[*Vorobev and Krasnilnikova* (1994)] Vorobev, V. V., and T. G. Krasnilnikova, Estimation of the Accuracy of the Atmospheric Refracive Index Recovery from Doppler Shift Measurements at Frequencies Used in the NAVSTAR System, *Phys. Atmos. Ocean*, *29*, 602–609, 1994.

[*Wickert* (2002)] Wickert, J., Das CHAMP-Radiookkultationsexperiment: Algorithmen, Prozessierungssystem und erste Ergebnisse, *Tech. Rep. Scientific Technical Report STR02/07*, GeoForschungsZentrum Potsdam, Germany, 2002.

[*Wickert et al.* (2002)] Wickert, J., T. Schmidt, C. Marquardt, C. Reigber, K. H. Neumayer, G. Beyerle, R. Galas, and L. Grunwald, GPS radio occultation with CHAMP: First results and status of the experiment, Proc. of IAG Scientific Assambly, 2.-7. September, Budapest, in *Proc. of IAG Scientific Assambly*, vol. 125, 2002.

[*Wickert et al.* (2001)] Wickert, J., et al., Atmosphere sounding by GPS radio occultation: First results from CHAMP, *J. Geophys. Res.*, *28*, 3263–3266, 2001.